NASA
Technical
Paper
2288

February 1984

Molecular Clouds and Galactic Spiral Structure

Thomas M. Dame

NASA

NASA Technical Paper 2288

1984

Molecular Clouds and Galactic Spiral Structure

Thomas M. Dame

Goddard Institute for Space Studies
New York, New York

National Aeronautics and Space Administration

Scientific and Technical Information Branch

TABLE OF CONTENTS

ACKNOWLEDGEMENTS

I wish to express my sincere appreciation to my thesis advisor, Patrick Thaddeus, for his constant encouragement, contagious enthusiasm, and tireless efforts at improving this work. Each time I left his office it was with a renewed sense of excitement about my work and with a determination to be a better scientist.

Special thanks also go to Richard Cohen, whom I considered my second advisor. He was a constant source of information on every aspect of my work and his critical and insightful thinking was of great help to me on innumerable occasions.

I would like to thank all the members of the Columbia faculty for their concern and guidance throughout my graduate work. Bruce Elmegreen, in particular, provided many cheerful and helpful discussions.

I am grateful to my fellow graduate students for their encouragement and friendship, to Joe Montani, Dennis Mumma, and Sam Palmer for their assistance in keeping the telescope running smoothly, and to Alison Smith for her help with the data analysis.

Finally, I would like to express my deepest gratitude to my father, who provided daily support and encouragement through many years of hard work culminating with this thesis.

I. INTRODUCTION

A. Molecular Clouds and Spiral Structure

Until the late 1960's, there was little evidence that molecules were an important component of the interstellar gas. The interstellar medium was thought to consist mainly of atomic hydrogen, either in the form of neutral hydrogen HI clouds or in the form of ionized HII regions surrounding bright, young stars, most of the mass being HI. The only direct observations of interstellar molecules came from optical absorption lines, which indicated the existence of small amounts of CH, CH^+, and CN in neutral clouds. Even the detection of radio emission from the OH radical (Weinreb et al. 1963) did not alter the view that molecules in space were rare, since the relative abundance of OH/H was apparently low. It was only following 1968 with the advent of millimeter-wave observations of the rotational transitions of molecules, particularly the CO molecule, that our concept of the interstellar medium changed drastically.

Today molecules are known to be a major component of the interstellar medium. The new field of interstellar chemistry has flourished with the discovery of over 50 molecules ranging from simple diatomics such as CO and CS to long linear carbon chains, the largest being $HC_{11}N$.

In the inner galaxy, the fraction of gas in molecular form is comparable to that in atomic form. Much of this molecular gas, primarily H_2, is contained in giant clouds with masses in excess of 10^6 $M_\odot$ (see chapter VIII). These giant clouds, now believed to be the most massive objects in the galaxy, are the main sites of massive star formation. As such, they are providing a means of investigating the process of star formation on a galactic scale.

Since its discovery over a decade ago, millimeter-wave emission from the CO molecule has proven to be the best general-purpose tracer of the molecular component of the interstellar medium. The $J = 1 \rightarrow 0$ rotational transition of CO could almost be said to be the molecular analog of the 21-cm line for the study of galactic structure. Its importance lies in the fact that molecular hydrogen, by far the most abundant molecule, has no radio frequency spectrum (it has no dipole moment and hence no electric-dipole rotational transitions, and the intervals between its rotational levels in any case lie in the middle infrared). Although typically four to five orders of magnitude less abundant by number than H_2, CO can be easily detected in virtually all dark and molecular clouds, and the ratio of CO to H_2 appears to be reasonably constant over a wide range of physical

conditions (Thaddeus 1977). Thus CO is an excellent qualitative molecular tracer and is also useful as a rough quantitative probe.

A principal reason for carrying out the large-scale galactic CO surveys is the hope that molecular clouds may trace the spiral structure of the galaxy more clearly than either the diffuse atomic gas or the HII regions. This hope was based on a number of theoretical and observational results. Local observations have revealed that essentially all OB associations are accompanied by molecular clouds (Blitz 1978), and massive molecular clouds are rarely observed without accompaning OB stars (Elmegreen and Elmegreen 1979). Thus giant molecular clouds appear to be intimately related to OB associations and their accompanying HII regions - the classic tracers of spiral arms in external galaxies. It is also apparent that CO is an excellent tracer of dust as well as of H_2 (Dickman 1975). This is consistent with the generally accepted belief that H_2 is formed from H by the reaction $H + H \rightarrow H_2$ on the surfaces of interstellar dust grains (Goodman 1978). The close relationship between dust and molecules again suggests that molecular clouds should be a good tracer of spiral structure, since the dust lanes in external galaxies are excellent optical tracers of spiral arms (Lynds 1970).

Theoretical support for the notion that molecular clouds are formed in spiral arms is provided by the density-wave theory of spiral structure. Roberts (1969) has shown that the interstellar gas could respond in a highly non-linear way to the passage of a spiral density wave, resulting in a spiral shock near the potential minimum of the wave. This shock front could initiate the formation of molecular clouds within spiral arms (Elmegreen 1979).

Despite high initial expectations, the usefulness of CO as a spiral tracer is currently a very controversial issue, some 7 years after the first large-scale surveys were reported. Scoville, Solomon, and Sanders (1979) have asserted "it is clear from the absence of a recognizable spiral form ... that most of the clouds cannot be situated within a regular pattern of spiral arms", while Burton and Gordon (1978) noted that "clearly there is some higher-order arrangement of dark clouds within the Galaxy, be it simple clustering or a large-scale design such as spiral structure". By contrast, my colleagues and I, in a preliminary discussion of our CO survey, stated that "molecular clouds are in fact an excellent tracer of spiral arms" (Cohen et al. 1980). Since the degree of confinement of molecular clouds to spiral arms has direct implications

for the lifetime of the clouds and, in turn, on the amount of molecular gas in the Galaxy, these are also very controversial issues.

In this thesis, I will argue that molecular clouds are relatively short-lived galactic objects which act as excellent spiral-arm tracers. The arguments will be primarily based on the results of a galactic CO survey carried out with the Columbia 4-foot telescope. A distinct advantage of this survey over others which exist is its much more complete sampling, made possible by the Columbia telescope's relatively large beam and the dedication of the instrument to survey work on molecular clouds. While other surveys (Scoville, Solomon, and Sanders 1979; Burton and Gordon 1978) observed total areas of less than 0.5 deg^2, the Columbia survey observed an area of 50 deg^2.

The discussion will emphasize the high-contrast emission features and deep minima in the CO data which are indicative of well-developed spiral structure. It will be shown that essentially the same large-scale features exist in both the CO and 21-cm data, with the CO features generally being more clearly defined and of higher contrast. I will argue that the higher contrast of the CO data makes it qualitatively superior to the 21-cm line for the study of galactic spiral structure.

In recent years, the use of the 21-cm line as a galactic probe has been questioned with the realization that subtle kinematic effects can strongly influence 21-cm spectra (Burton 1971). One could never be sure to what extent the large-scale 21-cm features reflected structure in the galactic velocity field or HI distribution. I will argue that kinematic effects cannot reasonably account for the high-contrast CO spiral features, and that CO observations should allow significant new progress to be made in the study of the large-scale structure of the Galaxy.

Some modest initial progress is made in this thesis. A simple spiral model is developed which accounts well for the large-scale features in the CO data and appear to represent a reasonable first-order approximation to the spiral structure of the inner galaxy. The validity of the model is further tested by computing distances and masses for the largest molecular clouds detected by the survey. The galactic distribution of these clouds fits an overall spiral pattern similiar to that inferred from the modeling.

B. Previous work

The earliest unbiased galactic surveys of CO (Burton, et al. 1975; Scoville and Solomon 1975) were very poorly sampled and generally confined to the galactic

plane. Because of this, both groups were unable to draw any conclusions on the possibility of spiral structure in the data. Nevertheless, their fundamental result concerning the galactic radial distribution of CO emission suggested that molecular clouds were very young objects.

The CO surveys of Burton et al. (1975) and Scoville and Solomon (1975) were adequate to show that the galactic radial distribution of CO emission was very similar to that of many extreme Population I objects and quite different from that of neutral hydrogen. This extreme Population I type of radial distribution, sometimes referred to now as the "molecular ring" distribution, is characterized by very strong emission near the galactic center, very weak emission between 0.5 kpc and 4 kpc, then a sharp rise to a broad peak about 2 kpc wide centered near R = 5.5 kpc. Extreme Population I objects and tracers which show a very similar radial distribution include HII regions (Burton et al. 1975), H166α emission (Lockman 1976), supernova remnants (Kodaira 1975), pulsars (Taylor and Manchester 1977), gamma rays (Strong 1975), and far-infrared emission (Hayakawa et al. 1977). This similarity suggests that molecular clouds should be included in the list of short-lived Population I objects which are the canonical tracers of spiral structure.

As the amount of observational data increased, so did the controversy concerning the degree of confinement of molecular clouds to spiral arms and the lifetime of the clouds. Based on a larger but still severely undersampled survey consisting of 1100 spectra, Scoville, Solomon, and Sanders (1979) concluded that molecular clouds existed in both arm and interarm regions and consequently must last more than 10^8 years. This conclusion was reached by transforming the data from the observed longitude-velocity plane into galactocentric coordinates of radius and azimuth, to yield a map of clouds projected on the plane as seen from above. In order to resolve the distance ambiguity involved in this transformation they identified certain CO features as being associated with HII regions for which the ambiguity had been resolved from absorption line studies. In other cases, the latitude of the feature was used -- high-latitude features were assumed to be at the near distance, low-latitude features at the far distance. The absence of a spiral pattern in the resulting picture led them to conclude that most of the clouds were not confined to a regular pattern of arms.

An additional argument presented by Scoville, Solomon, and Sanders (1979) for a long lifetime for molecular clouds is based on their determination that the plurality of the interstellar gas in the inner galaxy is

in molecular form (Solomon, Sanders, and Scoville 1979; Scoville and Hersh 1979). This determination was based on an adopted value of $N(H_2)/W_{CO}$, where $N(H_2)$ is the molecular-hydrogen column density and W_{CO} is the velocity-integrated CO emission $W_{CO} = \int T(CO)\, dv$. The value of this ratio is still a point of controversy today. If the hydrogen in the inner galaxy is constantly cycled through molecular, atomic, and ionic forms at a steady-state rate, and if most of the hydrogen at any time is in molecular form, then continuity requires that a given hydrogen atom spend more of its time as H_2 than as H or H^+. Taking 10^8 years as a typical timescale for the lifetime of a low-density atomic or ionized region, they estimated that molecular clouds must live at least this long, and possibly as long as 10^9 years.

A third argument supporting this point of view was raised by Solomon and Sanders (1980) and later by Liszt and Burton (1981). They pointed out that there are no large gaps in the distribution of molecular clouds along the terminal velocity curve over the longitude range $23° < \ell < 50°$. If molecular clouds were confined exclusively to the Sagittarius and Scutum spiral arms, the emission along the terminal-velocity ridge between their tangent directions at $\ell = 30°$ and $\ell = 50°$ would be weak or absent. The relatively high emission in this

region was cited as evidence for a low arm-interarm contrast for molecular clouds. The persistence of the terminal-velocity ridge is probably the most obvious and most often-cited characteristic of the CO data which is claimed to support a low arm-interarm contrast. In chapter VII, we will investigate whether these claims are justified.

The preliminary survey of Burton et al. (1975) mentioned above was greatly extended by Burton and Gordon (1978). This survey, also carried out on the NRAO 36-ft. telescope, was primarily confined to the galactic plane between 10° and 82° in longitude. Observations were taken every 0°.2 with an antenna beam whose full width at half power was 1.2' = 0°.02. In analyzing the data, a simple stochastic model was devised in order to study the cloud-cloud velocity dispersion, the typical cloud size, and the mean separation between clouds. The model distributed clouds randomly within the galactic disk, the density of clouds varying only with galactic radius. It was found that this azimuthal symmetry in the cloud distribution was one of the major shortcomings of the model. They noted that the data clearly indicated some higher-order arrangement in the galactic distribution of molecular clouds. Whether this higher-order arrangement took the form of a large-scale spiral pattern or not they were unable to say.

This ambivalent position on the possible existence of molecular spiral arms was maintained by Liszt and Burton (1981). With stochastic numerical models they demonstrated that, as with HI (see, e.g., Burton 1971), the existence of apparent spiral structure in the longitude-velocity map does not necessarily imply a genuine arm-interarm contrast in the galactic distribution of the clouds. Despite the fact that molecular clouds occupy only about 1 % of the volume of the galactic layer, the CO data is still influenced by the same well-known velocity crowding and blending effects which complicate the interpretation of the HI spectra -- apparent CO spiral structure can be produced by large-scale streaming motions. Furthermore, they pointed out that even if arm-interarm contrast exists for molecular clouds, it does not necessarily imply that the clouds are young, since even very long-lived clouds can show arm-interarm contrast, provided they move more quickly through the interarm regions. In chapter VI, I will argue that it is unlikely the very large arm-interarm contrast seen in our data can be due solely to such kinematic effects.

Yet another position on the question of CO spiral arms and the age of molecular clouds was developed in a series of papers by Frank Bash and co-workers (Bash and Peters 1976; Bash, Green, and Peters 1977; Bash 1979).

They proposed a model in which molecular clouds created at a two-armed spiral shock wave were assumed to orbit as ballistic particles under the influence of the density-wave spiral potential. Clouds were assumed to exist until some adjustable "cutoff" age, determined by comparing the maximum observed radial velocity of CO clouds at each longitude with what is predicted by the model. If the clouds live for only a short time, they will not move far from their place of birth within the spiral arms and consequently will not be observed near the terminal velocity at longitudes displaced from the tangent directions of the arms. Bash (1979) found that the CO terminal velocities and the CO longitude-velocity map could be fit by a cutoff age of 40 million years.

The validity of this cutoff age was tested by surveying CO emission in and around 63 open star clusters whose earliest stars ranged from O5 to B4 (Bash, Green, and Peters 1977). It was found that about 90 % of the clusters young enough to still contain O stars also had associated CO clouds, but less than 10 % of the clusters whose O stars had evolved off the main sequence had associated CO clouds. There appeared to be a cutoff in CO emission for clusters older than about 15 million years - the main sequence lifetime of a B0 star. The difference between this cutoff age and the dynamical cutoff of 40 million years determined from the run of CO

terminal velocities was attributed to the time required for the molecular cloud to form stars after its birth at the spiral shock. They could not determine whether the clusters dissipated their parent molecular clouds or merely separated from them.

More observational data in support of a large arm-interarm contrast for molecular clouds was presented by Stark (1980). Using the 7-meter antenna at Bell Laboratories, he observed ^{13}CO in three regions, each about one degree square, which sampled emission near the tangent directions of the Scutum and Sagittarius arms and at an intermediate direction between the arms. The observations revealed that both the average size and number of molecular clouds were significantly increased in the spiral-arm regions. These results are particularly important because with the excellent Bell 7-meter telescope the low cloud density in the interarm region cannot be blamed on low sensitivity or poor sampling. Observations were taken on a 3 arc-min grid (every other beam) at an rms noise level of 0.1 K. Even dark clouds only a few parsecs in size could be detected.

After examining the available observational and theoretical evidence, Blitz and Shu (1980) concluded that the lifetime of giant molecular clouds must be relatively short. They argue that the kinetic energy imparted to the clouds by the massive stars they produce is probably

much larger than the gravitational binding energy of the clouds, even if the process if very inefficient, and so the clouds should be completely disrupted in a few times 10^7 years. In order to refute the notion that molecular complexes might exist for long periods without forming massive stars, they point to the observed clumpiness of the complexes (see, e.g., Blitz 1978; Crutcher, Harthopf, and Giguere 1978), which in the absence of massive stars probably could not be maintained for more than a few times 10^7 years.

C. Present Work

The large CO survey on which this thesis is primarily based was carried out between 1977 and 1979 with the Columbia 4-foot millimeter-wave telescope. As the survey progressed, its more complete sampling began to reveal spiral features and interarm regions which had largely escaped notice in the more undersampled surveys. With approximately half of the Columbia survey data in hand, Cohen, Tomasevich, and Thaddeus (1979) first reported the detection of large-scale features in the CO data which resembled 21-cm features which had been identified with spiral arms. As the survey neared completion, the CO spiral arms became increasingly clear and, in fact, emerged as the dominant morphological features of the data. The completed survey was briefly

discussed by Cohen et al. (1980). In that paper, we reported the identification of molecular counterparts to five of the classical 21-cm spiral arms: the Perseus, Local, Sagittarius, Scutum, and 4-kpc arms. These molecular arms were found to be better defined and of higher contrast than their 21-cm counterparts. We noted that the existence of CO spiral structure limited the lifetime of molecular clouds to less than 10^8 years, the time required for interstellar matter to cross between spiral arms. This thesis is, in large part, an amplification of the ideas presented in that paper.

Using the results of a well-sampled CO survey of the first galactic quadrant, I will argue that molecular clouds are relatively short-lived galactic objects which act as excellent large-scale tracers of our galaxy's spiral arms.

The next chapter contains a description of the telescope used to take the data and a discussion of the techniques employed for collecting, calibrating, and reducing the data. In chapter III the basic survey data is presented in various forms and is briefly discussed. Consideration of the galactic molecular-cloud distribution begins in chapter IV with a discussion of the average thickness, displacement, and radial distribution of the galactic CO layer. This is followed in chapter V by a discussion of CO spiral

structure and the lifetime of molecular clouds. I will discuss the aspects of the data which support a high arm-interarm contrast for molecular clouds as well as the aspects which, at least on the surface, do not appear to support this view. The actual arm-interarm contrast for the CO emission and for molecular clouds is considered in chapter VI. This is followed, in chapter VII, by the presentation of a simple spiral model which probably represents a reasonable first-order approximation to the galactic distribution of molecular clouds. Finally, in chapter VIII, distances and masses for the largest molecular clouds in the inner galaxy are determined. The locations of these clouds in the galactic plane are shown to support the spiral pattern presented in chapter VII.

II. INSTRUMENTATION AND OBSERVING TECHNIQUES

A. The Columbia Sky Survey Telescope

The observations presented in this thesis are mainly of the J = 1 → 0 rotational transition of CO at 115.2712 GHz, supplemented by a limited number of observations of the rare isotopic species ^{13}CO at 110.2014 GHz. Both species were observed with the 4-foot millimeter-wave telescope on the roof of the Pupin Physics Laboratories at Columbia University, a facility operated jointly by Columbia and the Goddard Institute for Space Studies. This telescope has been in operation since 1974, and is generally used from October to May when atmospheric water vapor is low. The 5 main components of the telescope system - the antenna, mount and drive, receiver, spectrometer, and computer - are described briefly below.

1. Antenna

The antenna is a fast Cassegrain reflector (effective f/D=2.8) consisting of a 1.2 meter parabolic primary (f/D=0.375) and a 15 centimeter hyperbolic secondary. The rms surface accuracy of the primary was measured by the manufacturer, Philco Ford, to be 35 microns, or $\lambda/75$ at a wavelength of 2.6 mm. This is significantly better than the criterion for surface accuracy of $\lambda/40$ generally adopted for a diffraction limited system (Silver 1964).

To verify that the system was indeed diffraction limited after delivery and alignment, the antenna pattern was measured with a 115 GHz transmitter at a distance of 420 meters, and compared to the pattern predicted by scalar diffraction theory (Cohen 1978). The excellent agreement between the theoretical and observed patterns and the depths of the nulls between sidelobes - more than 28 dB - confirmed that the antenna surface and the alignment of the secondary and scalar feed were adequate to produce a diffraction limited system.

The above-mentioned scheme was also used to measure the beamwidth and main beam efficiency. The beamwidth (FWHM) is 8.3 arc min at the CO frequency and 79 % of the forward power is within the first nulls at 10 arcmin.

The antenna is housed in a 12-foot astrodome which rotates on a circular track under computer control. Observations are made through a slit about 4 feet wide which is covered by a screen of nylon fabric highly transparent to millimeter waves. The screen protects the telescope from the weather and enables the interior of the dome to be kept at a constant temperature.

2. The Mount and Drive

A schematic picture of the telescope and its mount and drive is presented in figure II-1. The altitude-azimuth mount is driven by direct-drive torque motors,

each able to exert a maximum torque of about 11 ft.lb. Each axis is equipped with a tachometer generator and a 16 bit (19.8 arc-sec resolution) optical shaft encoder. One hundred times per second the output of these devices is read by the computer and the torque commands are corrected. The magnitude of these torques is based on an approximate solution of the telescope-mount system's equations of motion. Because of the small size and mass of the antenna, changes in pointing can be accomplished swiftly and efficiently -- the telescope can acquire a new position 10 degrees away in less than one second. This rapid switching ability was especially valuable for the galactic-plane observations reported here, since emission-free comparison positions were usually several degrees off the plane.

It is impractical to check the pointing of a small millimeter-wave telescope with the planets, the standard "point" sources observed with larger telescopes, since they are extremely faint. The disk of the sun is used instead as the standard celestial source. By offsetting the telescope in azimuth and elevation beyond the limb of the sun, a computer program is able to locate the actual center of symmetry of the radio disk and compare it to the computed solar position. This pointing test, done every few days, yielded errors which were always less than 1.5 arcmin and generally less than 1 arcmin (1/8 of a beam).

To determine the pointing errors as a function of azimuth and elevation over the whole sky, an optical telescope collimated with the radio axis was used. The eyepiece of the optical telescope contains crosshairs centered on a circle the size of the solar image. The collimation was accomplished by first locating and tracking the center of the radio disk of the sun (by finding its center of symmetry) and then adjusting the alignment of the optical telescope until the solar image fell precisely within the circle. Once the optical telescope is collimated, pointing errors towards 50 or so bright stars widely distributed in azimuth and elevation were measured. These errors are used by a least-squares fitting routine which yields the average rms pointing error and corrections to the pointing parameters. These corrections generally produced only a negligible improvement in the pointing, the rms pointing error being on the order of 1 arcmin. Details of this "star-pointing" technique are given in the thesis of R. Cohen (1978).

As a further check on the pointing, a peak position in the molecular cloud associated with the HII region W51 (located nearly in the galactic plane at ℓ=49°.5) was observed at the start of each observing session. A mapping of the region indicated that a pointing error of more than half a beamwidth would produce a significant change in the integrated emission of the source.

3. The Receiver

Signal detection was accomplished by means of a room temperature, double sideband (DSB) superheterodyne-type receiver with a noise temperature of about 420 K (DSB). A block diagram of the receiver's main components is shown in figure II-2. The incoming signal was collected by the scalar feed horn and mixed with the local oscillator (LO) signal by means of a Ga-As Schottky-barrier diode mixer. A resonant ring injection cavity, designed and built by A. Kerr, was used to introduce the LO power into the mixer. Prior to the 1979-80 observing season, the LO signal was obtained from a phase-locked Varian klystron operating at 113.9 GHz. Subsequently, a klystron operating at half this frequency and followed by an efficient (~ 20 %) frequency doubler was used. The computer is interfaced with a Fluke synthesizer which controls the LO frequency via a conventional ("NRAO") phase-lock circuit.

The second stage or intermediate-frequency (IF) section is essentially a standard 21-cm receiver. The first IF at 1.39 GHz is amplified by a Micromega parametric amplifier with a noise temperature of 50 K and a gain of 17 dB. Further amplification is provided by a low-noise transistor amplifier with 30 dB of gain. A second local oscillator then down-converts the signal to 150 MHz. This second IF is further amplified (by about

35 dB) and sent to the spectrometer, located in the control room in the Columbia Astronomy Department one floor below the telescope.

4. The Backend

The spectrometer or backend, a 256-channel multifilter receiver of standard NRAO design (Mauzy 1974), had a frequency resolution of 250 kHz, corresponding to a velocity resolution of 0.65 km/sec and a total bandwidth of 166 km/sec. The total system is composed of an IF section, a filterbank, an integrator/multiplexer bank, and an analog-to-digital converter with computer interfacing. The 150 MHz signal from the receiver front end is divided by the IF section into 16 signals, each 4 MHz wide centered at 8 MHz. These 16 signals are passed through 16 identical filter boards, each containing 16 two-pole Butterworth filters followed by square-law detectors and post-detector amplifiers. Each group of 16 detected outputs is passed to the integrator/multiplexer board which integrates the data for 48 msec, then holds it 5 msec for readout to the computer through the analog-to-digital converter. The A/D converter has a 16:1 multiplexer to read the 16 multiplexed outputs of the integrator boards. The sucessive 48-msec samples are summed in the computer.

5. The Computer System

Telescope guidance and data acquisition were controlled by a Data General Nova 1200 minicomputer. A block diagram illustrating the main peripherals and telescope components to which the computer is interfaced is shown in figure II-3. During data acquisition, the computer accumulates data from the spectrometer and simultaneously controls the telescope's pointing. In addition to these primary tasks, the computer has enough free time left to execute user requested high-level programs, enabling the observer to reduce and analyze his data in real time.

The Nova 1200 computer is equipped with 64,000 bytes of core memory - sufficient to hold all the low-level assembly-coded programs necessary for telescope control and data acquisition, various data buffers, and many of the high-level programs available to the observer. Many more high-level programs reside on disk and are only compiled during execution. The largest buffer accumulates data from the backend until the completion of an observation, at which time it is written on disk.

Most of the storage capacity for the system is provided by a Control Data Corporation cartridge disk drive. The unit is equipped with 5 megabytes of storage on a fixed disk and an additional 5 megabytes on a removable disk cartridge. All of the system software is

permanently stored on the fixed disk while data is written to the removable disk cartridge. Each observer is assigned a disk cartridge capable of storing over 2000 spectra - typically an entire year's data.

The disk is supported by two IBM compatable tape drives (9 track, 12.5 ips, 800 bpi). Each observer dumps his data daily on a tape which is used to transport the data to the Goddard Institute for Space Studies for further processing. If both tape drives fail, a paper tape reader (300 cps) and paper tape punch (50 cps) are available as a backup storage system.

The main operator I/O device is a Tektronix graphics display terminal. Plots displayed on its CRT storage scope can be transferred to paper by means of a hard copy unit, and text hard copy can be produced on a matrix-type teleprinter. In addition, a teletype terminal provides a means of controlling the telescope from the dome. TV monitors in the control room and dome provide the observer with all the information he would normally need for monitoring the system. During observations, these displays are updated once per second.

The basic time standard is a crystal-controlled oscillator which sends an interrupt to the computer every sidereal millisecond. The computer keeps sidereal time (LST) by counting these interrupts and computes the Universal time (UT) using the first three terms of a

fractional expansion of the UT vs. LST. The UT and LST are displayed on the TV monitor and are periodically checked against accurate quartz clocks.

The telescope's control language or "Dictionary" is similar to the language FORTH developed at NRAO (Moore and Rather 1973) and now used at many observatories. The basic system consists of a compiler, interpreter, and a vocabulary of about 270 "permanent" words written in assembly language. New words can be defined in terms of the assembly-level words and pre-existing definitions. About 800 of these high-level commands are normally compiled from source code stored on disk. Users may also define new words directly from the terminal to meet particular needs.

B. Calibration and Observing Techniques

The previous section described the basic components of the telescope and the facilities available to all users; this section will discuss the specific techniques I used to collect, calibrate, and reduce the data for the first-quadrant CO work. The observing techniques for the galactic-plane and W44 surveys were nearly identical since W44 lies in the plane, and many spectra are common to both datasets. Data unique to W44, in particular some low spatial-resolution ^{13}CO observations, will be discussed in the context of that object (chap. VIII).

Good observing conditions in the millimeter-wave region generally prevail in New York from mid-October to mid-May, and about 6 hours per day can be devoted to the first quadrant when the weather is good. The galactic survey described here required all of the 1977-78 and 1978-79 seasons to complete: the additional observations needed to map fully the W44 complex required about 2 months during 1980-81.

Observations were taken when the optical depth of water vapor per air mass, as determined by antenna tipping, was less than 0.3. When the temperature on an outdoor thermometer was below freezing this criterion was met even on overcast days; above freezing clear skies were generally required. From October to May, 4 to 5 days per week on average were suitable for observing, but in mid-winter observations were often possible 6 or 7 days per week. On marginal days observations were generally confined to high elevations and were never taken at elevations below 28°.

The calibration of multichannel receivers requires a broadband source of radiation of known intensity. In the centimeter-wave band this source is usually a gas discharge tube; in the millimeter-wave band discharge tubes are too faint (the discharge becomes optically thin), and "chopper wheel" blackbody emitters are the preferred reference source (c.f., for example, Penzias

and Burrus 1973). In this method, the calibrating signal is the difference between an ambient blackbody and the sky. On the 1.2-meter telescope, the blackbody is a two-bladed chopper wheel coated with eccosorb, a carbon impregnated foam, which is alternately placed in front of, and removed from, the feed horn at a rate of 20 Hz. If the ambient temperature T_{AMB} and the atmospheric temperature T_{ATM} are nearly equal the calibrating signal is approximately proportional to

$$T_{AMB} - T_{ATM}(1 - e^{-\tau}) \approx T_{AMB}\, e^{-\tau}$$

where τ is the optical depth of the atmosphere at the signal frequency. The chopper-wheel technique is useful because the incoming spectral line is also attenuated by a factor $e^{-\tau}$, and the ratio of the line to the calibration signal is to first-order independent of τ.

In practice, a number of refinements to the basic chopper-wheel technique described by Penzias and Burrus (1973) are needed. Because the telescope is a double sideband receiver and the atmospheric attenuation is not equal at the two sideband frequencies, the calibration signals in the two sidebands differ somewhat. This is particularly troublesome for the ^{12}CO $J = 1 \rightarrow 0$ line since it lies on the shoulder of a pressure-broadened atmospheric O_2 line. A second refinement was needed to correct for the fact that the atmospheric temperature and

ambient temperature are not strictly the same, the sky generally being colder than the earth's surface. Since atmospheric absorption of the received spectral line is not fully compensated by sky emission, the atmospheric opacity must be determined and an elevation-dependent correction applied. Both of these refinements have been incorporated into the calibration procedure of Davis and Vanden Bout (1973).

A further refinement was added by Kutner (1978). The primary sources of atmospheric attenuation at the CO frequency are water vapor and molecular oxygen. Because the oxygen is well mixed throughout the troposphere and stratosphere, its opacity shows little seasonal variation, and its brightness temperature and opacity are nearly constant. Most atmospheric water vapor on the other hand is within a few kilometers of the ground and its opacity can change as rapidly as the weather. It was hence useful to approximate the atmosphere by a two-layer model in which attenuation is produced by a large-scale-height oxygen layer with relatively constant opacity and effective temperature, and a small-scale-height water layer with a variable opacity and effective temperature which must be measured frequently.

The chopper-wheel technique described by Kutner (1978) was used to express line intensities in terms of antenna temperature corrected for atmospheric absorption;

a further correction for beam efficiency yielded units of radiation temperature T_R, directly proportional to the radiation intensity I_ν by the Rayleigh-Jeans formula $I_\nu = 2kT_R/\lambda^2$. A 5 second calibration was performed before the start of each observation. The effective temperature and opacity of the water layer were determined every 6 hours, or more frequently when the weather was changing rapidly, by means of an antenna dipping which measures the sky brightness as a function of elevation angle and fits the data using the two-layer atmospheric model.

The power entering the spectrometer is the amplified sum of the radiation from space, local radiation (atmospheric emission, spillover, emission from the antenna surfaces and receiver waveguides, etc.), and continuum noise generated by the receiver. To remove the local and receiver contributions and hence to assure flat baselines, position switching was employed. At roughly 15-second intervals, the telescope was alternately switched between the observed position and emission-free reference positions. The on-source and off-source data are integrated separately by the computer until the completion of the observation, when they are subtracted to produce the final spectrum.

A list of the emission-free reference positions used is given in table 1. These positions were initially found by frequency-switching: changing slightly the

klystron and hence receiver frequency to generate a comparison spectrum rather than by moving the telescope off the source. They were then position-switched against each other to assure that they contained no emission stronger than the rms noise level of the survey (~0.4 K).

Towards the inner galaxy it was essential to have flat spectral baselines, as the CO Doppler structure covers a significant fraction of the spectral range of our spectrometer. It was difficult to obtain flat baselines since the reference positions had to be located well away from the intense galactic-plane emission. The further one has to switch in elevation between on and off positions, the greater is the difference in power entering the spectrometer and, in general, the poorer the baselines. It was found that position switching between the on position and a single off position often produced spectra with significant baseline curvature. To overcome this problem, 3 off positions, surrounding the on position, were used for each observation. The fraction of total observing time spent on each "off" was adjusted so that the time-weighted average of the vectors to the three off positions was exactly at the "on". This scheme generally produced baselines which were flat to within the noise. In cases where the linearity of the baselines was questionable, observations were repeated.

Each spectrum had a linear baseline removed and was smoothed to a resolution of 1.3 km/sec (2 channels). The baseline was removed by fitting a straight line to the emission-free ends of the spectrum. The spectra were smoothed by convolution with a Gaussian of full-width at half-maximum of 1.3 km/sec.

Each position was observed until the rms noise level of the smoothed spectrum was less than 0.45 K. This gave an adequate signal-to-noise ratio for typical galactic features with temperatures between 2 and 6 K. A typical observation including the time spent off source required ~10 minutes.

III. OBSERVATIONS

In this chapter, data from two large-scale CO surveys of the first galactic quadrant which I carried out over the last few years will be presented. The first of these, a well-sampled survey of the galactic plane, will be discussed at length since it is the main survey on which this thesis is based. The second, a low spatial-resolution survey with wide latitude coverage, will be discussed briefly at the end of the chapter; it contributes little to the main topic of this thesis, the CO distribution in the inner galaxy, but as chapter VIII shows is of value in computing masses for nearby clouds with large latitude extents.

The galactic-plane survey consists of 3083 CO spectra taken within 1 degree of the galactic plane between the galactic longitudes of 12° and 60°. A diagram which illustrates the spacing of observations is shown in figure III-1. A 1/2° strip centered on the galactic plane was fully sampled; elsewhere observations were taken every other beamwidth.

The spatial extent of the survey was constrained by limits on observing time and source elevation, but was adequate to cover most of the inner-galaxy emission. The observation of points at longitudes much less than 12° was impractical because of their low declination, the

galactic plane at ℓ = 12° being above 28° less than one hour per day. The high-longitude limit of 60° lies beyond the tangent direction of the Sagittarius arm and below a region ℓ = 60° to 80° which is known to be relatively deficient in HI and other spiral tracers (Gosachinskii and Rakhimov 1978). A preliminary out-of-plane survey by Cohen (1978) showed that the first-quadrant CO layer was only about 1°.2 thick (FWHM), and so a latitude range of 2° was adopted. As the data will show, this latitude range includes most of the emission from the thin disk of molecular clouds in the inner galaxy.

Since previous surveys of this region (Burton et al. 1975; Scoville and Solomon 1975) had not detected any CO emission at negative velocities or at velocities greater than that of the HI rotation curve, the 166 km/sec bandwidth of the receiver was set to cover mainly the range of positive HI allowed velocities. This insured that all emission from within the solar circle would lie within the spectrometer coverage. Over most of the survey region ℓ = 12° to 55° the velocity coverage was from -13 to 153 km/sec. Since the maximum permitted radial velocity decreases towards higher longitudes, beyond ℓ = 55° the receiver was shifted to a lower velocity range: -55 to 111 km/sec.

In displaying the survey data, we are faced like 21-cm astronomers with the problem of representing a three-dimensional array on a two-dimensional page. The best that can be done is to either display the array as viewed from various "perspectives", integrated over one (or two) of the coordinates (longitude, latitude, and velocity) or to display a "slice" of the data at a fixed value of one of the coordinates. Both of these techniques are employed below. As will be discussed, each representation has its merits, depending on what aspect of the CO emission one wants to highlight.

A sample of the spectra obtained by the survey, arranged by galactic longitude and latitude, is shown in figure III-2. These spectra illustrate the quality of the baselines and the typical signal-to-noise ratio. In all cases, the baselines appear to be flat to within the noise and the signal-to-noise ratio is adequate for the typical emission features shown. The continuity of adjacent spectra suggests that typical galactic features are fairly well resolved at our beamwidth sampling interval of 0°.125. The sample spectra also demonstrate that the latitude coverage as expected is sufficiently large to detect most of the molecular emission in the inner galaxy. Except for local low-velocity material, the emission nearly always drops to zero at b = ± 1°.

For comparison with gamma-ray, infrared, and other continuum surveys, it is worthwhile to integrate the survey over its full velocity extent to produce a conventional spatial map. Such a map is shown in figure III-3. Dispite the fact that the map is certainly influenced to some degree by optical-depth effects and temperature fluctuations, the intensities are probably roughly proportional to the column density of molecular matter (see, e.g., Liszt 1982).

Although the integration over velocity tends to smear together near and distant molecular clouds, several interesting regions stand out in figure III-3. The intense emission between ℓ = 13° and 15° is produced primarily by the large molecular complex near M17, with some higher-velocity emission associated with W33 also probably included. The tangent region of the 4-kpc spiral arm, one of the major arms of the inner galaxy, stands out as an intense region between ℓ = 23° and 25°. The tangent region of another major arm, the Scutum arm, is apparent in the region ℓ = 30°-31°. This region includes many large HII regions such as W40 and W43. The very large molecular complex associated with the supernova remnant W44, to be discussed in chapter VIII, produces the intense emission which extends to b = -1° near ℓ = 35°. Because of the general falloff in the number of molecular clouds at higher longitudes, it

becomes easier to distinguish individual clouds. For example, the molecular complex associated with the HII region W51 can be clearly seen near $\ell = 49°$.

Because the galactic CO layer is so thin, one sacrifices the least amount of information by integrating the survey over latitude. The resulting longitude-velocity (ℓ,v) map is the best way of representing the data when one is concerned with the distribution of the emission in the galactic plane. Such maps are shown in figure III-4. The first of these (figure III-4a) presents the data at the highest spatial resolution at which we have complete data, 0°.25, smoothed in velocity (as was all the data) to a resolution of 1.3 km/sec. To improve the signal-to-noise ratio and to emphasize the large-scale features, this map has been smoothed in two steps to 1/2 and 1/4 the original resolution in both ℓ and v, i.e., to 2.6 km/sec by 0°.5 (figure III-4b) and to 5.2 km/sec by 1°.0 (figure III-4c). In figure III-4c the effect of the instrumental noise of the individual spectra is insignificant, and even the small-scale structure is real: each resolution element represents more than 50 of the original spectra or a total integration time of more than 10 hours.

In the heavily smoothed figure III-4c the emission is dominated by twenty or so well-defined, intense emission

regions with typical dimensions of 1-2 degrees by 10-20 km/sec. In chapter VIII, it will be shown that many of these are large molecular complexes with masses close to 10^6 $M_\odot$. The W44 complex, which can be seen in figure III-4 near ℓ = 35°, v = 50 km/sec, is a typical example.

A grayscale version of the latitude-integrated ℓ,v map is shown in figure III-5. Although the limited dynamic range of this grayscale masks much of the small-scale structure visible in the contour map, it displays the large-scale structures fairly clearly, and better than a contour map allows gaps or holes in the emission to be distinguished from peaks. For example, the relatively empty region running from ℓ = 36° to 46° at v = 50 km/sec stands out clearly on the grayscale yet is easily overlooked on the contour map (figure III-4a). Because of its ability to highlight large-scale features, the grayscale display will be useful in the discussion of spiral structure to follow.

The distribution of emission with galactic latitude is displayed by the eleven longitude-velocity contour maps in figure III-6, one for each latitude strip observed in the survey. Using this series of maps, the location and extent of individual clouds can be determined more accurately than with the longitude-velocity map integrated over latitude. For example, a

well-defined and isolated cloud can be seen near $\ell = 52°$, $v = 60$ km/sec on the map at $b = -1°$. In the integrated map this cloud is masked by emission at other latitudes.

The low intensity of the emission in the $b = \pm 1°$ maps, especially at higher velocities, demonstrates that most of the molecular clouds in the inner galaxy lie within the latitude range of the survey. There is virtually no emission at velocities above 50 km/sec in the $b = +1°$ map. The relatively large cloud near $\ell = 40°$, $v = 35$ km/sec was mapped by the low spatial-resolution survey to be discussed below and was found to extend above a latitude of 2°. In the $b = -1°$ map, the W44 complex near $\ell = 35°$, $v = 30$ km/sec is the most intense high-velocity feature. It is even more pronounced at $b = -0°.75$. As will be shown later, this complex extends below the plane to -3° and beyond.

The only large-scale feature which does not fall off with increasing latitude is the vertical lane of emission near 10 km/sec running from $\ell = 18°$ to 40°. The low velocity and large latitude extent of this feature implies that it represents local material, and its existence was the primary motivation for carrying out the second large-scale survey mentioned above. We now turn to a discussion of that survey.

Figure III-7 presents a map of the low-velocity (v = -10 to 20 km/sec) CO emission from the first quadrant. The survey on which this map is based is fully-sampled at 1° spatial resolution over the latitude range -4° to +10°, except above ℓ = 60° where the latitude range is -4° to +6°. Additional scans were also taken where needed to fully map emission features, as in the region above b = +6° near ℓ = 95°.

In order to fully sample such a large region in a reasonable time, I implemented software on the Columbia telescope which effectively increases its beamsize by offsetting the pointing through a regularly spaced grid during data acquisition. For this survey the spatial resolution was degraded to 1°, each spectrum representing the average emission in a fully-sampled 1° square on the sky.

Figure III-7 demonstrates that the vertical lane of emission near 10 km/sec in our ℓ,v maps extends well beyond the latitude range of the in-plane survey. This emission is the molecular counterpart of a 21-cm feature which has been called "feature A" by Lindblad (1967). Like the CO emission, feature A has a very wide latitude extent and small velocity dispersion and its velocity coincides well with that of the CO. Lindblad et al. (1973) have interpreted feature A as an expanding ring of gas surrounding the sun. They suggested that it may be

related to the Gould Belt of early-type stars and dark clouds, but this connection could not be clearly established with the 21-cm data. Our CO observations, on the other hand, provide a clear connection between feature A and the dark clouds of the Gould Belt. This connection is demonstrated in figure III-8, which shows the low-velocity CO contours superimposed on the well-known Lund Observatory panorama of the Milky Way. The close correspondence between the CO emission and optical obscuration implies that feature A, or at least the molecular counterpart of feature A, does indeed arise from the dark clouds of the Gould Belt which produce the "Great Rift" in the northern Milky Way.

IV. THE AXISYMMETRIC DISTRIBUTION

Before discussing the relation of molecular clouds to spiral arms, it is important to consider their gross distribution as a function of galactocentric radius, neglecting any azimuthal variation entirely. This is an obvious first step since it avoids many of the difficulties inherent in a more refined discussion of the distribution. If molecular clouds are assumed to move on circular orbits subject to a known rotation curve, then each emission feature in the longitude-velocity map can be assigned to a unique galactocentric radius. On the other hand, a unique galactocentric longitude cannot be assigned kinematically, since for each positive-velocity emission feature in the first quadrant there corresponds two possible locations in the galaxy.

Even if this well-known ambiguity could be resolved, non-circular motions can produce large errors in the position of a source derived on the assumption of circular rotation. The corresponding error in galactocentric radius, however, will be significantly less. Typical non-circular streaming motions of 10 km/sec amplitude can produce as much as a 2.5 kpc error in the position of a source along the line of sight, while the corresponding error in galactocentric radius will always be less than 1.3 kpc within the region of our

survey and less than 0.7 kpc in the molecular-ring region ($4 < R < 8$ kpc) where most of the emission is concentrated.

The gross properties of the CO distribution can be deduced from the longitude-velocity map. Because the galaxy rotates differentially with the angular velocity increasing inward, material progressively closer to the galactic center will show progressively higher radial velocities with respect to the sun. One can estimate the galactocentric radius of an object or source on the ℓ,v map by bearing in mind that in the first galactic quadrant higher radial velocity implies smaller galactocentric radius. Assuming circular rotation, circles of constant radius in the galaxy transform into straight lines which pass through the origin ($\ell = 0°$).

With these considerations in mind, some of the overall properties of the molecular-cloud distribution are readily apparent in figure III-4 and figure III-6. We see first that there is very little emission at high velocities below $\ell = 22°$. The almost total absence of emission in this region makes it appear as if it were a "forbidden region" of longitude-velocity space, similar to the high-velocity region beyond the high-velocity ridge. This is not however the case: if the galaxy were uniformly filled with clouds, one would expect the

high-velocity ridge emission (which extends from $\ell = 60°$, $v = 30$ km/sec to $\ell = 22°$, $v = 110$ km/sec in the observed map) to continue to $\ell = 12°$, $v = 140$ km/sec and lower longitude. The region below the high-velocity ridge (at lower velocity) would also be filled with emission. The boundary between very strong and very weak emission can be roughly approximated by the straight line corresponding to a galactocentric radius of 4 kpc; this line passes through the origin and the point $\ell = 22°$, $v = 110$ km/sec. We see, then, that there is a relatively sharp transition zone near 4-kpc, with intense CO emission just outside this radius and weak emission within.

It is also clear from the longitude-velocity map that there is generally less emission at low velocities than at high. The only prominent features below 30 km/sec are the vertical lane of emission near 10 km/sec and the emission associated with M16 and M17 in the region $\ell = 12° - 20°$. As discussed earlier, the low-velocity vertical lane of emission between $\ell = 18°$ and $40°$ arises from a nearby cloud which forms part of the "Great Rift" in the optical Milky Way. The more distant M16-M17 region appears at a low radial velocity because of its low galactic longitude. The small amount of emission at low velocity implies a low density of clouds near the

sun. In fact, the straight line in the longitude-velocity map corresponding to a galactocentric radius of 8 kpc, which passes through the origin and the point $\ell = 52°$, v = 50 km/sec, divides the sparse emission at lower velocities and the widespread emission at higher velocities. Thus we can conclude that, at least in the first galactic quadrant, most of the emission lies between 4 and 8 kpc from the galactic center. This is the so-called "molecular ring" region of the galaxy.

The contour maps can also be used to discern the gross properties of the latitude distribution of the emission. The thinness of the CO layer is obvious in figure III-3, which presents spatial maps of the emission integrated over velocity. Except above $\ell = 45°$ where the emission is weak and relatively nearby, the galactic disk stands out as an intense emission strip roughly 1° wide (FWHM). Taking 6 kpc as the mean radius of the molecular ring, the average heliocentric distance to the emission is then about 8 kpc, the distance to the tangent point of the ring. At this distance, the angular thickness of the disk corresponds to about 140 pc (FWHM).

It is also apparent from the spatial maps (fig. III-3) that the mean latitude of the emission fluctuates about the galactic plane. Most obvious is the displacement of the emission towards negative latitude in the regions $\ell = 12° - 24°$ and $\ell = 36° - 48°$. This

displacement is immediately apparent on comparing the ℓ,v map at b = +0°.5 with that at -0°.5 (figure III-6c and i). These maps show that most of the displaced emission lies at relatively high velocity, implying that the displacement seen in the spatial maps results from a genuine large-scale warping of the plane, rather than from a local fluctuation in the CO layer. The mean latitude of the emission shows fluctuations on the order of 0°.3. If we again take 8 kpc as an average distance to the emission, this implies displacements of the CO layer from the plane on the order of 40 pc.

The thickness, displacement, and radial distribution of the emission have been investigated more quantitatively by fitting a simple axisymmetric model to the data. The model assumes the CO to be contained in many small clouds randomly distributed to give an average integrated volume emissivity (averaged over a volume containing many clouds and integrated over linewidth) of

$$\varepsilon(z,R) = \varepsilon_0 \exp\left[\frac{-(z-z_0)^2(\ell n 2)}{z_{\frac{1}{2}}^2}\right]$$

where z is the distance from the galactic plane. The CO distribution is characterized by a central emissivity ε_0, displacement z_0, and thickness $z_{\frac{1}{2}}$, which are taken to

be functions of galactocentric radius. The most likely values of the parameters $\varepsilon_0(R)$, $z_0(R)$ and $z_{\frac{1}{2}}(R)$ were obtained by dividing the galaxy into concentric rings of width 0.5 kpc. In each ring, the values giving the best least-squares fit of the data to the model distribution were then determined. A complete description of the model and the fitting procedure can be found in the thesis of R. Cohen (1978).

The results of this fitting procedure are shown in figure IV-1. The error bars represent the formal errors from the least-squares fit multiplied by a galactocentric radius-dependent correction factor $(N)^{1/2}$, where N is the number of data points (i.e., ℓ,b,v-positions) contained in a typical molecular-cloud emission feature. This correction increases the formal errors to account for the fact that the data is correlated over the emission volume of a cloud. N was estimated by assigning an average distance to each galactocentric radius and assuming that clouds have an average size of 50 pc and an average velocity extent of 6 km/sec; this yielded correction factors which increased from ~ 8 at R = 2 kpc to ~ 30 at R = 9 kpc.

These graphs confirm and quantify the three basic conclusions about the galactic CO distribution which were inferred from the maps discussed above: (i) the CO emissivity is strongly peaked near R = 5.5 kpc, (ii) it

shows deviations from the plane on the order of 40 pc, and (iii) it has a mean thickness (FWHM) of about 120 pc. The results are essentially in agreement with those of Cohen (1978), who used the same fitting procedure but only a small subset of the present survey data, and with those of Burton and Gordon (1978) and Solomon and Sanders (1980). The results are now well-known, and have been discussed in detail by these authors.

V. CO SPIRAL STRUCTURE

A. Introduction

Although the idealization of a molecular ring and an axisymmetric distribution of molecular clouds is a useful first step, it is immediately obvious from the ℓ,v map (fig. III-5) that the galactic CO emission departs greatly from axial symmetry. Most striking are the deep minima at $\ell = 25°$, v= 80 km/sec and at $\ell = 32°$, v = 60 km/sec which lie in the middle of the molecular ring itself. These minima lie adjacent to strong emission features which must arise from the same galactocentric radius. Examination of the ℓ,v maps at different latitudes (fig. III-6) will reveal similar fluctuations in the latitude distribution of the emission along lines of constant galactocentric radius (i.e., straight lines which pass through the point $\ell = 0°$, v = 0 km/sec).

It is possible that some of the apparent lack of axial symmetry is caused by large-scale non-circular motions or by large-scale variations in the kinetic temperature of the gas, but, as will be argued later, these effects are probably secondary. It is far more likely, considering the appearance of most external galaxies, that the distribution of molecular clouds has some higher-order arrangement which is not axisymmetric. Our comparison with HI suggests that this higher-order arrangement takes the form of spiral arms.

B. Comparison With HI

Over the past thirty years, it has been fairly well established that we live in a spiral galaxy. In the 1940's it was known that the galactic system was extremely flat, contained many OB associations, and had a nuclear bulge. As early as 1952, it had been observed that local HII regions "occur in two long, narrow belts similar to the spiral arms observed by Baade in the Andromeda nebula" (Morgan, Sharpless, and Osterbrock 1952). Since then, the study of young optical objects such as OB associations, clusters, and HII regions has firmly established the existence of 3 spiral-like segments in the solar neighborhood (see, e.g., Humphreys 1979). On a galactic scale, 21-cm emission (Burton and Shane 1970) and radio HII regions (Lockman 1979b) have provided considerable evidence for large-scale spiral features.

It has also been well established that HI traces spiral arms. The strongest evidence for this comes not from the study of our own galaxy, but from high-resolution interferometric 21-cm observations of external galaxies such as M81 (Rots and Shane 1974) and M101 (Allen et al. 1973), which show well-developed HI spiral arms. The 21-cm surveys of our own galaxy also show apparent spiral features, the best example probably being

the Perseus spiral arm, which can be easily traced in 21-cm surveys through 3 quadrants of galactic longitude (see, e.g., Weaver 1974). Although it is still not clear to what extent these apparent spiral features are due to large-scale streaming motions rather than to genuine HI spiral arms (see, e.g., Burton 1971), the fact that ours is a spiral galaxy and that the HI in external spirals concentrates in the arms strongly suggests that these apparent spiral features are also real arms.

Since CO is widespread and easily observed throughout the galaxy, it too should be useful as a spiral tracer. To investigate whether this is the case, we will study comparable CO and HI surveys to see whether the spiral-like features which exist in the HI data are also present in the CO.

The 8 arc-min resolution of the Columbia telescope makes our CO survey well suited for a comparison of this type. Because our beamwidth is similar to that of the largest 21-cm survey instruments, we can compare corresponding CO and HI spectra which arise from comparable volumes of space. Also, since our beamwidth is significantly larger than that of any other CO telescope, we have been able to produce the most extensive and well-sampled CO survey to date for comparison with the very large amount of available HI data.

Before comparing the CO and 21-cm data, it is important to clarify briefly what we mean by the "HI gas". In recent years, high-resolution 21-cm observations (see, e.g., Radhakrishnan 1974; Dickey 1981) have revealed the existence of narrow minima in HI profiles presumably due to self-absorption by cold HI clouds. Burton, Liszt, and Baker (1978) find a strong correlation between these HI self-absorption features and CO emission features. These observations suggest that the cold, absorbing HI is closely associated - and possibly well-mixed - with the CO clouds. Thus this cold-cloud component of the HI probably has a galactic distribution similar to the CO and can be considered part of the cold component of the interstellar medium which CO traces.

In what follows, we shall consider the galactic distribution of the warmer and more widespread HI which is <u>not</u> contained in these cold, optically-thick clouds and shall assume that this warm component is optically thin on a large scale. Although the absorbing clouds may contain a significant amount of atomic mass (see, e.g., Dickey 1981), in nearly all cases where absorption lines can be distinguished their equivalent widths are small with respect to the HI emission in the same direction. Baker and Burton (1975) have noted that the existence of the zero-velocity and high-velocity ridges in the 21-cm data is evidence of optical thinness on a large scale.

Using a two-component model for the galactic HI in which cold, optically-thick HI clouds are immersed in a warmer intercloud medium, they have shown that the 21-cm emission from the warm component is optically thin on a large scale in spite of the presence of the cold clouds. Thus although HI column densities derived from 21-cm emission-line profiles may be underestimated because of the HI which is concealed in the cold clouds, the warmer HI is probably fairly well represented by the profiles.

1. The Grayscales

The grayscale version of our longitude-velocity map is compared to a similar 21-cm map in figure V-1; the CO map is integrated over ± 1° in latitude, the 21-cm map over ± 10°. The contrast in the 21-cm map has been increased by setting all spectral channels with an antenna temperature less than 50 K to zero before integrating over latitude (Weaver 1974). The map is thus a highly nonlinear representation of the data, designed to highlight the most intense 21-cm features. It is important to keep this in mind since the CO map to which it is to be compared has not been similarly edited.

The large-scale features of the two maps are strikingly similar. The HI emission minima labeled 1 to 4, for example, have clear counterparts in the CO map.

We will henceforth refer to these minima by the names assigned in the figure. Along the terminal-velocity curves, the same bumps and notches can be identified in both maps, even on a scale as small as a few degrees. The bumps near ℓ = 50°, 30° and 24° are most obvious but note also the small notches, for example, near ℓ = 36°, 29° and 25°. The most conspicuous difference between the maps is the change in relative intensities between the molecular-ring region (at high velocities and low longitudes) and more local regions (at low velocity): in general, relative to CO the 21-cm emission is much more intense at low velocities. This difference mainly reflects the different radial distributions of the two species, the CO being much less abundant relative to HI in the outer galaxy.

One implication of the quite detailed similarity of the two maps concerns the large-scale motions of the two species. Since the appearance of the longitude-velocity map depends very sensitively on the large-scale kinematics of the emitting gas (Burton 1971), the similarity of the two maps, especially along the terminal-velocity curve, implies that the CO clouds and HI gas follow the same large-scale kinematics - a point on which the various CO observers seem to agree. Burton and Gordon (1978), for example, reach this conclusion

after a careful comparison of the CO and HI terminal-velocity curves. There are theoretical reasons for believing this must be the case. For example, Elmegreen (1981) has shown that if the magnetic-field strength inside a self-gravitating molecular cloud is large enough to prevent its free-fall collapse, the cloud cannot move as a ballistic particle through the surrounding interstellar medium, since the cloud will be magnetically coupled to its surroundings, and its motion will generally be constrained to follow the ambient medium.

A more obvious implication of the similarity between the maps is that if HI traces the galactic spiral structure, as argued above, then the CO must as well. The holes in figure V-1 labeled 1 to 4 have been identified by various 21-cm researchers (e.g., Burton and Shane 1970; Shane 1972) as interarm regions in the HI spiral structure. In a first-quadrant ℓ,v map, trailing spiral arms appear as loops of emission, with the low-velocity side of the loop corresponding to the near side of the arm. The main 21-cm arms which have been identified are shown schematically on top of the CO data in the insert to the CO grayscale. We see that the 4-kpc gap (labeled 1) lies between the Scutum and 4-kpc arms (labeled D and E, respectively), the Scutum gaps (labeled 2 and 3) lie between the Scutum arm and the Sagittarius arm (labeled C) and the Sagittarius gap (labeled 4) lies

within the very conspicuous loop of the Sagittarius arm. The fact that these features appear so clearly in CO implies that molecular clouds are excellent tracers of spiral arms.

2. The Perseus Arm

A CO survey of the second galactic quadrant with the Columbia telescope provides additional very clear evidence for this conclusion. A slightly irregular band along the galactic plane about 6° wide and 75° long, from ℓ = 104° to 180°, has been surveyed by H.I. Cong and J. Brock (see Cohen et al. (1980) for a preliminary version of this survey). The longitude-velocity map obtained by integrating this survey across the galactic plane is shown in figure V-2. Solid lines indicate the approximate locations of ridges of peak 21-cm emission from the Maryland-Green Bank survey (Westerhout 1973). Because there is no kinematic distance ambiguity for material located outside the solar circle, the spiral structure seen in this map is even more distinct than in the first quadrant. As in the first quadrant, the large-scale molecular cloud distribution correlates well with that of the HI gas. The emission from both species mostly lies in two parallel lanes, one between -60 and -40 km/sec (but tending towards less negative velocity

at higher longitudes) and another between -20 and 0 km/sec. These lanes are the Perseus and Local spiral arms, respectively. The almost total absence of emission between these arms is one of the most important findings of the survey; it does not necessarily mean that molecular gas is nonexistent in the interarm region - such gas could be so cold, or diffuse, or in such small clumps as to escape detection, but it does imply that molecular clouds as commonly defined by CO observations - objects larger than 5 pc with CO temperatures greater than 1-2 K - do not exist between the arms, or are extremely rare.

3. The Spectra

From the Columbia second quadrant survey it is clear that, at least for the Perseus arm, CO is a higher contrast tracer of spiral structure than is HI. By comparing individual CO and HI spectra, we will now show that this is also the case in the inner galaxy. The comparison is made in figure V-3. Spectra are presented every 2 degrees through the molecular-ring region, with the 4-kpc and Scutum gaps (labeled 1 to 3, as in figure V-1) indicated. For the purpose of this comparison, consider especially the high-velocity portion of the spectra where both species show strong emission. At low

velocities, the CO emission is generally too weak and the HI emission too strong to make a comparison worthwhile. We see here, as we did in the grayscale maps, that CO and HI generally show the same spiral features. But from the spectra it is also obvious that the CO spiral features are of much higher contrast. Note in particular the much higher contrast of the labeled interarm gaps in the CO spectra. At ℓ = 30° and 32°, for example, the Scutum gap labeled 3 is essentially devoid of CO emission while in the HI spectra the contrast is never more than 3:1.

4. The I(ℓ) Graph

A classic method of locating the tangent directions of arms in the Milky Way is to study the total integrated brightness of a spiral tracer such as the 21-cm line as a function of galactic longitude, since a good tracer should show enhanced brightness in these directions. In fact, assuming the tracer remains optically thin, the tangent directions should increase in brightness as the arm-interarm contrast of the tracer increases. The graph of integrated emission vs. longitude - the I(ℓ) graph - is thus a very good index of the arm-interarm contrast of a spiral tracer. I(ℓ) graphs for both the HI and CO are shown in figure V-4. The tangent directions of the Scutum and 4-kpc arms lie at about 31° and 24°, respectively. Both CO and HI show peaks at these

longitudes, but the CO peaks are much the stronger. The peaks labeled B and C, corresponding to the tangent points of the Scutum and 4-kpc arms, respectively, each show a drop in intensity of about a factor of 2 on their high-longitude side, at the point where the line of sight leaves the outer edge of the arm. In these directions, the corresponding HI peaks show a drop in intensity of only about 15 %. The relative prominence of the CO peaks suggests that molecular clouds are more strongly confined to the galactic arms than the clouds of diffuse atomic gas studied at 21-cm.

The CO peaks A and D in figure V-4 are produced by relatively nearby molecular complexes. This is demonstrated by means of figure V-5, which contains graphs similar to figure V-4 but with various lower limits on the integral over velocity. In the successive graphs a to f the lower limit on the velocity integral is systematically increased, thus eliminating more and more of the local emission. Clearly most of the emission contributing to peak D has a velocity less than 20 km/sec since the intensity of this peak is greatly reduced in figure V-5b. It is primarily produced by the molecular complex M17 in the nearby Sagittarius arm, at a distance of about 2 kpc. Similarily, figure V-5d illustrates that the emission contributing to peak A lies below 60 km/sec.

This peak is produced by the large complex associated with W44 at a distance of 3 kpc. On the other hand, the spiral-arm peaks B and C remain strong and, in fact, stand out even more as the local emission is removed.

Figure V-5e indicates that most of the emission contributing to peaks B and C lies at a velocity above 80 km/sec. This implies that the emitting gas must lie near the tangent region of the molecular ring, at a distance of about 9 kpc. Taking 3° as the width in longitude of these peaks implies a size scale for the emitting regions on the order of 500 pc. Individual molecular clouds are generally much smaller than this (see chapter VIII, especially table 7), so these peaks must be produced by many clouds in a region with a projected size of about 500 pc - a reasonable width for a spiral arm.

C. Discussion

We have seen that the large-scale structure of the galactic CO emission is dominated by several loop-like features whose counterparts in the 21-cm data have been identified as spiral arms. There are, however, some features of the CO data which do not fit into this simple pattern. In the following discussion we will consider these features as they relate to the apparent spiral structure of the Milky Way.

1. The Sagittarius-Arm Tangent and Near Side

Though the Sagittarius arm as we shall see in chapter VIII is actually one of the best defined spiral arms in the first quadrant, its near (low-velocity) side in the ℓ,v map (fig. III-5) is poorly-defined and there is no prominent peak in the I(ℓ) graph (fig. V-4) corresponding to its tangent direction at $\ell = 51°$. Both these aspects of the data can at least partially be explained by the special location of the Sagittarius tangent region and near side. Unlike the 4-kpc and Scutum arms, the near side of the Sagittarius arm lies well outside the molecular ring, in a region where the number of clouds is relatively small. Equally important, the Sagittarius tangent and near side lie relatively close to the sun, so the angular separation between clouds there is large. This projection effect is clearly illustrated in figure V-6, which plots in longitude-velocity space the positions of clouds which are equally spaced along two spiral arms. The arm labeled "near side" is similar in appearance to the near Sagittarius arm, which shows relatively few large clouds widely separated in longitude. Similarly, the proximity of the tangent region will cause its emission to be spread over a larger longitude range. Thus in retrospect, the poorly-defined nature of the Sagittarius tangent and near side might

well have been expected because of their special galactic location - outside the molecular ring and close to the sun.

2. The W44 "Bridge"

Another prominent feature in the longitude-velocity map (fig. III-5) is the bridge of emission near $\ell = 35°$ that apparently links the near side of the Sagittarius arm to the far, and is not predicted by the spiral pattern shown in the insert to figure III-5. In chapter VIII, we will argue that nearly all of this emission near $\ell = 35°$ between 30 and 50 km/sec, and probably much of the emission at the same longitude between 50 and 65 km/sec, is caused by a very large complex of molecular clouds associated with the supernova remnant W44 in the near side of the Sagittarius arm. The internal velocity width of this complex is large - about 10 km/sec (FWHM) - and causes the object on the ℓ,v map to spill over from the near Sagittarius arm to the far. Such a large velocity width for a single complex is not unprecedented: a similar object is seen in the Perseus arm towards the supernova remnant Cas A. It is possible that many of the emission features seen protruding from the high-velocity ridge, such as at $\ell = 50°$, 34°, and 24°, represent similar objects at greater distances.

3. The Aquila Spur

A further apparent exception to the straightforward pattern of spiral arms we have discussed is the bridge of CO emission between the Sagittarius and Scutum arms near the terminal velocity curve at 80 km/sec (between loops C and D in the insert to fig. III-5). At first sight, this appears to be evidence for a population of weak interarm clouds made visible by the velocity crowding near the terminal velocity. However, upon closer inspection it appears more likely that this emission arises from a distinct object - a small spiral segment which we will call the Aquila spur, lying between the Sagittarius and Scutum arms.

If the Aquila spur were simply due to such velocity crowding near the terminal velocity, the peak CO emission should follow the terminal-velocity curve as traced by the HI gas. Instead the peak CO emission in the region $\ell = 34°.5$ lies systematically below that of HI. This discrepancy between the highest-velocity CO and HI features was first noted by Bash and Peters (1976) at $\ell = 36°$. It is illustrated at $\ell = 35°$ in figure V-7, which compares CO and HI spectra in that direction. In the CO spectrum, the spur stands out as a well-defined feature centered near 80 km/sec, about 10 km/sec below the HI peak marking the high-velocity ridge. The sharp

low-velocity edge to the feature (near 65 km/sec) is also uncharacteristic of velocity crowding. Therefore, this CO feature is probably produced by material lying near the sub-central point, but not at it.

At higher longitudes (38°-40°) the Aquila spur indeed extends to the terminal-velocity curve, as expected for a spiral segment with a tangent direction in this region: the feature first appears well below the terminal-velocity curve (at ℓ = 34°.5, v = 80 km/sec) and extends nearly vertically, parallel to the far Sagittarius arm, until it intersects the terminal-velocity curve near ℓ = 40°. In chapter VII, the Aquila spur will be modeled as a small spiral segment lying between the Sagittarius and Scutum arms. A spur at precisely this location has indeed long been postulated by 21-cm observers (Weaver 1970; Shane 1972); the CO feature is simply its molecular counterpart.

The existence of minor irregularities in the overall pattern of spiral galaxies is of course the rule rather than the exception, as an inspection of the Hubble atlas of galaxies (Sandage 1961) will reveal. Spurs and branches are quite common in spiral galaxies, and it has been suggested that the Local arm in which the Sun is situated is such a spur, lying between the much larger Sagittarius and Perseus arms (Humphreys 1976). And it is hardly surprising that the spur lies close to the

terminal-velocity curve, since that is where because of velocity crowding a spur randomly placed in the inner galaxy is likely to be found.

The existence of the Aquila spur is probably one of the main reasons why CO spiral structure largely escaped notice in the previous CO surveys. It reduces the clarity of the Sagittarius arm by partially merging with its high-velocity side, and - more importantly - it fills much of the high-velocity ridge region between the Sagittarius and Scutum arms. In the absence of this spur, the Scutum gap (labeled 3 in figure V-1) would extend to the terminal-velocity curve, and the segregation of molecular clouds into spiral arms would be much more apparent in the CO ℓ,v map.

D. Summary

Since we live in a spiral galaxy and HI has been shown to trace the spiral structure of external galaxies, it is reasonable to postulate that the apparent spiral features seen in the 21-cm surveys of the galactic plane correspond to large-scale spiral arms. Since our CO survey reveals essentially the same features, generally with much higher contrast, molecular clouds must also trace the spiral arms. The similarity of the CO and HI ℓ,v maps would be unintelligible if the two species had different large-scale kinematics.

The overall structure of the CO emission appears consistent with molecular clouds being largely confined to a regular pattern of spiral arms, though there are apparent exceptions to this pattern. The poorly-defined nature of the Sagittarius tangent and near side is largely due to their special galactic location - well beyond the molecular ring and close to the sun. The emission near $\ell = 35°$ which apparently links the near and far sides of the Sagittarius arm arises from a single large complex in the near side of the arm. Finally, the emission near the terminal-velocity curve at $\ell = 36°$, which lies outside the regular pattern of spiral arms, and is designated here the Aquila spur, is the molecular counterpart of an interarm spur previously identified by 21-cm observers.

VI. THE ARM-INTERARM CONTRAST OF CO AND MOLECULAR CLOUDS

A. Introduction

We have seen that large-scale, putative spiral features in the CO longitude-velocity map are more clearly defined and of higher contrast than those seen at 21-cm. However, this higher contrast does not necessarily imply that the CO emission is more strongly confined to the arms than is the 21-cm emission. Though this is the most straightforward interpretation, and the one we will ultimately favor, two other possibilities must be considered. First, the higher CO contrast may be the result of a lower velocity dispersion for the CO clouds than for the HI, the 21-cm spiral features being less evident simply because the higher dispersion of the HI gas "washes out" the spiral features. And second, much of the arm-interarm contrast seen in the CO data may be caused by the large-scale streaming of molecular clouds. Both of these possibilities will be considered and the arm-interarm contrast of the CO emission will be compared with that of the 21-cm emission.

The more thorny issue of the arm-interarm contrast of the molecular clouds themselves will also be discussed briefly. We will consider the possibility that enhanced star formation or cosmic-ray density within the arms, or

both, or other mechanisms entirely, significantly heat up spiral-arm clouds, causing them to have a higher average CO luminosity than those between the arms.

B. The CO Arm-Interarm Contrast

1. The CO and 21-cm Velocity Dispersions

Before attempting to reach conclusions concerning the relative confinements of the CO and 21-cm emissions to spiral arms, their relative velocity dispersions must be determined. If that at 21-cm is much greater than that at CO the interarm holes in the 21-cm data will be of lower contrast than those in CO, even if the two species are equally well confined to the spiral arms. We will first show that the HI dispersion, though the larger of the two, is still too small to account for the considerably higher arm-interarm contrast of CO.

We are concerned with what we will call the overall velocity dispersion of the emission, a quantity which depends on (i) the random cloud-to-cloud velocities, (ii) the internal velocity dispersion of the clouds, and, at least for the HI, (iii) the velocity dispersion of the intercloud medium. It is the overall velocity dispersion which determines, for a given arm-interarm contrast of the emission in the galactic plane, the contrast between arm and interarm features in the ℓ,v map. The overall

velocity dispersions of the CO and HI can be compared by studying the extent to which the emission from each species extends beyond the terminal-velocity curve (see, e.g., Burton and Gordon 1978). This curve in the longitude-velocity map, which follows the maximum permitted radial velocity at each longitude, can be determined from the 21-cm high-velocity ridge. Once the terminal-velocity curve is known, the extent to which emission extends beyond this curve is easily derived.

Because some HI is present everywhere in the inner galaxy, first-quadrant 21-cm spectra invariably have an emission peak near the terminal velocity, and the velocity of this peak as a function of longitude is designated the high-velocity ridge on the ℓ,v map; beyond this ridge the emission falls rapidly to zero, and will be referred to as the "high-velocity tail" of the spectrum. The extent to which this tail extends beyond the terminal velocity is determined primarily by the overall velocity dispersion of the emitting gas. For a gas with no velocity dispersion, there would be no high-velocity tail: the emission would be zero at all velocities above the terminal velocity. (In practice, there would be a slight high-velocity tail owing to the variation of the terminal velocity across the telescope beam, but this effect is negligible for both the CO and HI data we will analyze.)

At each longitude, we define the velocity of the high-velocity ridge as

$$V_{HVR} = \frac{\sum_i v_i T_i}{\sum_i T_i}$$

where the sum extends over all spectral channels within ±15 km/sec of V_T, the terminal velocity predicted by a circular rotation curve $\theta(R)$. V_{HVR} in other words is simply the emission-weighted mean velocity within a 30 km/sec interval of the 21-cm spectrum, centered on the predicted terminal velocity V_T. V_{HVR} is used to define the position of the high-velocity ridge because V_T is not a very reliable predictor of its position. Because of large-scale streaming motions, the position of the high-velocity ridge can systematically vary by as much as ± 10 km/sec from V_T, the terminal velocity predicted from a circular rotation curve (see, e.g., figure 3 of Burton and Gordon 1978).

The terminal velocity is given by

$$V_T = \theta(R_o \sin \ell) - \theta(R_o) \sin \ell$$

where

$$\theta(R) = 250 + 4.05(R_o - R) - 1.62(R_o - R)^2. \quad (1)$$

R_o is the galactocentric radius of the sun, taken to be 10 kpc, and ℓ is the galactic longitude. For the rotation curve $\theta(R)$ we will adopt that derived by Burton

(1971) from 21-cm data. (For $3 < R < 10$ kpc, it differs from that of Schmidt by less than 3 km/sec.) The locus of computed V_{HVR} values is shown superimposed on an HI contour map in figure VI-1.

Figure VI-2 compares the average CO and HI high-velocity tails. The procedure for producing these curves is outlined below.

(1) Both the CO and HI spectra were integrated over latitude from -0°.25 to +0°.25. (If only b = 0° data are included, terminal-velocity emission displaced from the plane is missed.)

(2) For both CO and HI, emission at $V > V_{HVR}$ is taken to be the high-velocity tail. Note that V_{HVR}, as computed from the HI spectrum, was used to define both the CO and HI high-velocity tails.

(3) The high-velocity tails of the spectra near the tangent regions of the spiral arms were averaged to produce the curves in figure VI-2. The longitude ranges of the spectra included in the average are given in table 2.

By excluding spectra displaced from the tangent regions of the arms, we eliminate the possibility that some spectra might have no emission near the terminal

velocity. In fact, this was an unnecessary precaution. When all spectra at $\ell > 22°$ are averaged, the result is essentially the same (see figure VI-3). This is not surprising, since it is obvious from the CO longitude-velocity map (e.g., fig. III-5) that the CO high-velocity ridge is fairly continuous. (The simple spiral model to be discussed later will demonstrate that this rough continuity of the CO high-velocity ridge is not inconsistent with the confinement of molecular clouds to the spiral arms.)

Figures VI-2 and VI-3 show clearly that the overall velocity dispersion of CO is significantly less than that of HI. In order to quantify the difference in dispersion, we define the velocity dispersion of the high-velocity tail to be

$$\sigma_{HVT} = \frac{\sum_i (V_i - V_{HVR}) T_i}{\sum_i T_i}$$

where the sums extend over all spectral channels with $V > V_{HVR}$. The value of V_{HVR} computed from the HI spectrum is used for computing both σ_{HVT} (HI) and σ_{HVT} (CO). The average value of σ_{HVT} (CO)/σ_{HVT} (HI), which we will call R, provides a measure of the

difference in overall dispersion of the CO and HI:

$$R \equiv \left\langle \frac{\sigma_{HVT}\ (CO)}{\sigma_{HVT}\ (HI)} \right\rangle_{\text{AVERAGE OVER } \ell} \qquad (2)$$

Using the spectra in the longitude intervals given in table 2, we find

$$R = 0.68 \quad \text{(tangent regions)}.$$

Using all spectra at $\ell > 22°$ yields

$$R = 0.72 \quad \text{(all } \ell > 22°\text{)}.$$

These results verify and quantify the conclusion which is obvious from figures VI-2 and VI-3: the CO dispersion is significantly less than the HI dispersion.

The quantity R (as defined by eq. 2) has been used to determine the velocity dispersion (σ) of the galactic CO emission. (This quantity will be needed for the modeling in chapter VII.) By computing R for model CO and HI spectra with known velocity dispersions, it was found that R, which is defined in terms of σ_{HVT}, is in fact equal to σ_{CO}/σ_{HI}, where σ_{CO} and σ_{HI} are the velocity dispersions of the galactic CO and HI, respectively. (A description of how the model spectra were calculated and, in particular, how σ enters the calculation is given in Appendix B.) Thus we have

$$\sigma_{CO} = R\ \sigma_{HI}.$$

The velocity dispersion of local HI gas has been investigated by Falgarone and Lequeux (1973), who find σ_{HI} = 6.5 km/sec. This result is in good agreement with the gaussian analysis of 21-cm emission in the inner galaxy given by Burton (1971): although there is a weak dependence on galactic radius, the average value of the dispersion between 4 and 8 kpc from the galactic center is 6.4 km/sec (determined from his figure 3). Taking σ_{HI} = 6.5 km/sec and R = 0.7 yields

$$\sigma_{CO} = 4.5 \text{ km/sec.}$$

Having found a significant difference between the CO and HI dispersions, we must investigate whether this difference can account for the much higher arm-interarm contrast of the CO data. A simple way to do this is to increase the dispersion of the CO emission (by smoothing) until it equals that of the HI. The overall dispersions will be equal when the computed value of R is approximately 1. Smoothing the CO spectra until R = 1 yields the average high-velocity tails shown in figure VI-4, and as expected the high-velocity tails are almost identical.

With the CO spectra smoothed to the same dispersion as the HI, we can compare corresponding CO and HI spectra taken towards the important interarm regions of the inner galaxy. Rather than comparing individual spectra it is

most revealing to compare smoothed CO spectra and HI spectra which have been averaged over the approximate longitude ranges of the 4-kpc and Scutum gaps (labeled 1 and 3, respectively, in fig. V-1). Figures VI-5 and VI-6 compare the CO and HI spectra which result from averaging over the longitude intervals of these 2 interarm gaps. Note that in both sets of spectra, the CO and HI high-velocity tails are nearly identical, confirming again that the right amount of smoothing was applied to the CO spectra. These figures clearly demonstrate that the higher CO contrast is not due solely to the lower CO velocity dispersion: even when the dispersion of the CO spectra is increased to match that of the HI, the CO interarm gaps remain of higher contrast. In figure VI-5, the arm-interarm contrast for the gap near 80 km/sec is approximately 1.6:1 in the HI spectrum while it is greater than 3:1 in the CO spectrum. (An average contrast for the gap is obtained by averaging the contrast of the gap with respect to the emission peaks (arms) on either side.) In figure VI-6, the contrast of the interarm gap near 50 km/sec is less than 2:1 in the HI spectrum while it is nearly 4:1 in the CO spectrum.

To summarize, by comparing the average CO and HI high-velocity tails, we have shown that the overall

velocity dispersion of the CO is lower than that of the HI, the ratio of dispersions being about 0.7. By velocity smoothing the CO spectra until the CO and HI high-velocity tails are the same, we effectively increased the overall velocity dispersion of the CO to match that of the HI. In the smoothed CO spectra, the arm-interarm contrast remains significantly higher than in the HI spectra. We must conclude that the higher CO arm-interarm contrast is not due solely to the lower velocity dispersion of the CO emission.

This conclusion, of course, is based on the assumption that the 4-kpc and Scutum gaps do in fact correspond to interarm regions in the galactic spiral structure and not merely to statistical fluctuations in the positions of the largest clouds. This possibility is worth considering since in chapter VIII we will show that the galactic CO emission is dominated by a relatively small number of large clouds. If the gaps were simply holes between randomly-distributed large clouds, one would not expect these clouds to exhibit spiral structure. In fact, in chapter VIII we will show that the largest clouds, whose emissions dominate the ℓ,v map, are actually good spiral tracers. Thus the gaps may indeed be holes between the largest clouds, but these clouds lie in the arms and in large part <u>are</u> the CO spiral arms.

2. Large-Scale Streaming Motions

A classic problem in the interpretation of galactic spectral-line data via the ℓ,v map is how to determine the influence of large-scale, ordered velocity perturbations. It is well known that large-scale streaming motions can produce loop-like features in the longitude-velocity map that mimic the structure of real spiral arms. Burton (1971) indeed has shown that the galactic 21-cm emission can be accounted for fairly well in terms of a highly idealized model with a uniform distribution of HI, provided that small-amplitude streaming motions are imposed on the HI circular rotation. (Such a model is, of course, physically unrealistic since streaming motions will inevitably induce non-uniformities in the HI distribution, but is a useful demonstration of the strong influence of streaming motions on what one sees: the HI spectra and ℓ,v map.) The question we consider now is whether large-scale streaming of molecular clouds can account for the high-contrast spiral features seen in the CO longitude-velocity map.

To answer this question, consider two facts about the galactic CO emission that have previously been demonstrated: that the CO spiral features are of much higher contrast than the corresponding HI features, and that the terminal-velocity curves of the CO and HI data are very similar (see fig. V-1). The bumps on the terminal-velocity curves near

ℓ = 50° and l = 30°, corresponding to the tangent directions of the Sagittarius and Scutum arms, respectively, are the most direct evidence we have for the existence of streaming in the galactic disk. The fact that the amplitudes of these bumps in the CO and HI data are nearly identical implies that CO and HI clouds have nearly identical streaming motions. This being the case, the higher contrast of the CO spiral features cannot be attributed to larger-amplitude streaming motions for the CO clouds. Streaming motions can indeed produce spiral-like features in CO, as it does in the HI, as Liszt and Burton (1981) have shown by modeling the galactic CO emission as an ensemble of clouds with velocities perturbed by streaming. However, the difference in contrast between the CO and HI data can hardly be due to streaming, since the species have essentially identical streaming motions.

Thus neither streaming motions nor differences in velocity dispersion can plausibly account for the much higher contrast of the CO spiral features relative to the corresponding HI features. On the basis of these results, we can conclude that the galactic CO emission is more strongly concentrated to the spiral arms than the 21-cm emission. If our galaxy could be mapped face-on in both the CO and 21-cm lines, the spiral arms would be much more apparent in the CO map. The results presented here can be

shown to predict that the arm-interarm contrast of the CO emission would be at least twice that of the 21-cm emission.

C. The Molecular-Cloud Arm-Interarm Contrast

Does the high arm-interarm contrast of CO emission imply that molecular clouds do not generally exist between the galactic arms? Not necessarily, for it is conceivable that between the arms the clouds are cold and the emission is weak - in other words, that much or all of the CO arm-interarm contrast is due to enhanced heating of the clouds within the arms, rather than to an increase in their number density or size.

Regions of intense star-formation are a plausible source of heating for the spiral-arm clouds. Assuming that molecular clouds exist in the interarm regions, as they enter a spiral arm density-wave compression might initiate or enhance massive star formation. The radiation from these embedded, early-type stars can heat the gas, mainly by heating the surrounding grains which in turn heat the gas (Goldsmith and Langer 1978; Goldreich and Kwan 1974). This grain heating can produce "hot spots" in the cloud where the gas temperature reaches 40 K or more (Goldsmith, Plambeck, and Chiao 1975).

Despite the high temperature of these star-forming hot spots, their contribution to the total CO luminosity of a molecular complex is generally small. These hot spots tend to occur near early-type stars or protostars where the molecular-hydrogen density is greater than 10^5 cm^{-3}, for a density that high is required to effectively couple the temperature of the dust to that of the gas (Goldsmith and Langer 1978). A typical hot spot with a radius of 2 pc and a temperature of 40 K embedded in a molecular cloud with a radius of 30 pc and a temperature of 10 K will contribute less than 2% to the integrated CO emission over the face of the cloud. In the very active Orion-Monoceros region, for example, CO emission extends over about 85 deg^2 (Maddalena et al. 1982) while the 3 or 4 active star-forming hot spots cover less than 2 deg^2. It can be estimated from the data of Maddalena et al. that their total contribution to the CO flux of the region is less than 10%.

If star formation is unable to significantly increase the CO luminosity of a molecular complex, it is unlikely that it can account for the enhanced CO emission observed in the arms. Most of the CO emission from a typical molecular cloud like Orion comes not from these star-forming hot spots but from the extended cloud envelope which is probably heated primarily by cosmic rays (see discussion below).

There is also the question of whether molecular clouds can exist in the interarm regions without producing these star-forming hot spots. The time required for a cloud to pass between spiral arms is more than 100 times its dynamical (free-fall) timescale. There is no evidence that clouds can exist for such a long time without forming massive stars. Thus even if star-forming regions do make a significant contribution to the CO luminosity of the clouds, it is unlikely that they can account for the enhanced CO emission in the arms since interarm clouds would be expected to contain such regions.

Is it not possible, however, that the cosmic rays are enhanced in the arms, and they are the source of the cloud heating? As mentioned above, most of the projected area of a typical molecular cloud has a kinetic temperature of about 10 K. This is approximately the equilibrium temperature expected from a balance of cosmic-ray heating and CO line cooling (Elmegreen, Dickinson, and Lada 1978), CO line emission being the primary cooling mechanism for molecular clouds at densities $< 10^5$ cm^{-3} (Goldsmith and Langer 1978). Thus cosmic rays may be an important energy source for the CO emission from molecular clouds.

In appendix A we derive the dependence of a cloud's CO luminosity on the cosmic-ray density and estimate the maximum possible role of cosmic rays in increasing the arm-interarm contrast of the CO emission. It is shown that if the cosmic-ray arm-interarm contrast is as high as 4:1, roughly the upper limit set by the galactic-plane gamma-ray surveys, the average CO luminosity of clouds within the arms could be approximately doubled by cosmic-ray heating. This might marginally explain the difference in contrast between the 21-cm and CO emissions without requiring any molecular arm-interarm contrast beyond that which exists for the HI. It is argued however that the cosmic-ray arm-interarm contrast is probably lower than 4:1 and may not exist at all.

While it appears that neither of the major heat sources for molecular clouds - imbedded young stars and cosmic rays - can account for the high CO arm-interarm contrast, it is possible that a combination of heating mechanisms are responsible. Significant heating of molecular clouds could result from gravitational contraction, H_2 formation, supersonic turbulence, and magnetic fields (Goldsmith and Langer 1978; Elmegreen, Dickinson, and Lada 1978). Our lack of understanding of how molecular clouds are affected by passage through, or formation within, a spiral arm prevents us from saying

with certainty to what extent the high CO arm-interarm contrast reflects a high molecular-cloud arm-interarm contrast.

D. Summary

The spiral features apparent in CO are of significantly higher arm-interarm contrast than those seen at 21-cm. Some of this difference in contrast is due to the higher velocity dispersion of the 21-cm emission, which washes out the 21-cm spiral features in the longitude-velocity map. When the dispersion of the CO emission is artificially increased by smoothing the data to match that of the 21-cm emission, the contrast of the CO spiral features remains more than twice as high as the corresponding 21-cm features. Since the large-scale kinematics of molecular and atomic clouds are essentially identical, this remaining difference in contrast cannot be attributed to differences in streaming motions. We conclude that the arm-interarm contrast for the CO emission is more than twice that of the 21-cm emission.

Since the CO luminosity of molecular clouds depends on a variety of poorly-understood heating and cooling mechanisms, it is not possible to determine the molecular cloud arm-interarm density with any certainty. While it appears unlikely that enhanced cosmic rays or enhanced

star formation in the spiral arms can account for the high CO arm-interarm contrast, a combination of these and other heating and cooling mechanisms cannot be entirely excluded.

VII. A "NAIVE" SPIRAL MODEL

A. Introduction

In support of the notion that molecular clouds are largely confined to spiral arms, a very simple model will be developed in which nearly all the CO emission from the inner galaxy arises from spiral arms. The primary goal of the modeling is to demonstrate that the CO data - the high contrast holes in the longitude-velocity map, the strong peaks in the graph of integrated emission vs. longitude, the emission along the terminal-velocity curve - are readily explained by a model in which molecular clouds are formed as interstellar gas enters a spiral arm, and are destroyed before entering the interarm regions. The principal free parameter of the model, determined essentially from the width of the arms, is the lifetime of molecular clouds.

Although care was taken in adjusting the parameters of the model arms to give the best fit to the data, it must be emphasized that the model is not presented as a new picture of the spiral structure of the inner galaxy. The spiral pattern adopted is very similar to that derived from 21-cm data by, for example, Burton and Shane (1970). Anyone who wishes to use the CO data to determine the spatial structure of the inner galaxy

(i.e., the exact locations and orientations of the spiral arms) must deal with the same problems that have frustrated 21-cm observers for many years. Large-scale non-circular motions possibly associated with density waves (Burton 1971), bars (Lynden-Bell and Kalnajs 1972) and expansion from the galactic center (Sanders and Bania 1976), can alter the derived location and orientation of the arms. Fundamental too is the difficulty in resolving the distance ambiguity involved in the transformation from radial velocity to distance.

B. The Model

We model the galactic CO emission by an optically thin gas with a smoothly varying density distribution. The gas is assumed to be entirely confined to spiral arms, except for one ad hoc feature, the Aquila spur. The arms have a gaussian width which is determined primarily by the assumed lifetime of molecular clouds. Each arm is characterized by an inclination and a tangent direction which can be adjusted independently of the other arms: the arms in other words are not constrained to a two-armed logarithmic spiral pattern. In this regard, our approach resembles the analysis of neutral hydrogen in the inner galaxy given by Shane (1972). While the model is deliberately naive, it may represent a

reasonable first-order approximation to the distribution of CO emission in the inner galaxy. Since we concluded in chapter VI that enhanced heating of molecular clouds in the spiral arms probably does not significantly increase the CO arm-interarm contrast, the model may also be a reasonable approximation to the true distribution of molecular clouds, although this is less certain. As we concluded in chapter VI that streaming motions cannot account for the high-contrast CO spiral features, these too have been neglected. Details of the model are given in appendix B.

It is essential to stress that our intent here is not to produce a realistic model for the galactic CO emission which is valid on the scale of individual molecular clouds. The smoothly-varying density distribution of our model is obviously a poor approximation to the structure of the observed emission, which we will show in chapter VIII is dominated by a relatively small number of giant complexes. The intent of the model is instead to demonstrate that the large-scale structure of the CO emission is consistent with it being largely confined to spiral arms. How this emission is organized on the scale of clouds and complexes of clouds, roughly 100 pc and smaller, is not addressed by the model.

The model is essentially inspired by similar ones (e.g., Shane 1972) devised to account for the galactic

21-cm emission. We have seen that the structures of the CO and 21-cm ℓ,v maps are strikingly similar on a large scale (see, e.g., fig. V-1), and it is on this scale which we wish to study the galactic CO emission. Since models with smoothly-varying gas density have been routinely applied to the large-scale 21-cm emission, it seems reasonable to apply a similar model here, even if on smaller scales the model breaks down.

The model fitting proceeded in two stages. First, the parameters of the spiral arms were adjusted to produce a model longitude-velocity map which reproduced the main features of the data. This fitting was guided primarily by the locations of the three prominent interarm holes in the longitude-velocity map, the emission along the terminal-velocity curve, and the two prominent peaks in the graph of integrated emission vs. longitude (the $I(\ell)$ graph) which mark the tangent directions of the Scutum and 4-kpc arms. A detailed discussion of how the parameters of each of the spiral features were determined is given in appendix B. Once the location of the arms was established in this way, the number of free parameters was reduced to one - the cloud lifetime. The lifetime of molecular clouds, which in turn determines the width of the arms, was adjusted to reproduce the arm-interarm contrast in the longitude-

velocity map and the width and intensity of the peaks in the I(ℓ) graph.

The neglect of density-wave induced streaming of the clouds along the arms may cause us to underestimate the lifetime of molecular clouds since we assume the clouds move through the arms on unperturbed circular orbits. Since this streaming could more than double the time clouds spend within the arms, our derived cloud lifetime may be underestimated by this factor. Because of the uncertain influence of streaming, the most direct and reliable quantity to be determined by the model fitting will not be the lifetime of molecular clouds but the width of the molecular arms.

C. Results and Discussion

Figure VII-1 is a grayscale representation of the best-fit model galaxy. The inner arms are wider since in the model, the velocity of interstellar material with respect to the spiral pattern $R(\Omega - \Omega_p)$ increases towards the galactic center. The parameters of the arms are given in table 3.

1. The ℓ,v Map

Figure VII-2 is a grayscale version of the model longitude-velocity map produced by the distribution of CO emission shown in figure VII-1. The model should be

compared with the observed ℓ,v grayscale shown in figure III-5. To aid in the comparison, the heavy black line traces the main features of the observed ℓ,v map, namely, the high velocity ridge (for $\ell > 20°$), the large nearly empty region at high velocity below $\ell = 20°$, and the three main interarm holes. The vertical lane of emission near 10 km/sec between $\ell = 18°$ and 40°, prominent in the data, is produced by the local Great Rift clouds and need not concern us here (see chapter III).

Figure VII-2 illustrates that the main features of the observed ℓ,v map can be reproduced by a model in which molecular clouds are confined to a fairly regular pattern of spiral arms. The model assumes that clouds live for 15 million years after their birth at the spiral shock, producing molecular arms approximately 300 pc wide. Both the location and orientation of the main interarm holes are reproduced in the model. Of particular importance is the appearance of the high-velocity ridge. The claim has been often made (e.g., Liszt and Burton 1981; Solomon 1982) that the persistence of the high-velocity ridge for $\ell > 21°$ is a strong argument in favor of a relatively low arm-interarm contrast. Figure VII-2 demonstrates that the appearance of the high-velocity ridge in the first quadrant is consistent with molecular clouds being entirely confined

to three classical arms plus one ad hoc feature, the Aquila spur. In fact, we will show below that the high-velocity ridge is fit better by this model than by one which assumes lower arm-interarm contrast.

Although this naive model accounts for the data remarkably well in overall terms, several shortcomings are apparent. The near side of the Sagittarius arm is much more continuous in the model than is observed. This is clearly a result of our modeling the galactic CO emission as a smoothly distributed gas rather than as a collection of clouds. Because the near side of the Sagittarius arm is so close to the sun, this "continuum" approximation is especially inadequate there. Another disagreement is the nearly vertical empty lane which separates the far side of the Sagittarius arm from the spur in the model (ℓ = 35°-42°). Although there is some evidence for this lane in the data, it is much less obvious than in the model. This could be explained by the presence of several W44-type clouds in the far side of the Sagittarius arm between longitudes 38° and 42° which produce an apparent bridge of emission between the far Sagittarius arm and the spur. (It will be shown in chapter VIII that the giant molecular complex associated with the supernova remnant W44 has a velocity width in excess of 20 km/sec.) Finally there is the emission above ℓ=54° which is absent in the model. The kinematic

distance of this emission places it a few hundred parsecs outside the tangent region of the Sagittarius arm. The emission appears to be a very small spur-like extension of the Sagittarius arm, made prominent in the ℓ,v map by its special location - relatively close to the Sun and well separated (in angle) from the major arms. Similar extensions lying at more typical galactic locations would probably go unnoticed and may actually be fairly common.

2. The Spectra

Although the grayscale ℓ,v map is useful for judging the results of the first stage of the modeling, namely the choice of a suitable pattern of spiral arms, it is not well suited for studying the contrast between arm and interarm regions. For this purpose, some individual spectra, both model and observed, are shown in figure VII-3 (a-d). Each of the spectra chosen sample one or more of the main interarm gaps in the ℓ,v map. Since each of the gaps is at least a few degrees wide, the choice of which spectra to display is somewhat arbitrary. Most of the spectra within a degree or so of the selected spectra show the same large-scale structure. For each of the four directions chosen, three model spectra are shown corresponding to three assumed values for the cloud lifetime τ. Since the τ = 15 my model was judged to give the best overall fit to the data, it has the actual data

superimposed. The main interarm gaps are identified by number on the observed spectra, as they were in fig. V-1. The data has been summed over the latitude range of the fully sampled data, from b = -0°.25 to +0°.25.

The direction ℓ = 26° (figure VII-3a) samples the 4-kpc gap (# 1) at v = 80 km/sec. The Sagittarius arm in this direction is too weak to be seen. The arm-interarm contrast in the data is roughly 10:1, while the model contrast varies from approximately 20:1 to 5:1 between τ = 7.5 and 15 my. Thus the best fit is somewhat less than 15 my. The τ = 30 my spectrum illustrates how rapidly the interarm regions vanish as the molecular arms widen. It will be shown by several criteria that a cloud lifetime as long as 30 million years produces molecular arms which are too wide to match the observations.

At ℓ = 28° (figure VII-3b), we are observing the Scutum arm closer to its tangent direction. As one would expect, the near and far sides of the arm (at v = 80 km/sec and 100 km/sec, respectively) have increased in brightness and moved closer together in velocity, and the 4-kpc gap (# 1) has shifted to higher velocity (v = 90 km/sec). In this direction, we also sample one of the Scutum gaps (# 2) at v = 60 km/sec and a gap between the near and far sides of the Sagittarius arm, at v = 35 km/sec. Here again, a lifetime near 15 my gives the best

overall fit to the spectrum. For the 4-kpc gap, the data shows a contrast of ~3:1, while the model contrast varies from 7:1 to 2:1 between τ = 7.5 and 15 my. For τ = 30 my, the 4-kpc gap has vanished and the Scutum gap is of very low contrast.

The direction ℓ = 30° (figure VII-3c) views the Scutum arm close to its tangent direction and samples a wide section of the upper Scutum gap (# 3) at v = 60 km/sec. Because we are observing close to the Scutum tangent direction, its brightness has increased substantially, in excellent agreement with the model. For a lifetime as low as 7.5 my, the near and far sides of the arms are still resolved and the Scutum gap is essentially empty. For τ = 30 my, the intensity of the peak near 100 km/sec is too low and the Scutum gap is of too-low contrast. Thus, a cloud lifetime of 15 million years is again indicated.

Finally, the spectrum at ℓ = 38° (figure VII-3d) samples the upper Scutum gap (# 3) at v = 70 km/sec and the Sagittarius gap (# 4) at v = 50 km/sec. Although the contrasts here are not very sensitive to cloud lifetime, the best fit seems to occur closest to 15 million years. At τ = 7.5 my, the Scutum gap is almost empty, while at 30 my both gaps are of too-low contrast.

3. The I(ℓ) Graph

Another way to estimate the degree of confinement of molecular clouds to spiral arms is with the I(ℓ) graph of integrated emission vs. longitude, shown in figure V-4. This graph is of particular importance because it is independent of two effects which complicate the interpretation of the ℓ,v map. Unlike the arm-interarm contrast in the ℓ,v map, the appearance of the I(ℓ) graph is largely independent of the velocity dispersion of the clouds, since it has been integrated over velocity. For a similar reason it is insensitive to large-scale streaming motions, which produce contrast in the ℓ,v map by perturbing the emission in velocity, not ℓ (or b).

Figure VII-4 presents model I(ℓ) graphs in a format similar to that of the model spectra in figure VII-3. Model curves are presented for three values of the cloud lifetime τ, with the observed curve superimposed on the τ = 15 my graph. The data have been integrated from -0°.25 to +0°.25 in latitude and from 20 km/sec upward in velocity, and the models too have been integrated over velocity above 20 km/sec. Emission below 20 km/sec has been omitted to avoid a contribution from local material such as the Great Rift not included in the model.

The two most prominent features in both the data and the models are the emission peaks near ℓ = 24° and 31°,

associated with the tangent directions of the 4-kpc and Scutum arms, respectively. The lack of a prominent emission peak associated with the Sagittarius arm has been discussed in chapter V.

An examination of figure VII-4 will reveal that a cloud lifetime on the order of 15 million years again yields the best fit to the data. The intensity and width of the emission peaks associated with the Scutum and 4-kpc arms are seen to be quite sensitive to the assumed width of the arms. For a cloud lifetime as short as 7.5 my, the peaks associated with all four spiral segments are too strong. Even the Aquila spur, which does not reach to the subcentral point, produces a well-defined peak. For a lifetime as long as 30 my, the Scutum and 4-kpc peaks are poorly resolved.

The largest deviations between the τ = 15 my model and the data occur near ℓ = 14° and ℓ = 35°, where the data shows relatively strong peaks. As was discussed previously, these peaks are associated with two very large, nearby molecular complexes in the near side of the Sagittarius arm - the M17 complex near ℓ = 14° and the W44 complex near ℓ = 35°. Because the near side of the Sagittarius arm is so close to the sun, its CO emission as previously noted is poorly modeled by a smoothly distributed gas.

Figure VII-5 demonstrates that the fit to the data is significantly improved if the near Sagittarius arm emission is omitted. Figure VII-5 differs from figure VII-4 only by the lower limit of the velocity integral, the integral here including only emission above 60 km/sec. With a lower limit of 60 km/sec, we have eliminated any contribution from CO in the Local arm as well as from CO in the near side of the Sagittarius arm. Most of the emission from the far Sagittarius arm and the inner arms is still included in the integral. The graph, in fact, represents the bulk of the emission from the so-called molecular ring region of the galaxy. The overall fit in figure VII-5 is seen to be quite good. Both the width and intensity of the peaks associated with the inner arms are well fit. In addition, with the more local emission removed, an emission peak associated with the spur can be seen in the data near $\ell = 38°$.

4. The High-Velocity Ridge

The continuity of the high-velocity ridge in the CO data is often cited as evidence of low arm-interarm contrast for molecular clouds (Liszt and Burton 1981; Solomon 1982). We will now show that the detailed structure of the CO high-velocity ridge is best fit by a model with very high arm-interarm contrast. The

high-velocity ridge emission will also provide another means of estimating the cloud lifetime in the model.

As a working definition, let us take the high-velocity ridge emission at any longitude to be the sum of all emission arising within 1.5 kpc of the subcentral point - the point along the line of sight closest to the galactic center. The high-velocity ridge emission at galactic longitude ℓ is then

$$HVE = \int_{V_L}^{\infty} T(v)dv$$

where V_L is the radial velocity of a point displaced 1.5 kpc along the line of sight from the subcentral point. Thus

$$V_L = R_0 \left(\Omega(R_L) - \Omega_0\right) \sin(\ell),$$

where

$$R_L = \left(1.5^2 + R_S^2 \right)^{1/2},$$

R_0 and R_S are the galactocentric radii of the sun and the subcentral point, respectively, Ω_0 is the angular velocity of the sun (25 km s^{-1} kpc^{-1}) and $\Omega(R)$ gives the angular velocity as a function of galactocentric radius. At low longitudes, V_L was about 10 km/sec less than the terminal velocity.

We will consider the high-velocity emission between the longitudes of 22° and 55°. This interval includes the tangent directions of all the spiral arms in the

model. Below ℓ = 22°, the high-velocity ridge is essentially absent from the data, while above 55°, beyond the tangent point of the Sagittarius arm, our simple model predicts no emission at all.

The observed high-velocity ridge emission, computed from the CO data integrated from b = -0°.25 to +0°.25, is shown in figure VII-6 along with some model versions of the curve. As previously, the observed curve has been superimposed on the model corresponding to a cloud lifetime of 15 million years. Recall that this graph displays, as a function of longitude, the emission from a 3-kpc long segment of the line of sight centered on the subcentral point. As one would expect, the data shows four emission peaks (labeled on the τ = 7.5 my graph) in the directions at which spiral arms cross the locus of subcentral points. (Although the spur does not cross the locus of subcentral points, it extends close enough to it to be detected.) At points along the locus of subcentral points displaced from spiral arms, such as near ℓ = 28°, 36°, and 44°, the CO emission is very weak or absent. The lack of CO emission in the subcentral region near ℓ = 36° has been cited by Bash (1979) as observational evidence for the concentration of CO into spiral arms. Stark (1979) reached a similar conclusion based on his high-sensitivity ^{13}CO observations of the region:

defining the subcentral region as we do here (i.e., as a 3-kpc long segment centered on the subcentral point), he found 14 large molecular clouds in a square degree of the subcentral region at $\ell = 34°$, compared to no such clouds in a similar field centered on $\ell = 36°$.

The models in figures VII-6 demonstrate that as the widths of the molecular arms increase, the emission along the high-velocity ridge becomes more uniform. For a cloud lifetime of 30 million years, the well-observed hole at $\ell = 36°$ vanishes and the hole at $\ell = 28°$ is of very low contrast. Thus, contrary to the claims of, for example, Liszt and Burton (1981) and Solomon (1982), the CO high-velocity ridge emission is actually entirely consistent with molecular clouds being confined to a fairly regular pattern of spiral arms.

Figure VII-6 also provides another means of estimating the cloud lifetime. As was discussed above, a lifetime as long as 30 million years seems to be ruled out on the basis of the high emission the model produces near $\ell = 28°$ and $\ell = 36°$. A lifetime of 7.5 million years produces too high a contrast between arm and interarm regions. Once again, a cloud lifetime of 15 million years produces the best approximation to the data.

The most obvious failing of the 15 million year model is the intensity of the peak near $\ell = 31°$ associated with the subcentral region of the Scutum arm. The greater intensity of the model peak may result from our assumption that the molecular galaxy is everywhere optically thin. Although cloud shadowing does not appear to be important overall (Burton and Gordon 1978), it may become important near the tangent regions of the major spiral arms. At $\ell = 31°$, the 3-kpc region being sampled lies along the brightest molecular arm in the first quadrant, and it is there if anywhere that cloud shadowing might be important.

D. Summary

A simple spiral model has been constructed which seems to represent a plausible first-order approximation to the distribution of CO emission in the inner-galaxy. It has been assumed that the galactic CO emission arises from molecular clouds in a fairly regular pattern of spiral arms. The locations and orientations of these arms were adjusted to reproduce the main features of the observed CO ℓ,v map. Once this was accomplished, the number of free parameters in the model was reduced to one - the cloud lifetime τ. With increasing τ, the widths of the CO arms in the model increases, and the

contrast between arm and interarm regions in the ℓ,v map decreases. While the model is deliberately naive, it accounts for the main features of our CO survey remarkably well. The contrast between arm and interarm regions in the ℓ,v map, the velocity integrated emission vs. longitude, and the emission along the high-velocity ridge were best fit by a model in which clouds live for about 15 million years after their formation in the spiral arms.

The derived cloud lifetime of 15 million years is probably an underestimate since the model neglects the possible influence of streaming on the orbits of the clouds through the arms. Since streaming could plausibly increase the time clouds spend within an arm by more than a factor of two, the actual cloud lifetime may be as high as 40 million years. A more direct result of the modeling is the width of the CO spiral arms: in the first quadrant the inner-galaxy CO emission appears to be largely confined to three spiral arms each of the order of 300 pc wide.

VIII. THE LARGEST MOLECULAR CLOUDS IN THE FIRST GALACTIC QUADRANT

A. Introduction

In discussing the distribution of molecular clouds in the inner galaxy we have so far analyzed mainly the CO ℓ,v map, concentrating on the loop-like features (see fig. III-5) and deep minima or "holes" suggestive of spiral structure. Because of the kinematic distance ambiguity of objects within the solar circle, it is not a simple matter to decide just where these apparent features lie in the galactic plane. Thus we have yet to show, for example, that the vertical lane of clouds marking the far side of the Sagittarius arm (near V = 60 km/sec, between ℓ = 30° and 52°) actually lies on the far side of the galaxy. We will now take an entirely different tack, and discuss the largest clouds apparent in our survey on the assumption that these are discrete objects with well-defined locations on the galactic plane. The distances to these clouds will provide strong support for our interpretation of the ℓ,v map by locating the spiral features in the galactic plane. We will show, for example, that the large clouds on the high-velocity side of the putative Sagittarius "loop" do, in fact, lie at the far kinematic distance.

Our discussion will proceed in several steps. We will first demonstrate that the largest molecular clouds are an important component of the interstellar medium. Using a section of the Perseus spiral arm to determine a mass (or luminosity) spectrum for molecular clouds, we will show that these clouds contain a significant fraction of the galactic molecular mass and CO luminosity. Next, one of the nearest of these large clouds, that associated with the supernova remnant W44, will be studied in some detail. This will provide us with a prototype for the class of large clouds which we will study. Finally, we will turn to an investigation of these large clouds on a galactic scale.

B. The Molecular-Cloud Mass Spectrum

The large, well-defined clouds to be investigated in this chapter are of great value in studying the distribution of molecular gas in the inner galaxy, since nearly all of them appear to be associated with known young objects (star clusters, giant H II regions, masers, etc.) whose distances can be determined. Clearly, however, not all of the molecular gas is confined to these large clouds. The emission in the high-resolution ℓ,v map (fig. III-4a) is quite complex, with structure apparent on many scales. Before proceeding with the

analysis of these largest clouds, it is important to demonstrate that they represent a substantial fraction of the galactic molecular mass. To do this, a portion of the Perseus spiral arm will be used to determine a mass spectrum for molecular clouds.

Although the inner arms of the galaxy have a higher density of clouds than does the Perseus arm, it is very difficult to obtain a mass spectrum from clouds within the solar circle because of the two-fold distance ambiguity. Many of the smaller clouds in the survey cannot be associated with the optical objects that allow resolution of the distance ambiguity. Near the terminal velocity, where the distance ambiguity becomes less important, velocity crowding makes it difficult to distinguish individual clouds. In contrast, the Perseus arm is ideally suited to the task, being somewhat the analog of a stellar cluster: it is fairly close, its clouds all lie at roughly the same distance, and there is no distance ambiguity.

A 1.6-kpc segment of the Perseus arm, between ℓ = 104° and 128°, has been used for the analysis. This region, which has been mapped in CO by H.I. Cong and J. Brock, is part of an extensive Perseus-arm survey done with the Goddard-Columbia telescope.

A spatial map of the Perseus-arm emission is shown in figure VIII-1. The emission has been integrated over the approximate velocity extent of the Perseus arm in this longitude range. Since the lowest contour corresponds to approximately 4 times the rms noise level, all of the features in figure VIII-1 will be considered statistically significant detections in the following analysis.

Most of the Perseus clouds have velocities between -60 and -40 km/sec. If these clouds are transformed kinematically into the galactic plane, they define an arm with a width in excess of 1 kpc. In fact, very little can be said about the actual width of the Perseus arm since most of the 20 km/sec spread in velocity could result from the clouds' random motions combined with the influence of streaming motions associated with the arm. However, we have previously found that the inner arms, which can be viewed tangentially, have widths less than 500 pc (see chapter VII). Thus it is plausible to assume that the width of the Perseus arm is less than the 1 kpc which the clouds' kinematic distances would imply. To avoid the large errors associated with these distances, we have assumed that all the clouds lie at the potential minimum of the arm. If the actual width of the arm is less than 1 kpc, this procedure should yield distances

which are, on average, more accurate than those determined kinematically. The location of the potential minimum of the arm was adopted from the spiral-arm model of Bash et al. (1977) and Yuan (1969).

Cloud masses were computed on the assumption that the integrated CO line intensity $W(CO) = \int T(CO)\, dv$ is proportional to the H_2 column density $N(H_2)$. The mass of a cloud computed in this way will be referred to as its CO mass M_{CO} to point up the fact that it is computed directly from the absolute CO luminosity of the cloud. While a detailed understanding of the radiation transfer is lacking, W(CO) appears to be roughly proportional to $N(H_2)$ despite its high optical depth. This conclusion follows from the observation that ^{12}CO lines generally mimic the shapes of ^{13}CO lines (Scoville and Solomon 1975, Burton et al. 1975), i.e., $W(CO) \propto W(^{13}CO)$. But since ^{13}CO lines generally have low opacity we expect $W(^{13}CO) \propto N(H_2)$. The proportionality of W(CO) and $N(H_2)$ may result from velocity gradients (Goldreich and Kwan 1974) or macro-turbulence (Bash et al. 1981) in the clouds which have similar effects on both the ^{12}CO and ^{13}CO line shapes. The assumption of a constant ratio $N(H_2)/W(CO)$ is now widely used for computing molecular masses from CO observations of external galaxies (Morris

and Rickard 1982), and it has recently been calibrated by Lebrun et al. (1982). Using gamma-rays as a tracer of the total-gas column density and the 21-cm line as a tracer of the atomic gas, they find

$$N(H_2)/W(CO) = 1\text{-}3 \times 10^{20} \text{ cm}^{-2} \text{ K}^{-1} \text{ km}^{-1} \text{ s}.$$

Adopting a value of 2×10^{20} cm^{-2} K^{-1} km^{-1} s and a mean molecular weight per H_2 molecule of 3.94×10^{-24} gm (Elmegreen, Lada and Dickinson 1979), the CO mass of a cloud can be expressed as

$$M_{CO} = 1.1 \times 10^3 \; I_{CO} \; D^2$$

where M_{CO} is in solar masses, D is the cloud's distance in kpc, and I_{CO} is the cloud's apparent CO luminosity, i.e., the total emission integrated over velocity and over the face of the cloud, in units of K km/sec deg^2. Since a cloud's CO mass is assumed to be directly proportional to its absolute CO luminosity, the mass spectrum to be determined below is fundamentally a luminosity spectrum for molecular clouds.

Positions, distances, and masses were determined for all the clouds in figure VIII-1, the distance assigned to each cloud equal to the distance to the center of the Perseus arm at the longitude of the cloud. The masses range over almost 3 orders of magnitude, providing an

adequate data base for the determination of a mass spectrum.

The data from figure VIII-1 is summarized in table 4, where the clouds have been binned in half-decade intervals of mass. The mass interval corresponding to each bin is given, along with the number of clouds in each bin (N), the total cloud mass in each bin (M_T), and the fraction of the total mass contained in each bin (f). The half-decade binsize provides adequate mass resolution while still maintaining a reasonable number of clouds per bin. While this binning is necessary to produce a log N - log M graph, it has no bearing on our final result. The mass spectrum (i.e., the slope of the log N - log M graph) was computed using a maximum-likelihood analysis which requires no binning of the data.

By analogy with the conventional analysis of radio-source counts, it has been assumed that the mass spectrum for molecular clouds may be approximated by the expression

$$N = kM^{-s} \qquad (3)$$

where N is the number of clouds with a mass greater than M. In this expression, k depends on the volume sampled and on the overall density of clouds in that volume and so is not required for the present discussion. On the other hand, the spectral index s is the fundamental

quantity which describes the cloud mass spectrum. For $s > 1$, the total cloud mass contained in any logarithmic mass bin increases as the central mass of the bin decreases, and clouds at the low-mass end of the spectrum contribute most of the emission and mass in any sample of clouds. For $s < 1$, the opposite is true: high-mass clouds dominate the total emission and mass.

The binned data in table 4 is represented as a log N - log M graph in figure VIII-2. It is easy to show that the slope of a linear fit through these points is equal to -s, with s defined as in equation 3. While a least-squares fit would yield an approximate value of s, the result would obviously depend on the choice of binsize. Fortunately, the log N - log M graph is an exact analog of the classic log N - log S graph of radio-source counts with cloud mass replacing the flux density of radio sources, and several techniques have been developed for determining s from data of this sort. The slope of the linear fit shown in figure VIII-2 was determined using the maximum-likelihood method of Crawford et al. (1970). This method makes the fullest use of the data while requiring no binning. Also shown in figure VIII-2 is the critical slope corresponding to $s = 1$. The best-fit line lies well below this critical line, indicating that the CO emission and molecular mass in the Perseus arm are dominated by the largest clouds.

The main source of ambiguity in this mass-spectrum analysis is the definition of individual clouds, but this is troublesome only for the 4 largest objects, which lie between ℓ = 108° and 112° (see fig. VIII-1). It is not clear whether these should be considered parts of a single cloud, or divided into 2, 3, or 4 individual clouds. Fortunately, the spectral index s does not depend sensitively on this decision. If they are individual clouds: $s = 0.43 \pm 0.08$, while if they are a single complex: $s = 0.49 \pm 0.09$. Thus the results may be considered fairly objective since they are not too sensitive to the ambiguity in the definition of individual clouds.

A final representation of the molecular-cloud mass spectrum is provided by figure VIII-3, where a histogram of the total cloud mass in each half-decade mass bin is presented. The plot illustrates quite clearly the main conclusion drawn from the maximum-likelihood analysis: most of the molecular mass in the Perseus arm is contained in the larger clouds.

C. W44, A Typical Giant Cloud

Later in this chapter, the distribution and masses of the largest molecular clouds in the galaxy will be studied. Because these giant clouds, with typical masses

of 10^6 $M_\odot$, are few in number they are also generally quite distant. In the ℓ,v map, they are often surrounded by and immersed in more diffuse emission, both from surrounding halo gas and from unrelated foreground and background material at the same velocity. Sometimes too, the clouds lie close to the terminal velocity where the likelihood increases that what is taken to be a single cloud is actually a blend of several clouds at nearly the same velocity. In light of these difficulties in resolving individual clouds, one might question the existence of such large clouds. Fortunately, several nearby and well-defined examples of such clouds exist. The nearest examples are the cloud associated with NGC 7538 and the SNR Cas A in the Perseus arm (Cohen et al. 1980), the entire M16-M17 region in the near Sagittarius arm (Elmegreen, Lada, and Dickinson 1979), and the cloud associated with the SNR W44, also in the near Sagittarius arm. The entire Orion region might also be included in this list, but with a mass of only several times 10^5 $M_\odot$ (Maddalena et al. 1983) it is somewhat smaller than most of the clouds considered here. In this section, the structure and mass of the W44 cloud is studied in some detail: it can be considered the prototype of the class of giant clouds to be discussed below.

Our discussion of the W44 cloud will generally be limited to demonstrating the following points. First, we will argue that nearly all of the emission in the range ℓ = 34° to 36°, V = 30 to 50 km/sec, and probably much of the emission at the same longitude between 50 and 65 km/sec, is associated with this object. This will provide an explanation for the "bridge" of emission which apparently links the near and far sides of the Sagittarius arm in the integrated ℓ,v map (see the discussion of this "bridge" in chapter V). Second, we will show that the mass of the W44 cloud is in excess of 10^6 $M_\odot$, a factor of 5-10 above the masses of the largest molecular complexes in the solar neighborhood (see, e.g., Blitz 1980) and comparable to the masses of the large clouds to be studied later. And finally, it will be shown that the LTE and virial masses computed for the cloud are in rough agreement with the mass computed directly from its CO luminosity, its CO mass. This is important since only CO masses will be computed for the other clouds to be studied.

Compelling evidence that the emission in the region ℓ = 24° - 26°, V = 30-65 km/sec is part of a single complex is provided by the ℓ,v maps at b = -0°.75 and b = -1°.0 (figs. III-6j and III-6k, respectively). At b = -0°.75, in particular, the emission stands out as a

single coherent feature. While the emission does appear to consist of 3 clumps (at velocities of 35, 45, and 55 km/sec), it is very unlikely that 3 of the most intense features in the map would fall along the same line of sight by chance. Much more likely, these clumps are part of a single complex which extends well below the plane. As was pointed out in chapter V, such a large velocity width for a complex is not unprecedented. The well-defined complex associated with NGC 7538 in the Perseus arm has a similar width. (This complex can be seen near ℓ = 111° in figure V-2).

Since the W44 complex extends well below -1° in latitude, the limit of the in-plane survey, further observations were required to produce a complete map. The complex was fully sampled in ^{12}CO and in the rarer isotopic species ^{13}CO. The ^{12}CO observations were taken every beamwidth (0°.125) following procedures identical to those of the in-plane survey. In the ^{13}CO line, the cloud was also fully sampled but at a spatial resolution of 0°.5 and to a lower rms noise level: typically 0.2 K versus 0.45 K for the ^{12}CO spectra.

Before spatial maps of the complex can be produced, its full velocity extent must be determined. Some insight into this problem is provided by figure VIII-4, which presents a latitude-velocity map integrated over

the approximate longitude extent of the cloud. The map indicates that the emission between 30 and 50 km/sec is part of a single cloud with an extraordinarily large latitude extent. We have already seen from the ℓ,v map at b = -1° (fig. III-6k) that emission at a latitude of -1° is quite unusual in this velocity range. Yet here we see that the 30-50 km/sec emission extends to at least -2° in latitude. We will refer to this extended-latitude emission as the main body of the cloud. While the emission between 50 and 65 km/sec also has an unusually large latitude extent (corresponding to a linear size of 140 pc at the near kinematic distance of 4 kpc), we cannot assume that this emission is associated with the W44 cloud on this basis alone.

There is, however, further evidence that the emission between 50 and 65 km/sec is associated with the W44 cloud. We will argue that this high-velocity emission results from an interaction between the main body of the cloud (at a velocity of 30-50 km/sec) and the SNR W44. The surface brightness-linear diameter relation of Milne (1979) implies a distance of 3.1 kpc for this remnant, in good agreement with the kinematic distance of the main body of the molecular cloud. (Taking 40 km/sec as the central velocity of the cloud yields a near kinematic distance of 2.8 kpc). OH (Goss, et al. 1971), H_2CO

(Whiteoak and Gardner 1972), and HI (Knapp and Kerr 1974) absorption lines are observed against the continuum of the remnant at velocities between 30 and 50 km/sec, suggesting that the renmant lies beyond the main body of the cloud. No absorption lines however are observed in the range 50-65 km/sec, implying that this emission lies beyond the remnant. These conclusions are supported by the recombination-line observations of Bignell (1973). He reports the detection of a H166α recombination line in the direction of the remnant at a velocity of 50 km/sec, precisely the velocity one would expect for the remnant from the absorption-line results.

Thus the remnant appears to lie near the back of the cloud at a velocity of about 50 km/sec. If the supernova explosion accelerated molecular gas in the vicinity, we might expect an expanding shell of molecular gas to have developed. The near side of such a shell would be expanding into the main body of the cloud and would be observed at velocities less than 50 km/sec, the velocity of the remnant itself. This emission would be difficult to distinguish from the emission of the main body of the cloud. On the other hand, the far side of the shell would be expanding away from the cloud and away from the earth and so should be observable at velocities greater than 50 km/sec. In fact, the CO emission in the range

50-65 km/sec shows just such a shell, roughly centered on the direction of the remnant. The shell is clearly seen in figures VIII-5 and VIII-6, which present the ^{12}CO and ^{13}CO emission integrated from 50 to 65 km/sec. The direction of W44 is marked in both figures. Also shown is the approximate position of an expanding shell of cold HI gas detected by Knapp and Kerr (1974). This cold HI shell, which appears as a 21-cm absorption feature at a velocity of about 45 km/sec, may be the near side of the expanding shell.

To summarize, most of the CO emission in the vicinity of the SNR W44 is apparently associated with a large, coherent molecular cloud with a linear size of 100 to 150 pc and a velocity extent of at least 20 km/sec. Although the emission from this cloud is probably blended with unrelated galactic-plane emission, its spatial and velocity extents are well-defined by its much larger latitude extent. The SNR W44 lies towards the back of the cloud and may be responsible for its unusually large velocity width. The SNR is apparently surrounded by an expanding shell of gas, the far side of which can be seen in the cloud's high-velocity CO emission between 50 and 65 km/sec. The near side of the shell, expanding into the main body of the cloud and towards the earth, has

been detected in 21-cm absorption at a velocity of ~45 km/sec. The large velocity extent of the cloud is comparable with that of the cloud associated with the SNR Cas A (at ℓ = 111° in fig. V-2).

^{12}CO and ^{13}CO spatial maps of the emission integrated over the full velocity extent of the complex are presented in figures VIII-7 and VIII-8, respectively. Since the cloud is largely obscured by the local dust cloud Khavtassi 3 (Knapp 1974), optical observations of this region are not possible. A section of the cloud near the SNR W44 has been previously mapped in CO (Dickel, Dickel, and Crutcher 1976; Wootten 1977) and in other molecular tracers such as OH (Goss, Caswell, and Robinson 1971) and formaldehyde (Whiteoak and Gardner 1972; Dickel 1973), however, these observations were generally confined to within 1° of the SNR. Another small section of the cloud near W48 (ℓ =35°.2, b = -1°.7) has also been studied in CO (Zeilik and Lada 1978) and OH (Pashchenko 1977). This section of the cloud is a region of star formation containing numerous H_2O masers (Moorwood and Salinari 1981), IR sources (Zeilik and Lada 1978), and OH masers (Evans et al. 1979). The possibility that W44 and W48, which are more than 1°.3 apart, might be related was first raised by Pashchenko (1977), who proposed that both were embedded in a single molecular complex with a diameter of 100 pc.

Now that the full spatial and velocity extents of the cloud have been determined its mass can be estimated. Various mass estimates for the W44 cloud are presented below.

CO Mass:

CO masses for the largest molecular clouds in the inner galaxy, including the W44 cloud, will be given later in this chapter, with details of how the masses are computed. The CO mass there derived for the W44 cloud is 1.3×10^6 $M_\odot$.

LTE Mass:

^{13}CO column densities through the W44 cloud have been calculated under the assumptions of local thermodynamic equilibrium (LTE) and optically thick ^{12}CO lines (Dickman 1975), following the standard LTE analysis described by Blitz (1978). ^{13}CO masses were converted to total molecular masses by adopting a ratio $N(^{13}CO)/N(H_2) = 2 \times 10^{-6}$ (Dickman 1975) and a mean molecular weight per H_2 molecule of 2.36 (Elmegreen, Lada, and Dickinson 1979). The consistency and value of the ratio $N(^{13}CO)/N(H_2)$ are major uncertainties of the LTE approach. The ratio depends on the $^{12}C/^{13}C$ isotope ratio, the degree of fractionation of CO (Langer 1977), the depletion of carbon relative to the cosmic abundance,

and perhaps also on the average cloud density (Elmegreen and Elmegreen 1978). The various estimates of this ratio (Encrenez, Falgarone, and Lucas 1975; Dickman 1975; Tucker et al. 1976), determined from star counts and extinction measurements in diffuse clouds, cluster around Dickman's value with a scatter of about 50%.

All of the W44 ^{13}CO spectra are shown in figure VIII-9. These spectra fully sample the cloud at a spatial resolution of 0°.5. As the vertical lines at 40 and 50 km/sec illustrate, the emission is well resolved into 3 velocity components centered near 35, 45, and 55 km/sec. The velocity of each component is constant to within a few km/sec over the face of the cloud. Generally, one or two components can be seen in a given spectrum. (The appearance of adjacent spectra suggests that the strong feature seen at ℓ = 35°, b = -1°.5 is a blend of the two components at 35 and 45 km/sec.)

To determine the total mass of the W44 cloud, each of the 3 velocity components was treated as a separate cloud. Approximate peak ^{13}CO temperatures and line widths were determined for all of the shaded emission features in figure VIII-9 by fitting each with a gaussian by eye - a reasonable procedure in view of the complexity of the emission. The uncertainties associated with these

measurements are neglible compared with the other uncertainties associated with the LTE analysis (see, e.g., Elmegreen and Elmegreen 1978).

Average values for the measured quantities T_L^{12}, T_L^{13} and ΔV and the derived quantities T_x, τ_{13}, and $N(^{13}CO)$ for each of the 3 component clouds are given in table 5. Also given is the number of spectra N in which the component cloud was detected. The quantities given are simply an average of those derived from the N spectra in which the component cloud was detected. The total molecular mass M_T for each of the 3 component clouds is given in the last column.

The total LTE mass of the W44 complex, taken to be the sum of the component masses given in table 5, is then 1.0×10^6 $M_\odot$.

Virial Mass:

Another mass for the W44 complex can be obtained by assuming that the cloud is in virial equilibrium, supported by internal motions. For a uniform, spherical cloud of mass M, radius R, and 3-dimensional velocity dispersion σ, the virial theorem can be written as

$$M\sigma^2 - 3/5\ GM^2/R = 0.$$

Solving for M and converting to more convenient units, we can write

$$M = 210\ R\ \Delta V^2$$

where M is in solar masses, R is in pc and ΔV is the FWHM velocity extent of the cloud in km/sec.

Values of R and ΔV for the largest molecular clouds in the inner galaxy, including the W44 cloud, will be given later in this chapter. At that time, the details of how R and ΔV were determined will be discussed. For now we will simply state the results: R = 52 pc and ΔV = 10 km/sec. This yields a virial mass for the W44 cloud of $1.1 \times 10^6 M_\odot$.

For reference, our various mass estimates for the W44 cloud are compiled in table 6. The good agreement between the CO mass and the LTE and Virial masses demonstrates the usefulness of the ^{12}CO line as a molecular-mass tracer and indicates that our adopted value of $N(H_2)/W_{CO}$ is a reasonable one.

Our main conclusions concerning the W44 complex are summarized below.

(1) Most of the emission in the region ℓ = 34° - 36°, V = 30 - 65 km/sec arises from a single, large molecular complex associated with the SNR W44 in the near side of the Sagittarius arm.

(2) The mass of the complex is in excess of $10^6 M_\odot$, a factor of 5-10 above that of the largest molecular clouds in the solar neighborhood (e.g., the Orion region) and comparable to the CO masses of the giant clouds to be discussed below.

(3) The CO mass of the complex, based simply on the assumption that the integrated intensity of the CO emission, W_{CO}, is a good tracer of total molecular mass, is in good agreement with other mass estimates based on observations of the presumably optically thin isotopic species ^{13}CO and the virial theorem. This result demonstrates the usefulness of the ^{12}CO line as a molecular-mass tracer.

D. Decomposition of the Inner-Galaxy Emission

From our study of the Perseus arm, we have determined that the CO emission in the outer galaxy is dominated by the largest molecular clouds and we will henceforth assume that the largest clouds likewise dominate the emission in the inner galaxy. In the vicinity of the sun, these largest clouds appear to be excellent spiral-arm tracers. In the Perseus arm between ℓ = 104° and 180°, for example, the emission is dominated by the 3 largest clouds near ℓ = 111°, 134°, and 173° (see figure V-2). Similarly, in the closest section of the Sagittarius arm the emission is dominated by the M16-M17 complex near ℓ = 15°, V = 20 km/s and the W44 cloud near ℓ = 35°, V = 45 km/s (see fig. III-5). In the following analysis, the largest clouds detected by our inner-galaxy survey will be used to trace the spiral arms on a

galactic scale. These objects are particularly useful for this purpose since their distances can be generally determined from related stellar clusters and associations, H_2CO absorption, etc.

It is not clear what these largest molecular objects in the galaxy should be called. For simplicity they are referred to here as clouds, although some new term might be more appropriate. The terms "molecular cloud", "giant molecular cloud", and "molecular complex" are used interchangeably in the current literature, and all generally refer to objects with typical masses of 10^5 $M_\odot$ and dimensions < 100 pc (Blitz 1978). The objects considered below, of which W44 can be considered a prototype, have masses 5 to 10 times larger than a typical "giant molecular cloud" and are presumably conglomerates of such clouds.

We have seen that the CO emission from the W44 cloud represents one of the largest coherent features in the first-quadrant ℓ,v map. Similar objects in more distant parts of the galaxy would also produce prominent emission features. For example, a cloud comparable in size to W44 would subtend an angle of about 1° at the distance of the molecular ring. Such large features, with spatial and velocity extents much larger than the resolution of our survey, are best revealed by smoothing the ℓ,v map.

Smoothed versions of the integrated ℓ,v map are shown in figure III-4. In figures III-4b and III-4c, the data has been smoothed to 1/2 and 1/4 the original resolution, i.e., to 2.6 km/s by 0°.5 (fig. III-4b) and to 5.2 km/sec by 1°.0 (fig. III-4c). In both these figures, but most noticeably in figure III-4c, the emission appears to be dominated by 20 or so well-defined, intense emission features with typical dimensions of 1°-2° by 10-20 km/sec. It is these dominant molecular objects of the inner galaxy, comparable in size and mass to W44, which we now consider.

The task of defining the spatial and velocity extents of these inner-galaxy clouds is complicated by the high level of CO emission which exists throughout the inner first quadrant. While the Perseus-arm clouds considered above appear as isolated features in the ℓ,v map (fig. V-2), the inner-galaxy clouds are generally surrounded by and superimposed on a more extended background of CO emission - presumably the result of numerous smaller clouds similar to those which are scattered along the Perseus arm.

To remove this background and reveal the largest objects more clearly, the emission from small clouds was assumed to be axisymmetric with the same radial distribution as the total CO emission (i.e., that of the

"molecular ring"). A model ℓ,v map of the background emission constructed under these assumptions is shown in figure VIII-10. An ℓ,v map of this form was subtracted from the observed map (fig. III-4c) to produce the map shown in figure VIII-11. The absolute level of the background model was adjusted so that in the subtracted map most of the "intercloud emission" was removed but most of the large features obvious in the original map remained. At the chosen background level, approximately 3/4 of the total emission in figure III-4c was removed in producing figure VIII-11.

As a check on this background removal technique, the clouds' apparent luminosities I_{CO} were redetermined directly from figure III-4c following a second, independent technique. The extent of any emission feature was defined by the last closed contour which encircled only that feature and the value of this contour defined the local background level. The cloud luminosity was then taken to be the total emission volume encircled by, but lying above, this last closed contour. The emission volume encircled by, but lying below the last closed contour was not included in the cloud luminosity. Despite some ambiguity of the background level when two or more clouds lie close together in the ℓ,v map, this technique was judged to be the only one which was as

plausible and straightforward as the one described above and so it was used as a check on the cloud luminosities. All of the luminosities derived from this technique agreed with the values derived above to within a factor of 2 and the average discrepancy was on the order of 50%. Thus we estimate that the uncertainty on the cloud luminosities is about a factor of 2. Since the conversion to mass introduces the further uncertainty of the $N(H_2)/W_{CO}$ value (see discussion above), we estimate a factor 3 uncertainty on the cloud masses presented below.

While other background-removal techniques could obviously be devised, the technique adopted seemed the best compromise for the present purpose. A more complex procedure might be based on the plausible assumption that the background clouds are largely confined to the spiral arms but this would greatly increase the number of free parameters required to produce the model background. Using such a procedure, one would also run the risk of introducing spirality into the data. (The simplest procedure would be to subtract a completely uniform ℓ,v map but on reflection this is found to make little sense: because of the complex nature of the transformation from the galactic plane to the ℓ,v map, only a very complicated and completely ad hoc distribution of background emission could result in a uniform background level in the ℓ,v map).

The cloud masses were computed directly from their integrated ^{12}CO luminosities I_{CO} as determined from figure VIII-11. In the numerous cases where two or more obviously discrete features were enclosed by one or more common contours, the emission was divided between features as indicated by the cuts (straight lines) in figure VIII-11. In most cases, it was fairly clear where these dividing lines should be placed. For some of the nearer clouds, a correction was applied to I_{CO} to account for emission lying outside the latitude range of the survey. These corrections were determined from the lower spatial resolution "superbeam" survey described in chapter III.

In most cases, the cloud distances were determined kinematically using the rotation curve of Burton (1971) (eq. 1). Although no single method is entirely reliable for resolving the distance ambiguity, a variety of indirect methods is available. In many cases a cloud appears to be associated with one or more HII regions whose distances were resolved by atomic and molecular absorption measurements (see, e.g., Lockman 1979b). In other cases, the cloud itself appears as a H_2CO absorption feature in the continuum of one or more HII regions which are known to lie between the cloud's near and far distances. In such a case, the cloud must lie at

the near distance. Since larger clouds tend to have larger velocity extents (Dame and Thaddeus 1982), a comparison of a cloud's angular size with its velocity extent can sometimes provide an index of its distance. For example, a cloud with a large angular size but relatively small velocity extent can be assigned to the near distance, since at the far distance it would correspond to a massive cloud with an uncharacteristically small velocity extent. All of these methods were used where applicable to help resolve the distance ambiguity. For a few of the clouds, the more accurate spectroscopic distance of an associated stellar cluster was used instead of the kinematic distance. A brief discussion of the distance to each cloud will be given below.

All of the HII regions in the longitude range of our survey with known distances are shown superimposed on a smoothed ℓ,v map in figure VIII-12. Stars and circles are used to represent HII regions at the near and far kinematic distances, respectively. HII regions which were assigned to the subcentral point are not included since they are of no value in resolving the distance ambiguity of the clouds. This figure should be referred to whenever the distance ambiguity of a cloud is resolved on the basis of HII regions.

It is important to emphasize that the large emission features seen in figures III-4c and VIII-11 are not a consequence of the smoothing applied to these figures, but are well-defined objects in the original data. A comparison of figure III-4c with the higher-resolution map in figure III-4b will show that essentially the same large features appear in both maps. The same features also exist in the unsmoothed map figure III-4a, although most of them are not as apparent in this map because of the complexity of the contours.

The dominant emission features in the unsmoothed ℓ,v map can be brought out and better defined by following the procedure adopted by Weaver (1974) in producing the 21-cm ℓ,v map shown in figure V-1 (see the discussion of this figure in chapter V). Essentially all of the large emission features apparent in the smoothed ℓ,v maps (figs. III-4c and VIII-11) are clearly seen and are identified by number in figure VIII-13, which was produced by setting all channels with $T < 2$ K to zero before the integration over latitude. This "clipped" map clearly demonstrates the existence and, in fact, prominence of our large emission features in the unsmoothed data.

A striking panoramic view of the largest molecular clouds is shown in figure VIII-14. These maps were

produced following the same clipping procedure described above: all spectral channels with $T < 2$ K were set to zero before the integration over velocity. Essentially all of the large emission features in the smoothed ℓ,v maps appear as well-defined objects in these figures. The clouds identified by number in figure VIII-11 (those to be studied and catalogued below) are likewise identified in figure VIII-14.

The clouds' projected areas were measured from figure VIII-14 by assuming that the lowest contour level defined the edge of the cloud. While the definition of individual clouds was sometimes somewhat arbitrary (see, e.g., clouds 2, 3, 5, and 8), the clouds were generally well-enough defined that this was not a serious problem. The clouds' projected areas were subsequently combined with their distances to determine their projected areas in pc^2 (A). The effective radius of the cloud was then taken to be $(A/\pi)^{1/2}$. The clouds' mean latitudes were also measured from figure VIII-14.

The clouds' linewidths (FWHM) were determined from their composite line profiles. A composite profile was produced by averaging together all spectra within a square region centered on the cloud position, the size of the region taken equal to the angular diameter of the complex as determined above. The spectra used in this analysis were clipped by setting all spectra channels

with T < 2 K to zero. This clipping procedure, the same as was employed in producing figures VIII-13 and VIII-14, was useful in distinguishing the clouds from the weaker and more extended background. The fact that all of the clouds originally identified in the unclipped CO map (fig. III-4c) appear as well-defined features in the clipped ℓ,v and spatial maps (figs. VIII-13 and VIII-14, respectively) indicates that most of the emission associated with the clouds lies above our adopted clipping level of 2 K.

A catalogue of the largest molecular clouds detected by our first-quadrant survey, those identified by number in figures VIII-11 and VIII-14, is presented in table 7. The longitude (ℓ) and velocity (v) were taken from the smoothed ℓ,v map in figure III-4c, and so represent the emission-weighted mean ℓ and v of the cloud. The cloud mass (M) was determined from figure VIII-11, the radius (R) and latitude (b) from figure VIII-14, and the linewidth (ΔV) from a composite spectrum of the cloud. The distance (D) is given along with a letter (Dist. Note) indicating which distance criterion was judged the most useful and reliable in determining the cloud's distance. A brief discussion of each cloud in table 7 is given below.

1. Notes on Individual Clouds

Notes on the individual clouds listed in table 7 are given here. The notes mainly concern the clouds' distances and the identification of associated HII regions and clusters. Such associations are made on the basis of coincidence in both angular position and velocity. The catalogue of HII regions in Downes et al. (1980) is abbreviated by DWBW, and the catalogue in Georgelin and Georgelin (1975) by GG. The associated HII regions are identified by their galactic longitudes.

(1) M17 - This cloud is visible as a dark nebula and is clearly associated with the HII region M17. We adopt the spectroscopic distance to M17 derived by Crampton, Georgelin and Georgelin (1978).

(2) The near kinematic distance was assigned on the basis of this cloud's proximity to three near HII regions at ℓ = 13°.998, 14°.600 and 14°.626 from DWBW. The low-longitude edge of this cloud was taken to be 13°.5. The emission below this longitude is associated with another cloud near W33 that has a much larger velocity extent, but is not included in the catalogue since it extends outside the longitude range of the survey. Although the longitude extent of cloud 2 is ambiguous in the highly-smoothed ℓ,v map (fig. III-4c), it appears as a well-defined feature in the higher-resolution maps (figs. III-4a or b).

(3) The near kinematic distance was assigned on the basis of this cloud's large angular size and small velocity extent. At the far distance, the cloud would have a radius of 187 pc (larger than any cloud in the catalogue) and would extend more than 130 pc below the plane.

(4) M16 - The spectroscopic distance to the nearby stellar cluster NGC 6611 was adopted (#9 from GG). The cloud mass has been increased by 63% to account for emission from outside the latitude range of the in-plane survey. The correction was determined from the low-resolution survey discussed in chapter III.

(5) The near kinematic distance was assigned on the basis of this cloud's proximity to the near HII regions at ℓ = 18°.143, 18°.185, 18°.231, and 18°.258 from DWBW, and the optical HII region #10 from GG.

(6) W39 - The near kinematic distance was assigned on the basis of this cloud's proximity to the near HII regions at ℓ = 18°.881, 18°.936, 19°.066, and 19°.614 from DWBW.

(7) The spectroscopic distance to star cluster #11 from GG was adopted. There is also a near HII region (ℓ = 20°.988 from DWBW) in its vicinity. It is also seen as a H_2CO absorption feature at 25.5 km/sec in the continuum of the HII region at ℓ = 18°.936 from DWBW.

The cloud may be associated with the M16-M17 complex (clouds 1 & 4) which lie at approximately the same distance.

(8) The near kinematic distance was assigned on the basis of this cloud's proximity to the HII regions at ℓ = 19°.608 and 20°.074 from DWBW. Its latitude of -0°.75 also suggests that it lies at the near distance: at the far distance of 15 kpc, it would be centered 200 pc below the galactic plane.

(9) This cloud is seen as a H_2CO absorption feature at velocities near 55 km/sec in the continua of HII regions at ℓ = 22°.982 and 22°.760 from DWBW. Since the far kinematic distances of these HII regions are smaller than the far kinematic distance of the cloud, the cloud must lie at the near distance. At the far distance the cloud would have a suspiciously large radius of 200 pc.

This cloud may be associated with the supernova remnant Kes69 (at ℓ = 21°.8, b = -0°.6). The surface brightness-diameter relation of Milne (1979) yields a distance of 4.2 kpc for this remnant, in good agreement with the cloud's near kinematic distance of 4.4 kpc.

(10N & 10F) W41 - This feature may be a blend of 2 large clouds, one at the near kinematic distance (10N) and one

at the far distance (10F). A large number of far HII regions (e.g., at ℓ = 22°.760, 22°.947, 22°.982, and 23°.254 from DWBW) are coincident in direction and velocity with this feature, suggesting that a very massive and active star-forming cloud exists at the far distance. However, the large angular size of the feature argues strongly for the near distance: at the far distance of 12.6 kpc the cloud would have a diameter of about 350 pc. There is also a strong H_2CO absorption feature at 81 km/sec in the continuum of the HII region at ℓ = 23°.421 from DWBW, which lies near the subcentral point - again evidence for a fairly massive cloud at the near distance.

A blend of near and far clouds might be expected in this region since it lies at the intersection in ℓ,v space of the near side of the 4-kpc arm and the far side of the Scutum arm (see, e.g., fig. III-5). The large angular size and strong H_2CO absorption associated with the near feature, and the large number of HII regions at the far distance, suggest that both components are massive; for lack of further evidence we simply assume that the emission is divided equally between the two objects.

(11) The near kinematic distance was assigned on the basis of this cloud's proximity to the near HII region at ℓ = 23°.43, from Lockman (1979b). (This HII region was also assigned to the near distance by GG). There are a large number of HII regions in the direction of this feature, but they are too close to the terminal velocity for their distances to be resolved; the feature may therefore result from several clouds spread along the tangent region of the 4-kpc arm.

(12N & 12F) W42 - This feature may be a blend of 2 clouds, one at the near kinematic distance (12N) and one at the far distance (12F). Although the far component is not obvious in a spatial map integrated over the full velocity range of the feature, it does appear clearly in a more restricted velocity range surrounding the velocity of the far HII region W42 (at ℓ = 25°.382 from DWBW). The far component coincides well in direction and velocity with the far HII region W42. Its total CO luminosity was taken to be the integrated emission in the region ℓ = 25° to 25°.5, b = 0°875 to 0°.125 and v = 50 to 62 km/sec. The rest of the emission (~75%) was placed at the near distance on the basis of its latitude extent: at the far distance it would have an average diameter in excess of 400 pc.

As for feature 10, a blend of near and far clouds might be expected for feature 12 since it lies near the intersection in ℓ,v space of the near side of the Scutum arm and the far side of the Sagittarius arm (see, e.g. fig. III-5).

(13) The lack of HII regions associated with this large cloud is unusual. There are, however, many HII regions in the same direction near the subcentral point and this cloud is seen in absorption against 4 of them. The best examples are the HII regions at ℓ = 28°.658 and 28°.801 from DWBW, which have H_2CO absorption features at 82.0 and 79.5 km/sec, respectively. Thus the cloud must be at the near distance.

(14) An H_2CO absorption feature at the cloud's velocity is present in the continuum of the HII region at ℓ = 29°.944 from DWBW, which lies near the subcentral point. Thus the cloud must lie at the near distance. The mean latitude of the cloud (-0°.75) also argues for the near distance, since at the far distance it would lie about 190 pc below the plane.

The mass of this cloud is much smaller than others in the catalogue, but it is included for completeness since it appears clearly in figure VIII-11.

(15) The near kinematic distance was assigned on the basis of this cloud's absorption in H_2CO of radiation from the HII regions at ℓ = 30°.602 and 31°.411, and its proximity to the near HII regions at ℓ = 30°.776 and 31°.401 (DWBW). There are many HII regions in the direction of this feature but most are too close to the terminal velocity for their distance ambiguities to be resolved reliably; the feature may therefore result from several clouds spread along the tangent region of the Scutum arm.

The apparent bifurcation of this cloud in figure VIII-11 may be an artifact produced by the background removal procedure: the high-velocity ridge in the model background which was removed passes through the center of this cloud. There is little evidence for such a bifurcation in the original data (see figs. III-4b or c). The cloud's mass may be underestimated because of this high-velocity ridge in the model background.

(16) The far kinematic distance was assigned on the basis of this cloud's proximity to the HII region at ℓ = 30°.539 from DWBW. Its large velocity extent and location precisely in the plane (see fig. VIII-14) are also consistent with it lying at the far distance.

(17) W44 - The near distance was assigned on the basis of this cloud's proximity to the HII regions at ℓ = 34°.254,

35°.063, 35°.194, 35°.346, 35°.603, and 35°.663 from DWBW. This cloud has been discussed in detail earlier in this chapter, where it was concluded that its mass may be overestimated by as much as 50% depending on the fraction of the emission in the range v = 50-65 km/sec actually associated with the cloud. The cloud mass has been increased by 24% to account for emission from outside the latitude range of the in-plane survey.

(18) The far kinematic distance was assigned on the basis of this cloud's proximity to the HII regions at ℓ = 37°.439 and 37°.538 from DWBW, which are coincident in latitude and velocity and lie at its extreme high-longitude edge.

The near HII region in its vicinity (at ℓ = 36°.4, v = 57.4 km/sec) is a Sharpless object (S72) listed in GG. It lies almost 3° below the plane and so is probably not associated with this cloud. Although the cloud is strongly blended with the W44 cloud (17) in the smoothed ℓ,v map (fig. III-4c), it appears as a well-defined feature in figure VIII-13 and is further distinguished from W44 by its much smaller latitude extent (see fig. VIII-14).

The cloud's mass may be underestimated if some of the emission at ℓ < 36° is associated with this cloud (see the discussion of W44 given earlier in this chapter).

(19) This is the Aquila spur, which is discussed in chapter V and later in this chapter. Although it does not appear in figure VIII-11 (the ℓ,v map with a background removed), it is included in the catalogue because of its prominence in the smoothed ℓ,v map (fig. III-4c).

(20) Low spatial-resolution mapping (discussed in chapter III) indicates that this cloud extends above +3° in latitude, and hence almost certainly lies at the near distance. It is probably associated with the nearby cloud 23, whose latitude extent is comparable. The mass has been increased by a factor of 2.3 to account for emission from outside the latitude range of the in-plane survey.

(21) This cloud appears small in the "clipped" ℓ,b map (fig. VIII-14) because it is a rather weak, extended feature. In the unclipped data, its latitude extent is ~1°, corresponding to a linear size of about 200 pc at the far distance. Its latitude extent, its rather large displacement from the plane (~0°.5), and its small velocity extent all argue for the near distance. It may be associated with the larger clouds 20 and 23.

(22) The far kinematic distance was assigned on the basis of this cloud's proximity to the far HII regions at ℓ = 37°.763 and 37°.871 from DWBW, with the same latitude

and velocity, but somewhat displaced in longitude. The far clouds 18 and 24 have roughly the same latitude extent and the same displacement below the plane, suggesting that all three clouds lie at roughly the same distance.

(23) Low spatial-resolution mapping (discussed in chapter III) indicates that this cloud extends above +3° in latitude, so it must lie at the near distance. It is probably associated with the nearby cloud 20, which has a similar latitude extent. The cloud mass has been increased by 64% to account for observed emission lying outside the latitude range of the in-plane survey.

(24) The distance to this cloud is uncertain, but it has been assigned the far distance on the basis of its similarity in the ℓ,b map (fig. VIII-14) to the far clouds 25 and 26. All three clouds have about the same latitude extent and show the same negative displacement from the plane. The cloud does not appear as a H_2CO absorption feature against the DWBW HII region at $\ell = 42°.108$, weakly suggesting the far distance, since both the near and far kinematic distances of the HII region lie between the near and far distances of the cloud.

(25) The far kinematic distance was assigned on the basis of this cloud's proximity to the DWBW HII region at ℓ = 45°.125, which lies at the cloud's high-longitude edge. Also, the cloud is similar in angular size, velocity extent, mean latitude, and apparent brightness to the far cloud 26.

(26) The far kinematic distance was assigned on the basis of this cloud's proximity to the DWBW HII regions at ℓ = 45°.125, 45°.451, and 45°.475. (There is some disagreement over the kinematic distance of the HII region at ℓ = 45°.451. Lockman (1979b) placed it at the near distance because of what was then thought to be a lack of higher-velocity absorption features, but DWBW cite HI absorption at velocities up to 70 km/sec as evidence for the far distance.) There is also a near HII region in the vicinity of this cloud (ℓ = 46°.50 from Lockman (1979b); see fig. VIII-12) but it is a very weak source and was assigned the near distance by Lockman (1979b) merely on the basis of a lack of high-velocity OH absorption. DWBW decided that the distance to this HII region could not be resolved on the basis of the present data.

(27) This cloud appears small on the "clipped" ℓ,b map (fig. VIII-14) because it is a rather weak, extended feature. In the unclipped data, its latitude extent is

at least 1°.5, corresponding to a linear size in excess of 300 pc at the far distance. Its large latitude extent and its small velocity extent argue for the near distance. Also, it may be responsible for the H_2CO absorption feature at 24.8 km/sec seen in the continuum of the HII region at ℓ = 45°.125, from DWBW.

(28) W51 - The far kinematic distance was assigned on the basis of this cloud's proximity to the DWBW HII regions at ℓ = 49°.384, 49°.437, and 49°.486. The VLBI measurements of relative proper motions of H_2O maser features in this source (Genzel et al. 1981) also yield a distance (7 ± 1.5 kpc) consistent with a far kinematic distance.

(29) The distance to this object is very uncertain. It has been assigned the far distance on the basis of its proximity to the far HII region at ℓ = 49°.407 from DWBW, although it seems possible that this HII region is actually associated with W51 (cloud 28).

(30) The velocity of this cloud is slightly greater than the terminal velocity, so it was placed at the subcentral point. It marks the tangent point of the Sagittarius arm.

(31) The near distance was assigned because of the large angular size and small velocity extent. This is a weak, extented feature with a latitude extent in the "unclipped" data in excess of 2°, corresponding to a linear size at the far distance of over 300 pc.

(32) The distance ambiguity could not be resolved for this cloud, but it has been placed at the subcentral point because it lies less than 10 km/sec from the terminal velocity. The uncertainty however is large: r = 3 - 8 kpc.

E. Discussion

The locations in the galactic plane of all clouds in the catalogue with masses > 10^5 $M_\odot$ are shown in figure VIII-15. Also shown are logarithmic spirals labeled Sagittarius, Scutum, and 4-kpc. The parameters of the Sagittarius spiral were determined by a least-squares fit to the positions of the 15 clouds (with M > 10^5 $M_\odot$) which outline that arm. Since the clouds do not define the Scutum and 4-kpc arms as well as they do the Sagittarius arm, these arms were not fit, but simply lifted from the best-fit model of chapter VII (fig. VII-1). Figure VIII-16 is the same, except that the 6 clouds with M < 10^5 $M_\odot$ are included, the spirals are omitted, and the clouds are numbered according to table 7.

Figure VIII-15 shows that these largest clouds are excellent spiral-arm tracers. While the clouds leave the structure of the inner arms somewhat uncertain, they trace the Sagittarius arm with exceptional clarity: a total of 15 clouds are distributed quite uniformly along a 15 kpc stretch of the arm. The spacing between these clouds is similar to that between giant HII regions, the "beads on a string" observed in other galaxies (Elmegreen and Elmegreen 1983). This suggests that the more fundamental "beads" are these giant clouds, the HII regions being their more optically prominent offspring.

Except for the absence of the Aquila spur, the spiral pattern found here is in qualitative agreement with that of the simple model discussed in chapter VII (figure VII-1). For the largest feature in both maps, the Sagittarius arm, there is also excellent quantitative agreement: both methods yield an inclination of about 5° and a tangent direction near $\ell = 51°$. Since the parameters of the inner arms (Scutum and 4-kpc) in figure VIII-15 are obviously uncertain, the most that can be said is that the distribution of giant clouds in that region is consistent with the morphology presented in chapter VII. This is illustrated by the Scutum and 4-kpc spirals shown in figure VIII-15, which were taken from the model. (Note that the 3 innermost clouds appear to

define an arm which has a much higher inclination than the 4-kpc spiral shown. This is because a radial expansion of the arm was assumed in deriving the parameters of the model 4-kpc arm shown (see the discussion of the velocity field in appendix B). Had radial motions been neglected in the model, the derived inclination of the 4-kpc arm would have been higher.)

While the clouds in the vicinity of the 4-kpc and Scutum arms appear to be largely confined to these arms, they do not reveal a spiral pattern which is as striking as that of the Sagittarius-arm clouds. This is apparently due to the fact that these clouds mainly cluster at the near kinematic distance, unlike the Sagittarius-arm clouds which are spread quite uniformly along its length. This fact in itself is quite striking. While it is true that clouds at the far kinematic distance are more difficult to detect, the fact that the distribution of giant HII regions in this region shows a similar asymmetry (see, e.g., the insert to fig. VIII-18) suggests that this is not the complete explanation. The clouds in the vicinity of the 4-kpc and Scutum arms produce the intense molecular-ring emission between 4 and 7 kpc from the galactic center. We note that if most of the molecular-ring clouds lie at the near distance, as figure VIII-15 indicates, then the CO luminosity and

consequently molecular mass of the inner galaxy has been overestimated by the model described in chapter IV, and by similar ones which assume the inner-galaxy emission to be axially symmetric about the galactic center.

The agreement between the spiral pattern revealed by the large clouds and that of our simple spiral model provides strong support for our interpetation of the CO ℓ,v map. The high contrast of the spiral features in the CO ℓ,v map, reinforced by the spiral distribution of large clouds in the Sagittarius arm, leaves little room for a kinematic interpetation of the CO data. The spiral-like features in the CO data are a consequence of genuine molecular arms and not of subtle perturbations in the CO velocity field. Furthermore, since the 21-cm data shows essentially the same large-scale features it seems likely that the HI also traces these same spiral arms.

The Aquila spur was discussed in some detail in chapter V. It appears in the ℓ,v map (fig. III-4c) near $\ell = 37°$, v = 80 km/sec and in the ℓ,b map (fig. VIII-14) between $\ell = 32°$ and 38°. Its absence in figure VIII-15 suggests that it does not contain the type of large molecular clouds which trace the major spiral arms. Consistent with this is Lockman's (1979a) finding of a paucity of giant HII regions in this region. The prominence of this spur as an emission feature in the ℓ,v

map might be due to its orientation and proximity to the subcentral point: it may be a weak, extended feature viewed nearly edge-on, its emission enhanced by velocity crowding. The very intense CO emission near $\ell = 80°$ (see fig. III-7) may be produced by a similar object, the Local arm, in the same way: at $\ell = 80°$ we are viewing the Local arm almost edge-on in a direction of strong velocity crowding. Although the exact nature of the Aquila spur is not known, it is clearly an interesting object worthy of further study.

It is of interest to compare the spiral pattern revealed by the molecular clouds with earlier 21-cm and HII-region results. The locations of the major HI spiral arms in the first quadrant, as determined by the 21-cm analyses of Burton and Shane (1970) and Shane (1972), are shown superimposed on our molecular clouds in figure VIII-17. The HI spiral pattern is roughly consistent with the locations of our molecular clouds and is in fairly good agreement with the spiral patterns presented in figures VIII-15 and VII-1. This agreement is, of course, to be expected since we have seen in chapter V that the large-scale features in the CO and 21-cm ℓ,v maps are nearly identical (see fig. V-1). Any quantitative disagreement is probably largely due to the different velocity fields which were adopted for the

analyses. While in the kinematic calculation of the molecular-cloud positions a purely circular velocity field was used, the 21-cm analyses employed a velocity field which incorporated density-wave streaming and - in the region of the Scutum and 4-kpc arms - radial expansion.

The locations of the major spiral arms in the first quadrant as determined from the distribution of HII regions is shown superimposed on our molecular clouds in figure VIII-18. The spiral pattern shown is essentially that of Georgelin and Georgelin (1976), but it has been slightly modified by Downes et al. (1980) to accommodate their more extensive first-quadrant data. The same spiral arms are shown in the insert, superimposed on the HII-region distribution of Downes et al. (1980). While the Downes et al. pattern does not include a 4-kpc arm, the insert shows that there are several HII regions which could be identified with that arm. In general, the molecular-cloud distribution is in excellent agreement with the spiral pattern shown. In fact, at least for the Sagittarius arm the molecular clouds appear to trace out a more clearly-defined spiral pattern, indicating that they are indeed superior spiral-arm tracers. This is hardly surprising, since one could not expect the HII regions to trace the arms as well as their parent

objects, the molecular clouds. It appears from figure VIII-12 that the HII regions typically have random velocities of 5-10 km/sec with respect to their parent molecular clouds. If this is generally the case, the kinematically-computed distribution of HII regions will not show as clear a spiral pattern as the kinematically-computed distribution of molecular clouds even if both species are equally well-confined to the arms, since the random velocities of the HII regions will produce large errors in their kinematic distances.

Finally, it is natural to ask whether the total mass (or equivalently, total luminosity) of the large clouds we detected is consistent with what would be expected from our earlier mass-spectrum analysis. The axisymmetric model of chapter IV yields a total molecular mass within the solar circle of 8×10^8 $M_\odot$ (assuming $N(H_2)/W(CO) = 2 \times 10^{20}$ cm^{-2} K^{-1} km^{-1} s). According to our mass spectrum, roughly half this mass, or 4×10^8 $M_\odot$, should be contained in clouds with $M > 5 \times 10^5$ $M_\odot$. In the region of our survey we actually find 20 such clouds with a total mass of 3×10^7 $M_\odot$. Extrapolating this result to the entire inner galaxy, and applying an approximate correction for distant clouds which escaped detection (Dame et al. 1983), we find a total mass contained in clouds with $M > 5 \times 10^5$ $M_\odot$ of 2×10^8 $M_\odot$. Thus we find too few large clouds by roughly a factor of 2.

Several possible explanations for this discrepancy immediately come to mind. It may be that more distant clouds were missed than we estimated, their emission being either included with that of more nearby clouds or removed as part of the background. It is also possible that the mass spectrum for inner-galaxy clouds differs from the spectrum we derived from the Perseus arm. In fact, Elmegreen (1979) has suggested that fewer, more massive clouds might be expected in the outer galaxy where tidal forces are important in limiting the collapse of low-density dust lanes into clouds. Such a shift to a greater dominance of massive clouds in the outer galaxy would be a natural explanation for the discrepancy. And finally, as was suggested above, it may be that the total molecular mass of the inner galaxy has been overestimated by our axisymmetric model because of a significant asymmetry in the molecular-cloud distribution in the inner galaxy.

IX. SUMMARY

A well-sampled CO survey of the first galactic quadrant has been used to study the distribution of molecular clouds in the inner galaxy. The survey covers a uniform band 2° wide centered on the galactic equator, extending from ℓ = 12° to 60°. The basic survey data were presented in various forms, including velocity-integrated spatial maps, latitude-integrated longitude-velocity maps, and longitude-velocity maps at each latitude observed.

As a first step in the analysis, the axisymmetric galactic distribution of molecular clouds was considered. In agreement with previous findings, it was found that molecular clouds are concentrated in a broad ring 6 kpc in radius and are confined to a thin layer, approximately 120 pc thick, with an average displacement of 40 pc below the galactic equator.

The large-scale morphology of the galactic CO emission was found to be dominated by the existence of several well-defined spiral-arm features. Contrary to previous findings, molecular clouds were shown to constitute a highly specific tracer of spiral structure. To each of the classical 21-cm (HI) arms of the inner galaxy there corresponds a CO (molecular) arm which is generally more clearly defined and of higher contrast. The similarity of the CO and 21-cm ℓ,v maps, particularly

along the terminal-velocity curve, means that the two species must have the same large-scale kinematics.

While the CO spiral features are generally of higher contrast than those observed at 21-cm, some of this difference in contrast is due to the higher velocity dispersion of the HI gas. Since the large-scale kinematics of the molecular and atomic clouds are essentially identical, the remaining difference in contrast cannot be attributed to differences in streaming motions. We thus concluded that the arm-interarm contrast for the galactic CO emission is more than twice that of the 21-cm emission. While the enhanced CO emission in the arms is best understood in terms of the creation of molecular clouds when gas enters a spiral arm and their destruction before they leave, it cannot be ruled out that a variety of heating mechanisms at work within the arms may be at least partially responsible.

A simple model was developed in which all of the CO emission from the inner galaxy arises from spiral arms. The modeling results suggest that molecular clouds are essentially transient objects, existing for 15 to 40 million years after their formation in a spiral arm, and are largely confined to spiral features about 300 pc wide.

A section of the Perseus spiral arm was used to determine a mass spectrum for molecular clouds. It was found that the largest molecular clouds dominate the galactic CO emission and molecular mass. One of the nearest of these clouds, that associated with the SNR W44, was studied in detail and presented as a prototype of such clouds. A variety of methods were employed to estimate distances and masses for the largest clouds detected by the survey and a catalogue was compiled. The largest of these clouds have masses in excess of 10^6 $M_\odot$ and linear dimensions in excess of 100 pc. The clouds reveal an overall spiral pattern similar to that inferred from the modeling and trace the Sagittarius arm with unprecedented clarity.

APPENDIX A

COSMIC-RAY HEATING OF MOLECULAR CLOUDS

We wish to consider how much cosmic-ray heating increases the CO arm-interarm contrast. The dependence of a cloud's CO luminosity on the cosmic-ray density is first derived and the arm-interarm contrast of galactic cosmic rays is then discussed.

The cosmic ray heating rate (Γ_{CR}) in molecular clouds is given by

$$\Gamma_{CR} = \zeta_{CR}(H_2)\Delta Q n(H_2)$$

where $\zeta_{CR}(H_2)$ is the direct (primary) cosmic-ray ionization rate of H_2, ΔQ is the energy deposited as heat as a result of this ionization, and $n(H_2)$ is the molecular-hydrogen density (Goldsmith and Langer 1978). The total molecular cooling rate (Λ) is approximately

$$\Lambda = (6.5 \times 10^{-30}) n(H_2) T^{2.2} \text{ ergs cm}^{-3}\text{sec}^{-1}$$

for $n(H_2)$ > few times 10^2 cm^{-3} (Goldsmith and Langer 1978). Since both the heating and cooling rates depend on the first power of the density, the equilibrium cloud temperature is independent of density. Equating the

heating and cooling rates yields the dependence of the cloud kinetic temperature on the cosmic-ray ionization rate:

$$T_K = 8.1\left(\frac{\zeta_{CR}}{2 \times 10^{-17}}\right)^{\frac{1}{2.2}} \quad K \qquad (A\text{-}1)$$

This result is essential to our discussion. It indicates that the cloud kinetic temperature, and hence the CO luminosity of the cloud, does not depend very sensitively on the cosmic-ray density. For example, a five-fold increase in the cosmic-ray density would be required to double a cloud's kinetic temperature.

Although poorly known, some constraints can be set on the cosmic-ray arm-interarm contrast from the recent high-energy gamma-ray surveys of the galaxy. A common assumption, made, for example, in the galactic gamma-ray emission models of Bignami et al. (1975) and Cesarsky et al. (1977), is that on the scale of spiral arms the cosmic-ray density is proportional to the total gas density. This assumption is supported by the work of Parker (1966 and 1969) who showed that the cosmic rays and magnetic fields can only be contained by the mass of the gas through which the magnetic fields penetrate, and

hence the cosmic rays are tied to the matter. Bignami et al. (1975) assumed that the atomic gas, molecular gas and cosmic rays all have an arm-interarm contrast of about 3.5:1 for the spiral arms within the solar circle. On this assumption they were able to reproduce the rather low-contrast peaks on the gamma-ray longitude profile corresponding to the tangent directions of the inner-galaxy spiral arms. This result suggests that the maximum cosmic ray arm-interarm contrast consistent with the gamma-ray data is about 3.5:1. If the molecular or atomic arm-interarm contrasts, or both, are larger than assumed the cosmic-ray arm-interarm contrast is lower still - otherwise the gamma ray peaks corresponding to the inner spiral arms would be more prominent than observed. The cosmic-ray arm-interarm contrast could only be increased by decreasing the arm-interarm contrast of the gas. But a cosmic ray arm-interarm contrast significantly larger than that of the gas would be difficult to justify theoretically, as the work of Parker (1966 and 1969) mentioned above shows. Thus the rather low contrast of the gamma-ray peaks corresponding to the tangent directions of the inner arms sets a limit on the cosmic-ray arm-interarm contrast. It is at most in the

range 3 to 4 and may be significantly less if, as is suggested here, the molecular arm-interarm contrast is greater than that of the HI.

In order to estimate the maximum possible influence of cosmic-ray heating on the spiral-arm molecular clouds, we will assume that the cosmic rays have an arm-interarm contrast of 4:1 - the upper limit set by the gamma-ray data. The coldest molecular clouds which have been detected (by means of H_2CO absorption) have kinetic temperatures of about 5 K (Evans, Rubin, and Zuckerman 1980; Zuckerman and Kuiper 1980), but such clouds are quite rare. Dark clouds in the solar neighborhood typically have T_K = 10 K (Dickman 1975), but such clouds cannot be considered typical interarm clouds since the sun is located within a spiral feature (the so-called Orion or Local arm). Taking 8 K as the typical kinetic temperature of interarm clouds, equation A-1 implies that a four-fold increase of the cosmic-ray density within the arms will heat the clouds to a temperature of about 15 K. Assuming local thermodynamic equilibrium within the clouds, the kinetic temperature can be related to the observed ^{12}CO line temperature (T_L^{12}) by the formula (Blitz 1978)

$$T_K = 5.53\left(\ln\left(1 + \frac{5.53}{T_L^{12} + 0.819}\right)\right)^{-1}$$

This equation implies that T_L^{12} increases from ~5 K for interarm clouds to ~12 K for spiral-arm clouds. Thus a four-fold increase in the cosmic-ray density within the arms would only be expected to roughly double the average CO luminosity of spiral-arm clouds. This might marginally explain the difference in contrast between the CO and 21-cm spiral features if the lower velocity dispersion of the CO emission is also taken into account.

It should be emphasized that the cosmic-ray arm-interarm contrast we have assumed (4:1) is merely an upper limit set by the gamma-ray data. This data does not set any lower limit on the contrast. In fact, Stecker et al. (1975) have shown that the gamma-ray data is consistent with an axisymmetric distribution of cosmic rays. Furthermore, Stecker (1977) argues against any significant enhancement of cosmic rays in the arms, citing, for example, the lack of any cosmic-ray anisotropy in the direction of the Orion arm and the long-term consistency of the cosmic ray flux at the earth (Brecher and Burbidge 1972). If the cosmic-ray arm-interarm contrast is significantly less than 4:1, then enhanced cosmic-ray heating in the arms cannot totally account for the difference in contrast between the CO and 21-cm spiral features.

APPENDIX B

THE "NAIVE" SPIRAL MODEL

A. Details of the Model

1. CO Emission

The galactic CO emission is modeled as an optically thin gas with a smoothly varying density distribution entirely confined to spiral-arm segments. Since the emission actually arises from a collection of clouds which are optically thick in CO, such a model obviously requires some justification. Although the individual molecular clouds are generally optically thick, Burton and Gordon (1978) have shown that cloud shadowing does not play an important role in determining the appearance of CO spectra. Thus the molecular disk can be considered optically thin in the sense that we can observe most of the clouds. Modeling the galactic emission as a collection of clouds rather than as we do here would be an unnecessary refinement for our purposes since we are interested in the distribution of emission on a scale much larger than the dimensions of an individual cloud, i.e., on a galactic scale. Thus the galactic CO emission can be usefully modeled as an optically thin "continuum" in the same sense that a similar model can be applied to the optical light from a galaxy.

2. Velocity Field

The velocity field is assumed to be purely circular except for an axisymmetric expansion which only becomes important within 5 kpc of the galactic center. The circular velocity as a function of galactocentric radius, derived by Burton (1971) from 21-cm data, is given by equation 1 (chapter VI). The axisymmetric expansion was imposed to avoid having to assign an unusually high inclination for the inner two arms. (Burton and Shane (1970) present a detailed discussion of the difficulties encountered when trying to model the inner arms without expansion.) The expansion is given by

$$V_{exp}(R) = 145\ e^{-((R-2)/1.76)^2} \qquad R > 2 \text{ kpc}$$

where V_{exp} is the radial expansion in km/sec and R is in kpc. This is an approximation to the expansion imposed by Burton and Shane (1970) on their models of 21-cm emission from the inner spiral arms. Since our model has no emission inside of 4 kpc, the expansion is only important between 4 and 5 kpc from the galactic center, where the expansion decreases from 40 to 8 km/sec. It should be emphasized that the expansion was introduced merely to yield more reasonable inclinations for the inner arms. It is of no consequence for our objective of studying the degree of confinement of molecular clouds to spiral arms.

3. Arm Widths

The widths of the CO arms in the model depend on the assumed lifetime of molecular clouds (the principal free parameter) and on the adopted angular speed of the spiral pattern through which the clouds migrate. According to the density-wave theory of spiral structure (e.g., Roberts 1969), the spiral density-wave pattern remains quasi-stationary in a frame of reference rotating about the galactic center at an angular or "pattern" speed Ω_p. Except at the so-called corotation radius where the local angular velocity is equal to Ω_p, the stars and gas in the galaxy are continually moving through the density wave. In our galaxy, the corotation radius occurs at about 16 kpc from the galactic center (if Ω_p = 13.5 km s^{-1} kpc^{-1}), well outside the solar circle. Thus if molecular clouds in the inner galaxy are formed as gas enters the density wave, the width of the molecular arms W can be expressed as

$$W = V_\perp \tau \qquad \text{(B-1)}$$

where

$$V_\perp = R\left(\Omega(R) - \Omega_p \right) \sin(i) \qquad \text{(B-2)}$$

Here i is the inclination of the spiral arm (equal to zero for a circular arm), $V_\perp$ is the velocity component of interstellar material normal to the arm, W is taken to be the width (FWHM) of the arm for an assumed cloud lifetime τ, and Ω_p is taken to be 13.5 km s^{-1} kpc^{-1} (Lin, Yuan, and Shu 1969).

4. Emission Across the Arms

The integrated CO emission across an arm at any galactic radius was taken to be roughly proportional to the strength of the shock wave associated with the spiral density wave at that radius. This is reasonable if, as seems plausible, the formation of molecular clouds is induced by the passage of a spiral density wave. In fact, Shu (1973) has shown that the radial distribution of HII regions in the galaxy, which is quite similar to that of CO, can be understood in terms of the increase inward of the density-wave shock strength, combined with the increase inward of the frequency $(\Omega - \Omega_p)$ at which interstellar gas is periodically compressed. W. W. Roberts (1969) has shown that the strength of the shock and the degree of compression of the gas are proportional to the square of the ratio $W_\perp/a$, where $W_\perp$ is the total (unperturbed plus perturbed) velocity component of the gas normal to a spiral arm and a is the effective acoustic speed of the interstellar gas. Since a should be roughly equal to the sound speed associated with the intercloud medium (Roberts et al. 1975) we take it to be constant over the inner galaxy. $W_\perp$ oscillates along a streamline about its unperturbed value $W_{\perp_0}$ because of the forcing of the spiral gravitational field. Within the solar circle, $W_{\perp_0}$ is in the range 15-25 km/sec,

while the spiral perturbations are of the order 5-10 km/sec. Since the spiral perturbations are significantly less than $W_{\perp 0}$ and, in any event, should not be a strong function of radius (Roberts et al. 1975) we approximate the shock strength, and thus the integrated CO emission across an arm, as proportional to the square of the unperturbed value

$$W_{\perp 0}(R) = R(\Omega-\Omega_p) \sin(i) \qquad \text{(B-3)}$$

where Ω_p is the pattern angular speed and i is the inclination of the arm. Roberts et al. (1975) make the same approximation in order to classify external spiral galaxies in the context of the density-wave theory.

It should be emphasized that we use the density-wave theory merely as a way to estimate the pattern speed Ω_p, and from it widths for the arms as a function of cloud lifetime (eqs. B-1 and B-2) - and as a means of computing the integrated CO emission across the arms (eq. B-3).

5. Velocity Dispersion

The velocity dispersion of the model gas is taken equal to the cloud-cloud velocity dispersion of molecular clouds (σ_{CO}). We adopt σ_{CO} = 4.5 km/sec, the value

determined in chapter VI from a comparison of the CO and HI high-velocity tails.

It is important to choose the correct value of σ_{CO} since it determines, for a given cloud lifetime, the contrast between arm and interarm regions in the model ℓ,v map. The value of σ_{CO} adopted here is near the low end of current estimates. If we have underestimated the value of σ_{CO}, we will overestimate the lifetime of molecular clouds and the width of the CO spiral arms. This would only strengthen our conclusion that the clouds are short-lived and are strongly confined to the arms. In any case, one of the most important criteria for deciding what constitutes a good fit to the data is the graph of integrated emission vs. longitude, which is independent of σ_{CO}.

6. Calculation of Profiles

Once a velocity and density distribution had been specified, model line profiles were calculated at 1 degree intervals of longitude following the procedure described by Burton (1971). The line of sight was divided into intervals Δs = 100 pc. (Δs was reduced until the model results became insensitive to any further reduction). Spectra were calculated over the range 0-140 km/sec at 1.75 km/sec intervals. The contribution to the

emission at velocity V from one interval Δs_i is

$$\Delta T_i(V) = \frac{K}{\sigma} \exp \left\{ -\frac{1}{2} \left[\frac{V-V_i}{\sigma} \right]^2 \right\}$$

where σ is the velocity dispersion in km/sec, V_i is the radial velocity at the center of interval Δs_i, and K is a constant which determines the absolute scale of the model spectra. (K was adjusted to give the best fit to the graph of integrated emission vs. longitude). The total emission at velocity V is then

$$T(V) = \sum_i \Delta T_i(V)$$

where the summation is taken over all intervals Δs_i for which $|V - V_i| < 3\sigma$.

B. Details of the Fitting

The Sagittarius Arm:

The parameters of the Sagittarius arm were determined primarily from the shape of the Sagittarius ℓ,v loop above $\ell = 34°$, where both the near and far sides of the arm are well defined. Except for the M17 region near $\ell = 16°$, the near side of the arm below $\ell = 34°$ is traced by only a few small clouds - not an unexpected finding since the near side of the arm is close and subtends a large solid angle. The far side of the arm below $\ell = 34°$ is difficult to trace since its velocity approaches that of the near sides of the Scutum and 4-kpc

arms. A reasonable fit could be obtained with an inclination in the range 5°-7°. This is similar to that derived from 21-cm analyses. Yuan (1969) estimates an inclination of between 6° and 7° for the Sagittarius arm. Burton and Shane (1970) find the arm best fit with an inclination that varies from 8° at 5 kpc from the galactic center to 5° at 10 kpc.

The Aquila Spur:

The Aquila spur was modeled as a short segment of a spiral arm. The decision to assign the spur to the far distance was made on the basis of its small latitude extent (see chapter VIII, especially fig. VIII-14) and its orientation in the ℓ,v map. The parameters derived for the spur are quite similar to those of the spur referred to as feature Wd by Shane (1972). His feature Wd has an inclination of 8° and extends approximately between galactocentric longitudes 48° and 70°. The location and orientation of the spur makes it difficult to determine its length precisely. Since it lies near the subcentral point, our line of sight is almost parallel to its length. The spur does not extend through the subcentral point (towards lower galactocentric longitudes) since the I(ℓ) graph fails to show a peak towards its tangent direction at ℓ = 42°.

The Scutum Arm:

The tangent direction of the Scutum arm is well defined by the I(ℓ) graph which shows a strong emission peak near ℓ = 31°. The integrated emission drops by approximately a factor of two between 31° and 32° of longitude. The inclination of the arm was determined primarily by the appearance of the near side which passes between two large interarm holes in the ℓ,v map. Below ℓ = 22°, the near side becomes blended with the far side of the Sagittarius arm and the near side of the 4-kpc arm. The far side is well defined until it intersects the near side of the 4-kpc arm near ℓ = 22°, v = 90 km/sec. Since below this point the far side can no longer be distinguished in our data, the model imposes a strong exponential decrease in the Scutum-arm emission within 4.8 kpc of the galactic center. The Scutum arm as traced by both HII regions and 21-cm emission shows a similar phenomenon. In the spiral pattern of Georgelin and Georgelin (1976), derived from the distribution of HII regions, the Scutum arm ends abruptly near its tangent region. Similarly, in the schematic picture of the inner galaxy presented by Shane (1972) (see his fig. 13), the far side of the Scutum arm ends near a galactocentric longitude of 120°, near the point where it vanishes in our picture.

The 4-kpc Arm:

As with the Scutum arm, the tangent direction of the 4-kpc arm was determined primarily by the I(ℓ) graph, which shows a strong peak near ℓ = 24°. The inclination adopted is of little significance since the arm is also assumed to be expanding. If we had not imposed an expansion, the derived inclination of the arm would have been much higher. In effect, there is a trade-off between expansion and inclination: an expanding arm with small inclination will appear (in the ℓ,v map) very much like a non-expanding arm of larger inclination. The near side is well defined except below ℓ = 20°, where it runs parallel to the near side of the Scutum arm. The far side of the arm disappears as it spirals within 4-kpc of the galactic center. This lack of emission on the far side has already been noted in the 21-cm analysis of Shane (1972), and in the CO analysis of Bania (1980).

TABLE 1

EMISSION-FREE REFERENCE POSITIONS

$\ell(°)$	$b(°)$
12	-5
12	5
15	-5
15	5
20	5
22	-5
25	-5
25	10
30	-5
30	8
35	-5
35	5
40	-5
40	5
43	-2
45	2
45	3
50	-3
50	2
55	-5
55	5
60	-5
60	5

TABLE 2

LONGITUDE INTERVALS OF SPIRAL-ARM TANGENT REGIONS USED IN PRODUCING FIGURE VI-2

ARM	TANGENT REGION (ℓ)
Scutum	29° - 33°
Aquila Spur	37° - 42°
Sagittarius	49° - 54°

TABLE 3

MODEL SPIRAL-ARM PARAMETERS

ARM	i	t (ℓ)	COMMENT
Sagittarius	5°	51°	
Aquila Spur	8°	42°	Extends between galactocentric longitudes 57° and 85°
Scutum	9°	31°.5	Exponential decrease in emission within R = 4.8 kpc
4-kpc	8°	24°	No emission within R = 4 kpc

Explanation:

i - inclination

t - tangent direction (galactic longitude)

TABLE 4

MASS BINNING OF PERSEUS-ARM CLOUDS, ℓ = 104° - 128°

LOG($M/M_\odot$)	N	$M_T(x10^3 M_\odot)$	f
3 - 3.5	12	21	0.01
3.5 - 4	8	46	0.03
4 - 4.5	8	119	0.08
4.5 - 5	5	220	0.15
5 - 5.5	2	402	0.27
5.5 - 6	2	702	0.46

Explanation:

N - number of clouds in corresponding mass bin

M_T - total cloud mass in corresponding mass bin

f - fraction of total mass in corresponding mass bin

TABLE 5

AVERAGE PARAMETERS FOR THE COMPONENT CLOUDS OF W44

Component Velocity	$\langle T_{12} \rangle$	$\langle T_{13} \rangle$	$\langle \Delta V \rangle$	$\langle T_x \rangle$	$\langle \tau_{13} \rangle$	$\langle N_{13} \rangle$	N	M_T
35 km/sec	2.7	0.59	5.6	5.8	0.28	3.6×10^{15}	18	4.20×10^5
45 km/sec	2.8	0.67	5.2	5.9	0.27	3.8×10^{15}	9	2.21×10^5
55 km/sec	3.0	0.62	6.3	6.1	0.24	4.0×10^{15}	15	3.93×10^5

Explanation:

$\langle T_{12} \rangle$ - Average peak ^{12}CO temperature (K)

$\langle T_{13} \rangle$ - Average peak ^{13}CO temperature (K)

$\langle \Delta V \rangle$ - Average ^{13}CO linewidth (FWHM, km/sec)

$\langle T_x \rangle$ - Average excitation temperature (K)

$\langle \tau_{13} \rangle$ - Average ^{13}CO optical depth

$\langle N_{13} \rangle$ - Average ^{13}CO column density (cm^{-2})

N - Number of spectra in which component cloud was detected (0°.5 beam)

M_T - Total mass of component cloud ($M_\odot$)

TABLE 6

MASS ESTIMATES FOR THE W44 COMPLEX

METHOD	MASS ($\times 10^6$ $M_\odot$)
CO	1.3
LTE	1.0
VIRIAL	1.1

Table 7

POSITIONS AND PROPERTIES OF THE BRIGHTEST CO SOURCES IN THE FIRST GALACTIC QUADRANT

No.	ℓ (°)	b (°)	v (km s^{-1})	Δv(FWHM)	D (kpc)	Dist. Note	R (pc)	log ($M/M_\odot$)
1	14.4	-0.4	20	10	2.3	a	53	5.81
2	14.2	-0.1	39	9	4.4	b	50	5.76
3	16.8	-0.2	44	9	4.4	c	56	5.63
4	16.8	0.4	22	11	2.0	a	33	5.67
5	18.2	-0.3	48	8	4.4	b	48	5.86
6	18.8	-0.5	65	9	5.5	b	58	5.43
7	19.5	0.0	26	5	2.2	a	14	4.60
8	20.0	-0.7	42	9	3.8	b	35	5.28
9	22.1	-0.2	53	10	4.4	d	61	5.86
10N	23.0	-0.1	78	14	5.9	d	81	5.81
10F	23.0	-0.1	78	16	12.6	b	<174	6.47
11	23.8	0.1	99	15	7.1	b	116	6.12
12N	24.5	-0.2	54	12	4.2	c	66	5.95
12F	25.3	-0.5	54	13	13.9	b	97	6.54
13	28.8	-0.1	80	10	5.7	d	86	5.98
14	29.0	-0.7	52	3	3.8	d	12	4.30
15	30.5	0.0	95	18	6.9	b	113	5.98
16	31.0	0.0	48	12	13.7	b	123	6.00
17	35.0	-0.7	44	10	3.1	b	52	6.11
18	36.3	-0.1	57	11	12.1	b	107	6.39
19	33-39	~0.0	82	13	9.5	f	*	*

* This feature corresponds to the Aquila spur; its mass cannot be obtained by the method used for the other clouds because the emission disappears after subtracting the background model.

Table 7 (cont'd.)

POSITIONS AND PROPERTIES OF THE BRIGHTEST CO SOURCES IN THE FIRST GALACTIC OUADRANT

No.	ℓ (°)	b (°)	v (km s^{-1})	Δv(FWHM)	D (kpc)	Dist. Note	R (pc)	log $(M/M_\odot)$
20	38.9	0.4	32	6	2.2	c	37	5.64
21	39.0	-0.5	42	3	2.9	c	16	4.85
22	39.6	-0.3	59	11	11.2	b	105	5.98
23	41.1	0.0	37	5	2.6	c	31	5.69
24	41.9	-0.4	63	14	10.2	f	131	6.30
25	44.5	-0.2	60	8	9.6	b	74	5.28
26	45.9	-0.2	59	9	9.2	b	100	5.87
27	46.0	0.2	25	3	1.8	c	12	4.30
28	49.5	-0.3	59	10	7.3	b	74	5.73
29	50.2	-0.5	45	6	3.6	c	35	4.92
30	52.1	-0.3	59	9	6.1	e	81	6.09
31	53.4	0.0	24	3	1.9	c	12	4.60
32	55.7	0.0	36	6	5.6	e	54	5.54

Distance notes:

a: Spectroscopic parallax of optical cluster

b: CO kinematic distance with ambiguity resolved by associated H II region

c: Near kinematic distance indicated by the large latitude extent of the cloud

d: Near kinematic distance indicated by H_2CO absorption at the cloud velocity in the continum of an H II region lying between the cloud's near and far kinematic distances

e: Velocity close to or greater than the terminal velocity so assigned to the subcentral point

f: other -- see notes on individual cloud

FIGURE CAPTIONS

Figure II-1 : Schematic diagram of the 1.2 meter telescope. The individual components are discussed in the text.

Figure II-2 : Block diagram of the RF and IF sections of the Columbia telescope's receiver. The main components are discussed in the text.

Figure II-3 : Block diagram of the minicomputer system controlling the pointing and data acquisition of the 1.2 meter telescope. Analog and digital signals are represented by thick and thin lines, respectively. The main components are discussed in the text.

Figure III-1 : Sampling of the Columbia CO survey of the galactic plane. Each observed point is marked by a circle with a diameter of 0°.125, roughly the beamwidth (FWHM) of the Columbia telescope.

Figure III-2 : A collection of spectra from the galactic CO survey ordered by galactic longitude and latitude. Each spectrum consists of 256 channels of 0.65 km/sec width. All spectra have a linear baseline removed and have been smoothed to a velocity resolution of 1.3 km/sec.

Figure III-3 : Contour maps of the CO emisson integrated over the full velocity range observed. Below ℓ = 55° the integration range is from -13 to 153 km/sec, above from -55 to 112 km/sec. The contour interval is 25 K km/sec. The contours at 75, 150, and 225 K km/sec (every third contour) are heavy to emphasize the most intense emission regions. Contours enclosing depressions (down-going contours) are dotted.

Figure III-4 : Longitude-velocity contour maps of the CO emission integrated over latitude from -1° to +1°. Figure a displays the full-resolution data, while figures b and c display the data smoothed to 1/2 and 1/4 the original resolution, respectively.

Figure a : The resolution is 0°.25 by 1.3 km/sec. The contour interval is 0.75 K deg.

Figure b : Smoothed to a resolution of 0°.5 by 2.6 km/sec. The contour interval is 0.5 K deg.

Figure c : Smoothed to a resolution of 1° by 5.2 km/sec. The contour interval is 0.25 K deg.

Figure III-5 : Longitude-velocity grayscale map of the CO emission integrated over latitude from -1° to +1°. The resolution is 0°.25 by 1.3 km/sec. This is a grayscale version of figure III-4a. The insert locates the main 21-cm spiral arms with respect to the CO ℓ,v map. A and B are Lindblad's local ring according to the analyses of, respectively, Burton and Shane (1970) and Lindblad et al. (1973); C is the Sagittarius arm according to Burton and Shane (1970); D and E are, respectively, the Scutum and 4-kpc arms according to Shane (1972).

Figure III-6 : A series of longitude-velocity maps of the CO emission at each latitude observed. On all the maps the contour interval is 1.4 K and the velocity resolution is 1.3 km/sec. The spatial resolution is 0°.25, except in the latitude range $-0°.25 \leq b \leq 0°.25$ where it is 0°.125.

Figure III-7 : Low spatial resolution map of the low-velocity CO emission from the first galactic quadrant. The integration is from -10 to 20 km/sec and the contour interval is 4 K km/sec. The spatial resolution is 1° and the survey is fully sampled in the region indicated. The contours have been smoothed using a bicubic spline two-dimensional interpolation routine.

Figure III-8 : The contours from figure III-7 overlayed on a section of the Lund Observatory panorama of the Milky Way.

Figure IV-1 : Displacement (Z_0), full-width at half-maximum thickness (FWHM), and central emissivity (ε_0) of the galactic CO layer as functions of galactocentric distance, as determined from the axisymmetric model described in the text. The error bars represent the formal errors from the fit multiplied by a factor which accounts for the fact that the data is correlated over the emission volume of a cloud (see text).

Figure V-1 : A comparison of the CO longitude-velocity grayscale map (figure III-5) with a corresponding 21-cm map which has been processed to bring out the most intense emission features. The HI map is a reproduction of part of figure 3 from Weaver (1974). The 21-cm map was produced by first setting all spectral channels with $T_A < 50$ K to zero, then integrating over latitude from -10° to + 10°. The four main interarm gaps which are discussed in the text are labeled in the HI map; corresponding gaps in the CO map are clearly visible. The maps have the same longitude scales but somewhat different velocity scales.

Figure V-2 : Longitude-velocity map obtained by integrating the Perseus-arm CO survey over latitude from -4° to 4°. The data were clipped by setting all spectral channels with T < 0.9 K to zero before integrating over latitude. The contour interval is 0.5 K deg. Above ℓ = 128° spectra were taken rapidly and the data has been smoothed to a longitude resolution of 0°.5 to enhance the signal-to-noise ratio. The solid lines denote ridges of peak 21-cm emission determined from the Maryland-Green Bank Survey (Westerhout 1973).

Figure V-3 : A comparison of CO and 21-cm spectra at 2° intervals between ℓ = 24° and 34°. Both sets of spectra have been averaged over the inner half-degree of galactic latitude. The galactic longitude is indicated near the left edge of each spectrum. The HI data is from the Maryland-Green Bank 21-cm survey (Westerhout 1973). The temperature scales are omitted for clarity. The main interarm gaps are labeled 1 to 3; these gaps are similarly labeled in figure V-1.

Figure V-4 : CO and 21-cm emission integrated over latitude and velocity, as a function of galactic longitude. For both curves, the emission has been integrated over latitude from -1° to +1° and over velocity from -12 to 154 km/sec. The CO intensity scale,

in units of K deg km/sec, is shown on the left. The letters label prominent features discussed in the text.

Figure V-5 : CO emission integrated over latitude and velocity, as a function of galactic longitude. In the figures a-f, the lower limit on the velocity integral is increased in steps of 20 km/sec from 0 to 100 km/sec. In all 6 figures the upper limit on the velocity integral is 154 km/sec and the latitude integral is from -1° to +1°. The integrated emission is in units of K deg km/sec. The letters label prominent features discussed in the text.

Figure V-6 : The positions in longitude and velocity of points equally spaced along two logarithmic spiral arms. The arms lie roughly at the positions of the Sagittarius and Scutum arms, the larger loop corresponding to the Sagittarius arm, and the points are spaced about 400 pc apart along the arms. The points lying in the near and far sides of the Sagittarius arm are so labeled in the figure.

Figure V-7 : CO and 21-cm spectra at ℓ=35°, averaged over the inner half-degree of galactic latitude. The HI data is from the Maryland-Green Bank Survey (Westerhout 1973). The figure demonstrates that the CO emission from the Aquila spur lies well below the terminal velocity, which is marked by the HI high-velocity ridge.

Figure VI-1 : The locus of V_{HVR} superimposed on a 21-cm longitude-velocity map. V_{HVR} is the emission-weighted mean velocity within a 30 km/sec interval of a 21-cm spectrum, centered on the terminal velocity predicted by a circular rotation curve. The 21-cm emission is integrated over latitude from -0°.25 to +0°.25. The contour interval is 10 K deg. The 21-cm data is from the Maryland-Green Bank Survey (Westerhout 1973).

Figure VI-2 : The average CO and 21-cm high-velocity tails for spectra near the tangent regions of the spiral arms. The longitude intervals of the spectra included in the average are given in table 2. The high-velocity tail of a spectrum is defined to be the emission above V_{HVR} - see figure VI-1 and the text. The CO and HI spectra used were integrated over the inner half-degree of latitude. The 21-cm data is from the Maryland-Green Bank Survey (Westerhout 1973).

Figure VI-3 : The average CO and 21-cm high-velocity tails for spectra between ℓ = 22° and 60°. (see caption to figure VI-2).

Figure VI-4 : The average CO and 21-cm high-velocity tails for spectra near the tangent regions of the spiral arms. The longitude intervals of the spectra included in the average are given in table 2. The CO spectra used were smoothed to the same velocity dispersion as the HI by gaussian weighting the temperature in each channel by all neighboring channels within ± 14 km/sec. The gaussian smoothing function had a width (FWHM) of 22 km/sec.

Figure VI-5 : Average CO and 21-cm spectra in the direction of the 4-kpc gap (labeled # 1 in fig. V-1), a prominent interarm region lying between the near and far sides of the Scutum arm (labeled). The 30 CO and 18 21-cm spectra in the region ℓ = 24°.5 to 25°.75, b = -0°.25 to +0°.25 have been averaged to produce the spectra shown. Each of the CO spectra used was smoothed in velocity to match the velocity dispersion of the HI (see caption to figure VI-4). The 21-cm data is from the Maryland-Green Bank Survey (Westerhout 1973).

Figure VI-6 : Average CO and 21-cm spectra in the direction of the Scutum gap (labeled # 3 in fig. V-1), a prominent interarm region lying between the far side of the Sagittarius arm and the near side of the Scutum arm (labeled). The 65 CO and 39 21-cm spectra in the region ℓ = 30° to 33°, b = -0°.25 to +0°.25 have been averaged to produce the spectra shown. Each of the CO spectra used was smoothed in velocity to match the velocity dispersion of the HI (see caption to figure VI-4). The HI data is from the Maryland-Green Bank Survey (Westerhout 1973).

Figure VII-1 : A grayscale representation of the CO emission in the best-fit model galaxy. The widths of the arms have been computed assuming a molecular-cloud lifetime of 15 million years. The parameters of the spiral arms are given in table 3. This distribution of CO emission yields the model longitude-velocity map shown in figure VII-2.

Figure VII-2 : Model longitude-velocity grayscale map produced by the best-fit distribution of CO emission shown in figure VII-1. The figure has the same scale as the observed longitude-velocity grayscale map (fig. III-5) to which it should be compared. The heavy black line aids this comparison by outlining the main features

of interest in the observed map -- the high-velocity ridge (for $\ell > 20°$), the large nearly empty region at high velocity below $\ell = 20°$, and the four large interarm gaps.

Figure VII-3 : Observed and model CO spectra at $\ell = 26°$ (a), 28° (b), 30° (c), and 38° (d). At each longitude 3 model spectra are shown, corresponding to an assumed cloud lifetime (τ) of 7.5, 15, or 30 million years (my). The model spectra were produced by the pattern of CO spiral arms shown in figure VII-1 with the arm widths a function of τ. The observed spectra (labeled "DATA") are an average over the inner half-degree of latitude and are shown superimposed on the $\tau = 15$ my models. The main interarm gaps are indicated by number, as they were in figure V-1.

Figure VII-4 : Model graphs of galactic CO emission integrated over velocity and latitude, as a function of galactic longitude. Three model graphs are shown, corresponding to an assumed cloud lifetime (τ) of 7.5, 15, or 30 million years (my). The models were produced by the pattern of CO spiral arms shown in figure VII-1, with the arm widths a function of τ. The observed graph (labeled "DATA") is shown superimposed on the $\tau = 15$ my model. Both the observed graph and the models are

integrals over velocity from 20 to 130 km/sec. The observed graph was integrated over the inner half-degree of latitude; the models are two-dimensional and so are integrals over velocity only. The observed graph has been smoothed in longitude to a resolution of 1°.

Figure VII-5 : Model graphs of galactic CO emission integrated over velocity and latitude, as a function of galactic longitude. Three model graphs are shown, corresponding to an assumed cloud lifetime (τ) of 7.5, 15, or 30 million years (my). The models were produced by the pattern of CO spiral arms shown in figure VII-1, with the arm widths a function of τ. The observed graph (labeled "DATA") is shown superimposed on the τ = 15 my model. Both the observed graph and the models are integrals over velocity from 60 to 130 km/sec. The observed graph is an integral over the inner half-degree of latitude; the models are two-dimensional and so are integrals over velocity only. The observed graph has been smoothed in longitude to a resolution of 1°.

Figure VII-6 : Model graphs of the high-velocity ridge emission as a function of galactic longitude. Three model graphs are shown, corresponding to an assumed cloud lifetime (τ) of 7.5, 15, or 30 million years (my). The models were produced by the pattern of CO spiral arms

shown in figure VII-1, with the arm widths a function of τ. The observed graph (labeled "DATA") is shown superimposed on the τ = 15 my model. The graphs display, as a function of longitude, the total emission from a 3-kpc long segment of the line of sight centered on the subcentral point. The observed graph is an integral over the inner half-degree of latitude; the models are two-dimensional and so are integrals over velocity only. Peaks corresponding to the main spiral features are labeled on the τ = 7.5 my model.

Figure VIII-1 : A spatial map of the velocity-integrated CO emission from the Perseus arm. The emission has been integrated over velocity from -65 to -30 km/sec. The contour interval is 5.8 K km/sec.

Figure VIII-2 : Mass spectrum for the Perseus-arm clouds shown in figure VIII-1. N is the number of clouds in the corresponding half-decade interval of mass and $M_{CO}/M_{\odot}$ is the CO mass expressed in solar masses. The error bars indicate an error of $\pm (N)^{1/2}$ on the value of N. The slope of the solid line was determined by a maximum-likelihood analysis of the data (Crawford et al. 1970). The critical slope corresponds to the case where each logarithmic mass bin contains the same total cloud mass.

Figure VIII-3 : Histogram of the percentage of the total cloud mass contributed by clouds in each half-decade interval of mass, for the Perseus-arm clouds shown in figure VIII-1. $M/M_{\odot}$ is the CO mass expressed in solar masses.

Figure VIII-4 : A latitude-velocity map of the CO emission integrated over longitude from 34° to 36°, the approximate longitude range of the W44 molecular cloud. The contour interval is 0.625 K deg.

Figure VIII-5 : Spatial maps of the high-velocity CO emission from the W44 molecular cloud. The map is fully-sampled at 0°.125 spatial resolution and has been integrated from 50 to 65 km/sec in velocity. The contour interval is 2.6 K km/sec. The cross marks the approximate center position of the W44 continuum source, as determined from the 4.875 GHz map of Altenhoff et al. (1978). The circle marks the approximate position of the expanding HI shell discussed by Knapp and Kerr(1974); the radius of the circle was determined from their figure 2.

Figure VIII-6 : Spatial map of the high-velocity ^{13}CO emission from the W44 molecular cloud. The map is fully-sampled at 0°.5 spatial resolution and has been integrated from 50 to 65 km/sec in velocity. The contour interval is 0.325 K km/sec. The cross marks the

approximate center position of the W44 continuum source, as determined from the 4.875 GHz map of Altenhoff et al. (1978). The circle marks the approximate position of the expanding HI shell discussed by Knapp and Kerr(1974); the radius of the circle was determined from their figure 2.

Figure VIII-7 : Spatial map of the CO emission from the W44 molecular cloud. The map is fully sampled at 0°.125 spatial resolution and has been integrated from 25 to 65 km/sec in velocity. The contour interval is 4.55 K km/sec.

Figure VIII-8 : Spatial map of the ^{13}CO emission from the W44 molecular cloud. The map is fully sampled at 0°.5 spatial resolution and has been integrated from 25 to 65 km/sec in velocity. The contour interval is 0.65 K km/sec.

Figure VIII-9 : All of the ^{13}CO spectra taken towards the W44 molecular cloud, ordered by galactic longitude and latitude. The spectra were taken using a 0°.5 "superbeam", meaning that each is an average of the emission in a 0°.5 square on the sky, centered on the position indicated. Emission features used in the LTE mass calculation are shaded. The vertical lines at 40 and 50 km/sec roughly divide the emission into 3 velocity components centered near 35, 45, and 55 km/sec.

Figure VIII-10 : Longitude-velocity map expected from an optically thin gas which is axisymmetric about the galactic center and has the same radial distribution as the galactic CO emission. The analytic approximation to the CO radial distribution given by Burton and Gordon (1978) was taken as the radial distribution of the model gas. The gas was assumed to have a velocity dispersion of 8 km/sec, the value derived for low-mass ($< 10^4$ $M_\odot$) clouds by Stark (1979). The intensity scale is arbitrary. This map was scaled and subtracted from the observed longitude-velocity map (fig. III-4(c)) to produce figure VIII-11. The scaling was such that 75 % of the total emission in figure III-4(c) was subtracted in producing figure VIII-11.

Figure VIII-11 : Longitude-velocity map which results when a scaled version of the model background (fig. VIII-10) is subtracted from the observed longitude-velocity map (fig. III-4(c)). The intensity of the model background was scaled such that 75 % of the total emission in the observed map was removed in producing this map. The large clouds discussed in the text and compiled in table 7 are indicated by number. The contour interval is 0.25 K deg.

Figure VIII-12 : All of the HII regions between ℓ = 12° and 60° with known distances, shown superimposed on a smoothed CO longitude-velocity map. Stars and circles represent HII regions assigned to the near and far kinematic distances, respectively. Most of the HII regions shown are from the catalogue of Downes et al. (1980); HII regions from the catalogues of Lockman (1979b) and Georgelin and Georgelin (1976) were also included when they did not appear in the more extensive Downes et al. catalogue. HII regions which were assigned to the subcentral point are not included. The CO contour map is the same as the one in figure III-4(c) but the contour interval here is 0.625 K deg.

Figure VIII-13 : The longitude-velocity map which results from integrating the CO emission with T > 2 K over latitude from -1° to +1°. All spectral channels with T < 2 K were set to zero before the integration over latitude. The large clouds discussed in the text and compiled in table 7 are indicated by number. The contour interval is 0.75 K deg.

Figure VIII-14 : Spatial maps of the large clouds discussed in the text and compiled in table 7. Clouds in the Sagittarius arm are shown in figure (a) and those in the Scutum and 4-kpc arms are shown in figure (b). The maps were produced by setting all spectral channels with $T < 2$ K to zero before integrating over velocity. The velocity integration limits change in discrete steps along the maps in order to follow the velocity of the arm; the limits are indicated directly above each map. The contour interval in all the maps is 9.8 K km/sec.

The figures between the maps show the distribution of the clouds in the galactic plane as viewed from the perspective of an observer located 2 kpc above the sun. The circle diameters are proportional to the cube-roots of the cloud masses and the inverses of the cloud distances and all the clouds are assumed to lie in the galactic plane. Straight lines from the galactic center at galactocentric longitudes of 0°, 45°, 90°, and 135° are also shown in perspective. The 6 clouds with masses less than 10^5 $M_\odot$ are not shown in the figure but are shown and labeled in the spatial maps. The dotted curves are logarithmic spirals shown in perspective. The parameters of the spirals are the same as in figure VIII-15 (next caption).

Figure VIII-15 : The locations in the galactic plane of the large clouds catalogued in table 7. The circle sizes are proportional to the cube-roots of the cloud masses and a mass scale is shown. The 6 clouds with masses less than 10^5 $M_\odot$ are not shown.

The Sagittarius spiral is a least-squares fit to the positions of the 15 clouds which outline that arm; it has a pitch angle of 5°.3 and crosses the sun-center line at R = 8.24 kpc. The Scutum and 4-kpc spirals were not fit through the clouds, but were taken from the best-fit model shown in figure VII-1. The Scutum spiral has a pitch angle of 9° and crosses the sun-center line at R = 6.13 kpc; the 4-kpc spiral has a pitch angle of 8° and crosses the sun-center line at 4.80 kpc.

Figure VIII-16 : A reproduction of figure VIII-15, except that the 6 clouds with masses less than 10^5 $M_\odot$ are included, the spirals are omitted, and the clouds are identified by number as in table 7.

Figure VIII-17 : A reproduction of figure VIII-15, except that the spiral arms were determined from 21-cm data. The inner two arms are from figure 6 of Shane (1972) and indicate the major HI arms determined by him. The outer arm is from figure 12 of Burton and Shane (1970) and indicates the position of the HI Sagittarius arm.

Figure VIII-18 : A reproduction of figure VIII-15, except that the spiral arms were determined from the galactic distribution of HII regions. The insert is a portion of figure 4 from Downes et al. (1980) which shows the locations in the galactic plane of the HII regions in their catalogue for which the distance ambiguity could be resolved; the spiral arms are from Georgelin and Georgelin (1976) but have been slightly modified by Downes et al. (1980) to incorporate their more extensive first-quadrant data. In the insert the sun is indicated by "S" and the galactic center by "GC". The two arms within the solar circle in the insert (Sagittarius and Scutum) are shown superimposed on our clouds in the main figure.

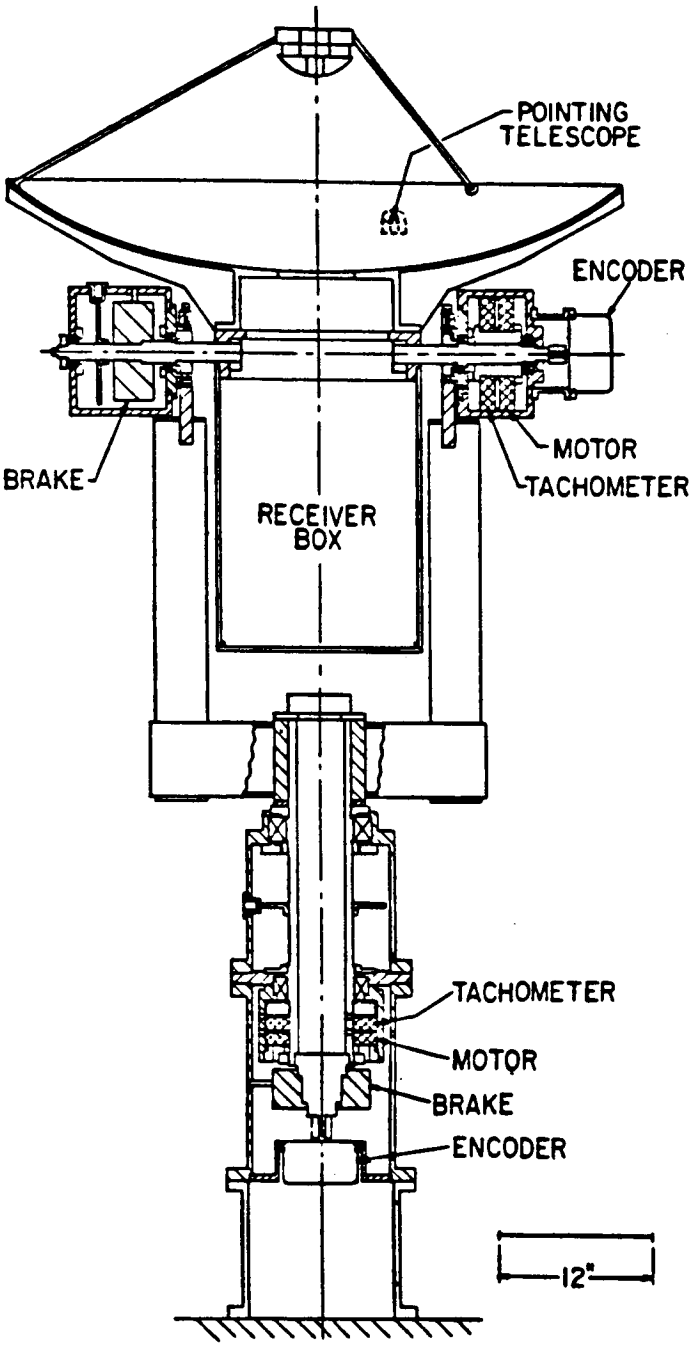
POINTING TELESCOPE
ENCODER
MOTOR
TACHOMETER
BRAKE
RECEIVER BOX
TACHOMETER
MOTOR
BRAKE
ENCODER
12"

Figure II-1

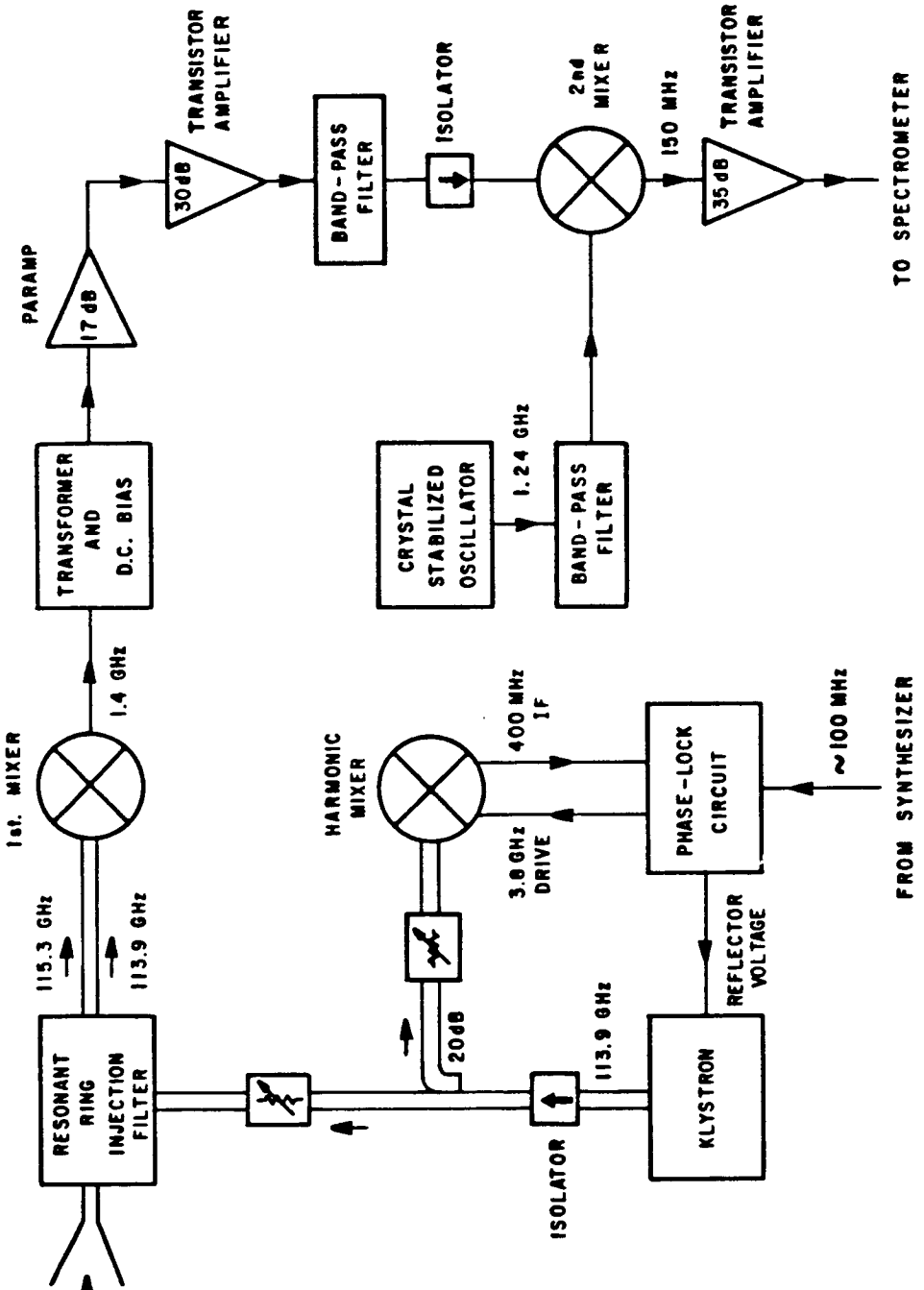
115.3 GHz
RESONANT RING INJECTION FILTER
115.3 GHz
113.9 GHz
1st. MIXER
1.4 GHz
TRANSFORMER AND D.C. BIAS
PARAMP
17 dB
30dB
TRANSISTOR AMPLIFIER
BAND-PASS FILTER
ISOLATOR
2nd MIXER
150 MHz
35 dB
TRANSISTOR AMPLIFIER
TO SPECTROMETER
CRYSTAL STABILIZED OSCILLATOR
1.24 GHz
BAND-PASS FILTER
HARMONIC MIXER
400 MHz IF
3.8 GHz DRIVE
20dB
PHASE-LOCK CIRCUIT
~100 MHz
FROM SYNTHESIZER
REFLECTOR VOLTAGE
KLYSTRON
113.9 GHz
ISOLATOR

Figure II-2

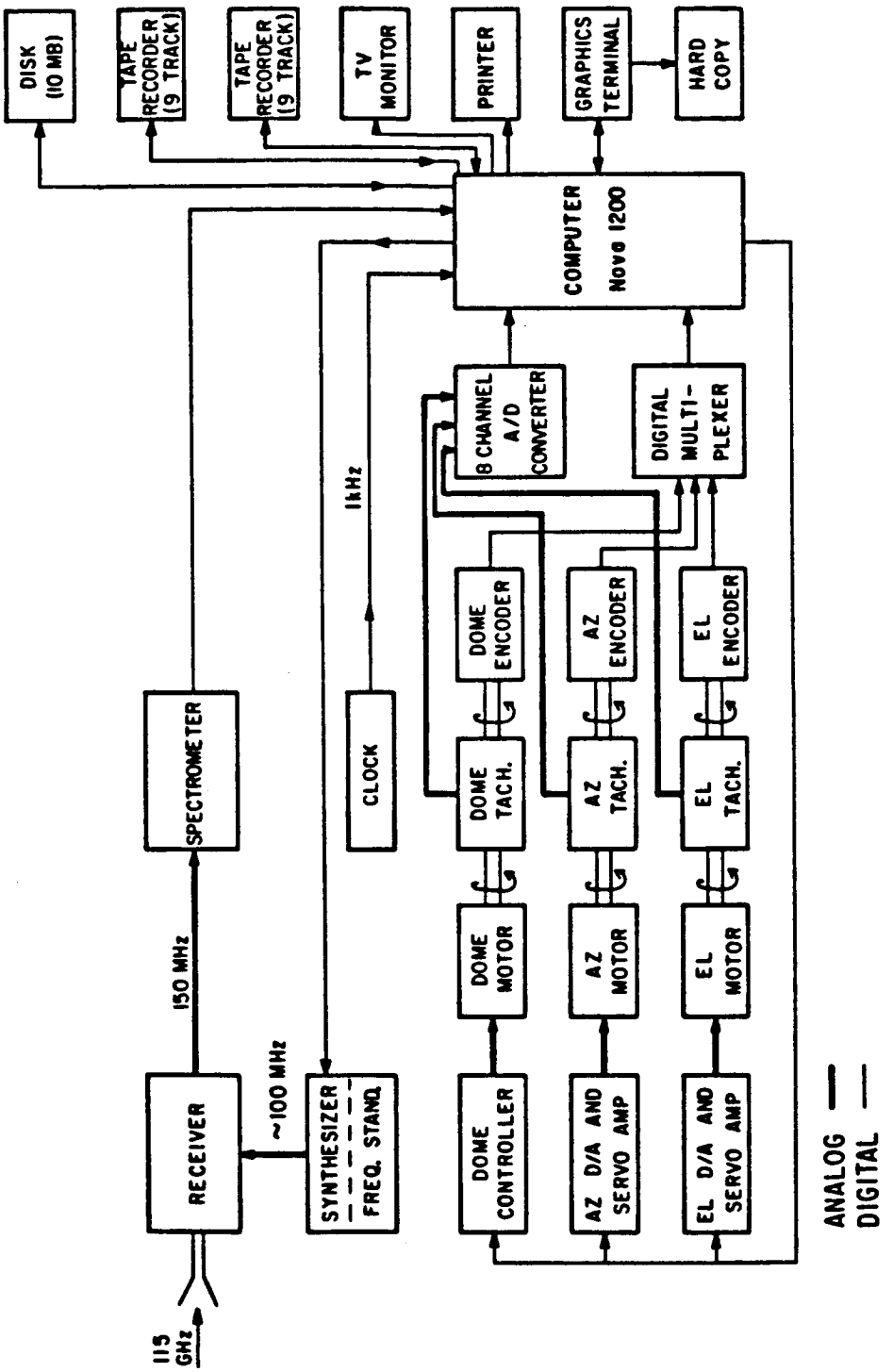
DISK (10 MB)
TAPE RECORDER (9 TRACK)
TAPE RECORDER (9 TRACK)
TV MONITOR
PRINTER
GRAPHICS TERMINAL
HARD COPY
COMPUTER Nova 1200
8 CHANNEL A/D CONVERTER
DIGITAL MULTI-PLEXER
1kHz
DOME ENCODER
AZ ENCODER
EL ENCODER
SPECTROMETER
CLOCK
DOME TACH.
AZ TACH.
EL TACH.
150 MHz
DOME MOTOR
AZ MOTOR
EL MOTOR
~100 MHz
RECEIVER
SYNTHESIZER FREQ. STAND.
DOME CONTROLLER
AZ D/A AND SERVO AMP
EL D/A AND SERVO AMP
115 GHz
ANALOG
DIGITAL

Figure II-3

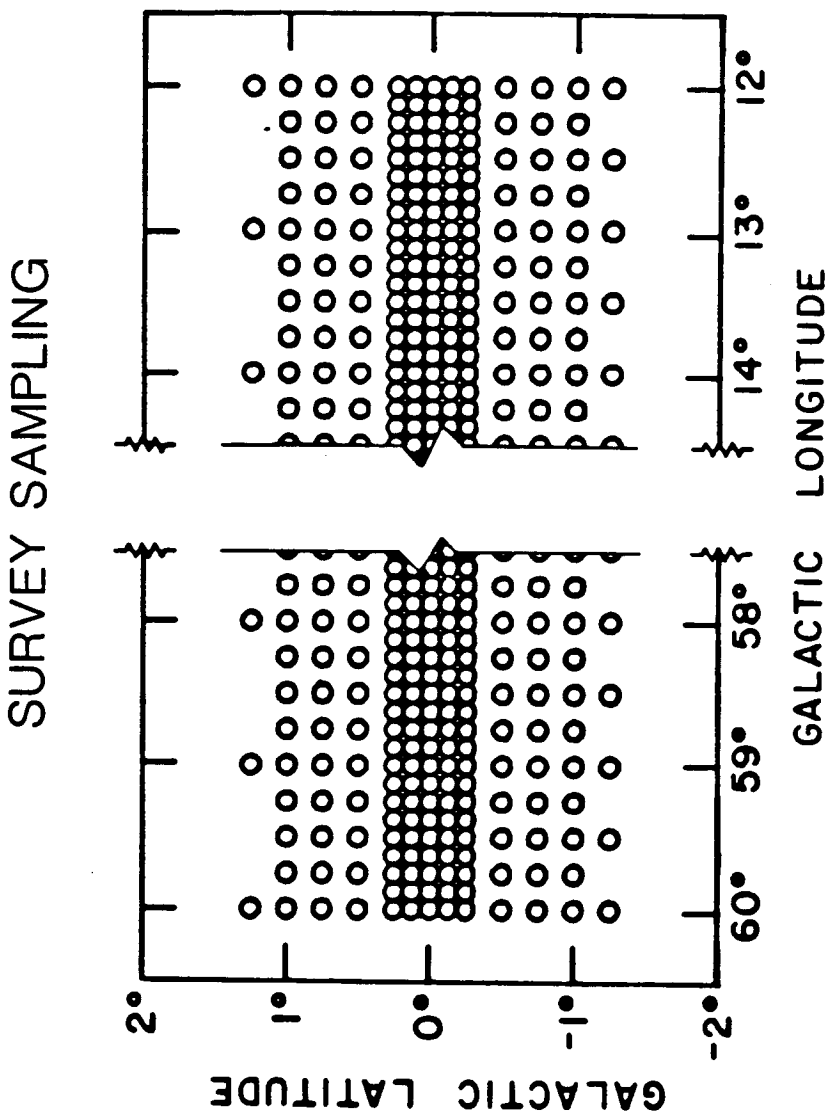
SURVEY SAMPLING
GALACTIC LATITUDE
2°
1°
0°
-1°
-2°
60°
59°
58°
14°
13°
12°
GALACTIC LONGITUDE

Figure III-1

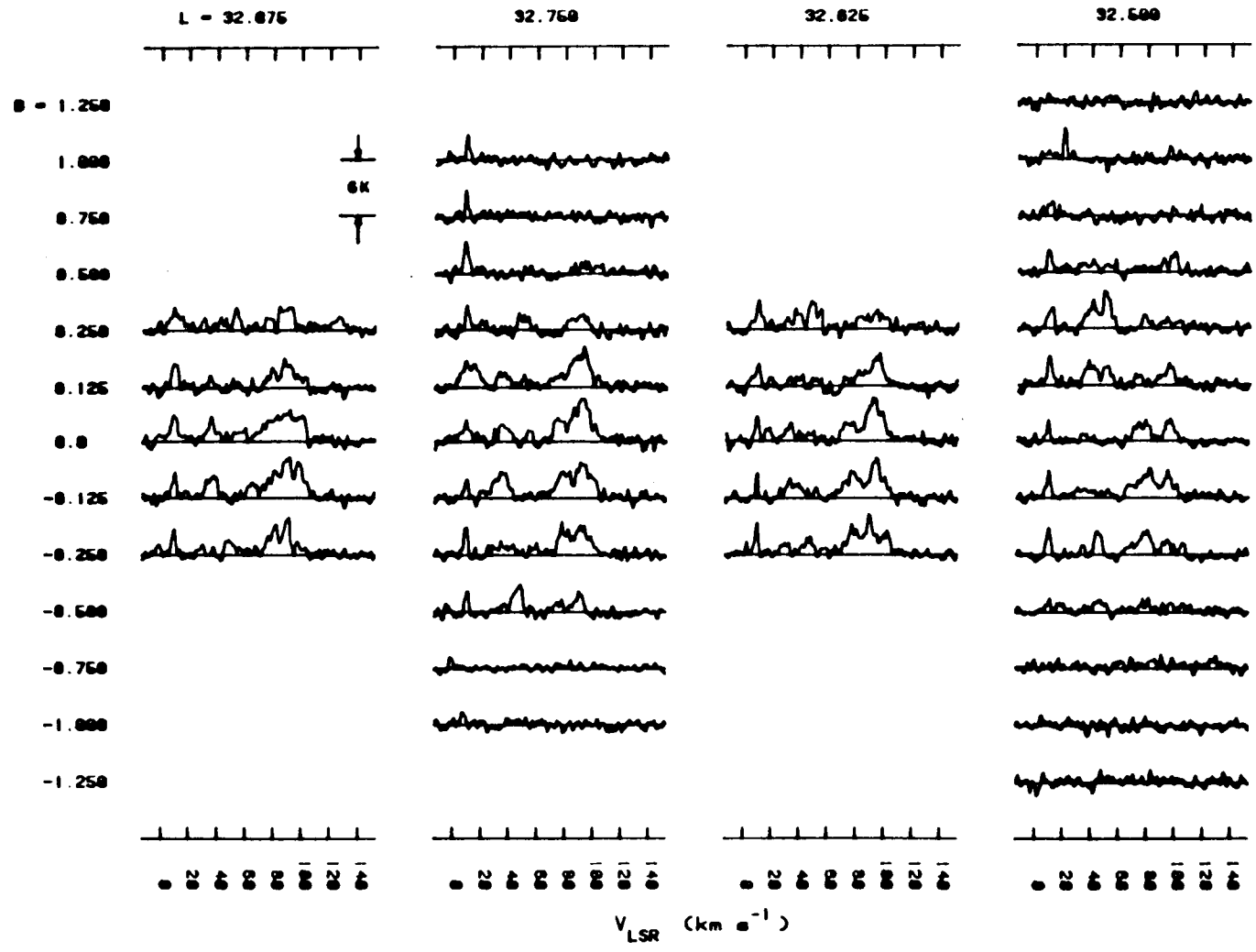
TYPICAL SPECTRA
L = 32.875
32.750
32.625
32.500
B = 1.250
1.000
0.750
0.500
0.250
0.125
0.0
-0.125
-0.250
-0.500
-0.750
-1.000
-1.250
6K
V_LSR (km s^-1)

Figure III-2

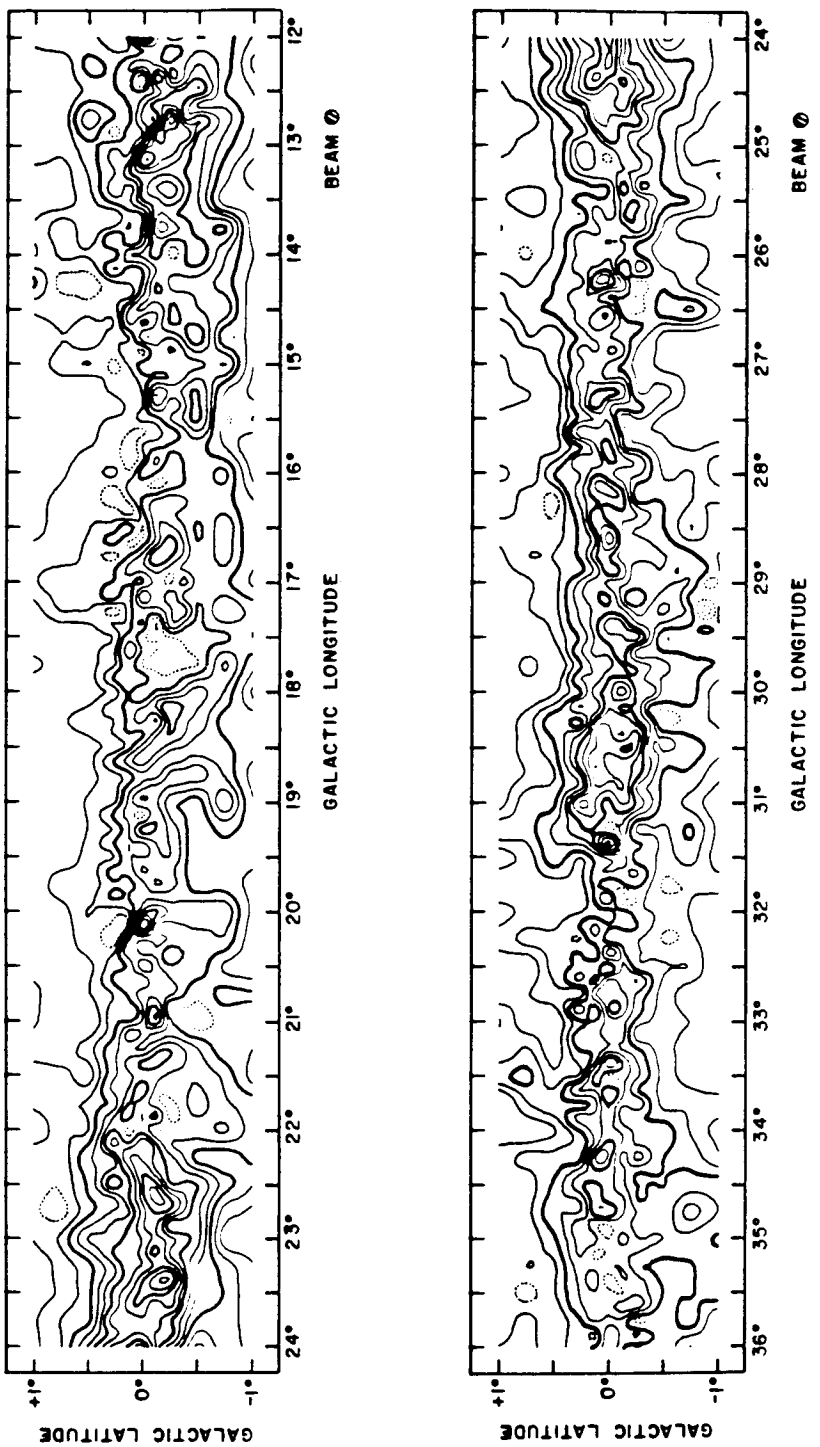

Figure III-3(a)

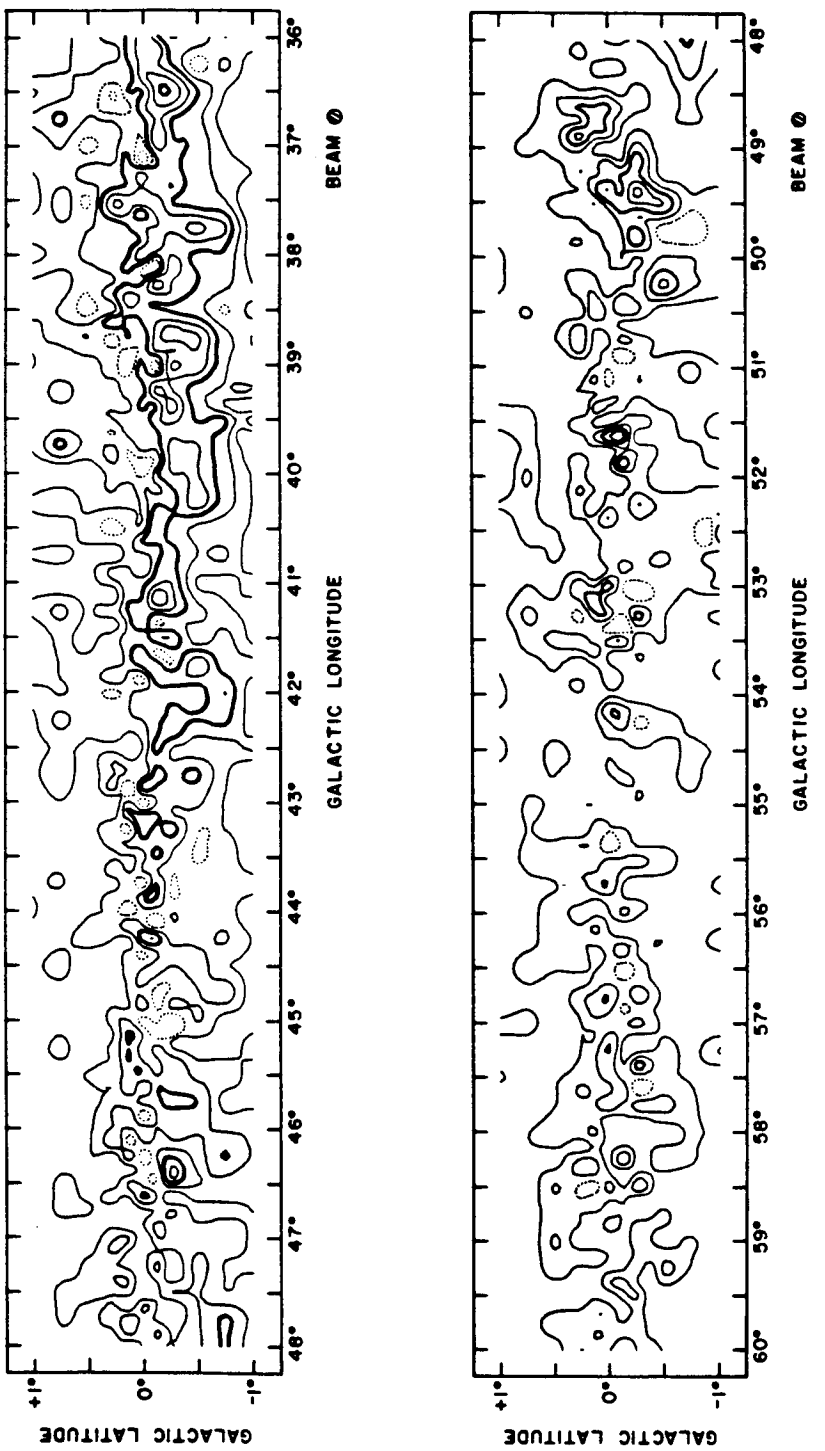

Figure III-3(b)

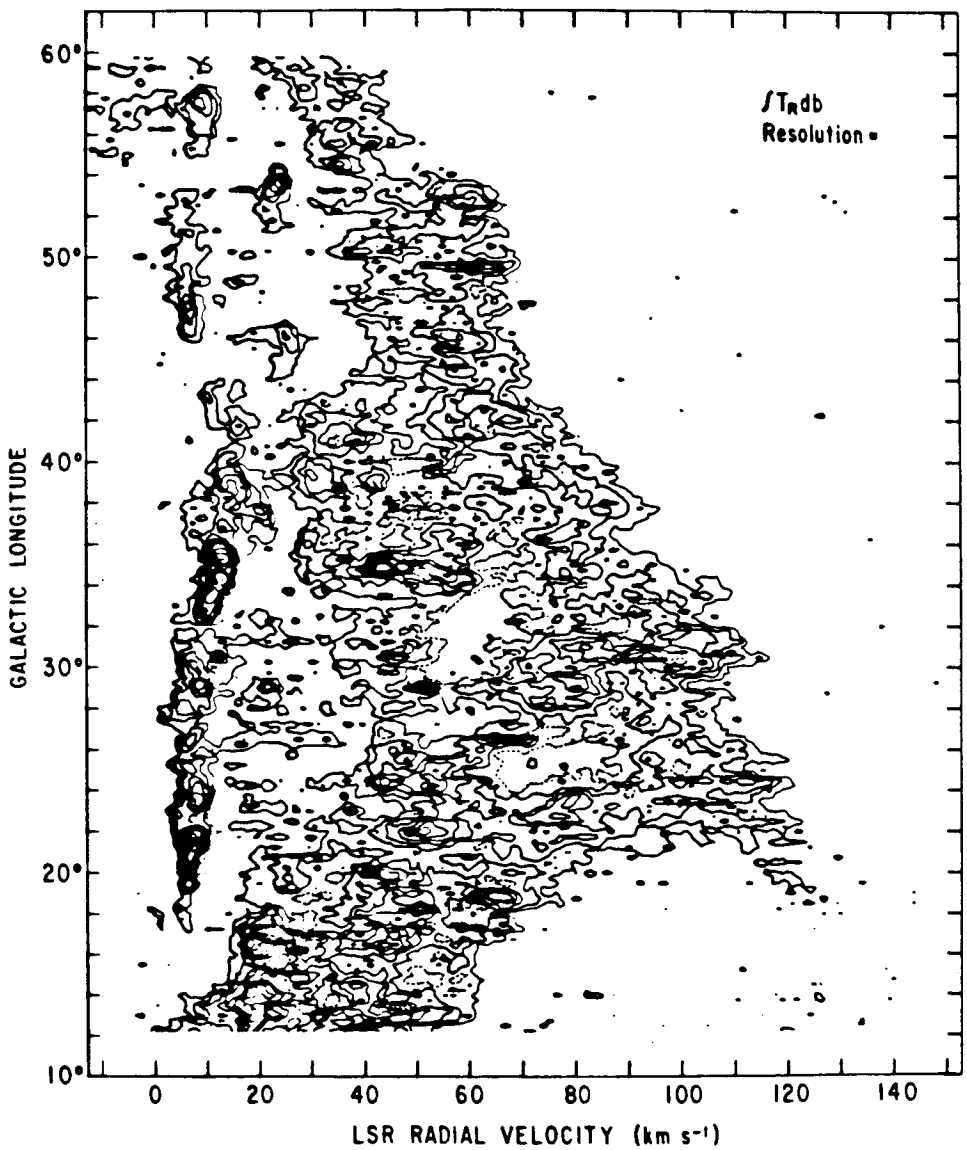

Figure III-4(a)

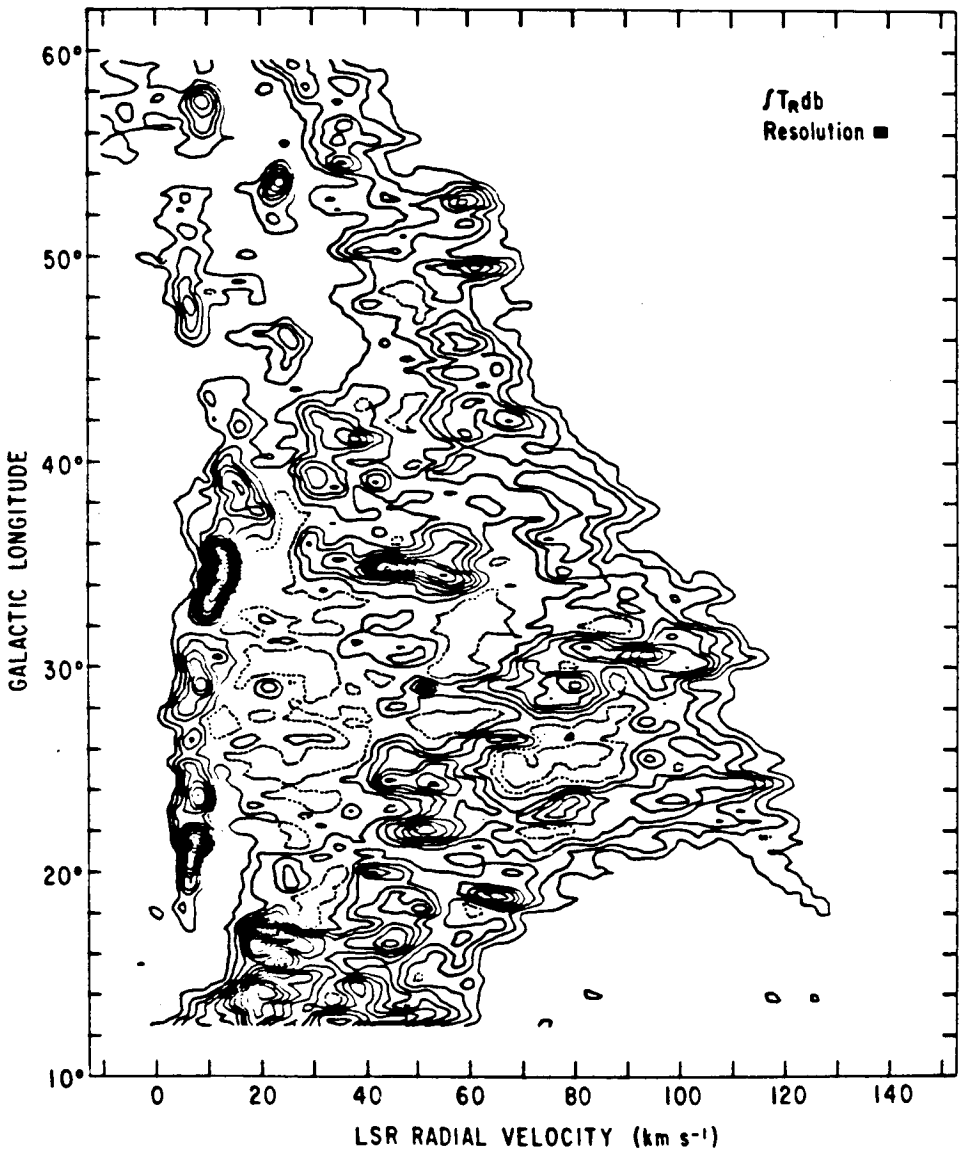

Figure III-4(b)

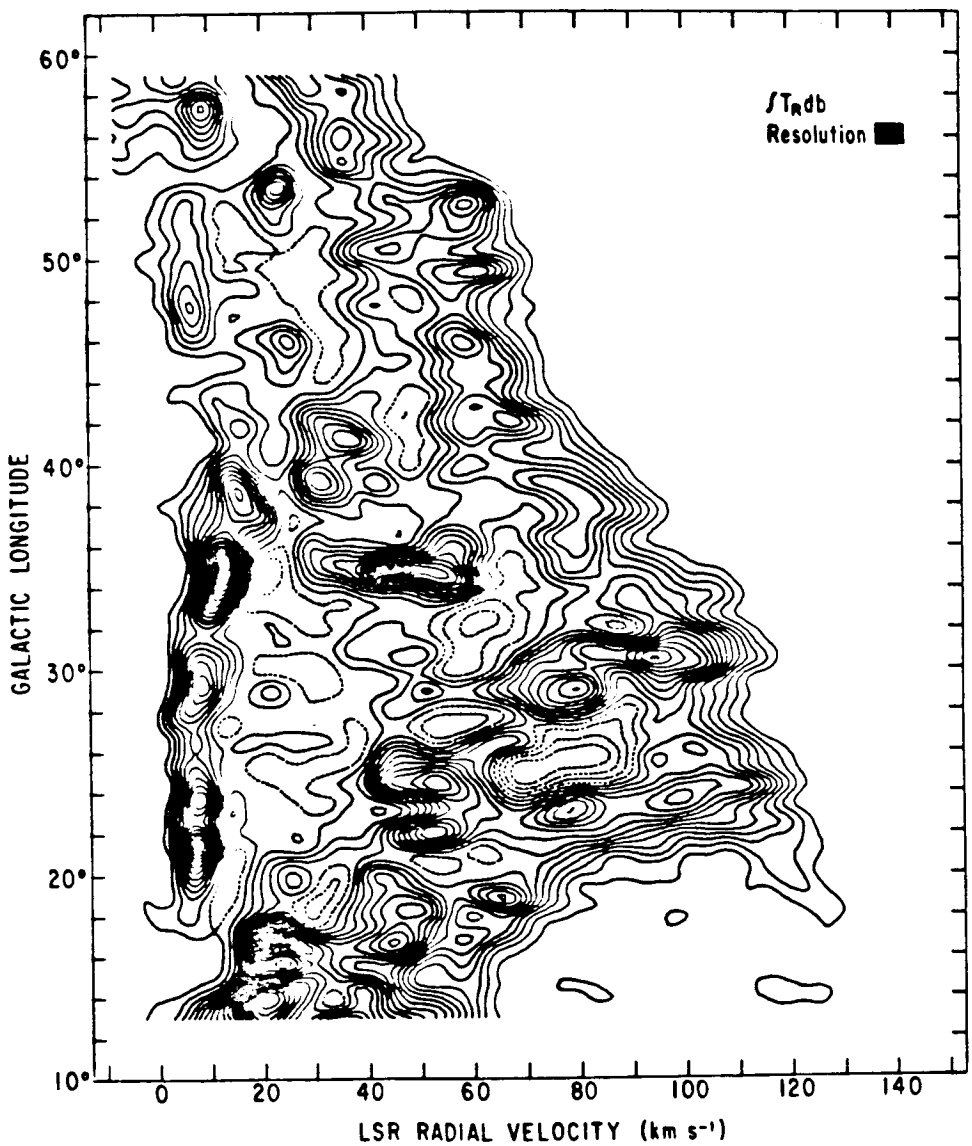

Figure III-4(c)

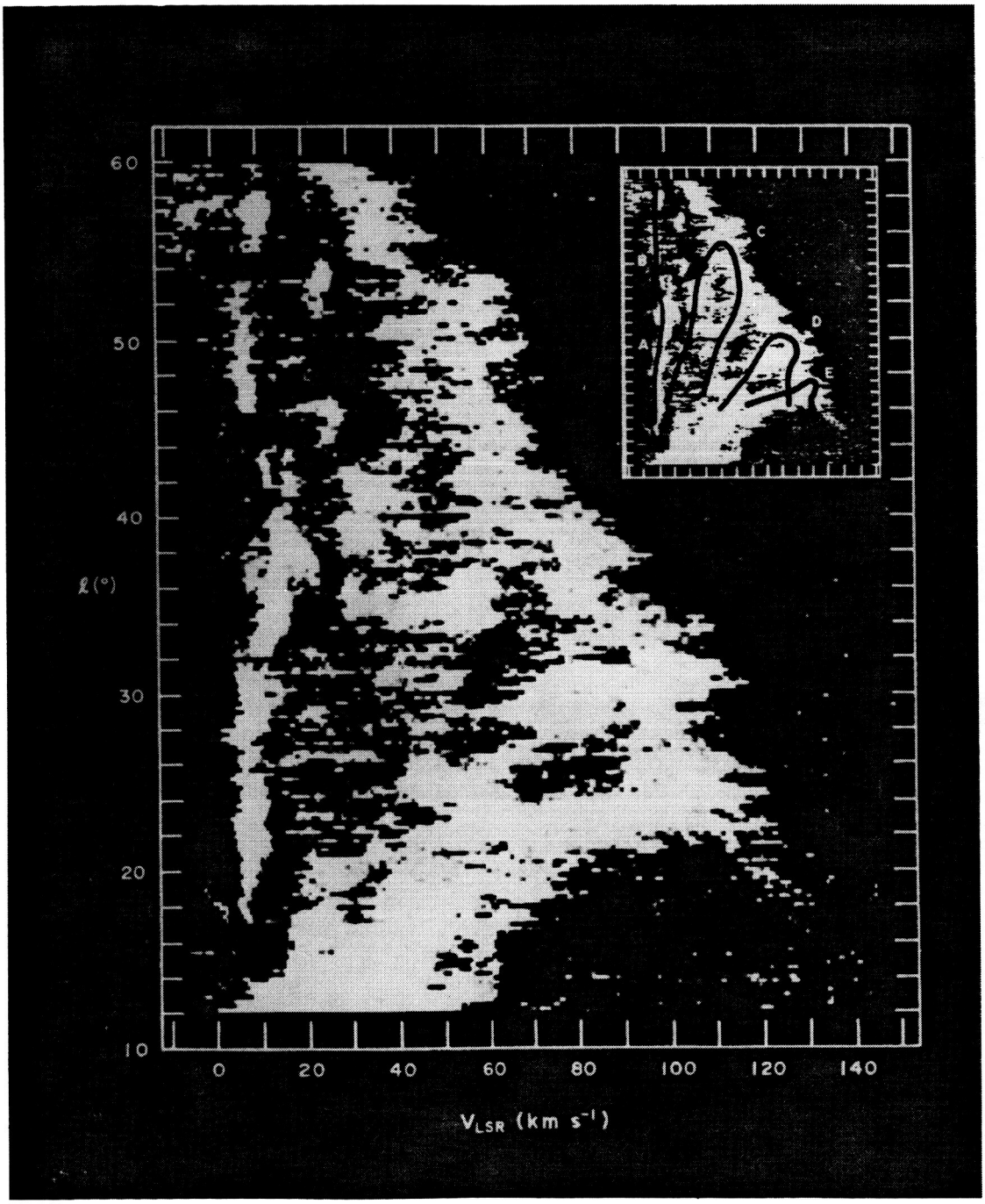

Figure III-5

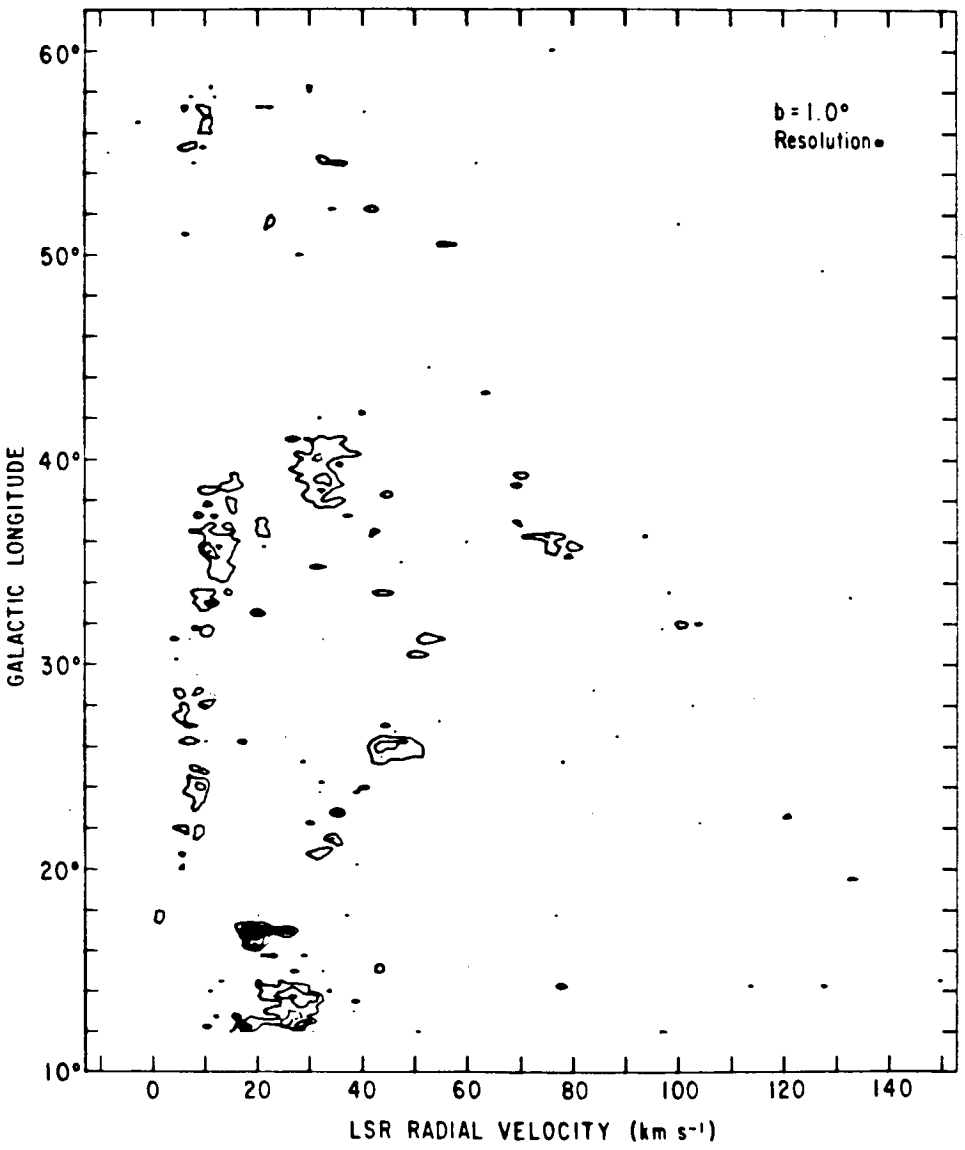

Figure III-6(a)

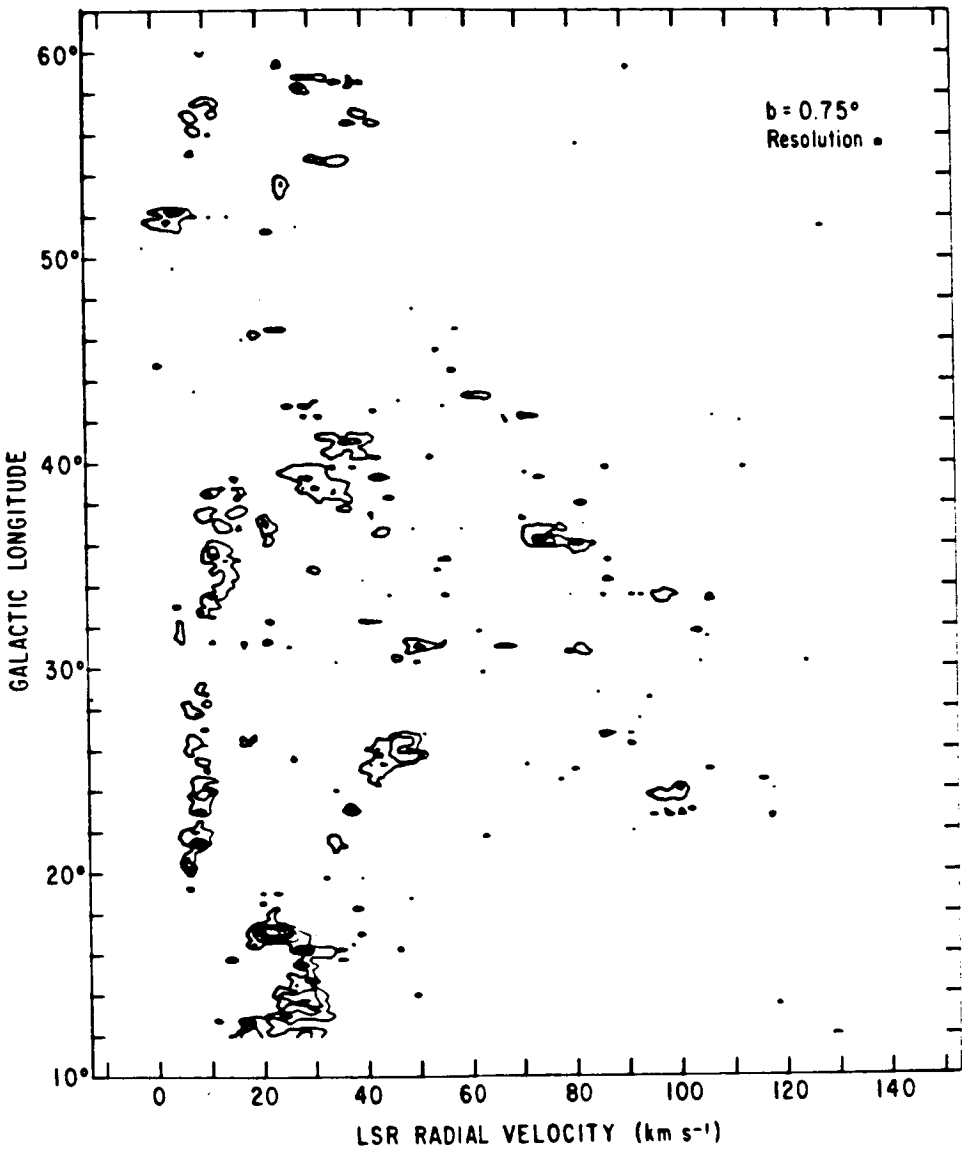

Figure III-6(b)

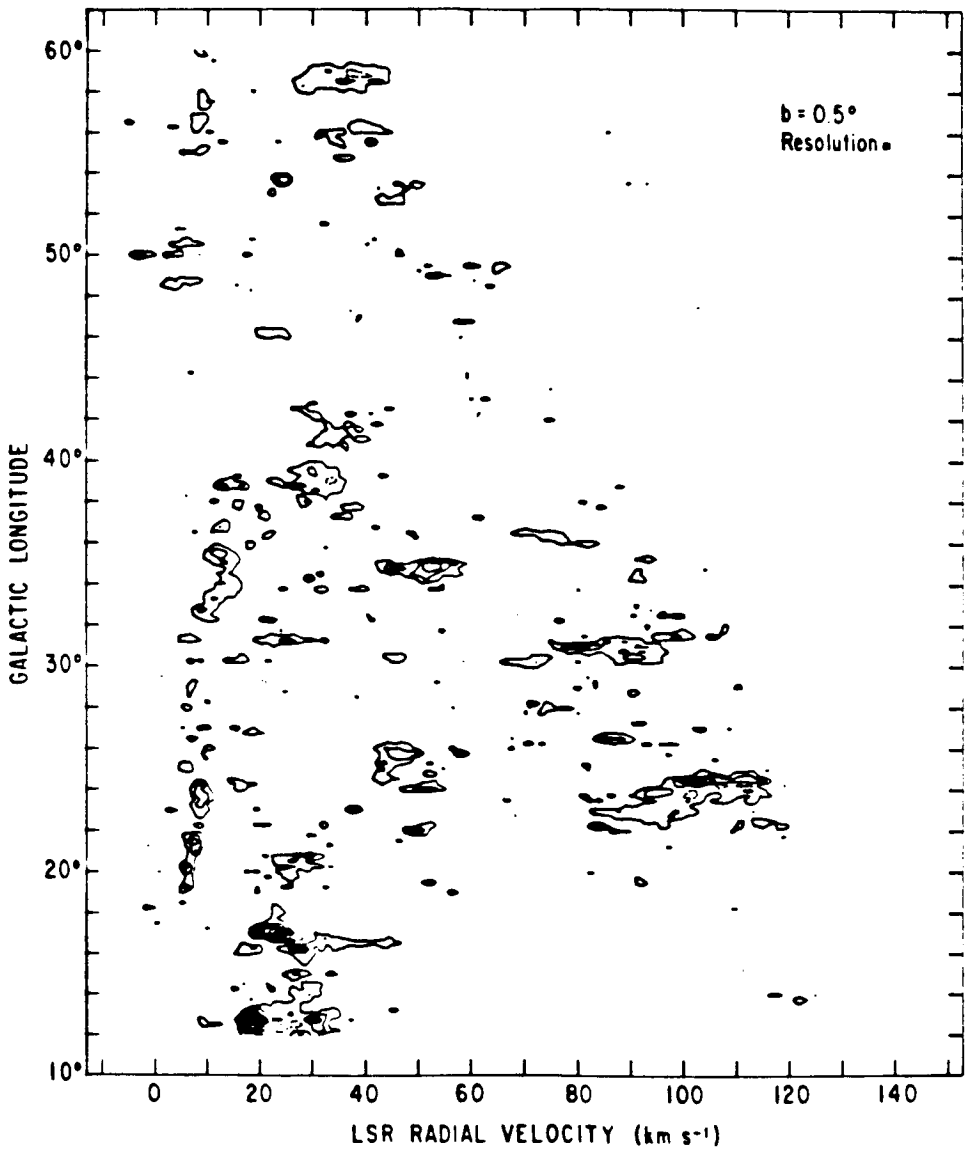

Figure III-6(c)

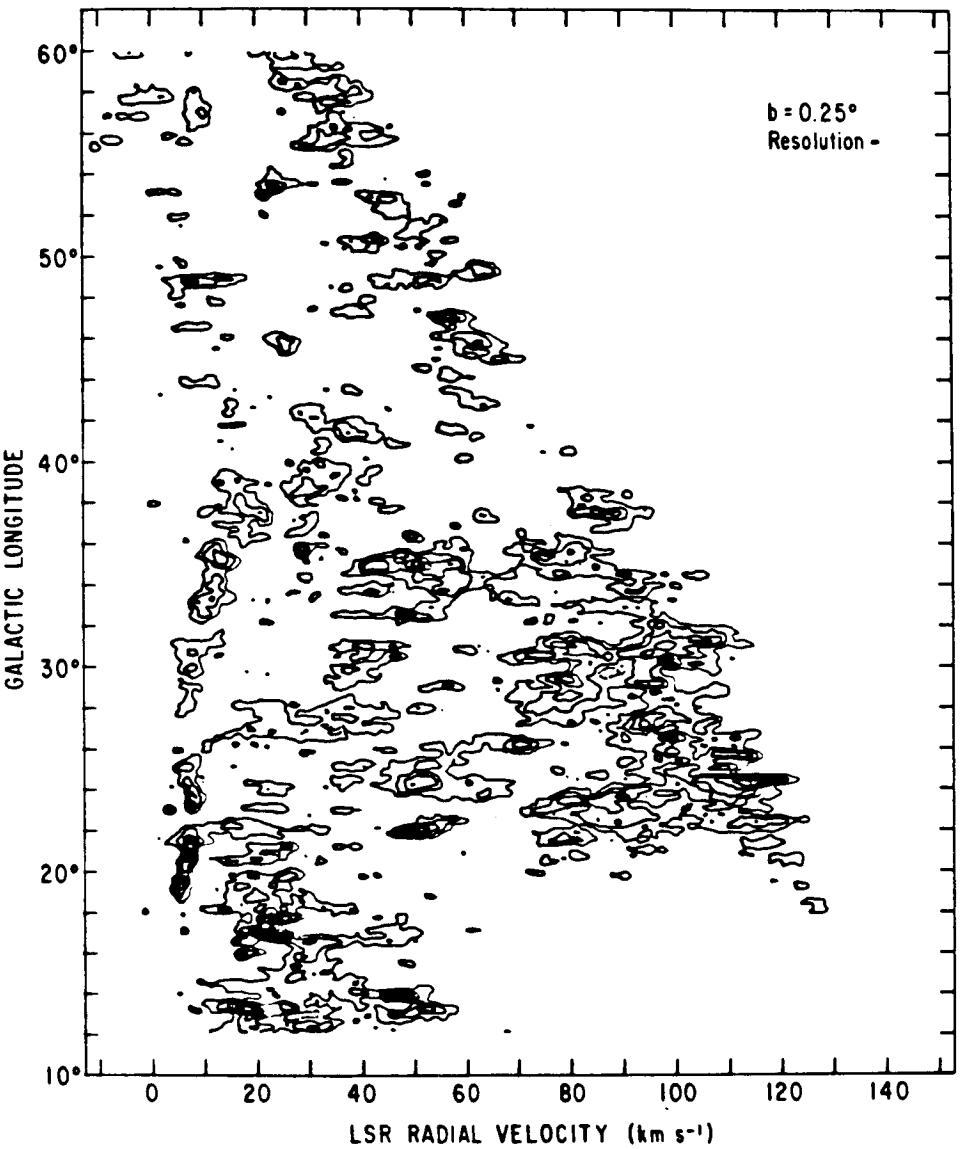

Figure III-6(d)

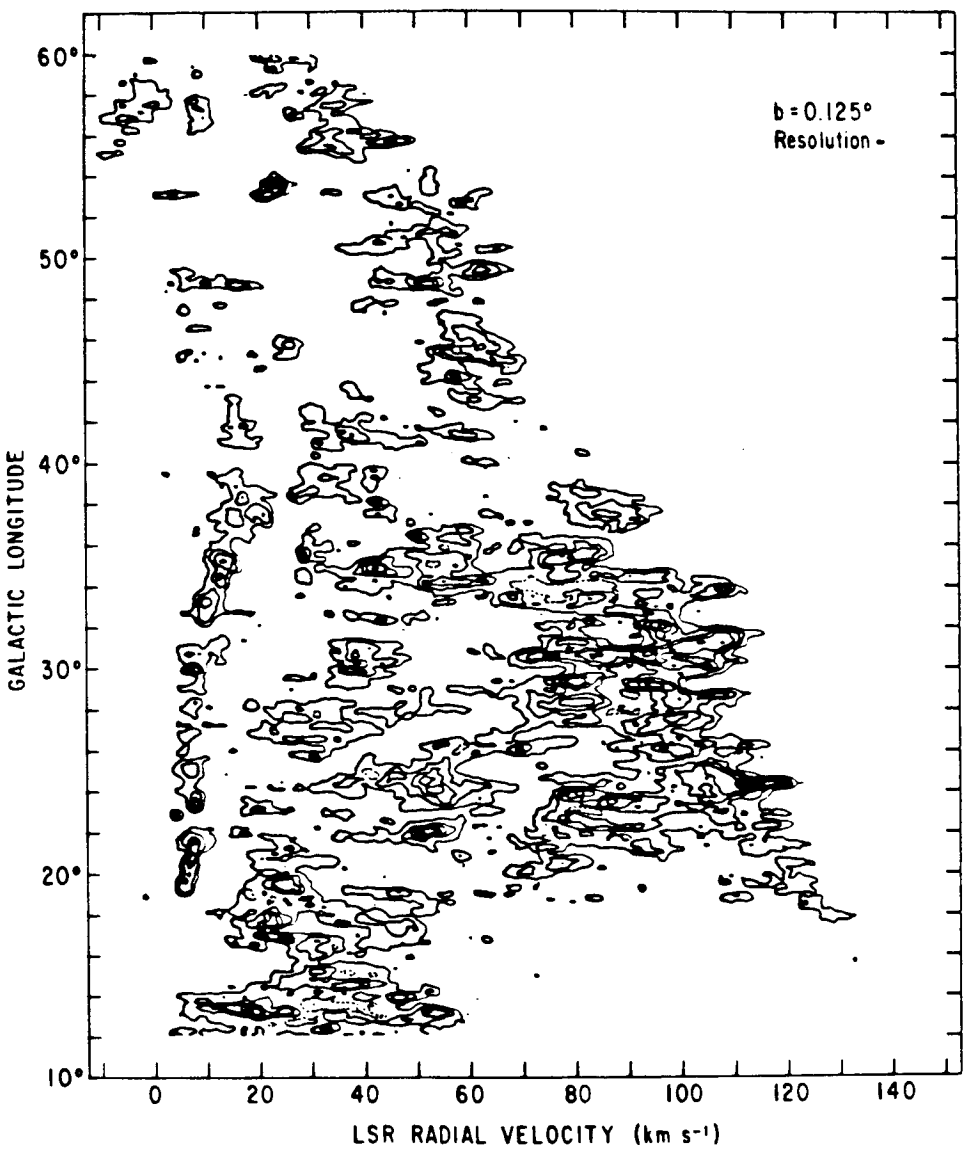

Figure III-6(e)

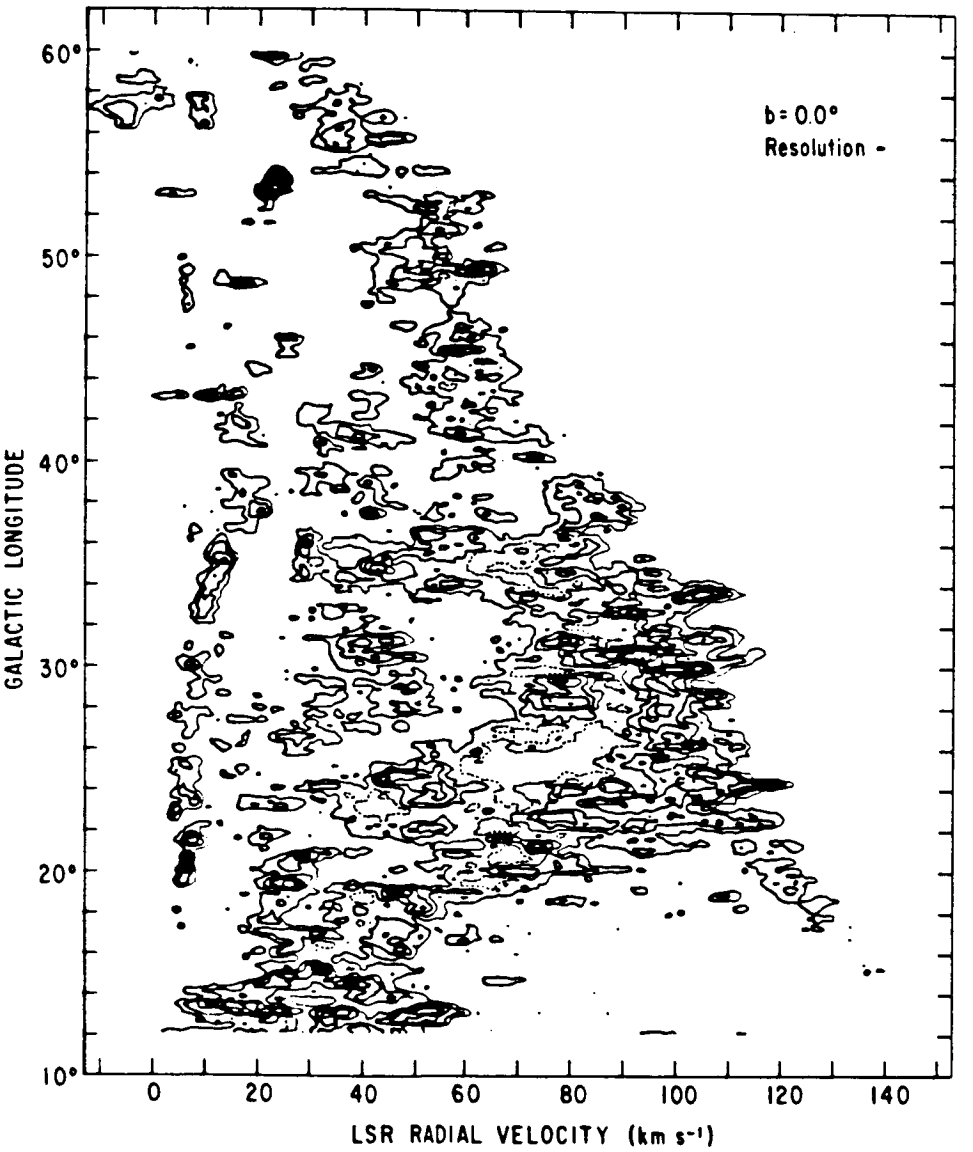

Figure III-6(f)

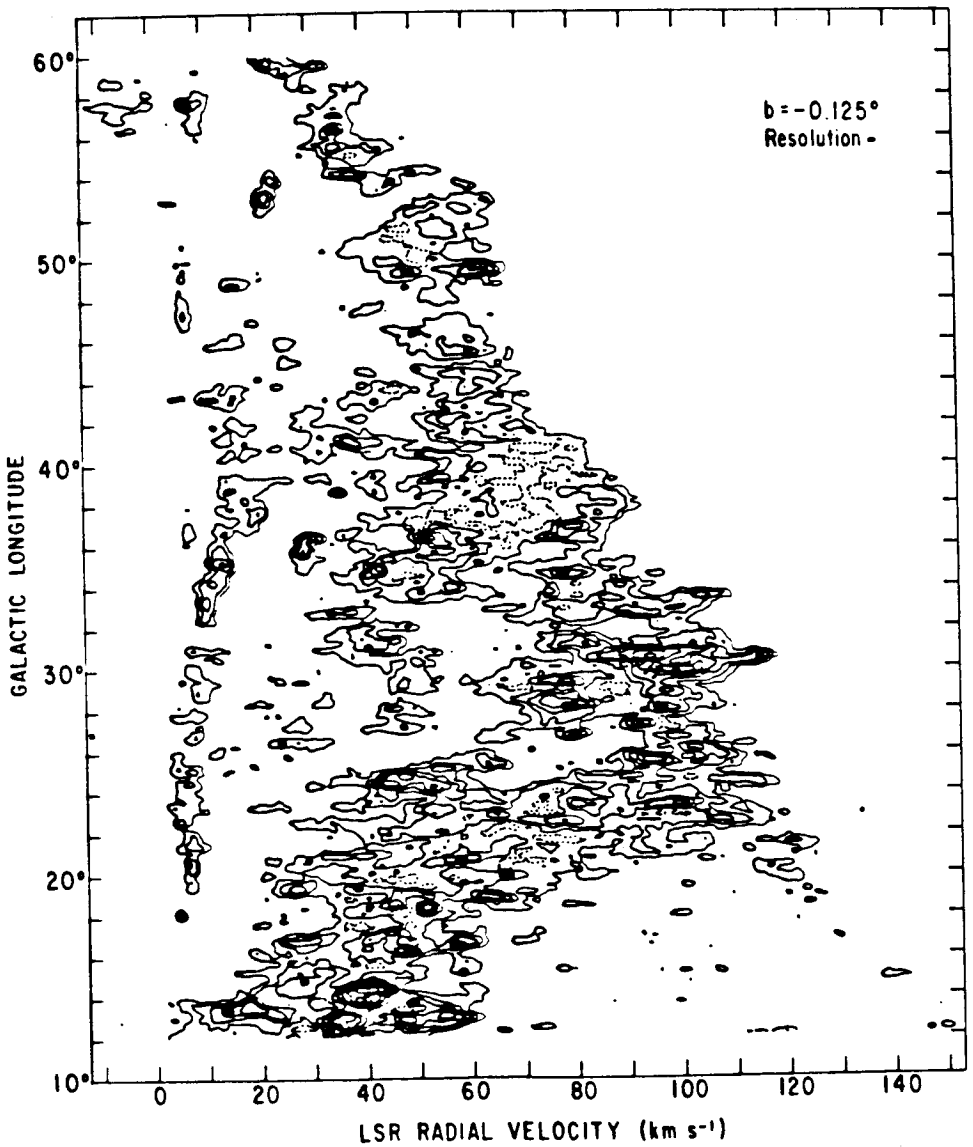

Figure III-6(g)

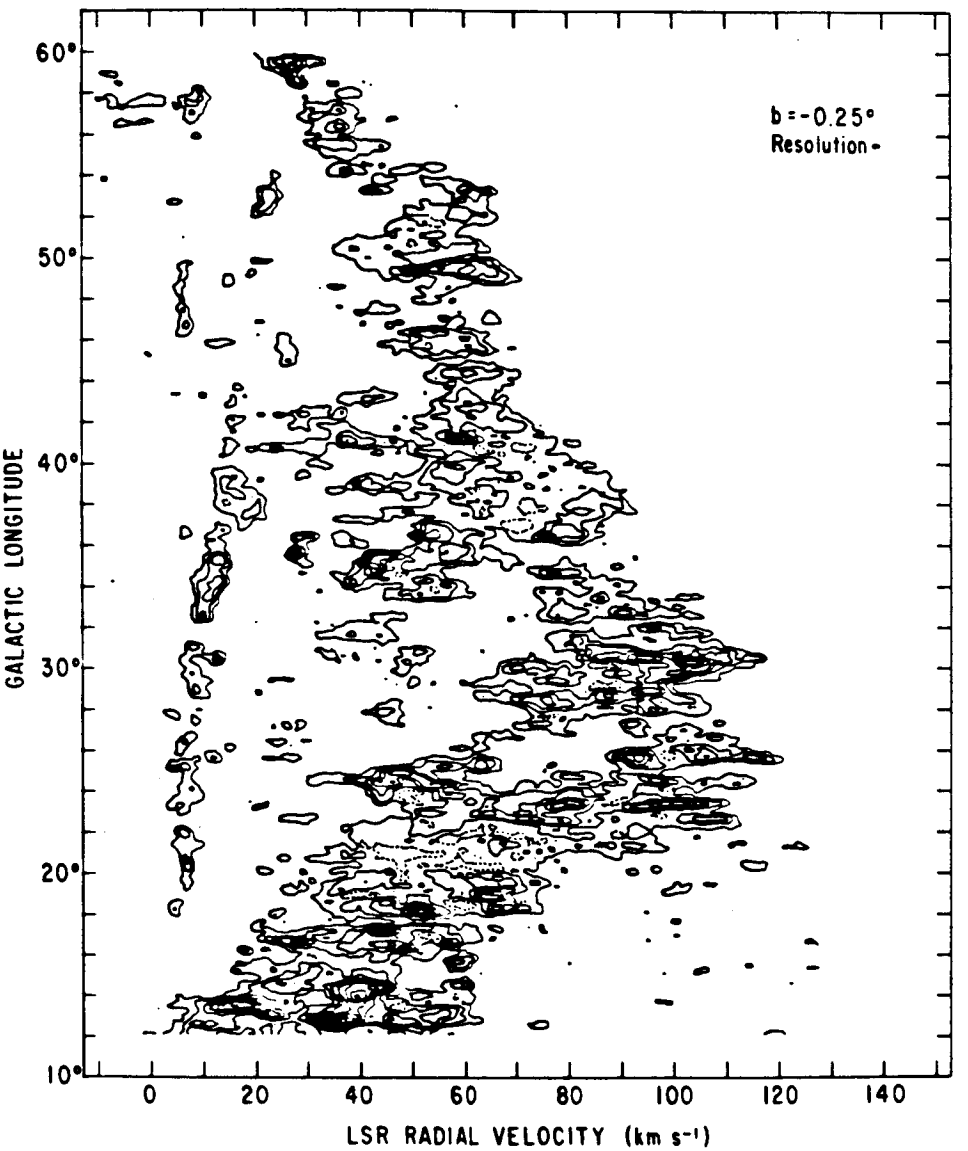

Figure III-6(h)

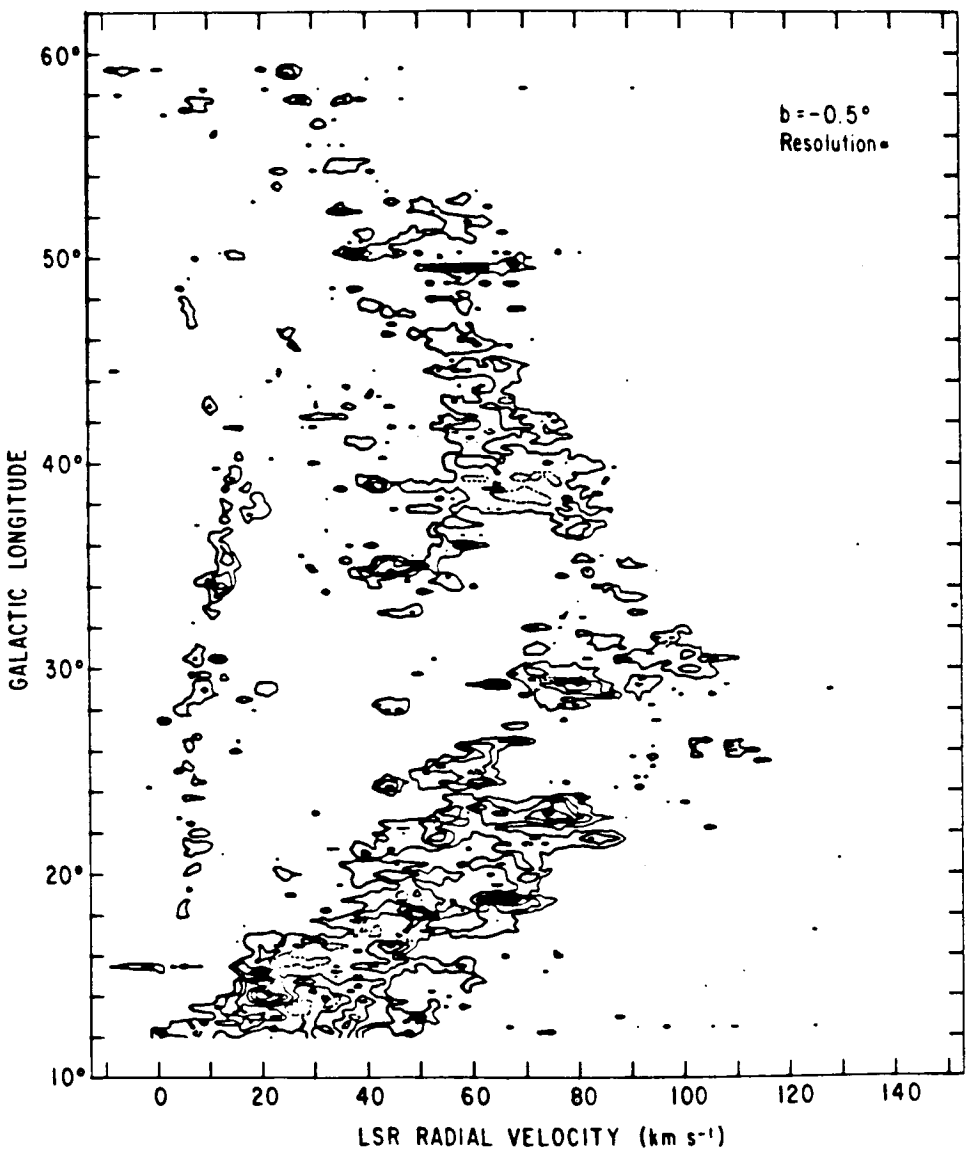

Figure III-6(i)

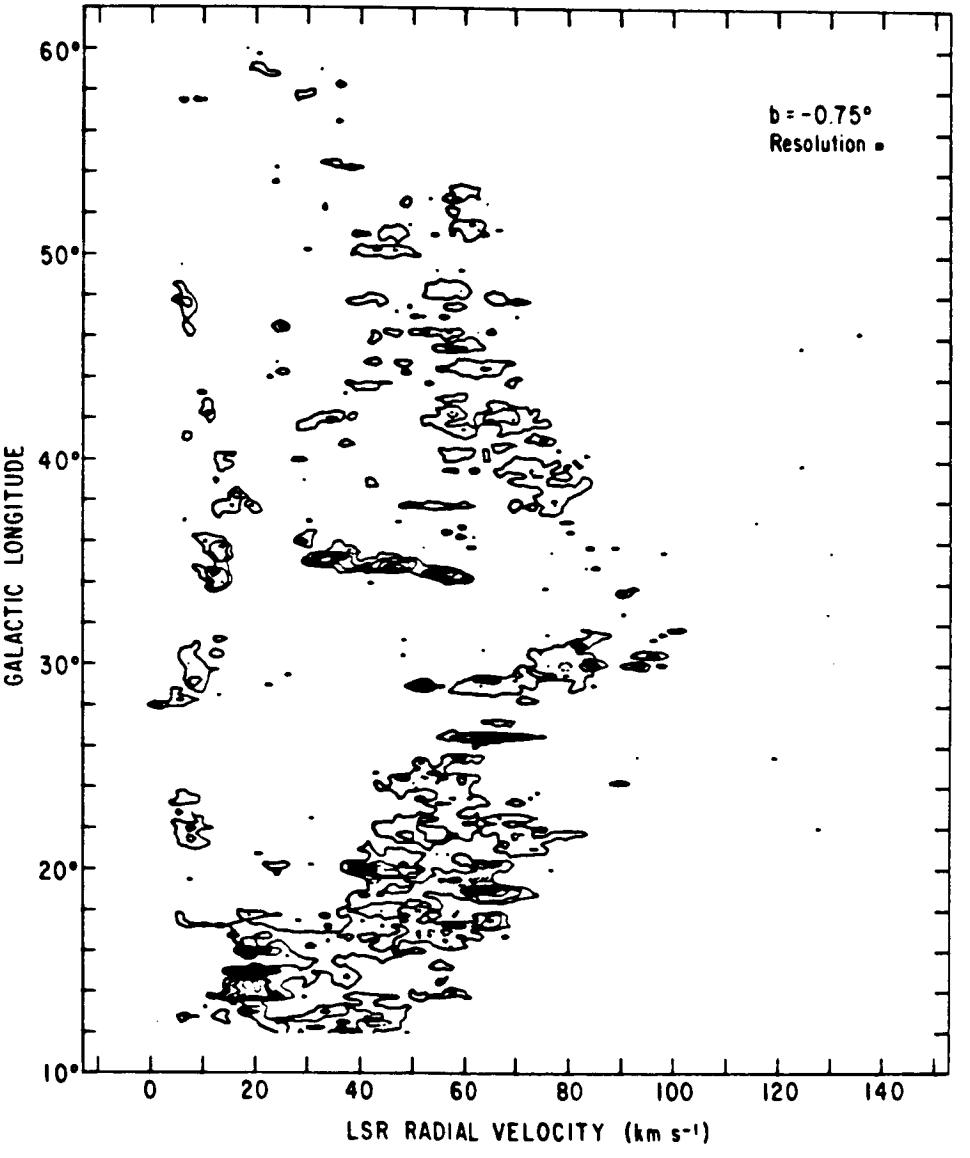

Figure III-6(j)

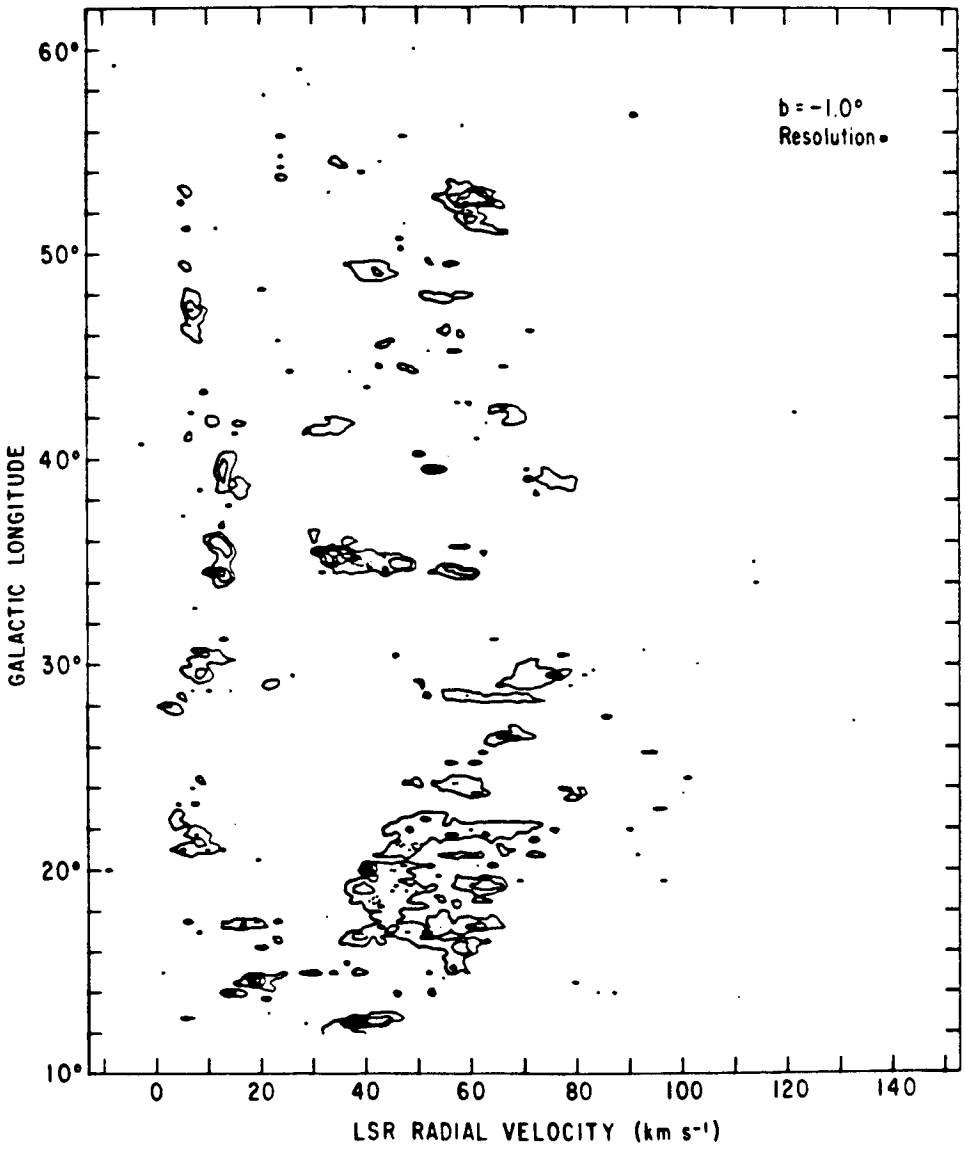

Figure III-6(k)

SUPERBEAM CO SURVEY
V = -10 to 20 km/sec
O BEAM
GALACTIC LONGITUDE
GALACTIC LATITUDE
10°
5°
0°
-5°
90°
80°
70°
60°
50°
40°
30°
20°

Figure III-7

OLD GALACTIC LATITUDE
20°
10°
0°
-10°
-20°
340°
0°
20°
40°
60°
80°
OLD GALACTIC LONGITUDE

Figure III-8

AXISYMMETRIC MODEL RESULTS

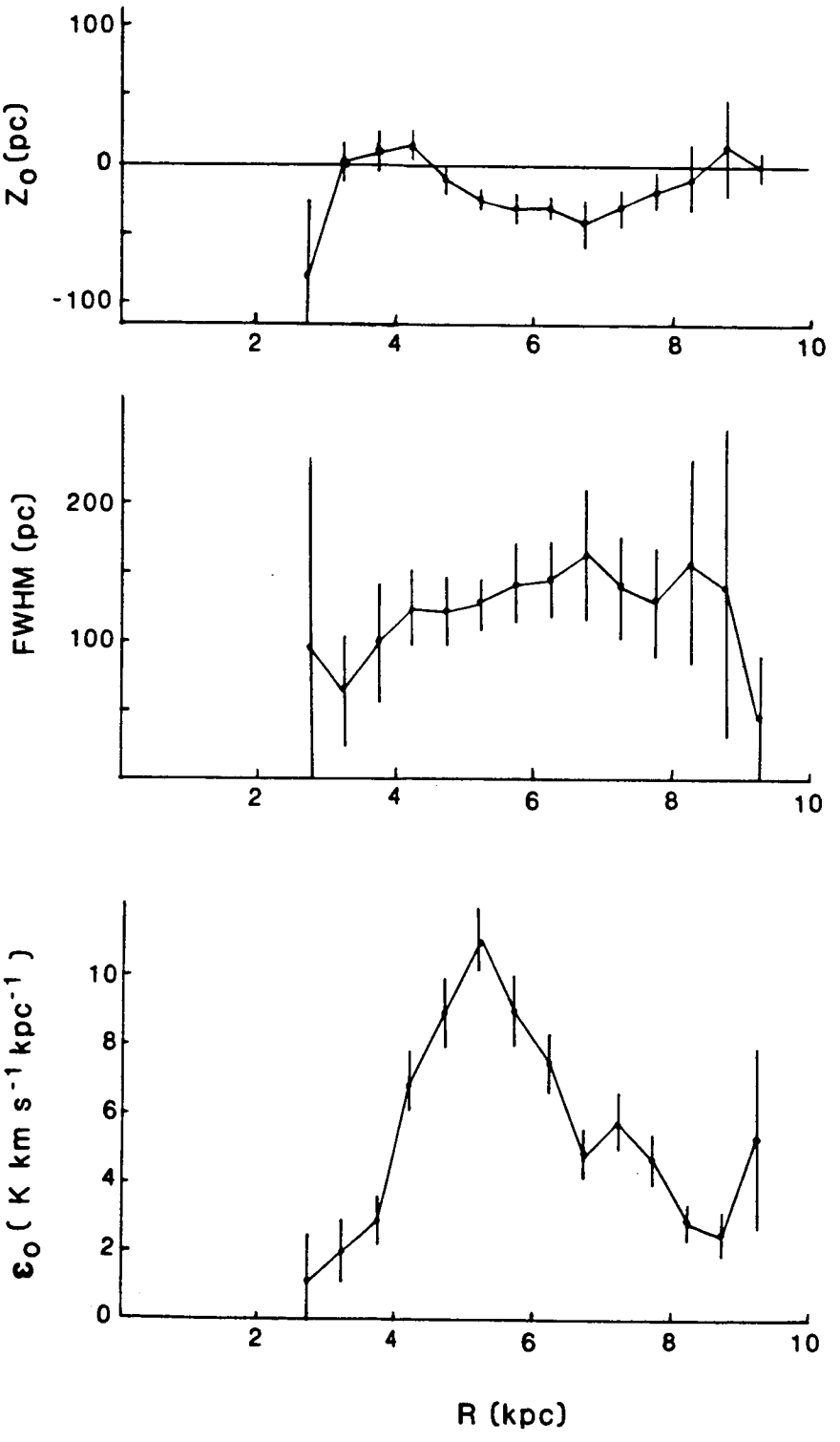

Figure IV-1

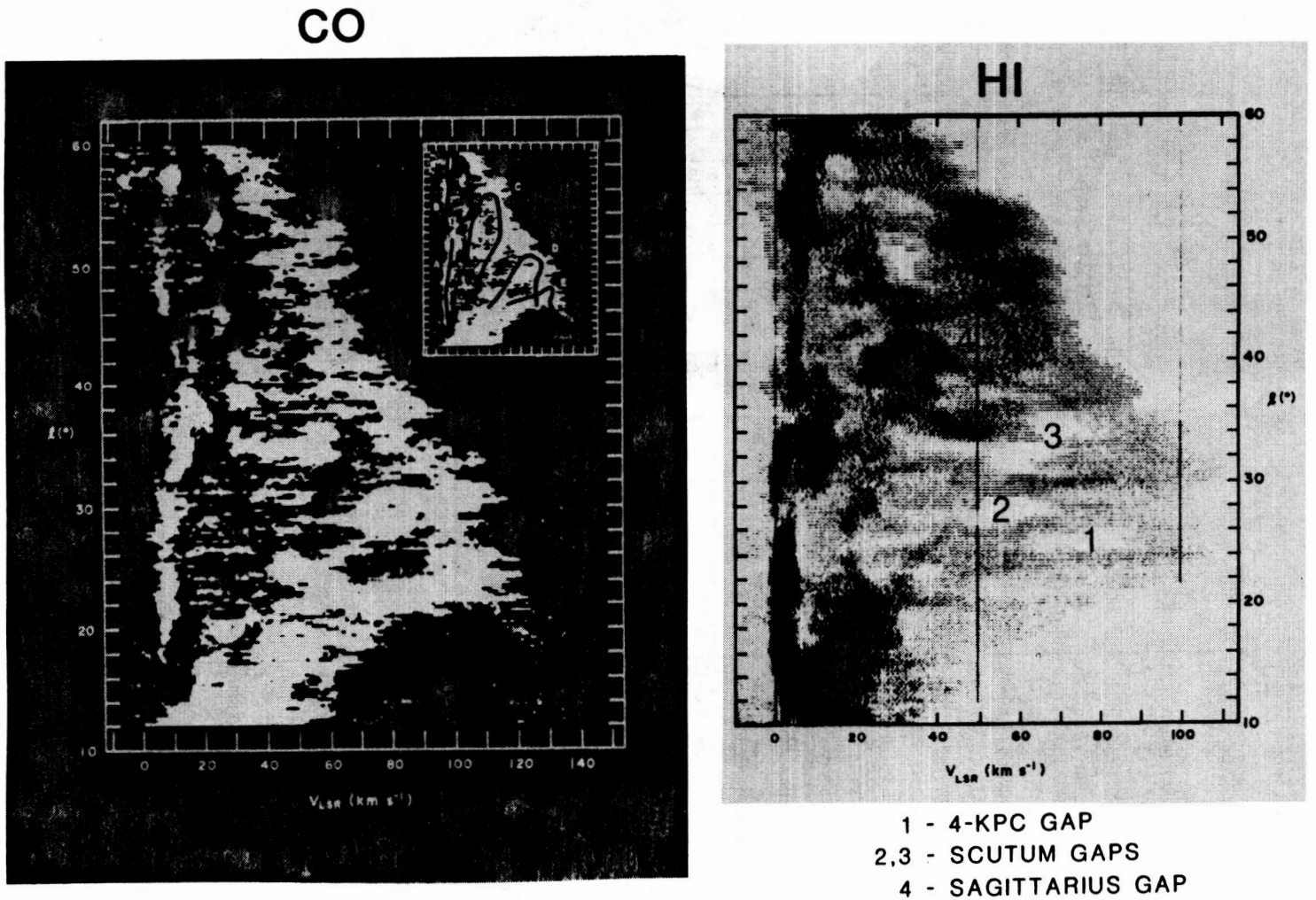
CO
HI
60
50
40
30
20
10
ℓ(°)
0
20
40
60
80
100
120
140
V_{LSR} (km s^{-1})
1
2
3
1 - 4-KPC GAP
2,3 - SCUTUM GAPS
4 - SAGITTARIUS GAP

Figure V-1

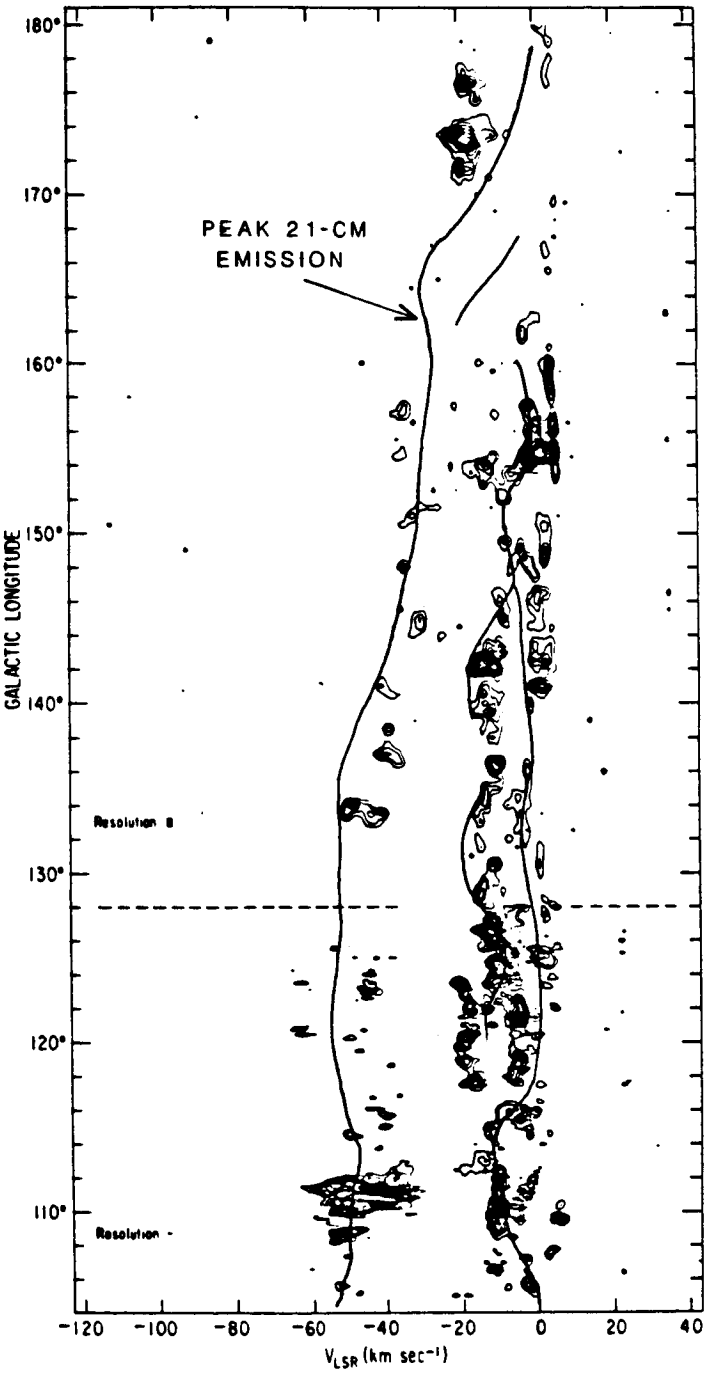
PEAK 21-CM
EMISSION
GALACTIC LONGITUDE
180°
170°
160°
150°
140°
130°
120°
110°
Resolution B
Resolution -
-120
-100
-80
-60
-40
-20
0
20
40
V_{LSR} (km sec^{-1})

Figure V-2

COMPARISON OF CO AND HI SPECTRA

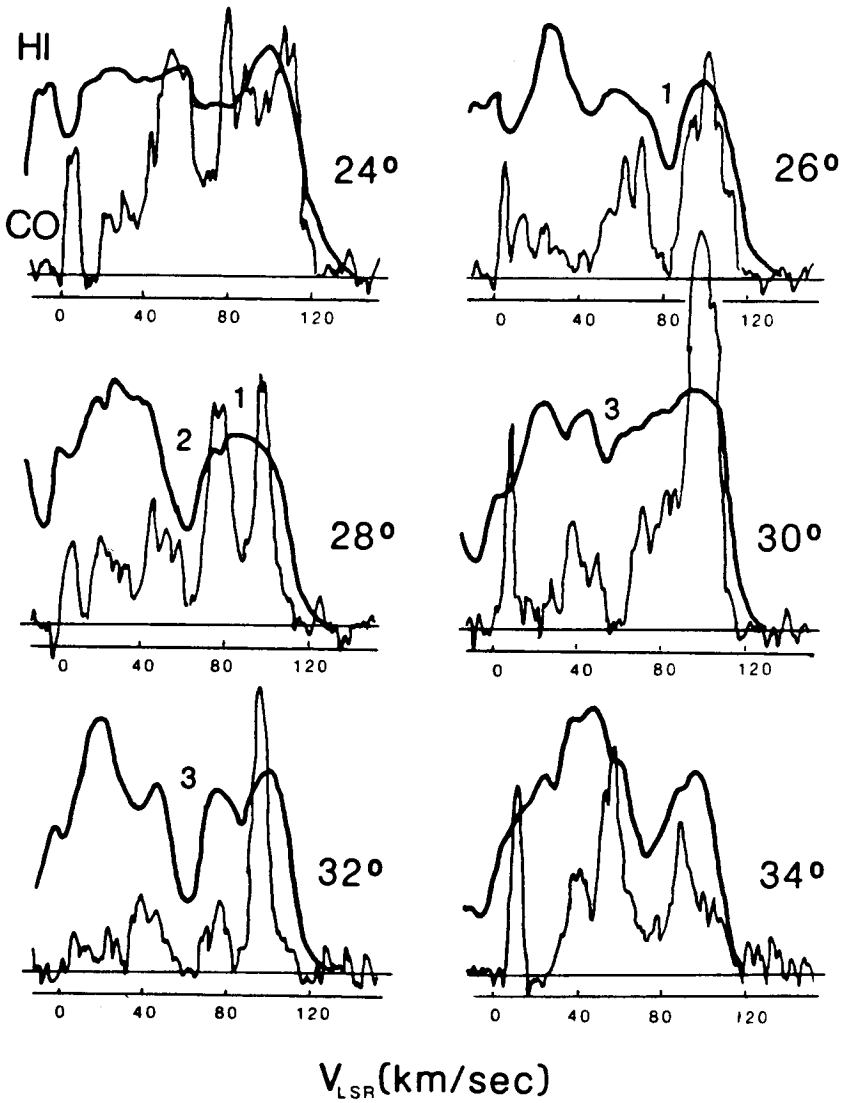

Figure V-3

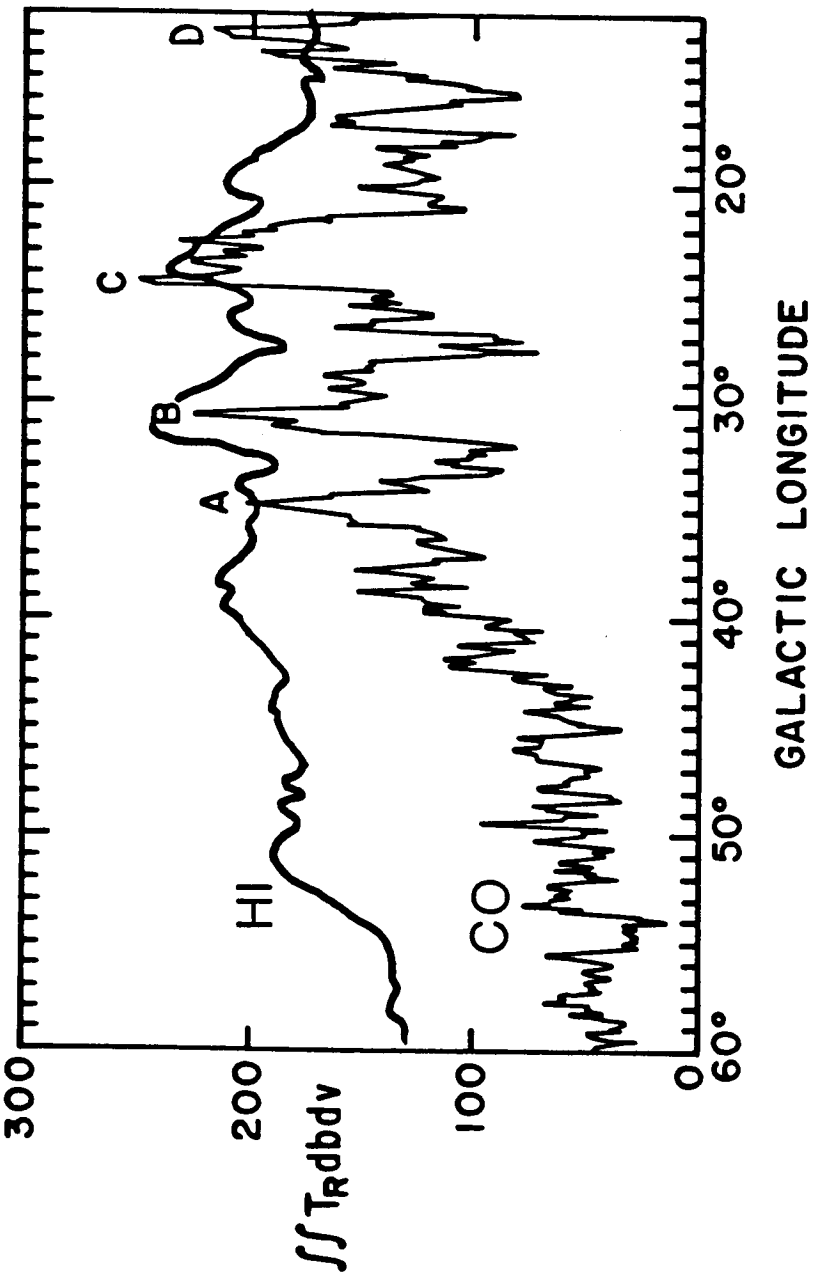
300
200
100
0
60°
50°
40°
30°
20°
GALACTIC LONGITUDE
∫∫ TR dbdv
HI
CO
A
B
C
D

Figure V-4

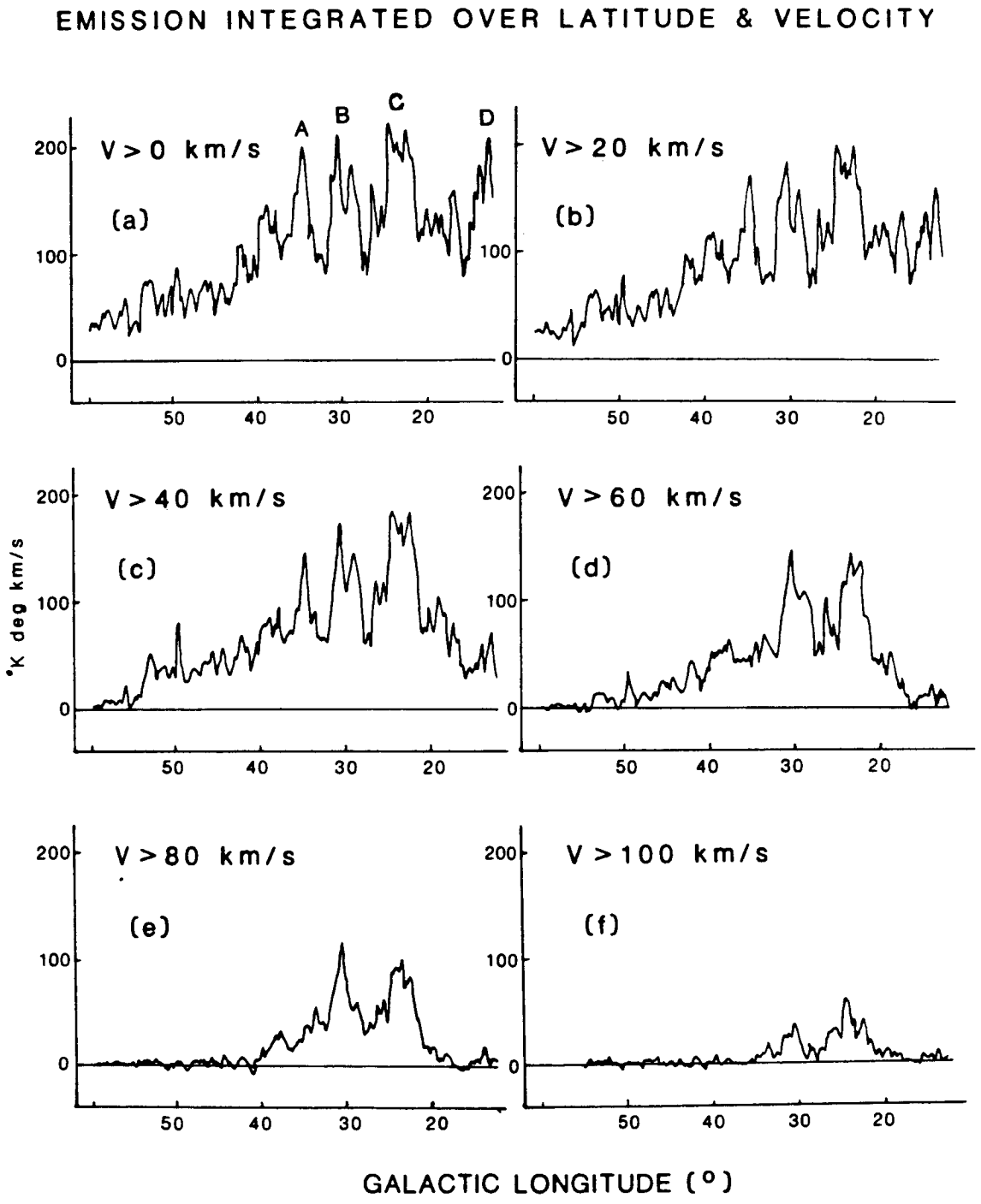
EMISSION INTEGRATED OVER LATITUDE & VELOCITY
V > 0 km/s
(a)
A
B
C
D
V > 20 km/s
(b)
V > 40 km/s
(c)
V > 60 km/s
(d)
V > 80 km/s
(e)
V > 100 km/s
(f)
200
100
0
50
40
30
20
°K deg km/s
GALACTIC LONGITUDE (°)

Figure V-5

CLOUDS EQUALLY SPACED ALONG TWO SPIRAL ARMS

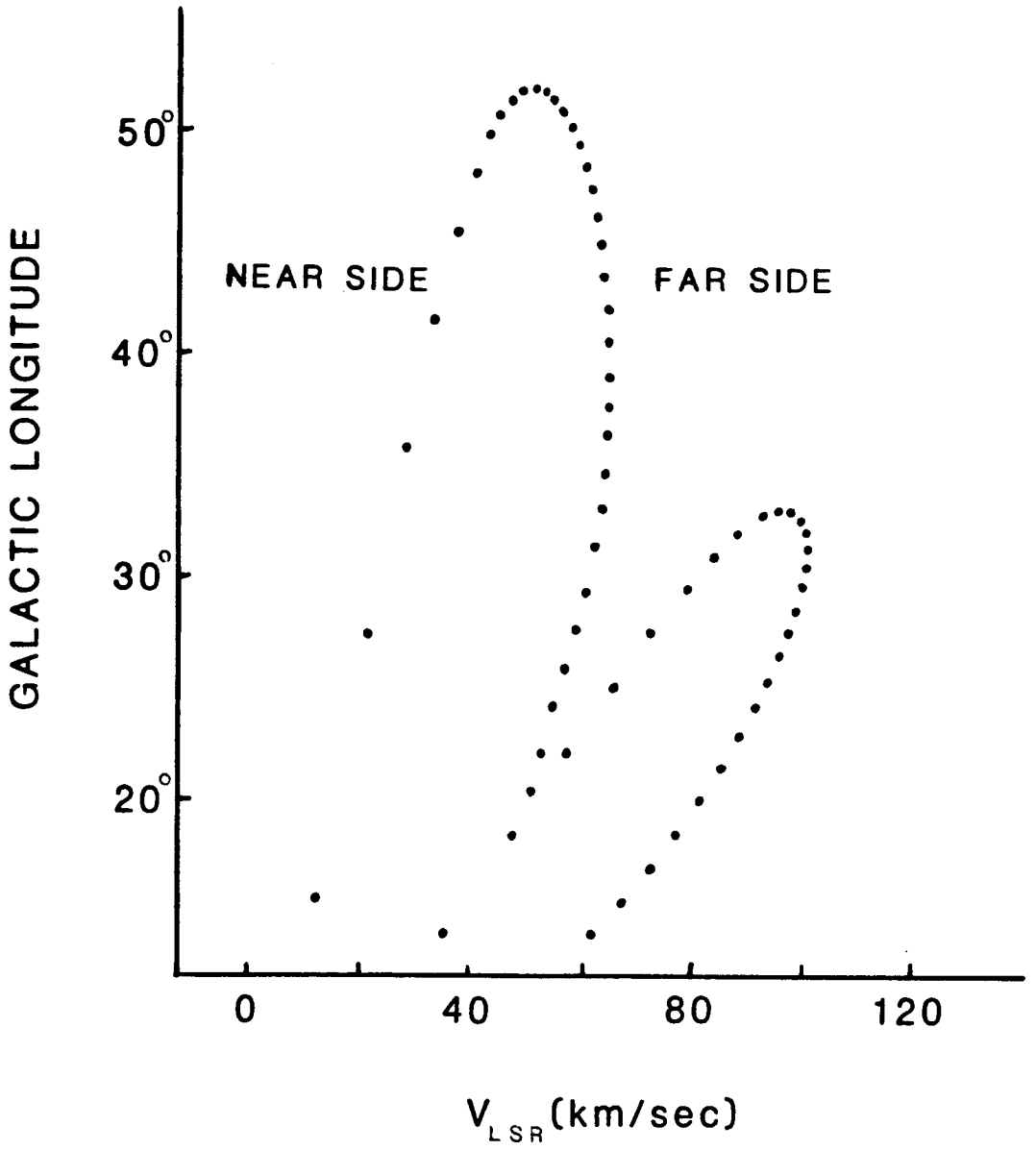

Figure V-6

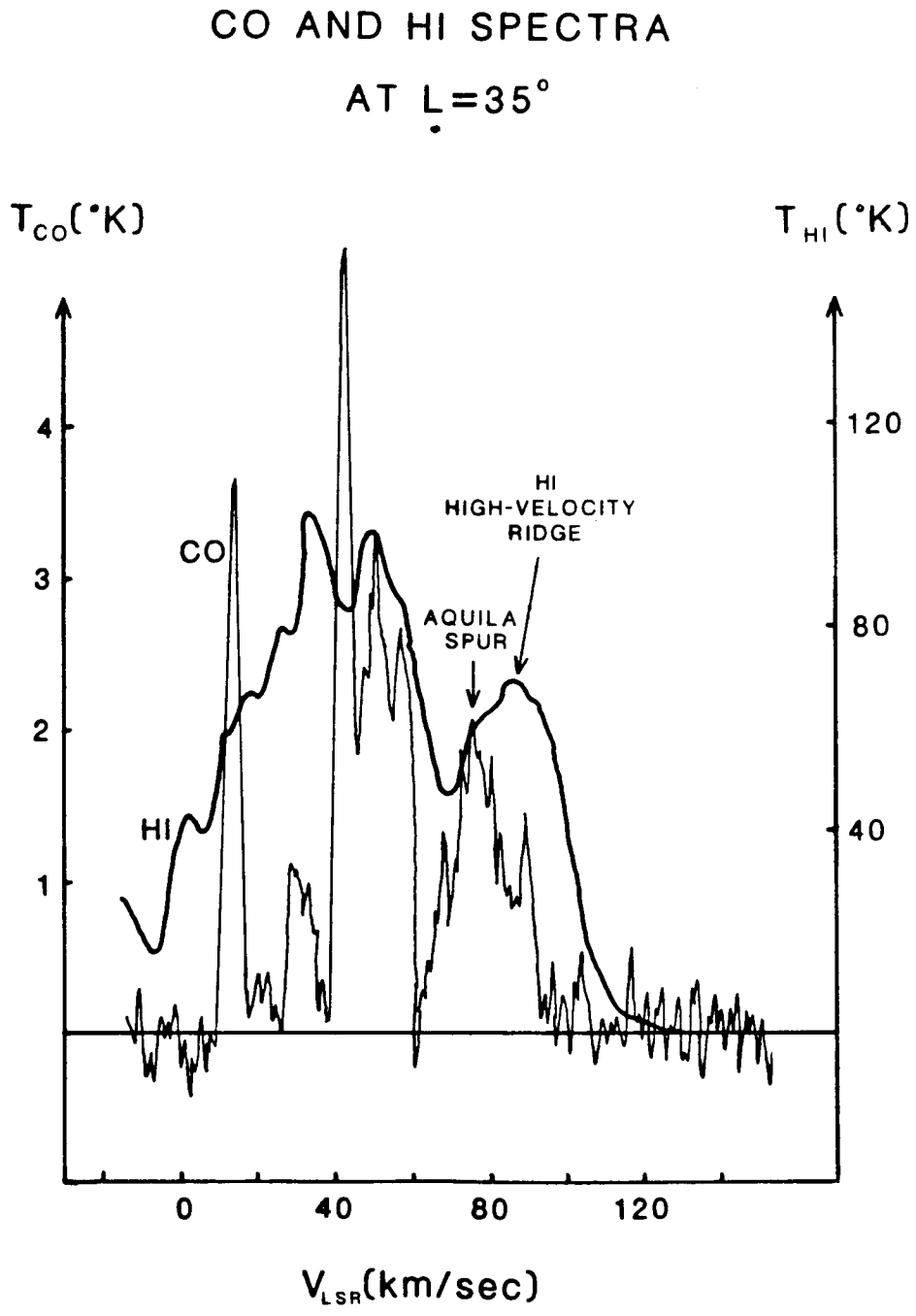
CO AND HI SPECTRA
AT L=35°
T_{CO}(°K)
T_{HI}(°K)
4
3
2
1
120
80
40
CO
HI
HI
HIGH-VELOCITY
RIDGE
AQUILA
SPUR
0
40
80
120
V_{LSR}(km/sec)

Figure V-7

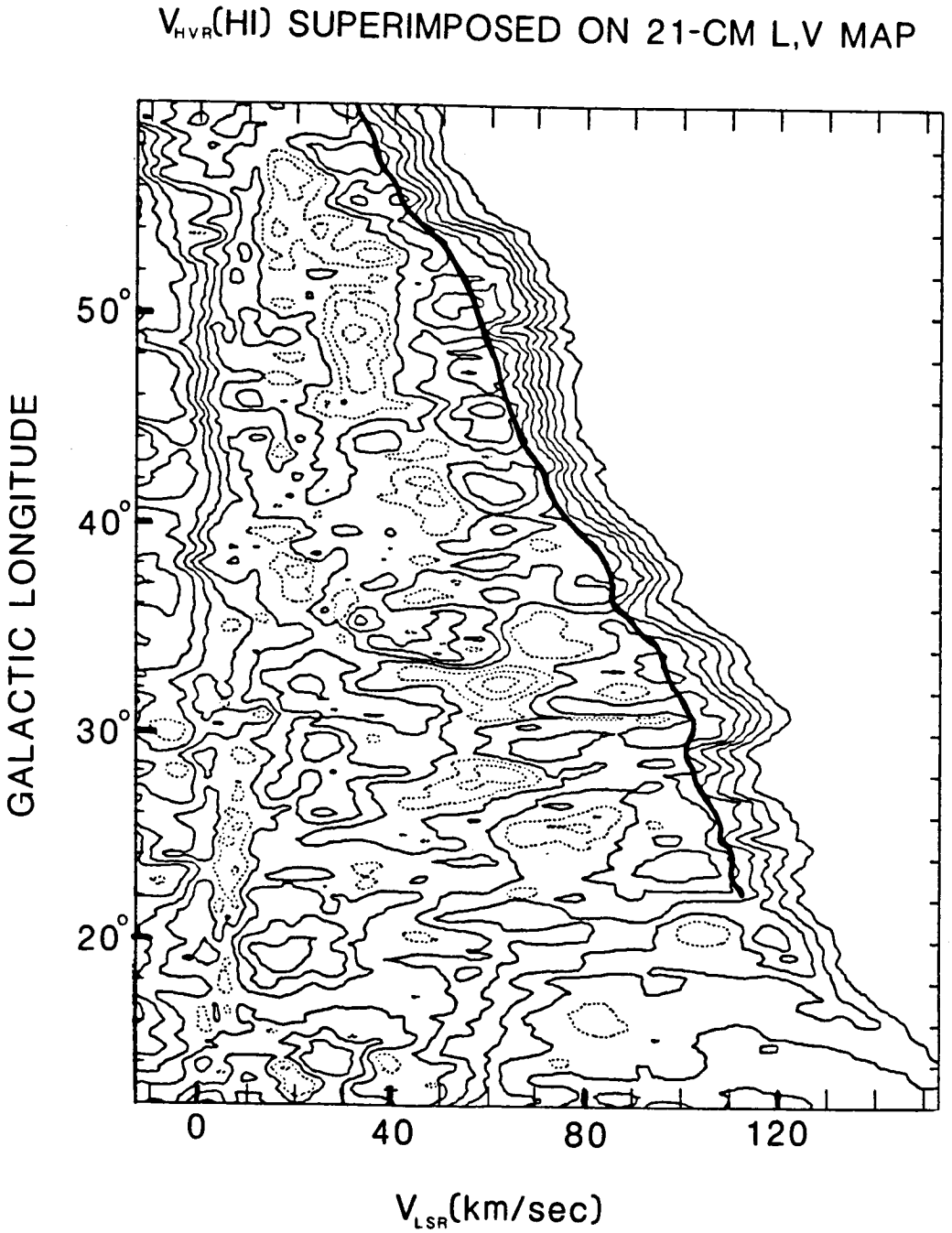
V_{HVR}(HI) SUPERIMPOSED ON 21-CM L,V MAP
GALACTIC LONGITUDE
50°
40°
30°
20°
0
40
80
120
V_{LSR}(km/sec)

Figure VI-1

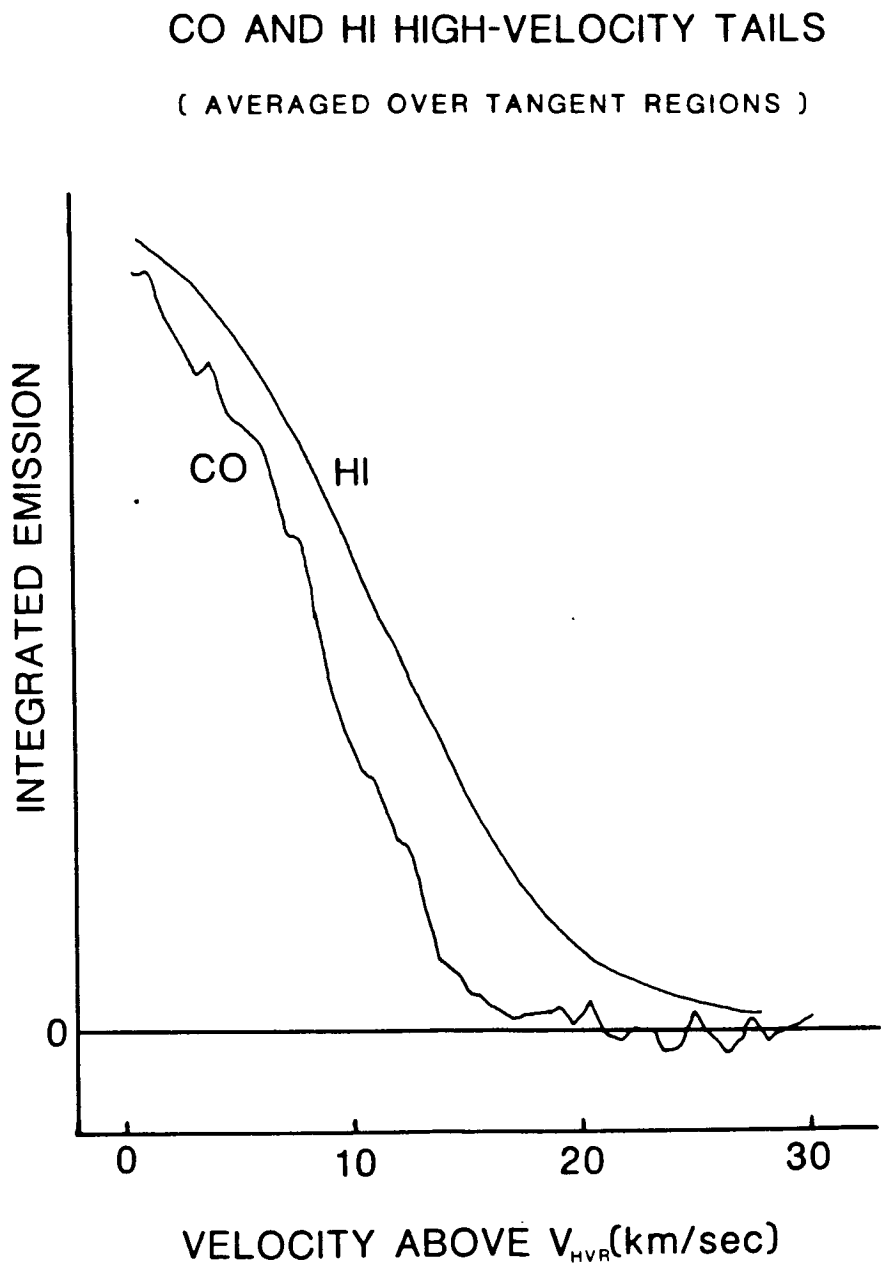
CO AND HI HIGH-VELOCITY TAILS
(AVERAGED OVER TANGENT REGIONS)
INTEGRATED EMISSION
CO
HI
0
0
10
20
30
VELOCITY ABOVE V_{HVR}(km/sec)

Figure VI-2

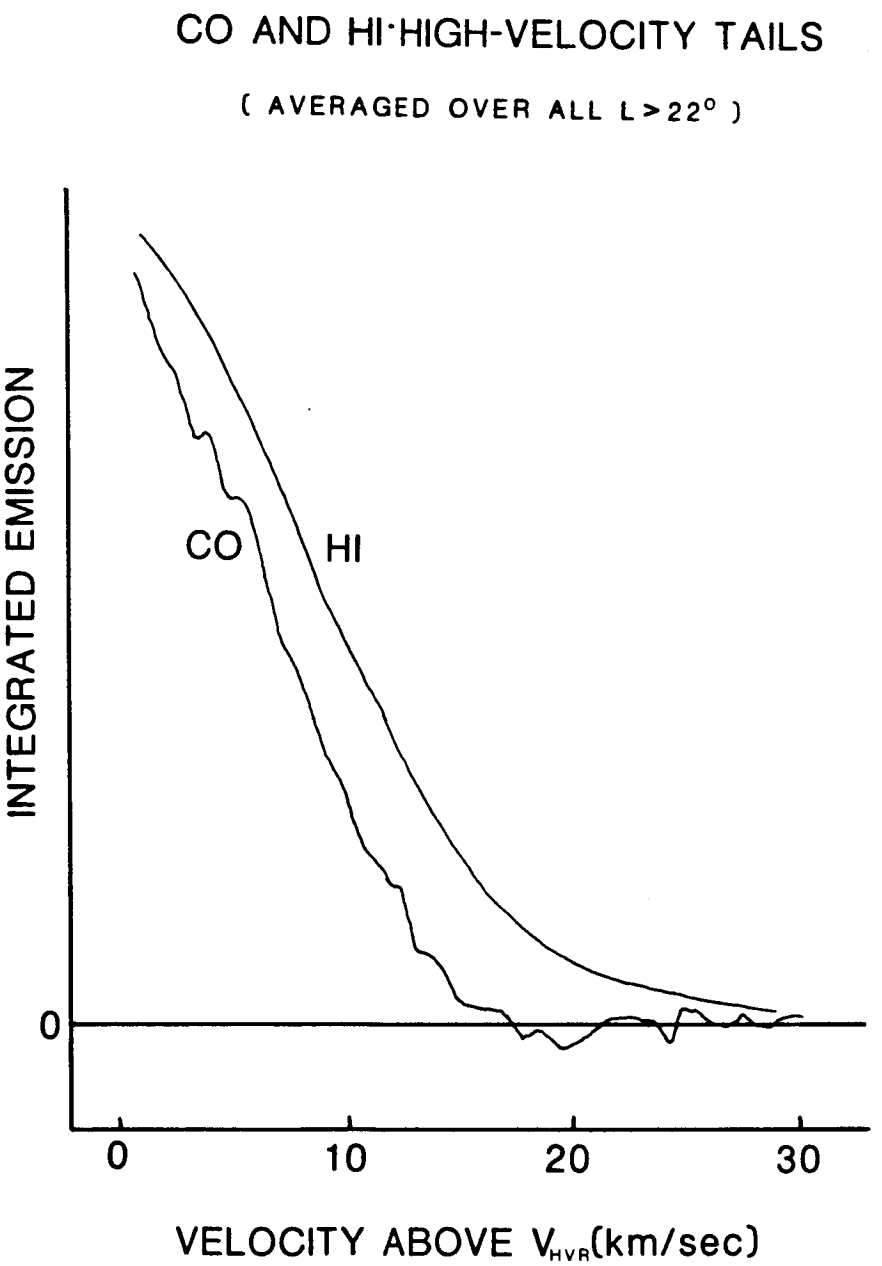
CO AND HI·HIGH-VELOCITY TAILS
(AVERAGED OVER ALL L>22°)
INTEGRATED EMISSION
CO
HI
0
0
10
20
30
VELOCITY ABOVE V_{HVR}(km/sec)

Figure VI-3

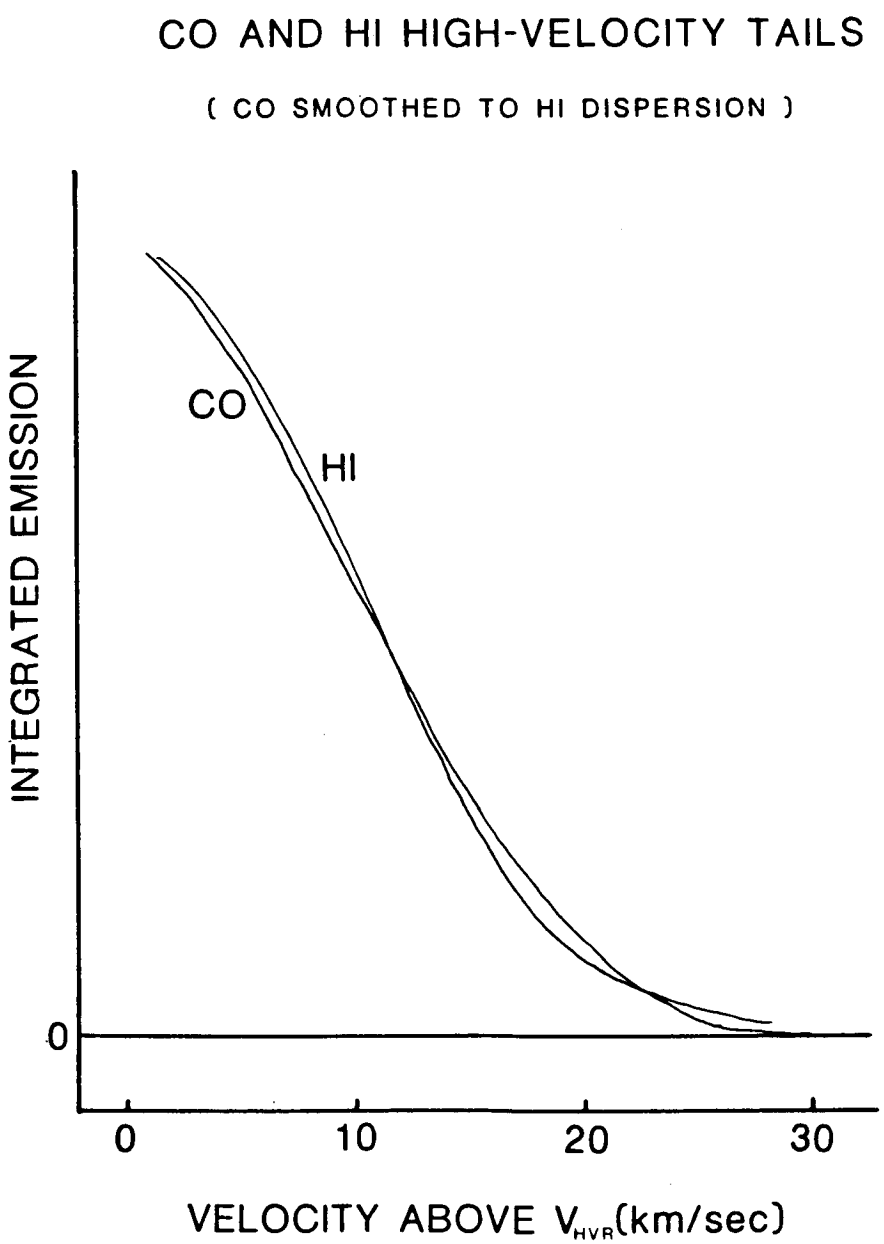
CO AND HI HIGH-VELOCITY TAILS
(CO SMOOTHED TO HI DISPERSION)
INTEGRATED EMISSION
CO
HI
0
0
10
20
30
VELOCITY ABOVE V_{HVR}(km/sec)

Figure VI-4

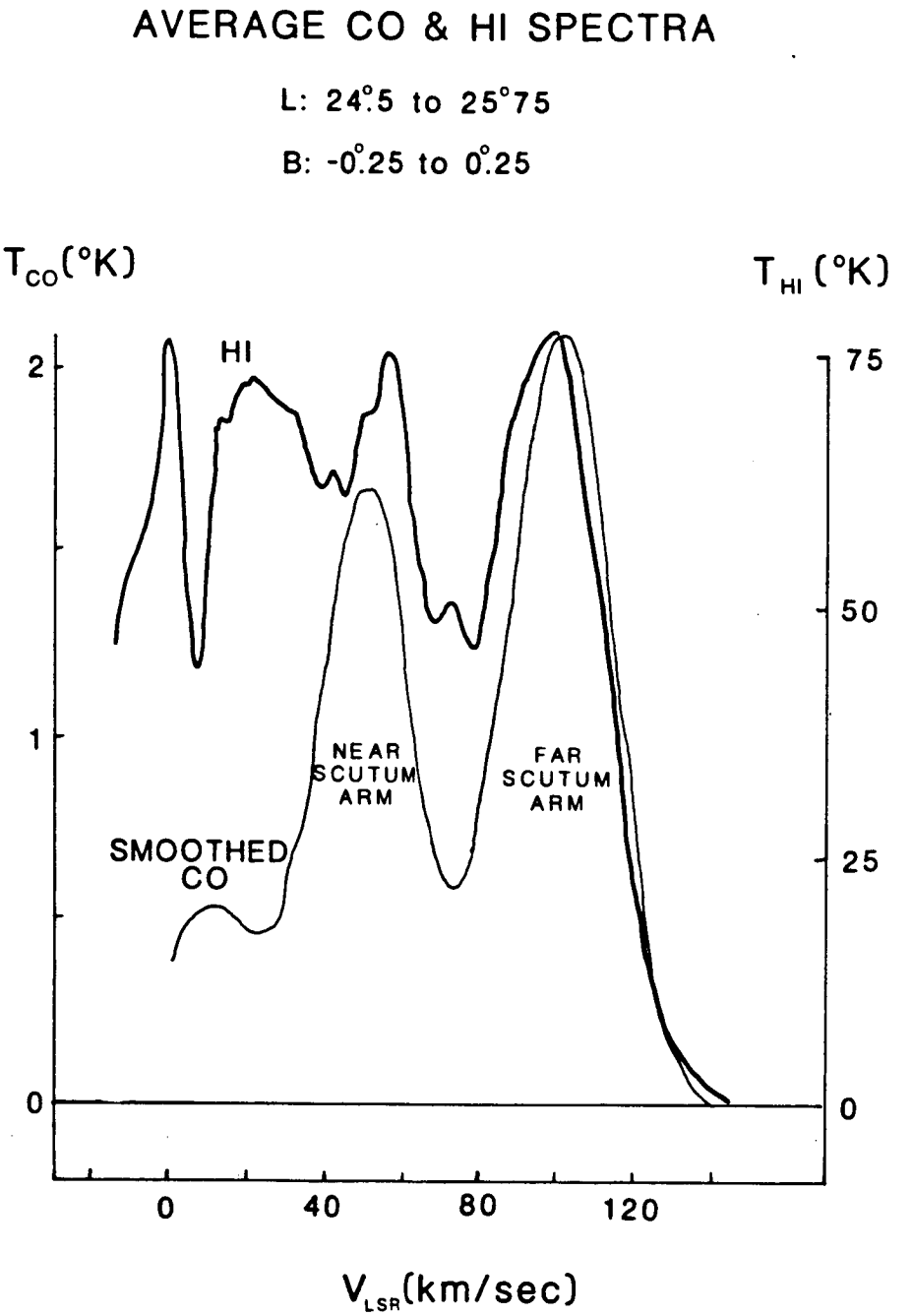
AVERAGE CO & HI SPECTRA
L: 24°.5 to 25°75
B: -0°.25 to 0°.25
T_{CO}(°K)
T_{HI} (°K)
HI
NEAR SCUTUM ARM
FAR SCUTUM ARM
SMOOTHED CO
2
1
0
75
50
25
0
0
40
80
120
V_{LSR}(km/sec)

Figure VI-5

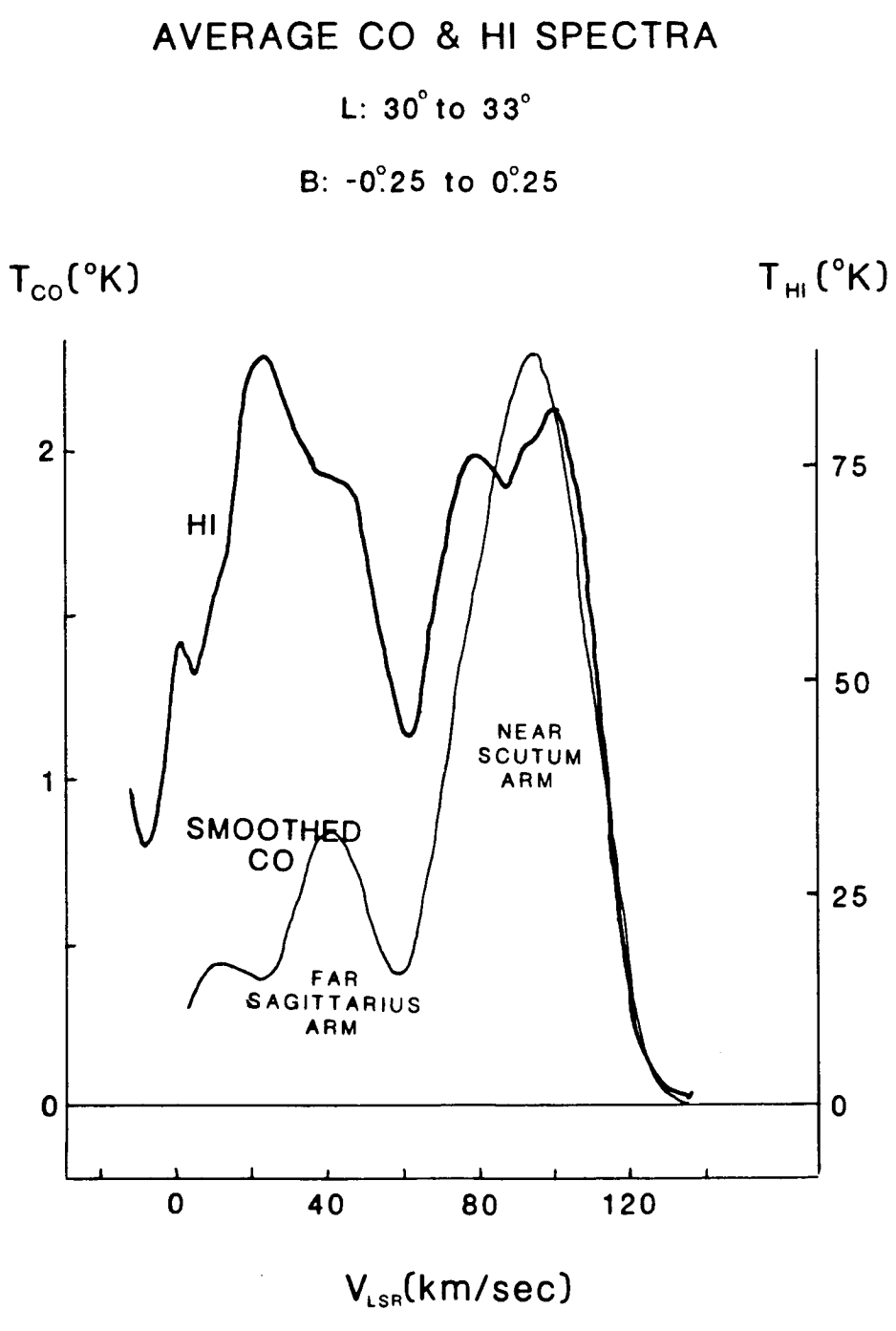
AVERAGE CO & HI SPECTRA
L: 30° to 33°
B: -0°.25 to 0°.25
T_{CO}(°K)
T_{HI}(°K)
2
1
0
75
50
25
0
HI
SMOOTHED CO
NEAR SCUTUM ARM
FAR SAGITTARIUS ARM
0
40
80
120
V_{LSR}(km/sec)

Figure VI-6

MODEL CO DISTRIBUTION

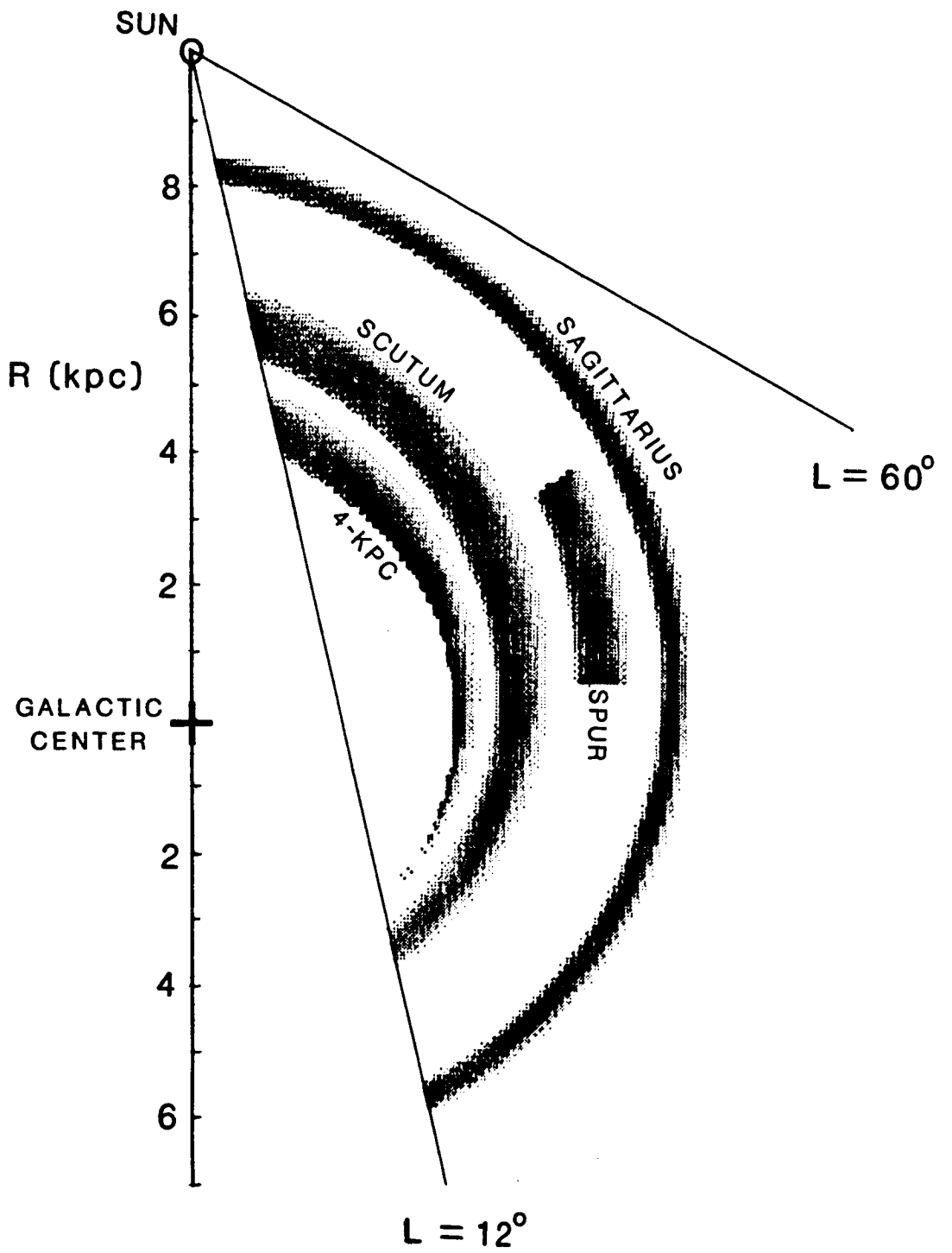

Figure VII-1

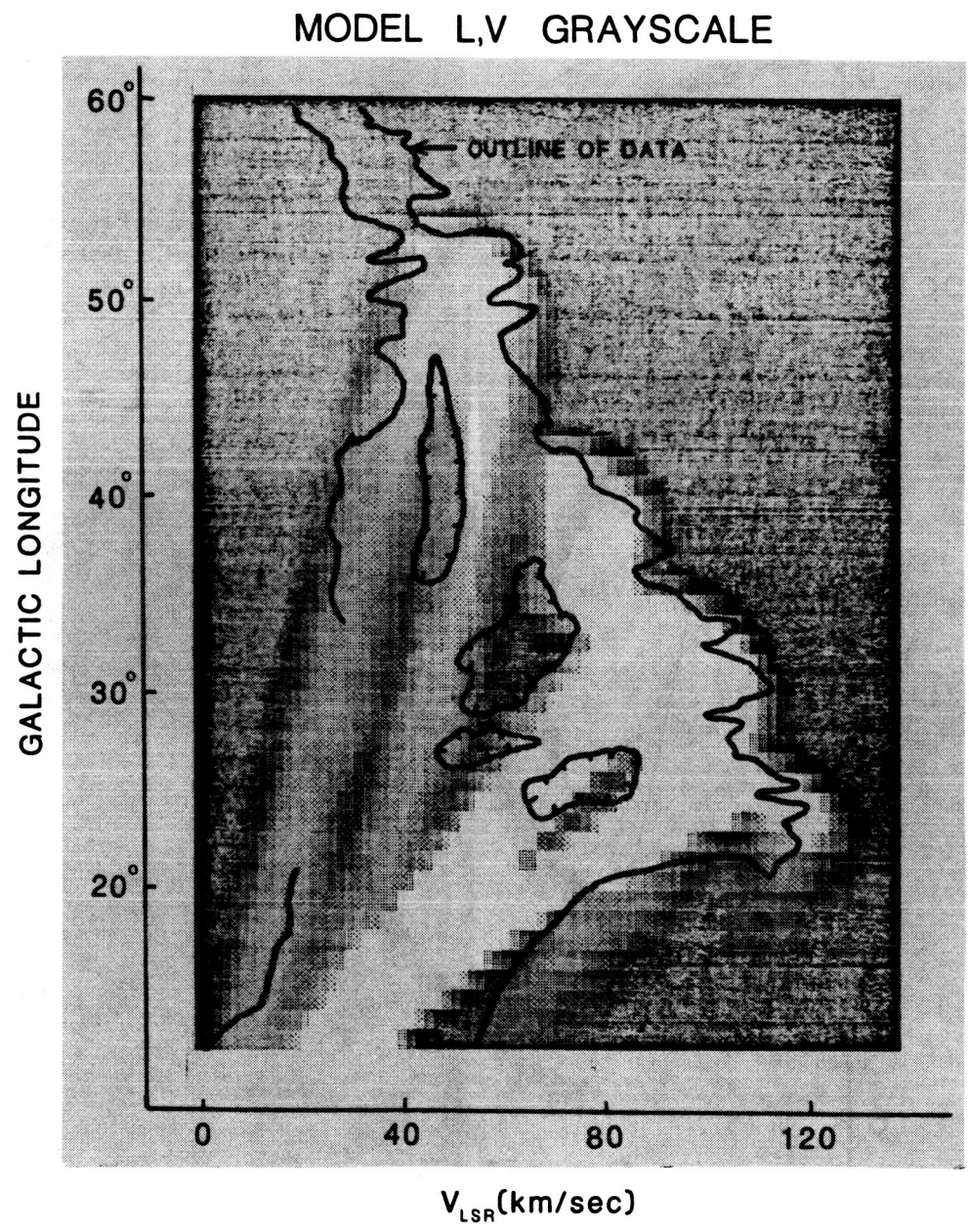
MODEL L,V GRAYSCALE
OUTLINE OF DATA
60°
50°
40°
30°
20°
GALACTIC LONGITUDE
0
40
80
120
V_{LSR}(km/sec)

Figure VII-2

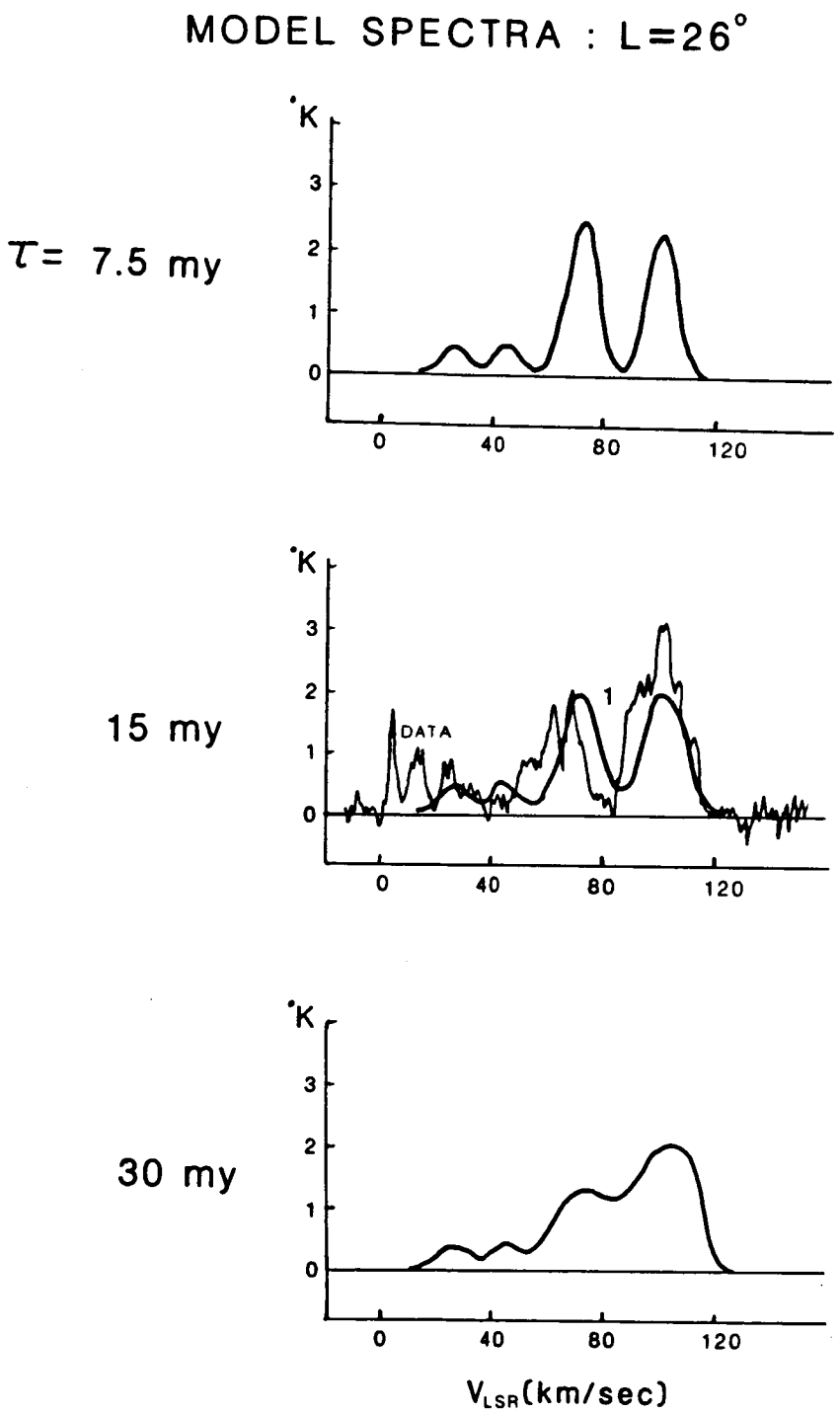

Figure VII-3(a)

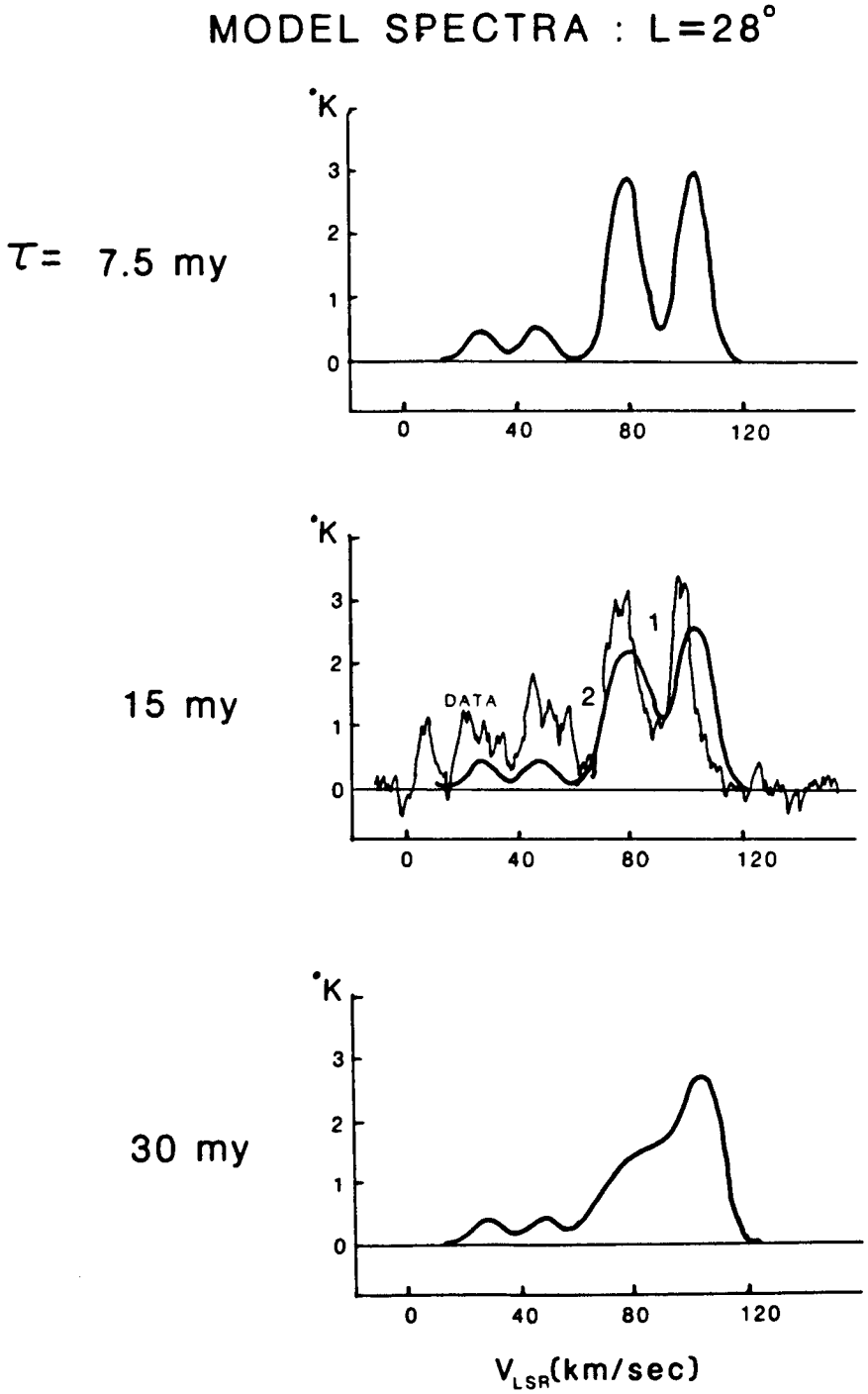

Figure VII-3(b)

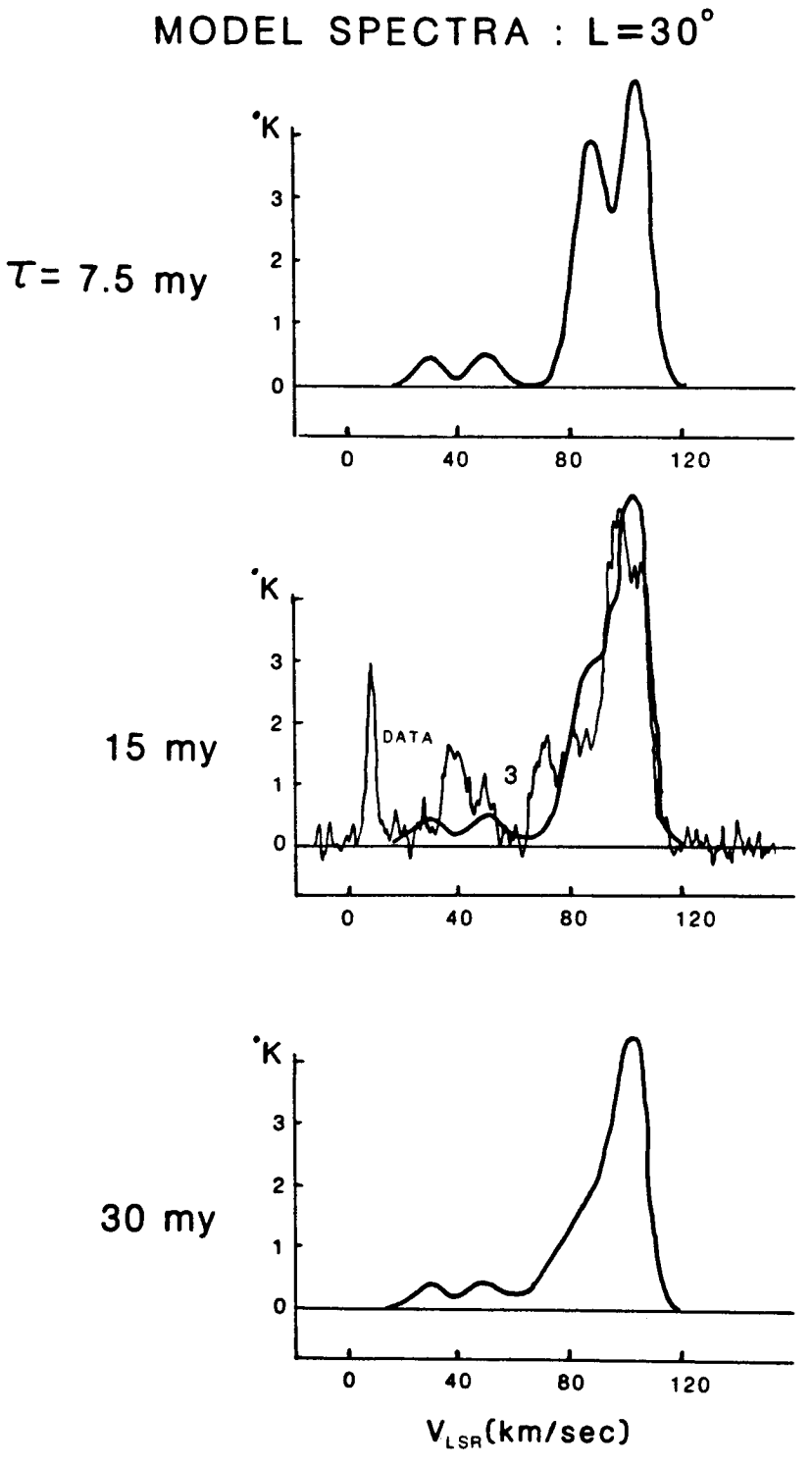

Figure VII-3(c)

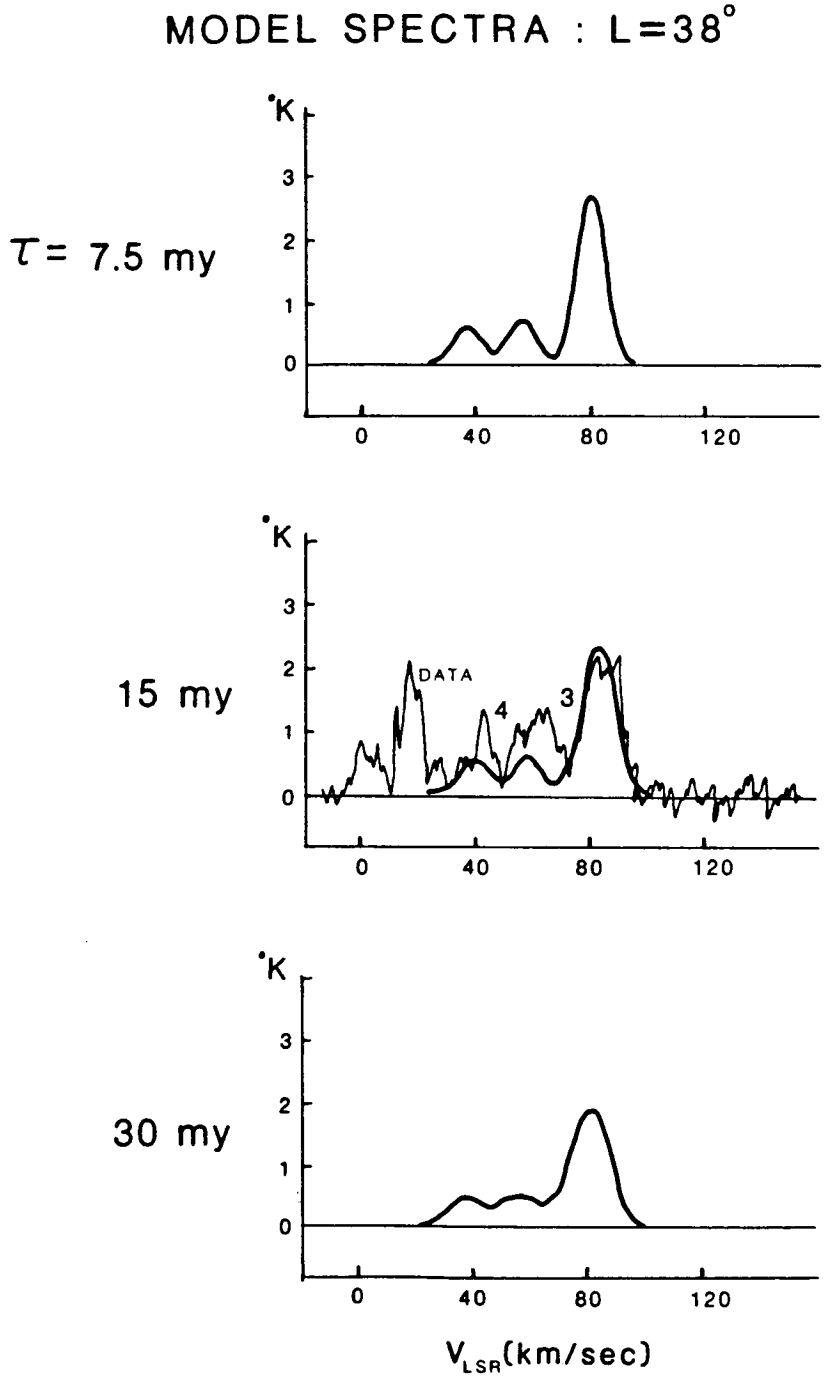

Figure VII-3(d)

τ= 7.5 my

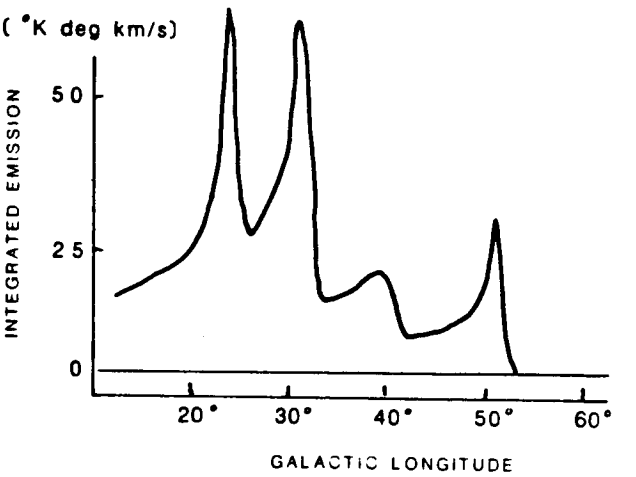

15 my

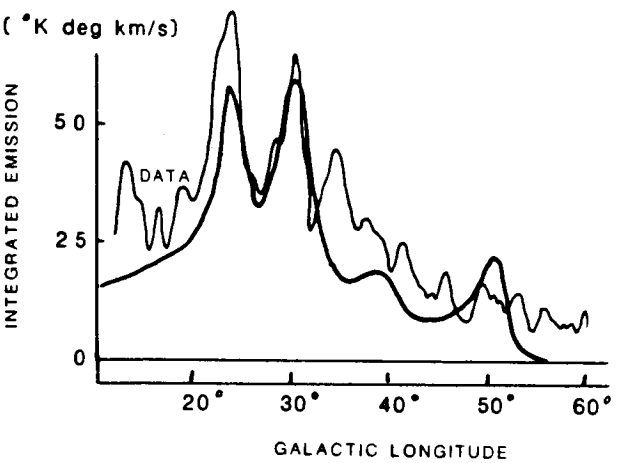

30 my

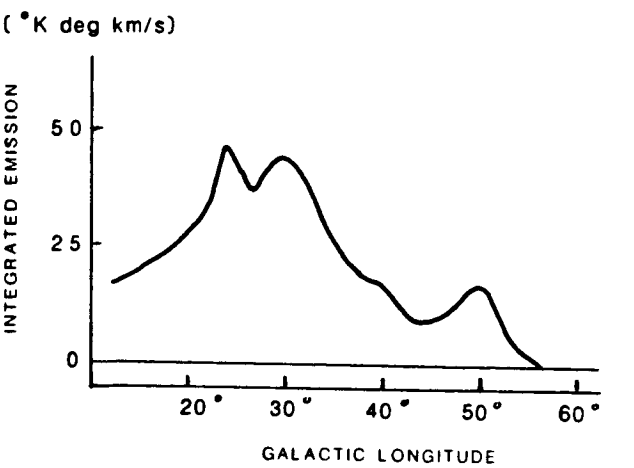

Figure VII-4

τ = 7.5 my

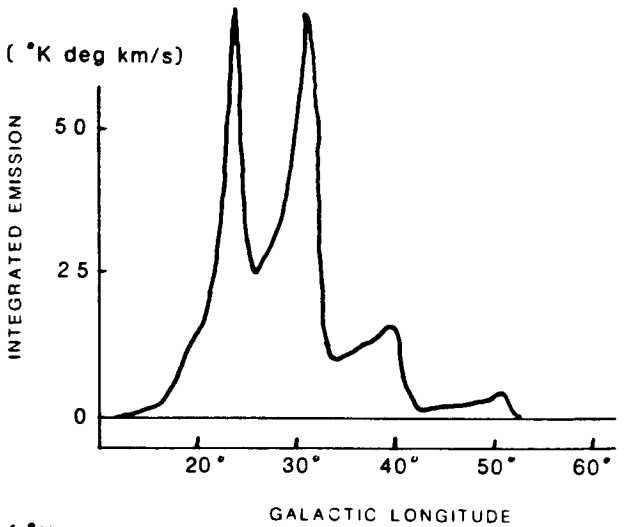

15 my

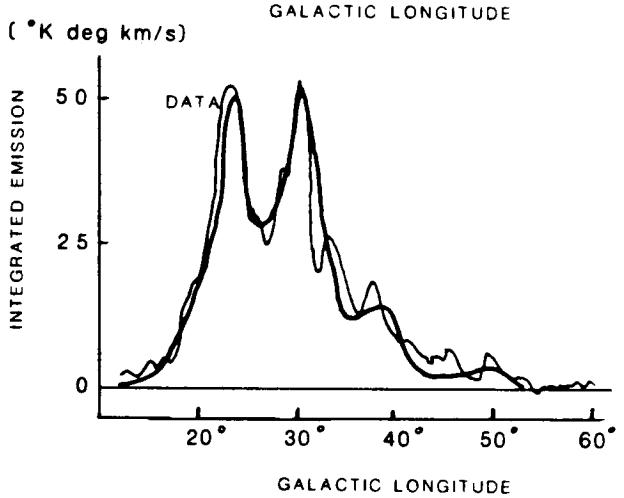

30 my

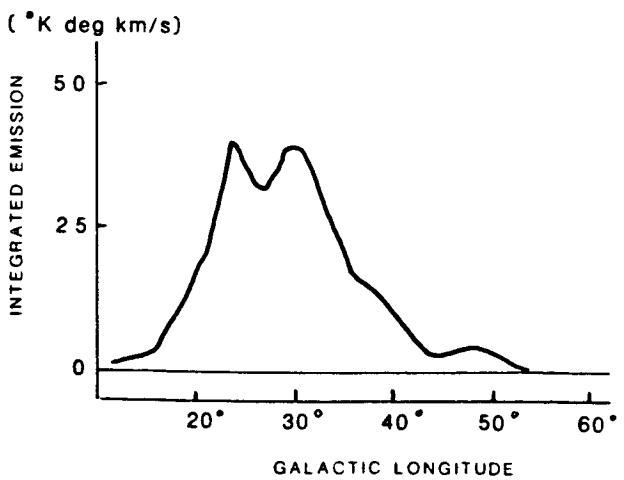

Figure VII-5

τ= 7.5 my

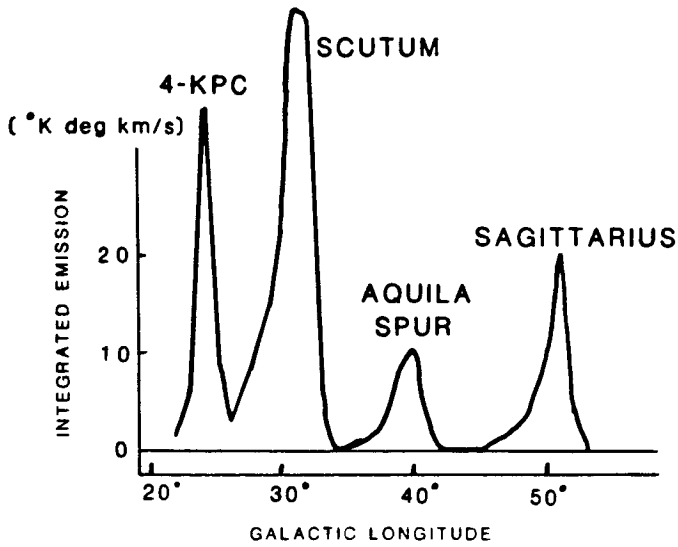

15 my

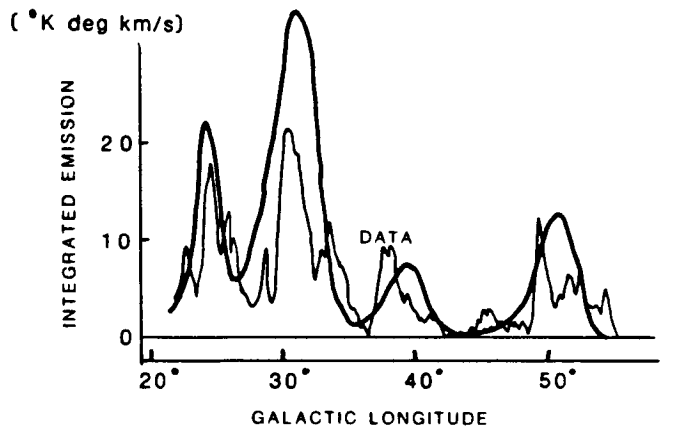

30 my

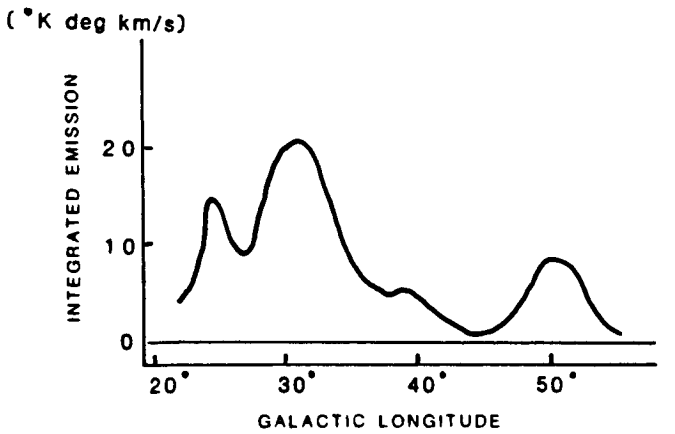

Figure VII-6

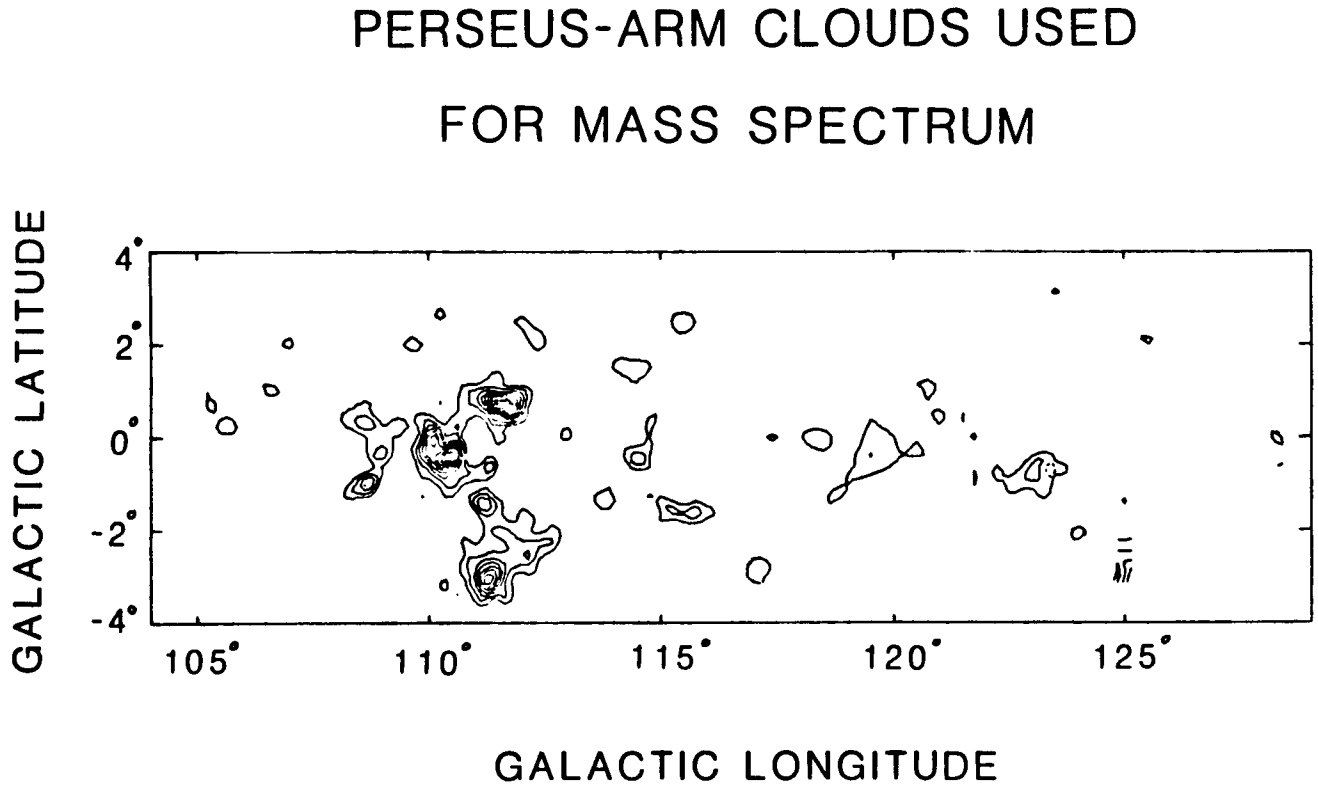

Figure VIII-1

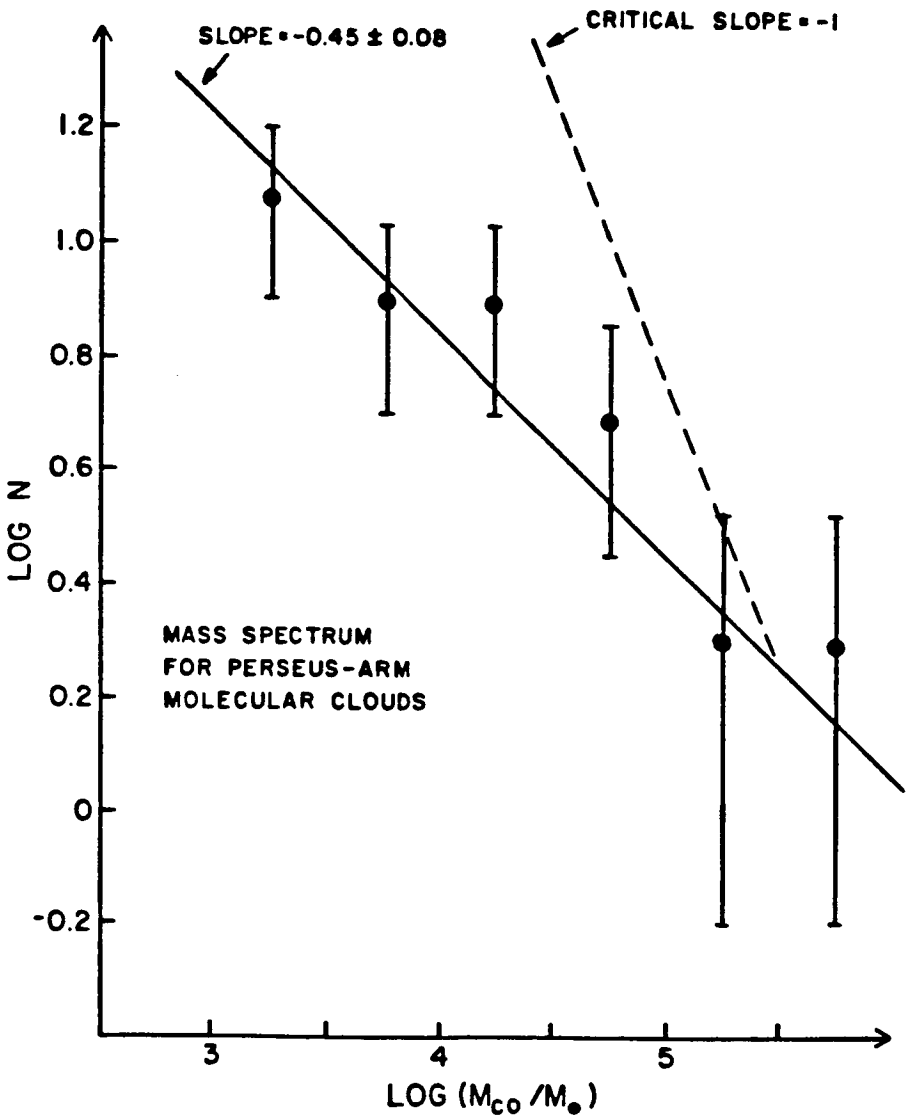

Figure VIII-2

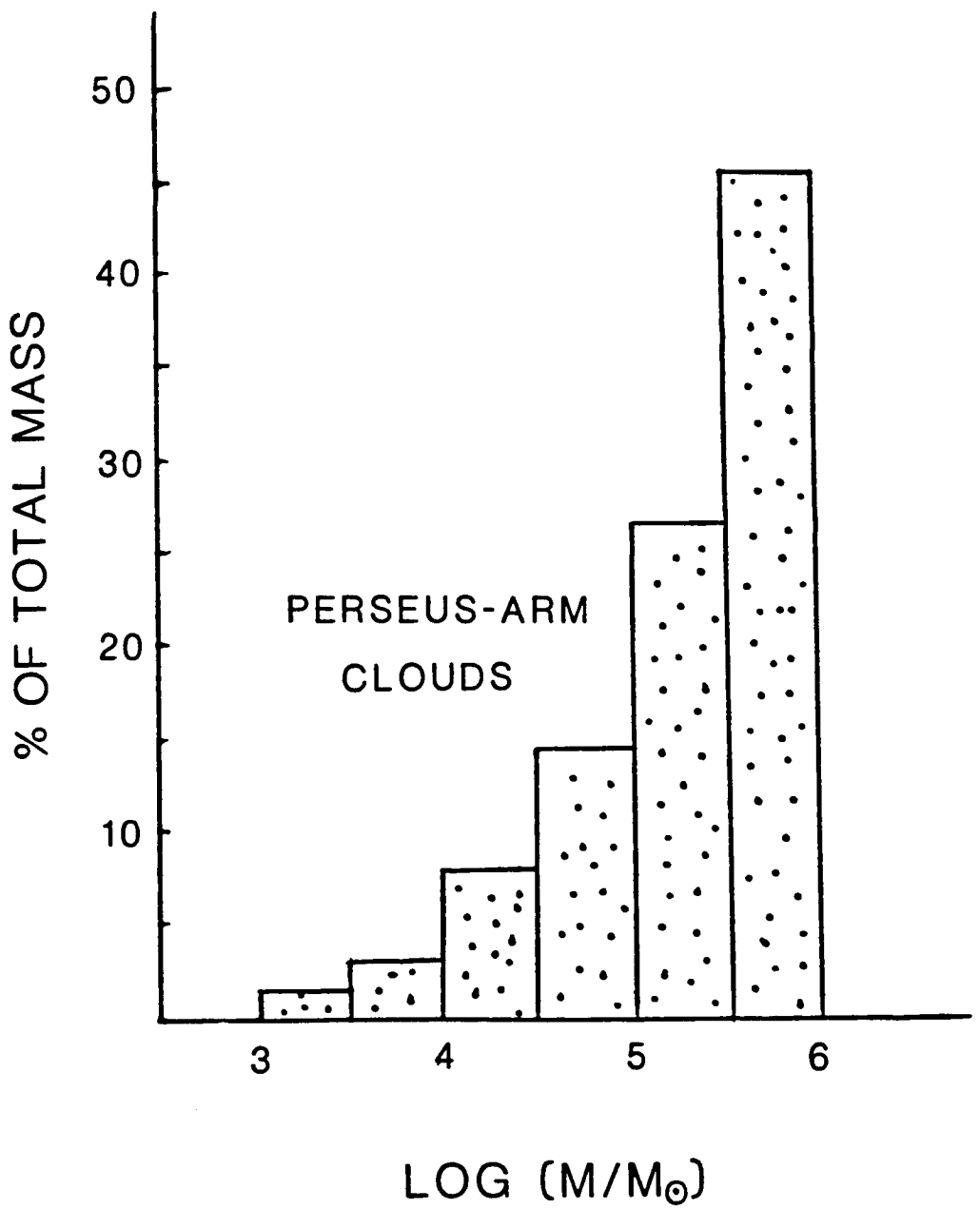

Figure VIII-3

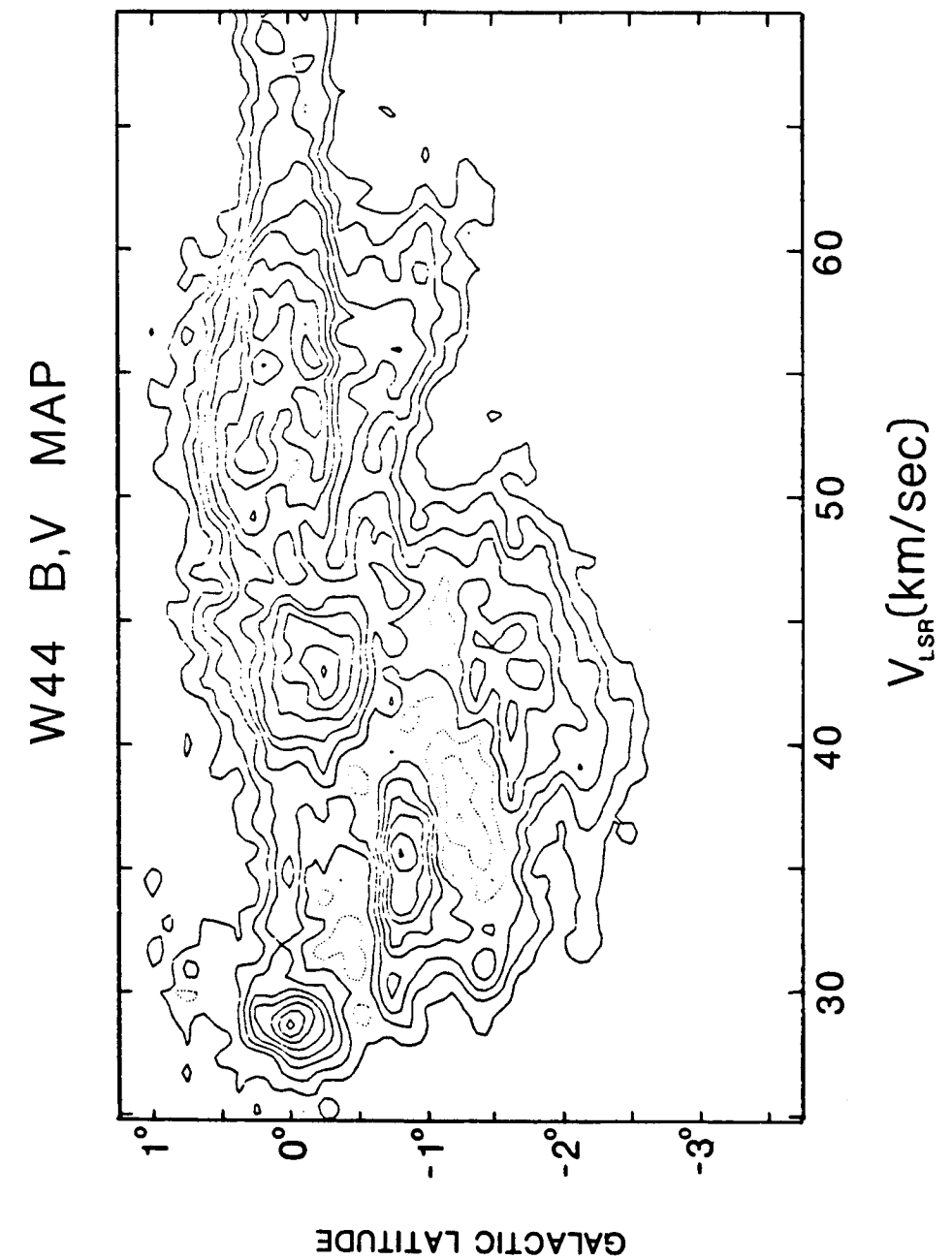

Figure VIII-4

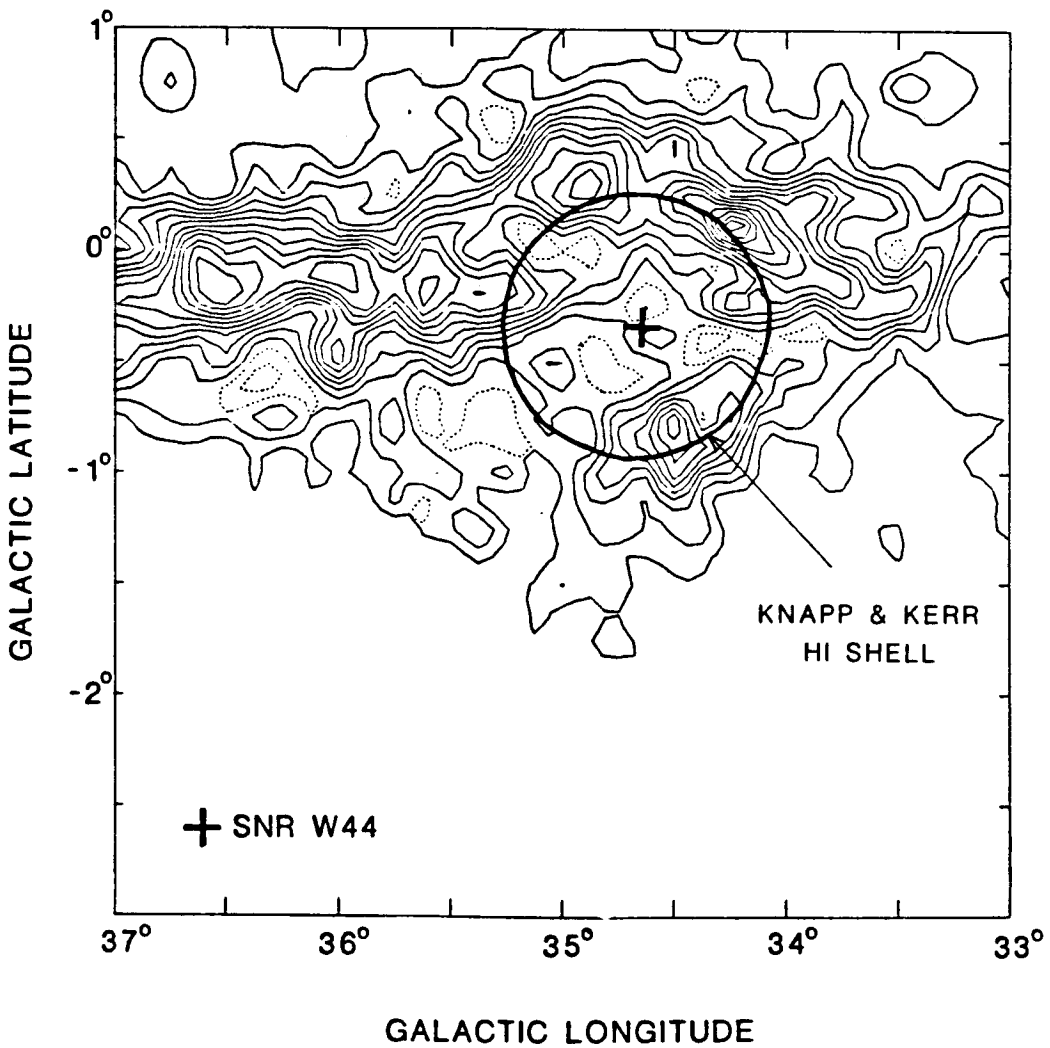

Figure VIII-5

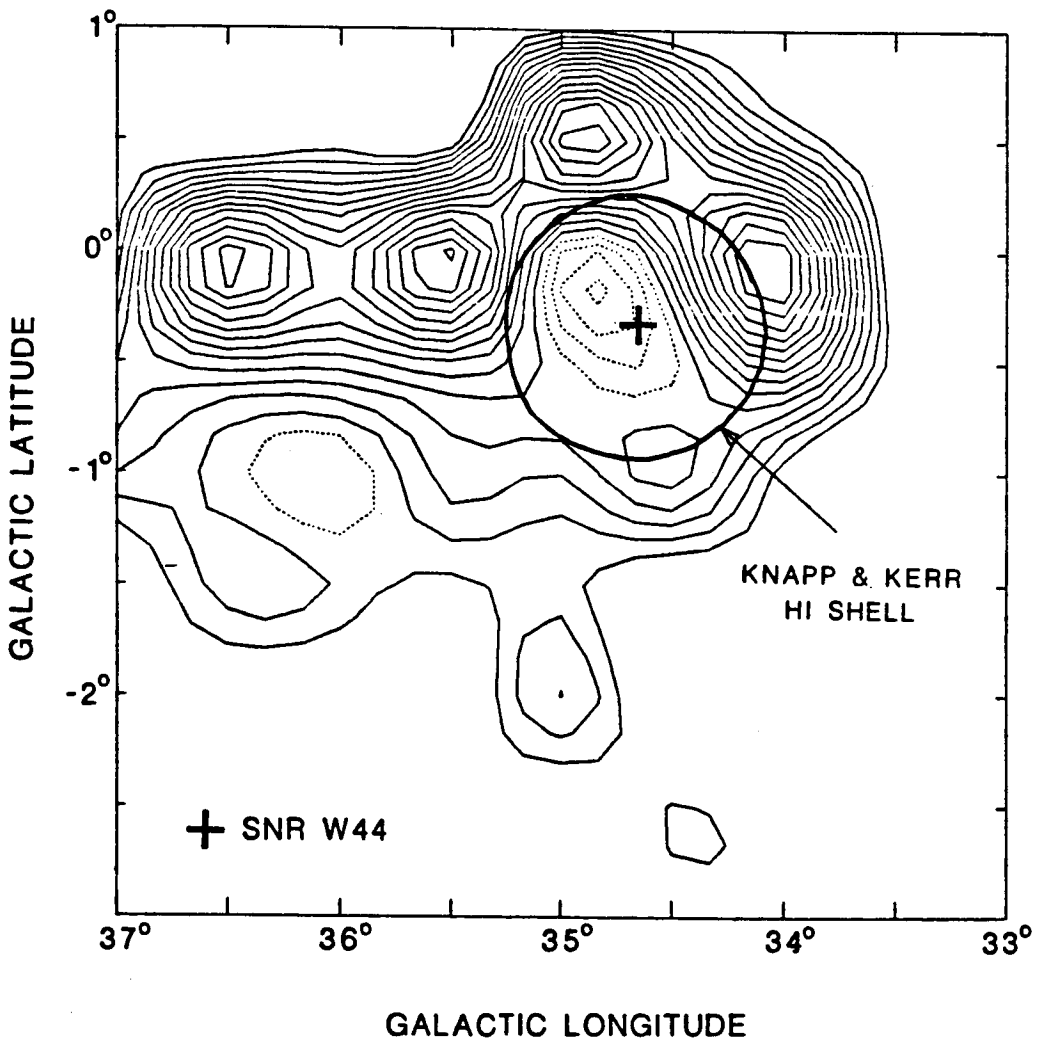

Figure VIII-6

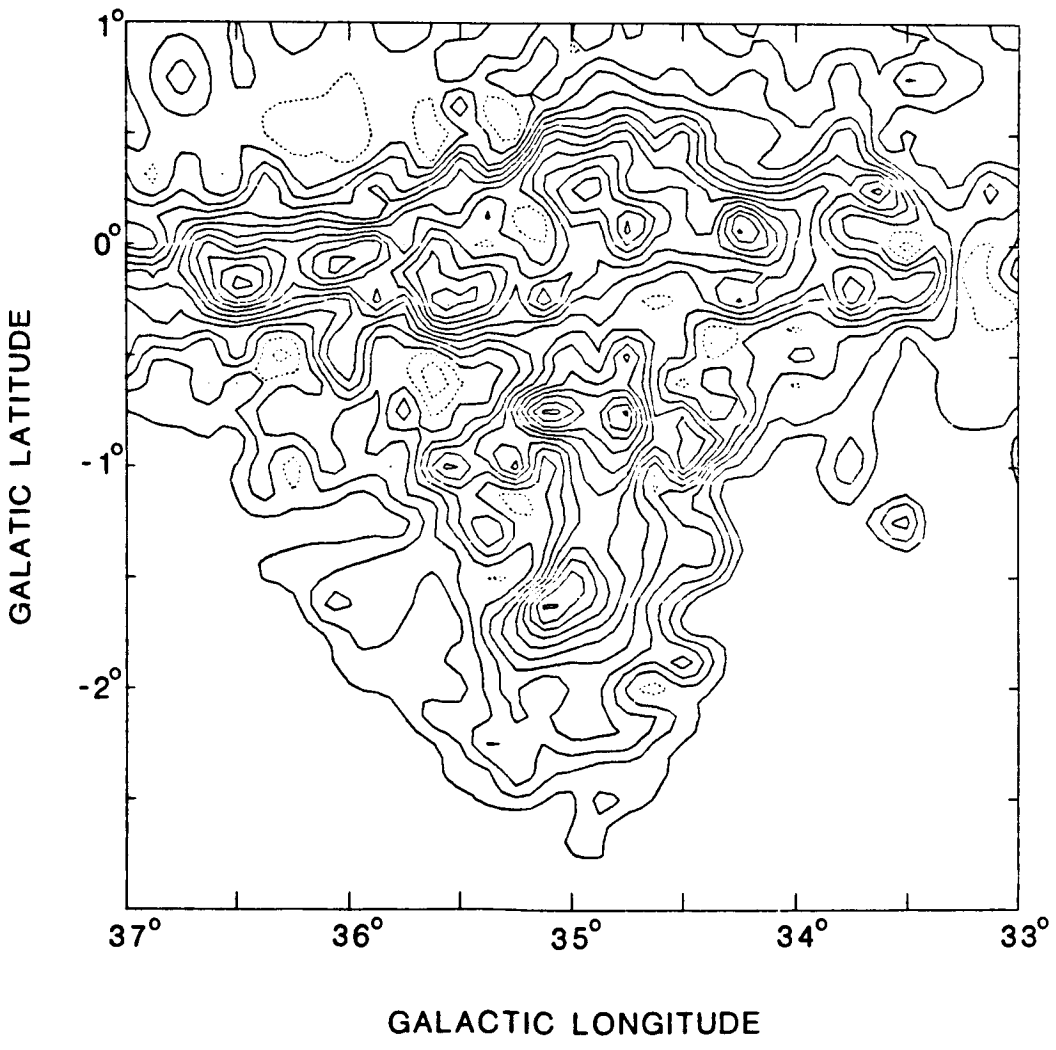

Figure VIII-7

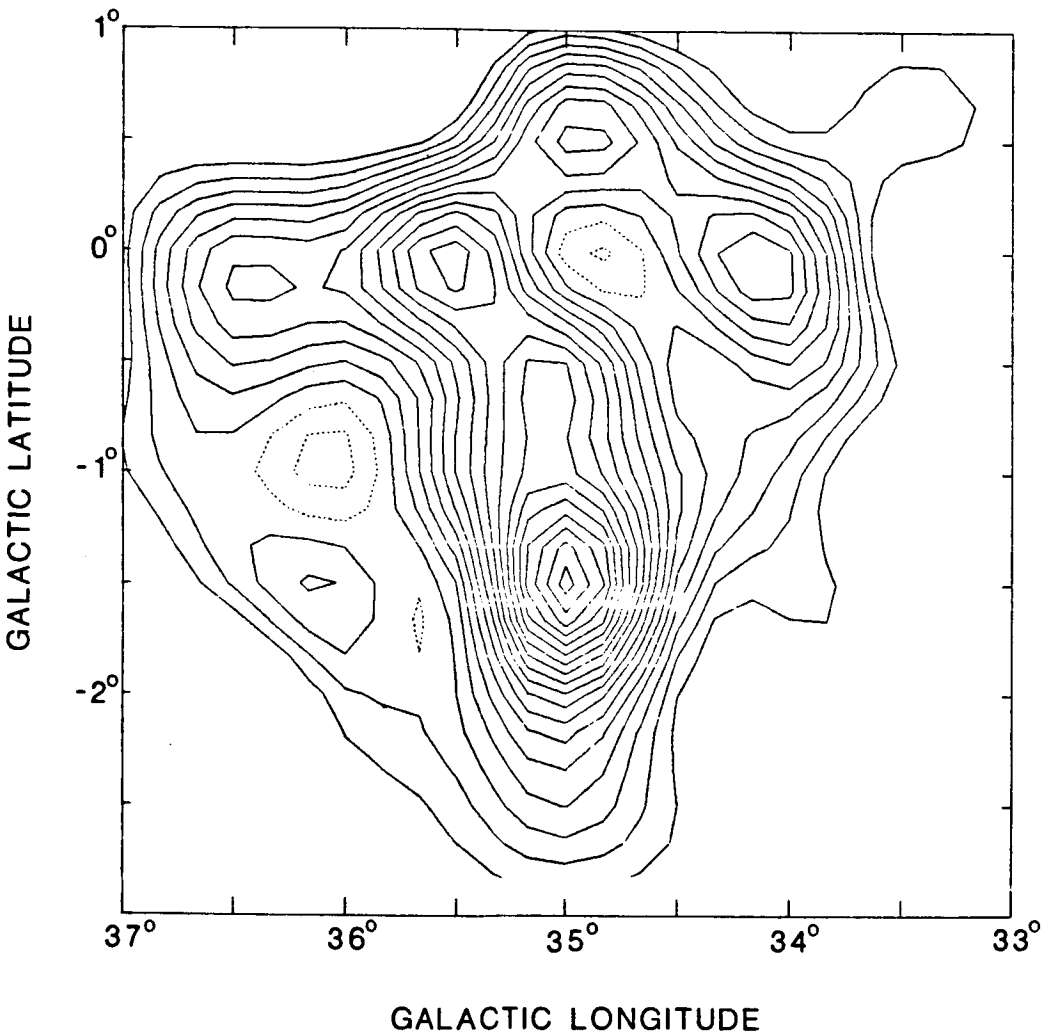

Figure VIII-8

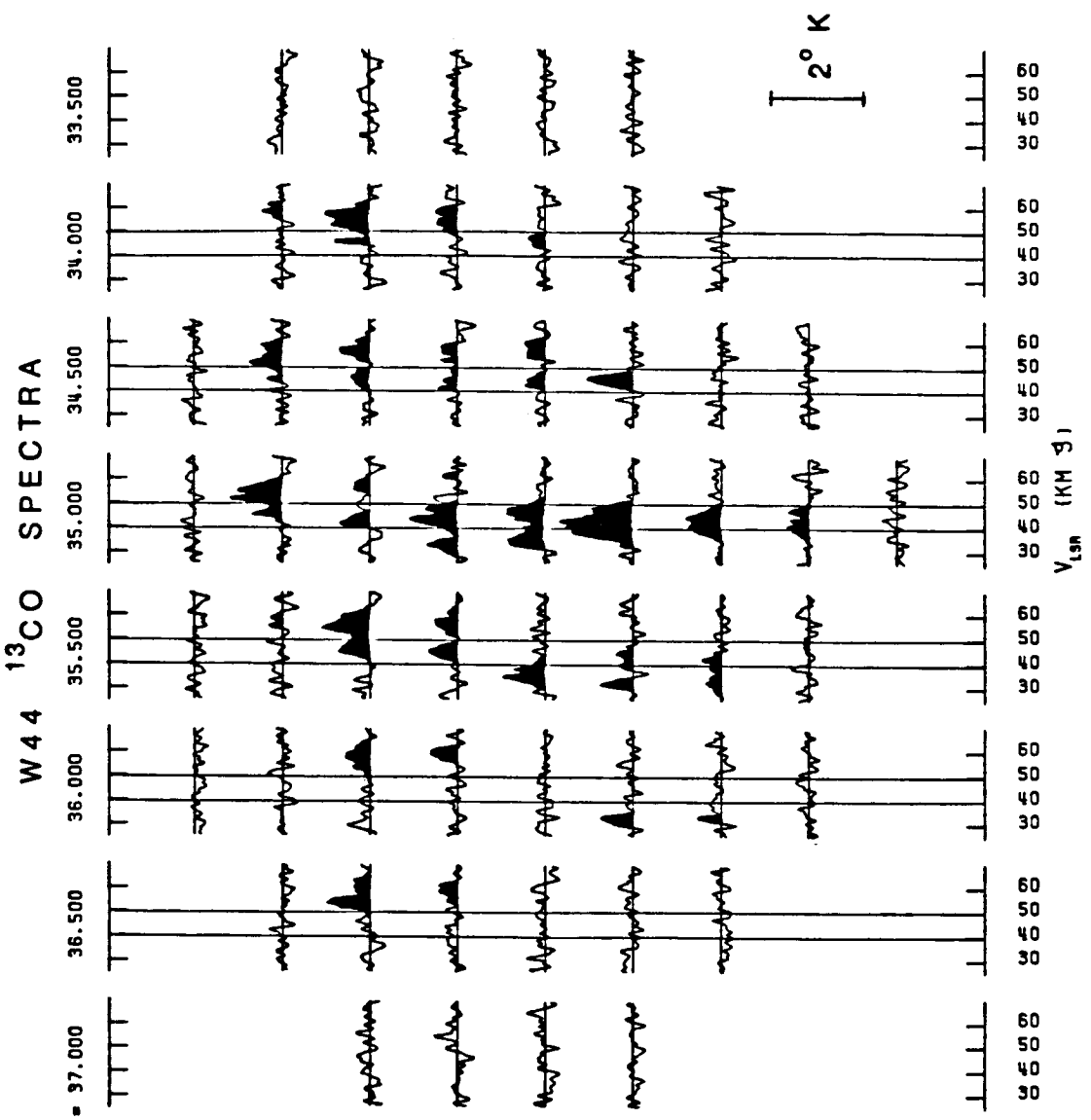

Figure VIII-9

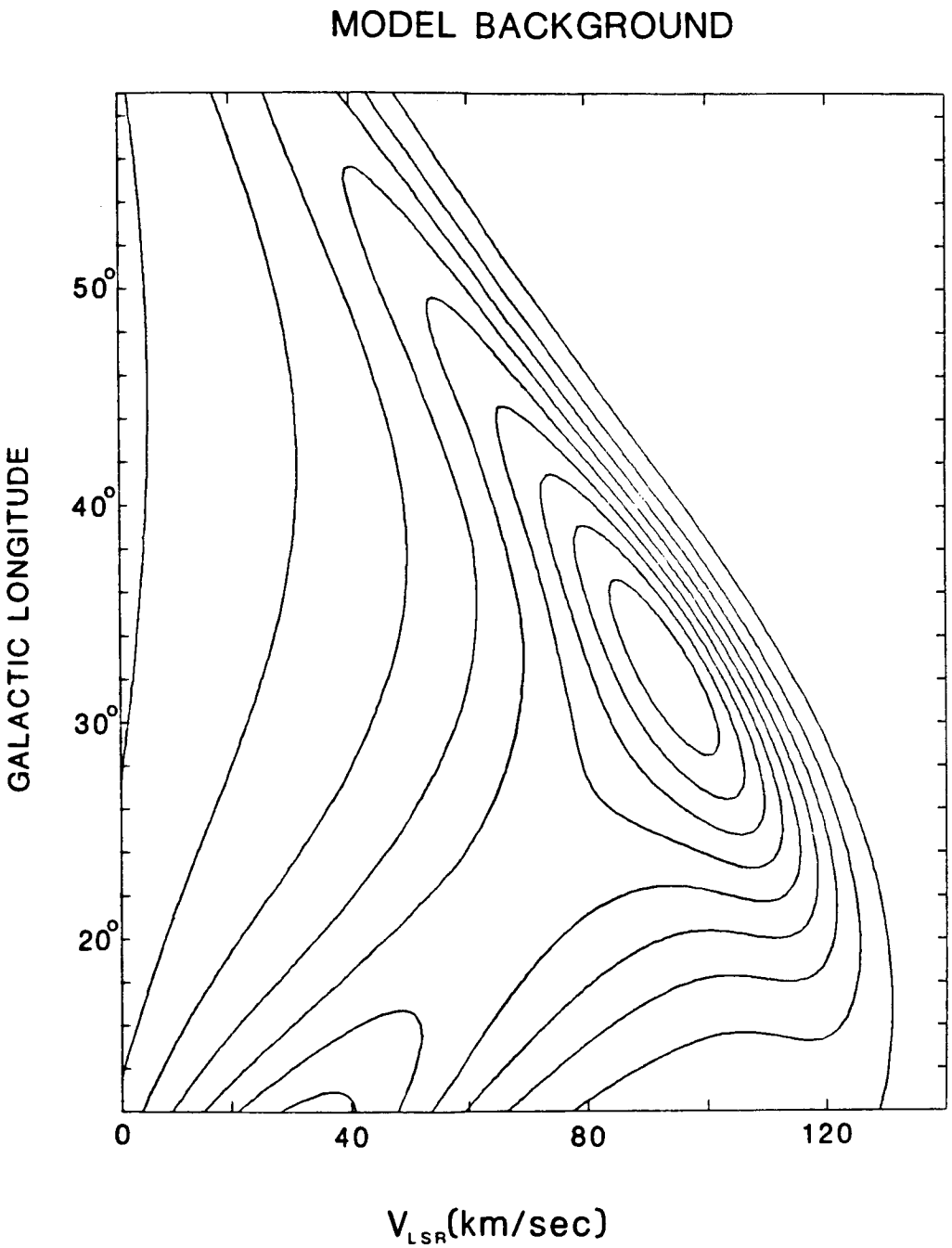

Figure VIII-10

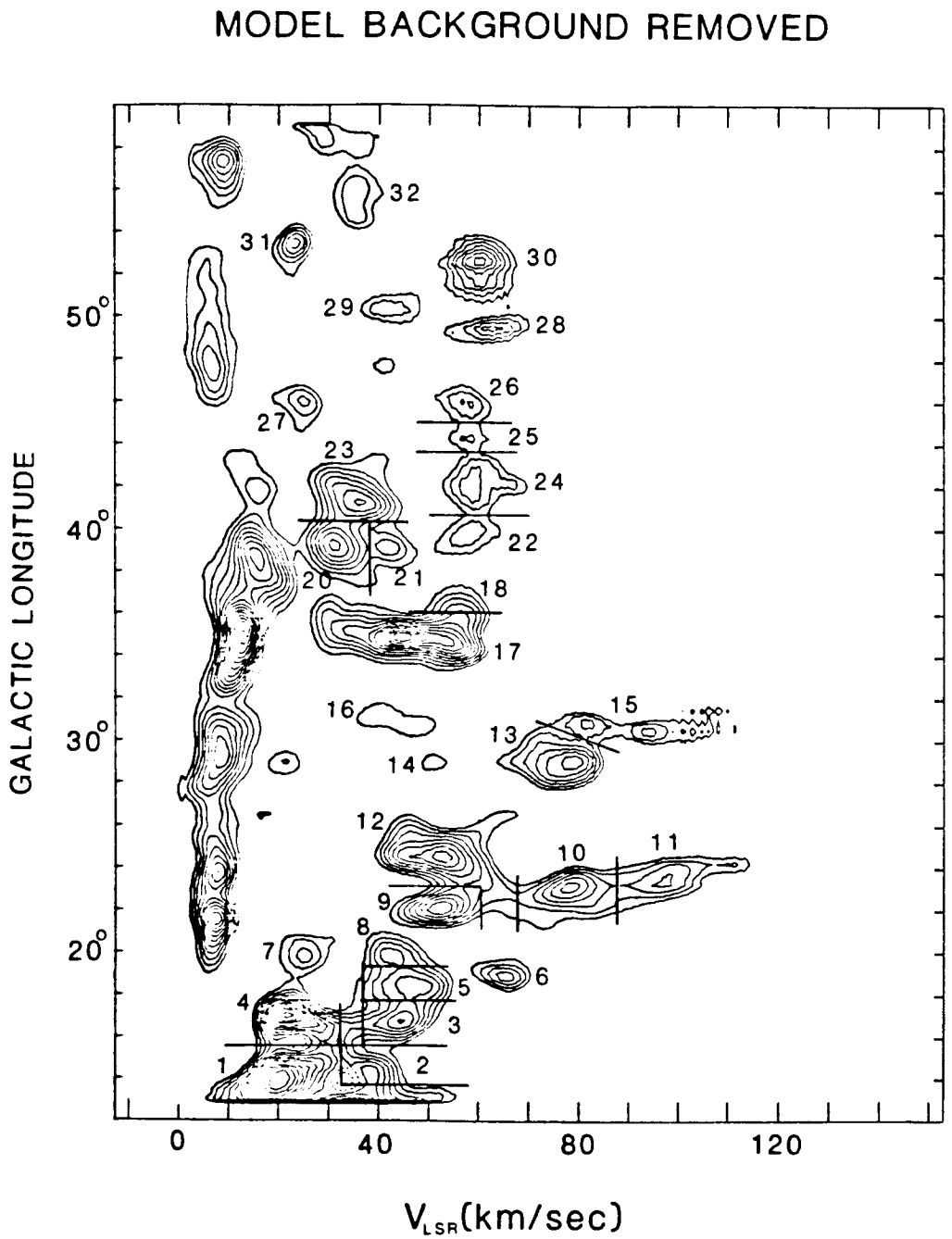

Figure VIII-11

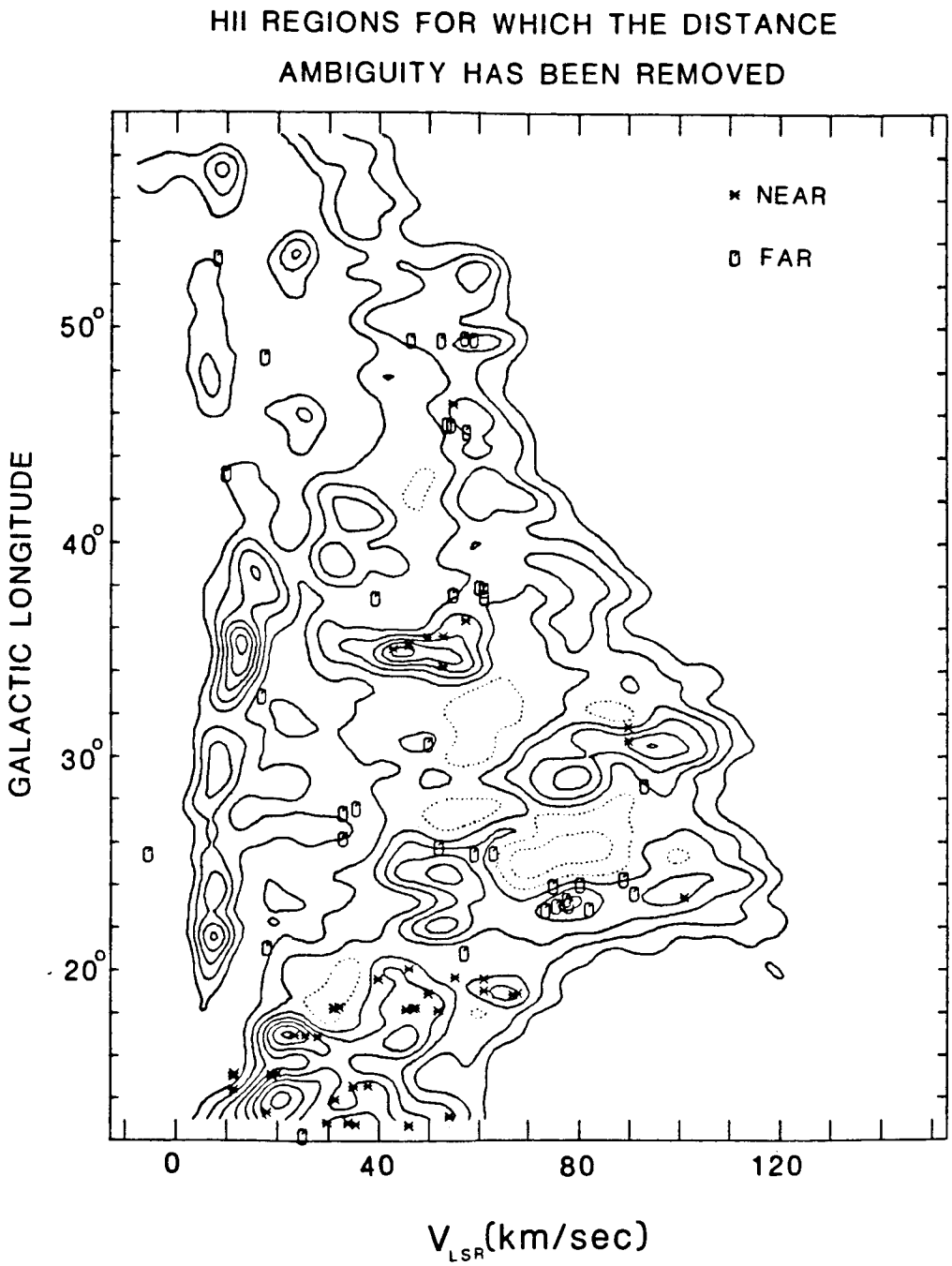

Figure VIII-12

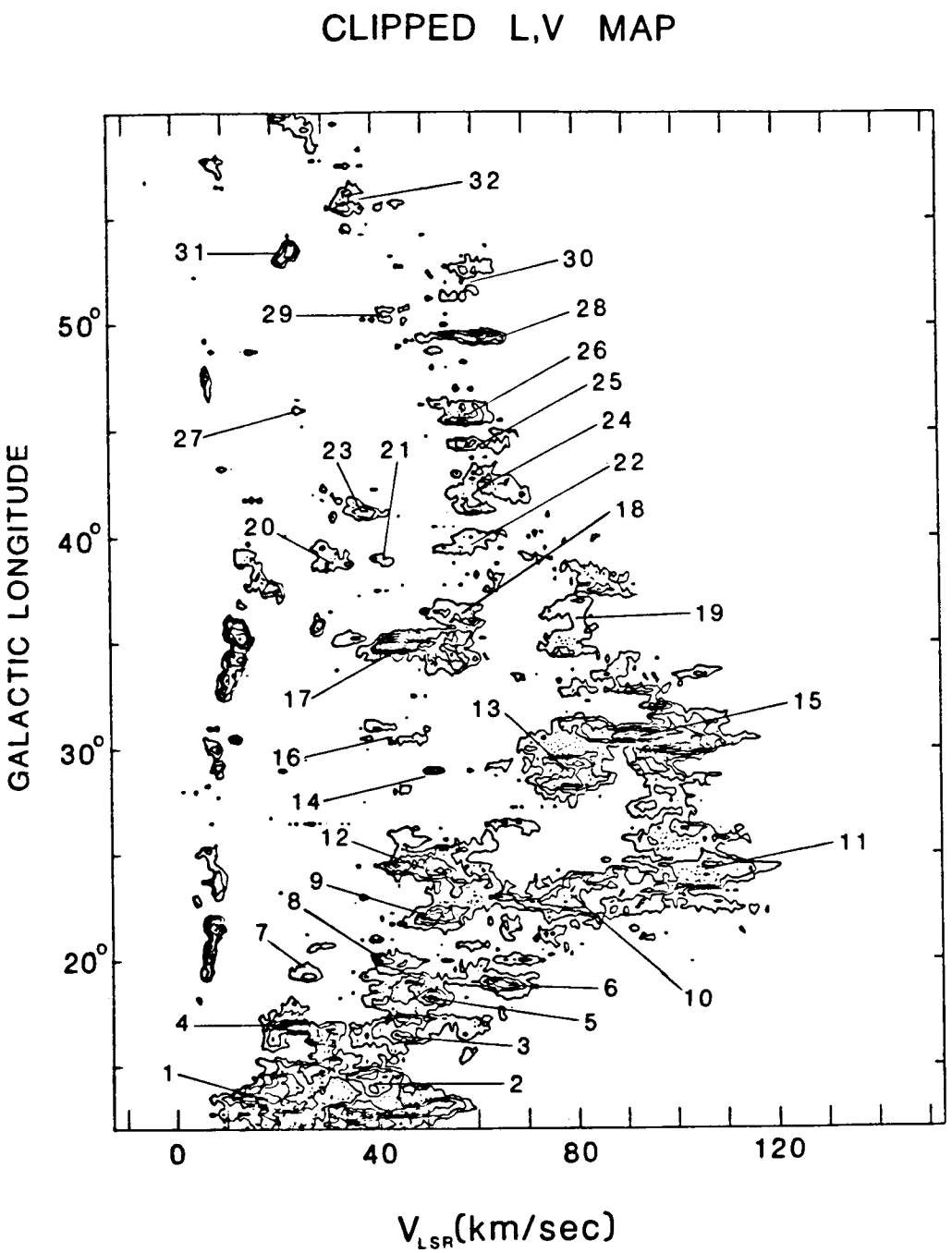

Figure VIII-13

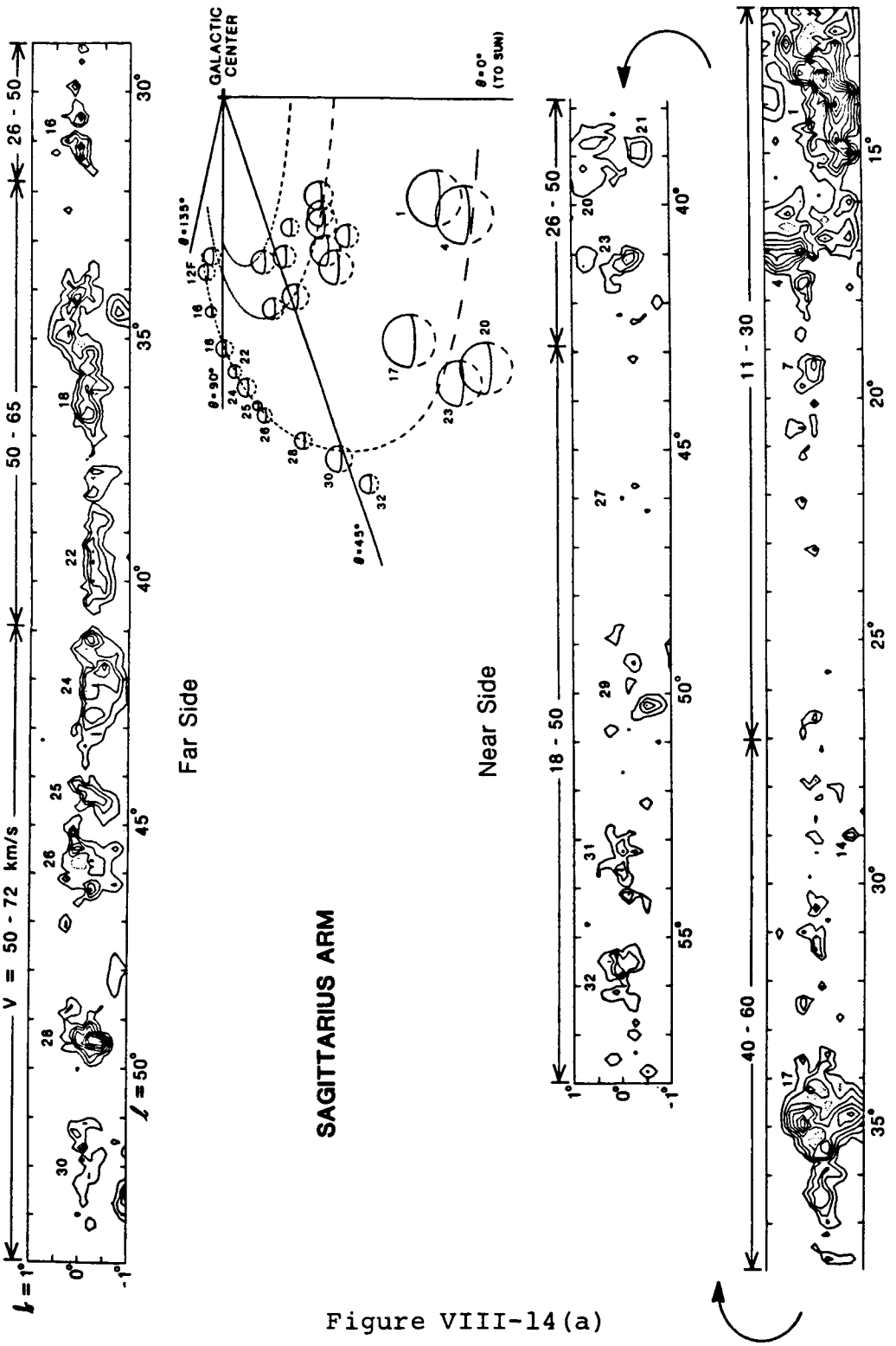

Figure VIII-14(a)

Figure VIII-14(b)

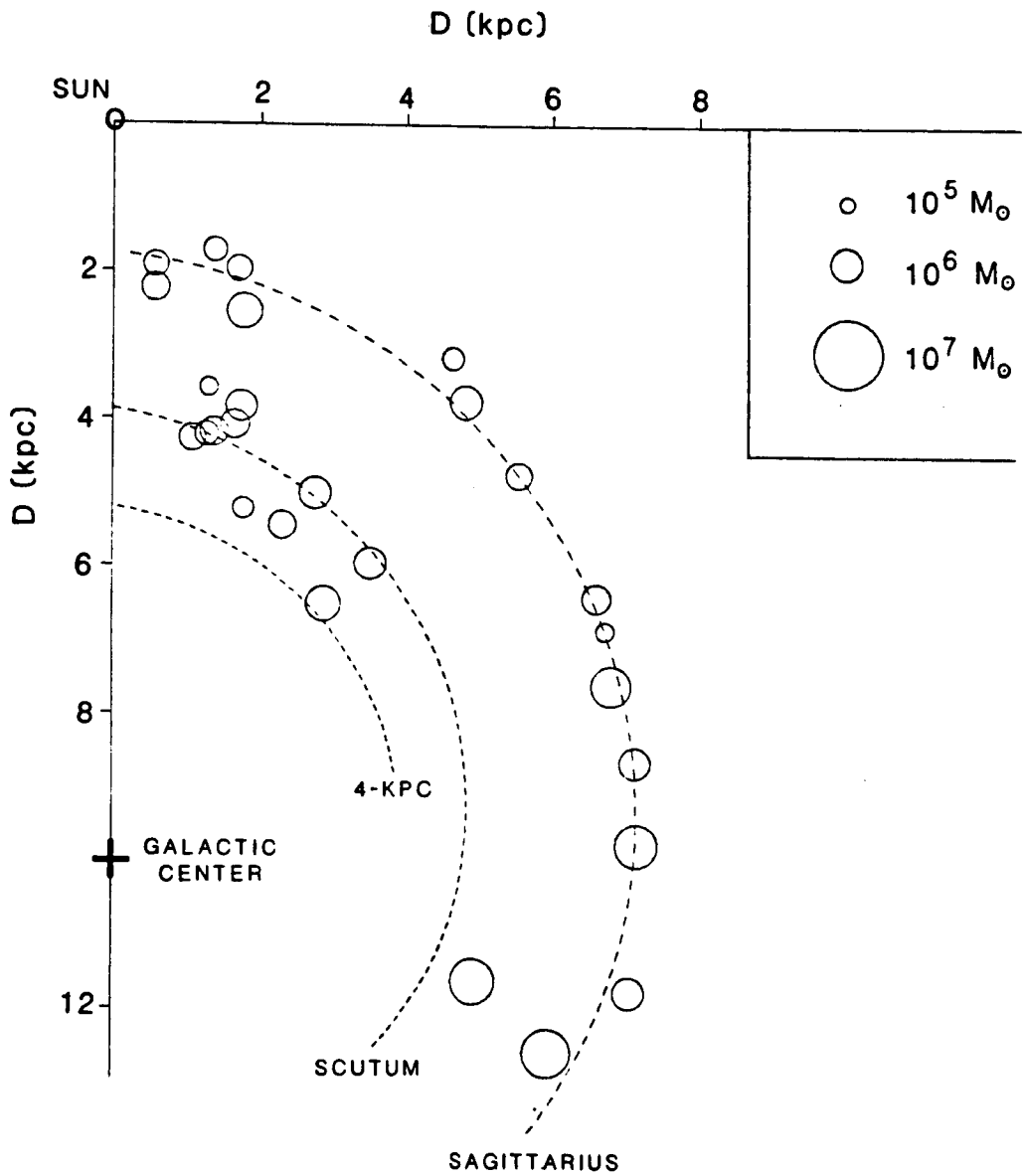

Figure VIII-15

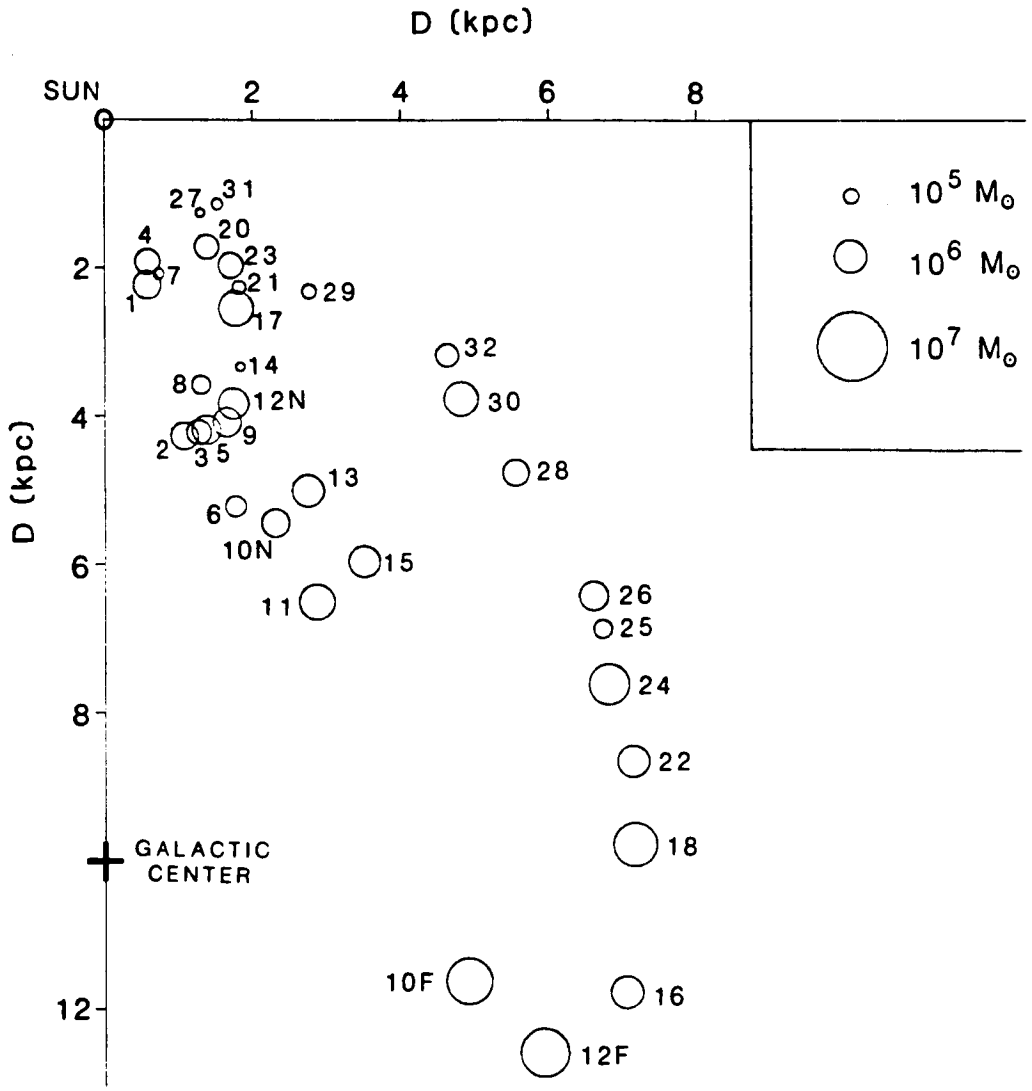

Figure VIII-16

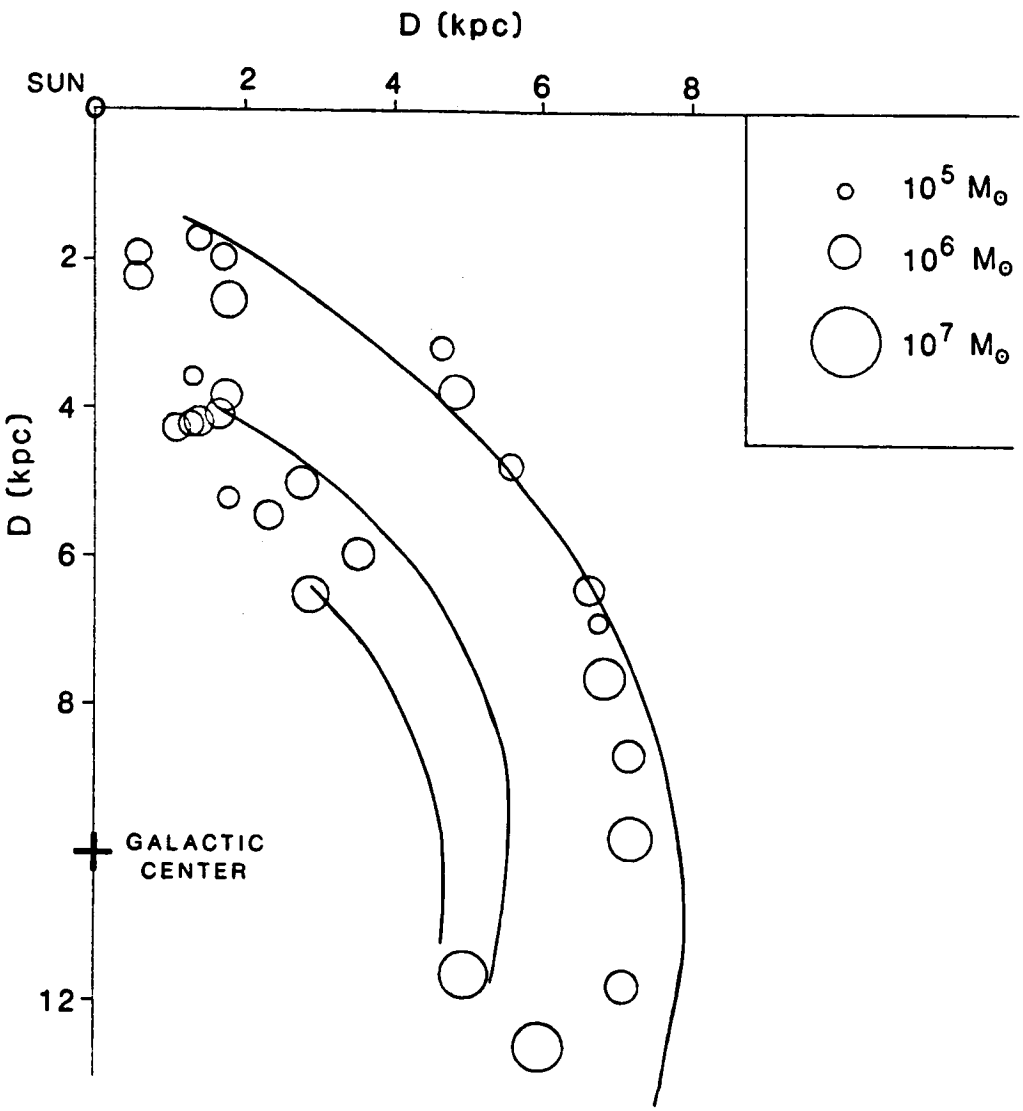

SPIRAL ARMS DETERMINED
FROM HI

Figure VIII-17

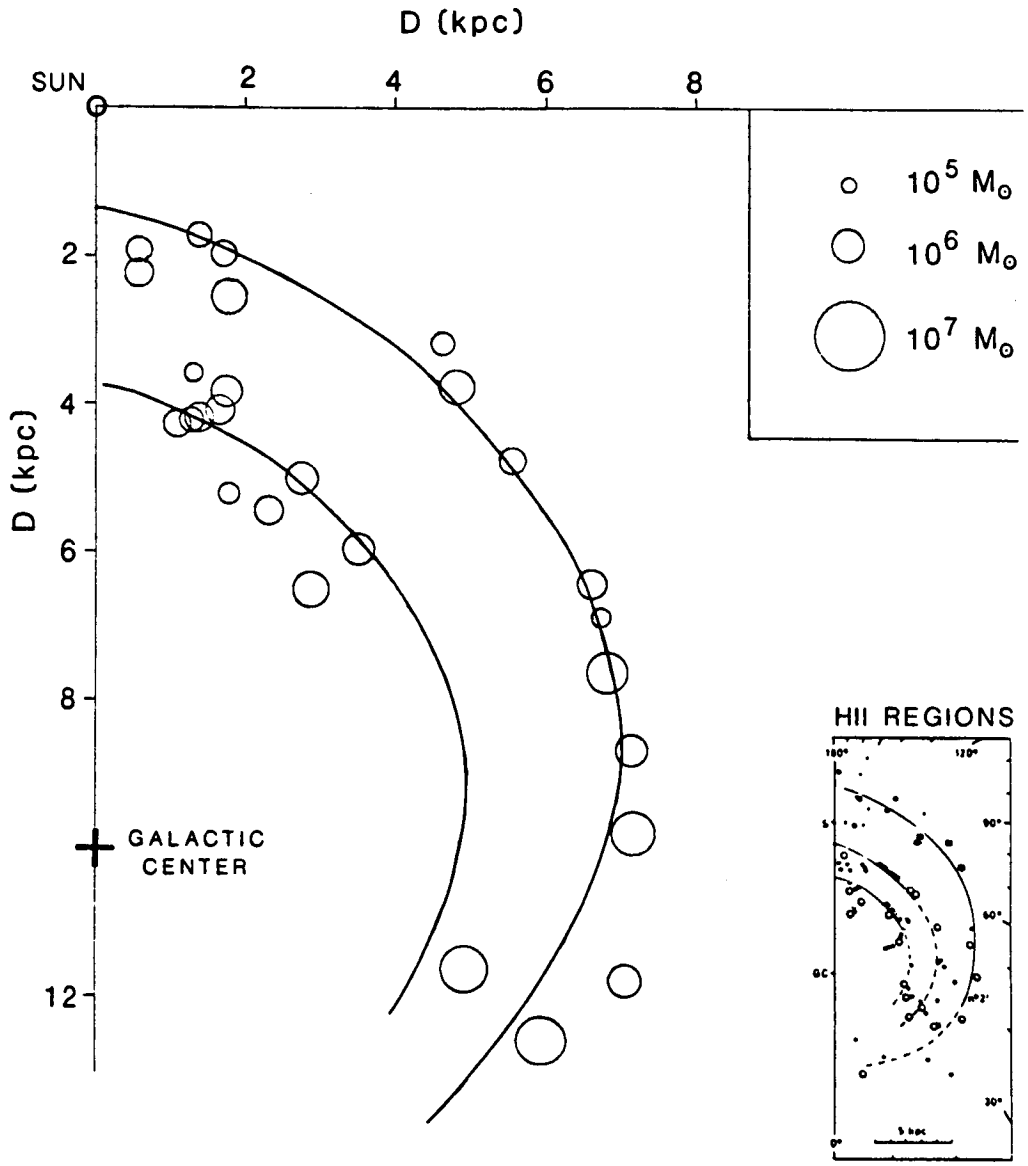

SPIRAL ARMS DETERMINED
FROM HII REGIONS

Figure VIII-18

REFERENCES

Allen, R.J., Goss, W.M. and van Woerden, H., 1973, Astron. Astrophys., 29, 447.

Altenhoff, W.J., Downes, D., Pauls, T. and Schraml, J., 1978, Astron. Astrophys. Suppl. Ser., 35, 23.

Baker, P.L. and Burton, W.B., 1975, Ap. J., 198, 281.

Bania, T.M., 1980, Ap. J., 242, 95.

Bash, F.N. and Peters, W.L., 1976, Ap.J., 205, 786.

Bash, F.N., Green, E. and Peters, W.L., 1977, Ap. J., 217, 464.

Bash, F.N., 1979, Ap. J., 233, 524.

Bash, F.N., Hausman, M. and Papaloizou, J., 1981, Ap. J., 245, 92.

Bignami, G.F., Fichtel, C.E., Kniffen, D.A. and Thompson, D.J., 1975, Ap. J., 199, 54.

Bignell, R.C., 1973, Ap. J., 186, 889.

Blitz, L., 1978, Ph.D. dissertation, Columbia University, published as NASA Tech. Memo. 79708.

Blitz, L., 1980, Giant Molecular Clouds in the Galaxy, ed. P.M. Solomon and M.G. Edmunds (Oxford: Pergamon), p. 1.

Blitz, L. and Shu, F.H., 1980, Ap. J., 238, 148.

Brecher, K. and Burbidge, G., 1972, Ap. J., 174, 253.

Burton, W.B. and Shane, W.W., 1970, IAU Symp. No. 38, The Spiral Structure of Our Galaxy, ed. W. Becker and G. Contopoulos (Dordrecht: Reidel), p. 397.

Burton, W.B., 1971, Astron. Astrophys. 10, 76.

Burton, W.B., Gordon, M.A., Bania, T.M. and Lockman, F.J., 1975, Ap. J., 202, 30.

Burton, W.B. and Gordon, M.A., 1978, Astron. Astrophys., 63, 7.

Burton, W.B., Liszt, H.S. and Baker, P.L., 1978, Ap. J. (Letters), 219, L67.

Cesarsky, C.J., Cassé, M. and Paul, J.A., 1977, Astron. Astrophys., 60, 139.

Cohen, R.S. and Thaddeus, P., 1977, Ap. J. (Letters), 217, L155.

Cohen, R.S., Tomasevich, G.R., and Thaddeus, P., 1979, IAU Symp. No. 84, The Large-Scale Characteristics of the Galaxy, ed. W.B. Burton (Dordrecht: Reidel), p. 53.

Cohen, R.S., 1978, Ph.D. dissertation, Columbia University, published as NASA Tech. Memo. 78071.

Cohen, R.S., Cong, H., Dame, T.M. and Thaddeus, P., 1980, Ap. J. (Letters), 239, L53.

Crampton, D., Georgelin, Y.M. and Georgelin, Y.P., 1978, Astron. Astrophys., 66, 1.

Crawford, D.F., Jauncey, D.L. and Murdoch, H.S., 1970, Ap. J., 162, 405.

Crutcher, R.M., Hartkopf, W.I. and Giguere, P.T., 1978, Ap. J., 226, 839.

Dame, T.M. and Thaddeus, P., 1982, B.A.A.S., 14, No. 2, p. 616.

Dame, T.M., Elmegreen, B.G., Cohen, R.S. and Thaddeus, P., 1983, in preparation.

Davis, J.H. and Vanden Bout, P., 1973, Astrophy. Lett., 15, 43.

Dickel, H.R., 1973, IAU Symp. No. 52, Interstellar Dust and Related Topics, ed. J.M. Greenberg and H.C. van de Hulst (Dordrecht: Reidel), p. 277.

Dickel, J.R., Dickel, H.R. and Crutcher, R.M., 1976, Publ. Astron. Soc. Pac., 88, 840.

Dickey, J., 1981, Proceedings of a Workshop on Extragalactic Molecules held at N.R.A.O., Nov. 2-4, 1981, ed. L. Blitz and M.L. Kutner.

Dickman, R.L., 1975, Ap. J., 202, 50.

Downes, D., Wilson, T.L., Bieging, J. and Wink, J., 1980, Astron. Astrophys. Supp. Ser., 40, 379.

Elmegreen, B.G., Dickinson, D.F. and Lada, C.J., 1978, Ap. J., 220, 853.

Elmegreen, B.G., Lada, C.J. and Dickinson, D.F., 1979, Ap. J., 230, 415.

Elmegreen, B.G. and Elmegreen, D.M., 1979, IAU Symp. No. 84, Interstellar Molecules, ed. B.H. Andrew (Dordrecht: Reidel), p. 191.

Elmegreen, B.G., 1979, Ap. J., 231, 372.

Elmegreen, B.G., 1981, Ap. J., 243, 512.

Elmegreen, B.G. and Elmegreen, D.M., 1983, M.N.R.A.S., 203, 31.

Elmegreen, D.M. and Elmegreen, B.G., 1978, Ap. J., 219, 105.

Encrenaz, P.J., Falgarone, E. and Lucas, R., 1975, Astron. Astrophys. 44, 73.

Evans, N.J., Beckwith, S., Brown, R.L. and Gilmore, W., 1979, Ap. J., 227, 450.

Evans, N.J., Rubin, R.H. and Zuckerman, B., 1980, Ap. J., 239, 839.

Falgarone E. and Lequeux, J., 1973, Astron. Astrophys., 25, 253.

Genzel, R., Downes, D., Schneps, M.H., Reid, M.J., Moran, J.M., Kogan, L.R., Kostenko, V.I., Matveyenko, L.I. and Rönnäng, B, 1981, Ap. J., 247, 1039.

Georgelin, Y.M. and Georgelin, Y.P., 1976, Astron. Astrophys., 49, 57.

Goldreich, P. and Kwan, J., 1974, Ap. J., 189, 441.

Goldsmith, P.F., Plambeck, R.L. and Chiao, R.Y., 1975, Ap. J. (Letters), 196, L39.

Goldsmith, P.F. and Langer, W.D., 1978, Ap. J., 222, 881.

Goodman, F.O., 1978, Ap. J., 226, 87.

Gosachinskii, I.V. and Rakhimov, I.A., 1978, Sov. Astron., 22, 12.

Goss, W.M., Caswell, J.L. and Robinson, B.J., 1971, Astron. Astrophys., 14, 481.

Hayakawa, S., Ito, K., Matsumoto, T. and Uyama, K., 1977, Astron. Astrophys., 58, 325.

Humphreys, R.M., 1976, Publ. Astron. Soc. Pac., 88, 647.

Humphreys, R.M., 1979, IAU Symp. No. 84, The Large-Scale Characteristics of the Galaxy, ed. W.B. Burton (Dordrecht: Reidel), p. 93.

Knapp, G.R., 1974, Astron. J., 79, 541.

Knapp, G.R. and Kerr, F.J., 1974, Astron. Astrophys., 33, 463.

Kodaira, K., 1974, Publ. Astron. Soc. Jpn., 26, 255.

Kutner, M.L., 1978, Astrophy. Lett., 19, 81.

Langer, W.D., 1977, Ap. J. (Letters), 212, L39.

Lebrun, F., Bennett, K., Bignami, G.F., Bloemen, J.B.G.M., Buccheri, R., Caraveo, P.A., Gottwald, M., Hermsen, W., Kanbach, G., Mayer-Hasselwander, H.A., Montmerle, T., Paul, J.A., Sacco, B., Strong, A.W., Wills, R.D., Dame, T.M., Cohen, R.S. and Thaddeus, P., 1982, Ap. J. (Letters), submitted.

Lin, C.C., Yuan, C. and Shu, F.H., 1969, Ap. J., 155, 721.

Lindblad, P.O., 1967, Bull. Astron. Inst. Neth., 19, 34.

Lindblad, P.O., Grape, K., Sandquist, Aa. and Schober, J., 1973, Astron. Astrophys., 24, 309.

Liszt, H.S. and Burton, W.B., 1981, Ap. J., 243, 778.

Liszt, H.S., 1982, Ap. J., 262, 198.

Lockman, F.J., 1976, Ap. J., 209, 429.

Lockman, F.J., 1979a, IAU Symp. No. 84, The Large-Scale Characteristics of the Galaxy, ed. W.B. Burton (Dordrecht: Reidel), p. 73.

Lockman, F.J., 1979b, Ap. J., 232, 761.

Lynden-Bell, D. and Kalnajs, A.J., 1972, M.N.R.A.S., 157, 1.

Lynds, B.T., 1970, IAU Symp. No. 38, The Spiral Structure of our Galaxy, ed. W. Becker and G. Contopoulos (Dordrecht: Reidel), p. 26.

Maddalena, R.J., Morris, M., Moscowitz, J. and Thaddeus, P., 1983, in preparation.

Mauzy, B., 1974, NRAO Electronics Division Internal Report, No. 146.

Milne, D.K., 1979, Aust. J. Phys., 32, 83.

Moore, C.H. and Rather, E.D., 1973, Proc. IEEE, 61, 1346.

Moorwood, A.F.M. and Salinari, P., 1981, Astron. Astrophys., 94, 299.

Morgan, W.W., Sharpless, S. and Osterbrock, D., 1952, Astron. J., 57, 3.

Morris, M. and Rickard, L.J., 1982, Ann. Rev. Astron. Astrophys., 20, 517.

Parker, E.N., 1966, Ap. J., 145, 811.

Parker, E.N., 1969, Space Sci. Rev., 9, 654.

Pashchenko, M.I., 1977, Sov. Astron., 21, 164.

Penzias, A.A. and Burrus, C.A., 1973, Ann. Rev. Astron. Astrophys., 11, 51.

Radhakrishnan, V., 1974, IAU Symp. No. 60, Galactic Radio Astronomy, ed. F.J. Kerr and S.C. Simonson (Dordrecht: Reidel), p. 3.

Roberts, W.W., 1969, Ap. J., 158, 123.

Roberts, W.W., Roberts, M.S. and Shu F.H., 1975, Ap. J., 196, 381.

Rots, A.H. and Shane, W.W., 1974, Astron. Astrophys., 31, 245.

Sandage, A., 1961, The Hubble Atlas of Galaxies, Publ. 618, Carnegie Institution of Washington.

Sanders, R.H. and Bania, T.M., 1976, Ap. J., 204, 341.

Scoville, N.Z. and Solomon, P.M., 1975, Ap. J. (Letters), 199, L105.

Scoville, N.Z. and Hersh, K., 1979, Ap. J., 229, 578.

Scoville, N.Z., Solomon, P.M. and Sanders D.B., 1979, IAU Symp. No. 84, The Large-Scale Characteristics of the Galaxy, ed. W.B. Burton (Dordrecht: Reidel), p. 277.

Shane, W.W., 1972, Astron. Astrophys., 16, 118.

Shu, F.H., 1973, American Scientist, 61, 524.

Silver, S. ed., 1964, Microwave Antenna Theory and Design, MIT Radiation Laboratory Series v. 12, Boston Technical Publishers, Inc.

Solomon, P.M., Sanders, D.B. and Scoville, N.Z., 1979, IAU Symp. No. 84, The Large-Scale Characteristics of the Galaxy, ed. W.B. Burton (Dordrecht: Reidel), p. 35.

Solomon, P.M. and Sanders, D.B., 1980, Giant Molecular Clouds in the Galaxy, ed. P.M. Solomon and M.G. Edmunds (Oxford: Pergamon), p. 41.

Solomon, P.M., 1982, Molecules in Interstellar Space, ed. A. Carrington and D.A. Ramsay (Cambridge: Royal Society), p. 480.

Stark, A.A., 1979, Ph.D. dissertation, Princeton University.

Stecker, F.W., Solomon, P.M., Scoville, N.Z. and Ryter, C.E., 1975, Ap. J., 201, 90.

Stecker, F.W., 1977, Ap. J., 212, 60.

Strong, A.W., 1975, J. Phys. A, 8, 617.

Taylor, J.H. and Manchester, R.N., 1977, Ap. J., 215, 885.

Thaddeus, P., 1977, IAU Symp. No. 75, Star Formation, ed. T. de Jong and A. Maeder (Dordrecht: Reidel), p. 37.

Tucker, K.D., Dickman, R.L., Encrenaz, P.J. and Kutner, M.L., 1976, Ap. J., 210, 679.

Weaver, H., 1970, IAU Symp. No. 38, The Spiral Structure of Our Galaxy, ed. W. Becker and G. Contopoulos (Dordrecht: Reidel), p. 126.

Weaver, H. and Williams, R.D.W., 1973, Astron. Astrophys. Suppl. Ser., 8, 1.

Weaver, H., 1974, IAU Symp. No. 60, Galactic Radio Astronomy, ed. F.J. Kerr and S.C. Simonson (Dordrecht: Reidel), p. 573.

Weinreb, S., Barrett, A.H., Meeks, M.L. and Henry J.C., 1963, Nature, 200, 829.

Westerhout, G., 1973, Maryland-Green Bank Galactic 21-cm Line Survey, 3d ed.; University of Maryland.

Whiteoak, J.B. and Gardner, F.F., 1972, Astron. Astrophys. 21, 159.

Wootten, H.A., 1977, Ap. J., 216, 440.

Yuan, C., 1969, Ap. J., 158, 871.

Zeilik, M. and Lada, C.J., 1978, Ap. J., 222, 896.

Zuckerman, B. and Kuiper, T.B.H., 1980, Ap. J., 235, 840.

1. Report No. NASA TP-2288	2. Government Accession No.	3. Recipient's Catalog No.
4. Title and Subtitle MOLECULAR CLOUDS AND GALACTIC SPIRAL STRUCTURE		5. Report Date February 1984 6. Performing Organization Code 980
7. Author(s) Thomas M. Dame		8. Performing Organization Report No.
9. Performing Organization Name and Address Goddard Institute for Space Studies 2880 Broadway New York, NY 10025		10. Work Unit No. 11. Contract or Grant No.
12. Sponsoring Agency Name and Address National Aeronautics and Space Administration Washington, D.C. 20546		13. Type of Report and Period Covered Technical Paper 14. Sponsoring Agency Code

15. Supplementary Notes

16. Abstract

Galactic CO line emission at 115 GHz has been surveyed in order to study the distribution of molecular clouds in the inner galaxy. Comparison of this survey with similar HI data reveals a detailed correlation with the most intense 21-cm features. To each of the classical 21-cm HI spiral arms of the inner galaxy there corresponds a CO molecular arm which is generally more clearly defined and of higher contrast.

A simple model is devised for the galactic distribution of molecular clouds. The modeling results suggest that molecular clouds are essentially transient objects, existing for 15 to 40 million years after their formation in a spiral arm, and are largely confined to spiral features about 300 pc wide.

17. Key Words (Selected by Author(s))	18. Distribution Statement
Molecular clouds, Galactic spiral structure, Carbon monoxide	Unclassified - Unlimited STAR Category 90 Astrophysics

19. Security Classif. (of this report)	20. Security Classif. (of this page)	21. No. of Pages	22. Price*
Unclassified	Unclassified	277	A13

*For sale by the National Technical Information Service, Springfield, Virginia 22161

NASA-Langley, 1984